Lidar-Assisted Control Concepts for Wind Turbines

A thesis accepted by the Faculty of Aerospace Engineering and Geodesy of the University of Stuttgart in partial fulfillment of the requirements for the degree of Doctor of Engineering Sciences (Dr.-Ing.)

by

David Schlipf

born in Baden-Baden, Germany

Main referee:	Prof. Dr. Po Wen Cheng
Co-referees:	Prof. Dr. Martin Kühn and Prof. Dr. Lucy Pao
Date of defense:	1st of June 2015

Institute of Aircraft Design

University of Stuttgart

2016

Acknowledgements

It will not be possible to thank all people that have contributed to this thesis, but the most important ones shall be mentioned here.
First of all, I would like to thank Po Wen Cheng, Lucy Pao and Martin Kühn for providing me with excellent advice, great support and never-ending encouragement. Further, I would like to thank my colleagues at the University of Stuttgart for their collaboration in research, their help in all fields of our daily work, and the pleasant atmosphere. Special thanks to Ursula Smolka and Juan José Trujillo. My deep gratitude is also addressed to the students I had the privilege to supervise, especially Valeria Basterra, Patrick Grau, Stefan Kapp, Timo Maul, Davide Trabucchi, Ines Würth, Jan Anger, Florian Haizmann, Steffen Raach, and Frank Sandner for their significant contribution to this thesis. Thanks to Andreas Rettenmeier, Martin Hofsäß, Oliver Bischoff, and Holger Fürst of the SWE Lidar group and to all the other people who helped in getting the lidar systems and wind turbines running. I wish to express my sincere gratitude to Paul Fleming, Andrew Scholbrock, Pieter Gebraad, Kathryn Johnson and Alan Wright, which not only hosted me during the field testing at NREL, but also made this time the most enjoyable period of my PhD project with their support and company. I am also grateful for the fruitful discussions and valuable exchange with Fiona Dunne, Eric Simley, Jake Aho, and Jason Laks from CU Boulder, with Jakob Mann and Ameya Sathe from Risø DTU, with Ervin Bossanyi from DNV GL, and with Simone Schuler from the IST in Stuttgart.
I also would like to thank my friends and family for showing an interest in my work, their help in forgetting about it for some time, and their understanding if this wasn't possible.
And finally and most importantly, I owe my deepest gratitude to my wife Ana and my son Leonardo for their unlimited support.
The work presented has been mainly carried out in the scope of two German joint research projects "LIDAR - Further development of lidar wind measuring techniques for offshore application" and "LIDAR II - Development of nacelle-based lidar technology for performance measurement and control of wind turbines" funded by the German Federal Ministry for the Environment, Nature Conservation and Nuclear Safety (BMU). Thanks to the foundation Karl Schlecht Stiftung (KSG) for their financial support during the field testing.

Contents

Abbreviations

1P	one-per-revolution
3P	three-per-revolution
AF	Adaptive Filter
BEM	Blade Element Momentum
CART2	Controls Advanced Research Turbine, 2-bladed
CART3	Controls Advanced Research Turbine, 3-bladed
CFD	Computational Fluid Dynamics
CNR	Carrier-to-Noise Ratio
CPC	Collective Pitch Controller
DBS	Doppler Beam Swinging
DEL	Damage Equivalent Load
DLC	Design Load Case
DLL	Dynamic Link Library
DOF	Degree Of Freedom
DSC	Direct Speed Controller
EOG	Extreme Operating Gust
EP	Energy Production
FAST	Fatigue, Aerodynamics, Structures, and Turbulence
FB	Feedback
FF	Feedforward
FFT	Fast Fourier Transform
FWHM	Full Width at Half Maximum
IEC	International Electrotechnical Commission
IFB	Institut für Flugzeugbau (Institute of Aircraft Design)
IPC	Individual Pitch Control
ISC	Indirect Speed Controller
LES	Large Eddy Simulation
lidar	light detection and ranging
MIMO	Multiple-Input Multiple-Output
MPC	Model Predictive Controller
NMPC	Nonlinear Model Predictive Controller
NREL	National Renewable Energy Laboratory

NWTC	National Wind Technology Center
OCS	Optical Control System
ODE	Ordinary Differential Equation
PDE	Partial Differential Equation
PI	Proportional-Integral
PP	Pole Placement
PSD	Power Spectral Density
SC	System Constraint
SISO	Single-Input Single-Output
SLOW	Simplified Low Order Wind turbine
STD	STandard Deviation
SWE	Stuttgart Wind Energy
TEQUILA	Tower EQUILibirum Accommodation
TTC	Trajectory Tracking Controller
VAD	Velocity Azimuth Display
WITLIS	WInd Turbine and LIdar Simulator

List of Symbols

Greek letters

α	angle of attack at blade segment
α_{h}	horizontal inflow angle
α_{L}	half opening angle of circular lidar scan
α_{shear}	wind shear exponent of exponential power law approximation
α_{ux}	longitudinal decay parameter
α_{v}	vertical inflow angle
β	twist angle of blade segment
δ_{h}	linear horizontal wind shear
δ_{v}	linear vertical wind shear
ε	rotor speed error
γ	coherence
κ	frequency dependent lateral decay parameter
λ	tip speed ratio
Λ_1	turbulence scale parameter
λ_{L}	laser wavelength
λ_{opt}	tip speed ratio chosen for region 2
μ	mode shape
ω	angular frequency
Ω	rotor speed: angular velocity [rad/s], displayed as rotational speed [rpm]
Ω_{W}	angular velocity of wind turbine wake
Ω_{G}	generator speed: angular velocity [rad/s], displayed as rotational speed [rpm]
ω_{PA}	undamped natural frequency of pitch actuator
η_{el}	efficiency of the electro-mechanical energy conversion
ϕ	angular coordinate
Φ	roll angle; phase angle
Ψ	yaw angle
ρ	air density
σ	standard deviation
τ	feedforward prediction time
θ	collective blade pitch angle
Θ	pitch angle
θ_{c}	controller output for collective blade pitch angle
θ_{fine}	minimum blade pitch angle for ensuring region 3 torque
ξ_{PA}	damping factor of pitch actuator

Roman letters

a	distance to focus point along laser beam; filter coefficient; amplitude
A	peak-to-peak amplitude of load cycle for fatigue load calculations
$\boldsymbol{A}$	matrix of known values for least squares method
a_{an}	angular induction factor
a_{ax}	axial induction factor
b	filter coefficient
c	chord of blade section; damping; speed of light
c_{D}	drag coefficient
c_{eT}	tower equivalent structural damping
c_{L}	lift coefficient
c_{P}	power coefficient
c_{T}	thrust coefficient
C_{WB}	Weibull scale parameter
$\boldsymbol{d}$	vector of disturbance inputs
D	rotor diameter; damping ratio
D_{a}	aerodynamic drag force
d_{s}	structural damping ratio
$\boldsymbol{f}$	general force vector
f	frequency
F	Force
f_0	undamped eigenfrequency
F_{a}	aerodynamic thrust
f_{D}	Doppler frequency shift
f_{L}	frequency of emitted light of lidar system
f_{RW}	lidar range weighting function
f_{s}	sampling frequency
f_{WB}	Weibull probability density function
g	gain
G	transfer function
h	running variable
i	running variable
i	imaginary unit
I	turbulence intensity, modified Bessel function of the first kind
i_{GB}	gearbox ratio
j	running variable
J	sum of the moments of inertia about the rotation axis
k	stiffness; wavenumber
$k_{0.5}$	coherence bandwidth: wavenumber at coherence level of 0.5
k_{eT}	tower equivalent bending stiffness
$\hat{k}$	maximum coherent wavenumber: wavenumber at transfer function level of $-3\,\mathrm{dB}$
k_{ISC}	gain of quadratic state feedback controller for indirect speed control in region 2
k_{WB}	Weibull shape parameter
L	integral length scale; modified Struve function
L_{a}	aerodynamic lift force
m	Wöhler exponent, mass

$\boldsymbol{m}$	vector of measured values for least squares method
$\boldsymbol{M}$	general mass matrix
M_a	aerodynamic torque
m_eT	tower equivalent mass
M_flp1	blade root flapwise bending moment of blade 1
M_G	generator torque
M_LSS	low-speed shaft torque
M_oop1	blade root out-of-plane bending moment of blade 1
$M_{y\mathrm{T}}$	tower base fore-aft bending moment
n_B	number of blades
n_C	number of data chunks
n_D	number of measurement distances
n_F	number of discrete frequencies
n_LC	number of cycles for fatigue load calculations
n_P	number of points per lidar scan
n_R	number of grid points in rotor disk
n_RW	number of discretized points of the range weighting function
n_S	number of blade or tower segments
p	pressure
P_el	electrical power
$\boldsymbol{q}$	vector of modal coordinates
r	radial coordinate; distance between points
R	rotor radius; cross correlation; coefficients of determination
$r_{\mathrm{L}i}$	distance from lidar system to measurement point i
$\boldsymbol{s}$	vector of unknown values for least squares method
S	cross-spectrum or auto-spectrum
t	time
T	time delay
T_ACQ	lidar acquisition time
T_B	time delay caused by blades and pitch actuator
T_buffer	buffer time of preview signal
$\boldsymbol{T}_{\mathcal{IW}}$	transformation matrix from the wind to the inertial system
T_scan	duration of a full scan with lidar system
T_Taylor	propagation time of wind field to rotor
$\boldsymbol{T}_{\mathcal{WI}}$	transformation matrix from the inertial to the wind system
$\boldsymbol{u}$	vector of control inputs
u	longitudinal wind speed
$\bar{u}$	mean wind speed
v	lateral wind speed
v_0	rotor effective wind speed
$v_{0\mathrm{L}}$	lidar estimate of the rotor effective wind speed
$v_{0\mathrm{R}}$	rotor estimate of the rotor effective wind speed
$\mathcal{V}$	three-dimensional wind field
v_inflow	inflowing wind speed at blade section
v_los	line-of-sight wind speed
v_rel	relative wind speed

w	vertical wind speed
x	longitudinal coordinate; longitudinal displacement
$x_{0\mathrm{T}}$	static longitudinal tower top displacement
x_{T}	longitudinal tower top displacement
$\boldsymbol{y}$	vector of measured outputs
y	lateral coordinate; lateral displacement
z	vertical coordinate; vertical displacement

Subscripts

$(\cdot)_a$	referring to distance a to a measurement point
$(\cdot)_{\mathrm{cutoff}}$	referring to a cut-off frequency of a filter
$(\cdot)_{\mathrm{d}}$	referring to a desired state
$(\cdot)_{\mathrm{f}}$	referring to a filtered signal
$(\cdot)_{\mathrm{FF}}$	referring to feedforward control
$(\cdot)_{\mathrm{filter}}$	referring to a filter
$(\cdot)_h$	referring to running variable h
$(\cdot)_{\mathrm{H}}$	referring to hub
$(\cdot)_i$	referring to running variable i
$(\cdot)_{\mathcal{I}}$	referring to inertial frame coordinate system
$(\cdot)_j$	referring to running variable j
$(\cdot)_{\mathrm{L}}$	referring to lidar
$(\cdot)_{\mathcal{L}}$	referring to lidar coordinate system
$(\cdot)_{\mathrm{max}}$	referring to a maximum value
$(\cdot)_{\mathrm{min}}$	referring to a minimum value
$(\cdot)_{\mathrm{n}}$	referring to normalized coordinate
$(\cdot)_{\mathrm{R}}$	referring to rotor
$(\cdot)_{\mathrm{rated}}$	referring to a rated value in region 3
$(\cdot)_{\mathrm{ref}}$	referring to a reference
$(\cdot)_{\mathrm{S}}$	referring to (ultra)-sonic anemometer
$(\cdot)_{\mathrm{ss}}$	referring to steady state
$(\cdot)_{\mathrm{T}}$	referring to tower top
$(\cdot)_{\mathcal{W}}$	referring to wind coordinate system

Operators

$\mathcal{F}\{\cdot\}$	Fourier transform
$\mathcal{F}^*\{\cdot\}$	complex conjugate of Fourier transform
$\delta(\cdot)$	Dirac delta function
$\Delta(\cdot)$	Dirac comb
$\hat{(\cdot)}$	estimated value of $(\cdot)$
$\mathrm{rect}(\cdot)$	rectangular function
$(\cdot)^+$	Moore-Penrose pseudoinverse
$(\cdot)^{\mathrm{T}}$	transposed

Abstract

In recent years lidar technology has found its way into wind energy. At the beginning of the research of the present thesis project, "Lidar-Assisted Control Concepts for Wind Turbines", the main application was the assessment of sites for wind turbine installations. The possibility to optimize the energy production and reduce the structural loads by nacelle or spinner based lidar systems was already considered a promising field of application. This is because of the fact that wind turbines are highly dynamic systems that are excited by stochastic influences from the wind and most of the wind turbine control is designed to deal with variations in this disturbance. However, traditional feedback controllers are only able to react to impacts of wind changes on the turbine dynamics after these impacts have already occurred. Lidar-assisted control algorithms, which can exploit preview information of the wind, are promising to provide improved operation over conventional control algorithms, with the ultimate aim of increasing the energy yield while keeping the structural loads low. The principle can be depicted by an analogue: a person riding, and thus controlling, a bicycle uses the vision and the prediction of the movements to circumvent obstacles instead of reacting to the impact of the obstacle on the wheels. In a similar way, lidar-assisted wind turbine control is expected to improve the control performance significantly over conventional feedback controllers.

Due to limitations in the lidar measurement principle, the complexity of the wind, and nonlinear dynamics of the wind turbines, lidar-assisted control of wind turbines is a highly interdisciplinary field of research, including meteorology, signal processing, remote sensing, mechanics and control. This thesis provides important pioneering work in the field of lidar-assisted wind turbine control by not only investigating possible control applications, but also by developing appropriate lidar data processing methods. Because of this holistic and integrated approach, the world's first proof-of-concept of lidar-assisted control could be successfully performed within this thesis project.

This final result has been achieved by dividing the overall problem in to separate measurement and control problems. The measurement problem addresses the question: how can signals which are useful for control be extracted from lidar measurements? The control problem addresses the question: how can these signals then be used to improve the performance of wind turbine

control. However, these questions are highly correlated with each other. While the data generated by the measurement device must contain useful information to allow for improving the control performance, the control algorithm itself requires continuous adaptation to the quality and information content present in the measurements. Furthermore, the level of detail of the computational models of the wind turbine and the disturbances employed by the control algorithm must also be in accordance with the measurement quality and at the same time they should meet the requirements imposed by the chosen control approach.

Based on these considerations, the first part of this thesis presents the work done in the field of processing raw lidar data. Here, two important issues have been addressed and solved for providing signals for lidar-assisted control from raw lidar data. The first issue addressed is the limitation of line-of-sight wind speeds. The lidar system measures the speed of the aerosols traveling in the direction of the laser beam, thus only a one-dimensional component of the three-dimensional wind vector. Therefore, it is mathematically impossible to measure a three-dimensional wind vector with a single nacelle or spinner based lidar system. To solve this issue, model-based estimation techniques have been developed to provide a good estimate of wind characteristics such as the rotor effective wind speed. The second important issue for processing raw lidar data is that the wind characteristics measured by a lidar system will differ from those experienced by the turbine, because of several effects such as wind evolution. In this thesis an analytic model has been developed which calculates the correlation between the lidar estimates and the reaction of the wind turbine. The model can be used to optimize lidar scan configurations and to design an adaptive filter essential for preview control of wind turbines.

The second part presents possible lidar-assisted control concepts. All controllers are designed first for the case of perfect wind speed measurements and then adjusted for realistic measurements. The most promising approach is the collective pitch feedforward controller using the knowledge of the incoming wind speed. The approach provides an additional control update to assist common collective blade pitch control and therefore is convenient for industrial applications. Significant improvement in rotor speed regulation and in load reduction were achieved in realistic simulations and have been confirmed with successful field tests on two research wind turbines. Further, a feedforward control strategy for the generator torque to increase the energy production has been developed. Although the controller is able to significantly increase the tracking of the optimal inflow conditions even under realistic simulations, only a marginal increase in energy output at the expense of raised fluctuations of the generator torque can be achieved. Moreover, a flatness-based feedforward approach has been designed that allows the calculations of the control action based on trajectories of the rotor speed and tower motion. With this approach, the tower loads can be regulated directly by providing an update to the collective pitch and the generator torque. An analysis with simulated lidar measurements reveals that the tower loads can be further reduced compared to the collective pitch feedforward controller. However, the flatness-based controller is more difficult to tune.

Kurzfassung

In den letzten Jahren hat die Lidar-Technology ihren Weg in die Windenergie gefunden. Zum Beginn der vorliegenden Doktorarbeit „Konzepte Lidar-basierter Regelung von Windenergieanlagen" wurden Lidar-Systeme hauptsächlich zur Standortbewertung eingesetzt. Aber auch ein weiteres Anwendungsgebiet wurde als sehr aussichtsreich eingestuft: die Installation von Lidar-Systemen auf Windenergieanlagen zur Optimierung des Energieertrags und zur Reduktion von strukturellen Lasten. Dies lag nahe, da eine Windenergieanlage ständig auf die Turbulenzen des einströmenden Windfeldes reagieren muss. Traditionelle Regelsysteme für Windenergieanlagen können jedoch erst dann auf Windänderungen reagieren, wenn diese schon auf die Struktur der Anlage gewirkt hat. Lidar-basierte Regelsysteme können die Windvorhersage nutzen und sind deshalb vielversprechend, um den Energieertrag zu erhöhen und gleichzeitig die Belastungen gering zu halten. Dies kann mit einer Analogie verdeutlicht werden: Um Hindernisse zu umfahren, ist es für einen Fahrradfahrer besser, seine Sicht für die Vorausplanung seiner Bewegungen zu verwenden, als darauf zu warten, bis die Hindernisse über den Kontakt mit dem Fahrrad selbst wahrgenommen werden. In ähnlicher Weise wird erwartet, dass Lidar-basierte Methoden gegenüber konventionellen Ansätzen die Regelung von Windenergieanlagen signifikant verbessern wird. Lidar-basierte Regelung ist durch Limitierungen im Lidar-Messprinzip, durch die Komplexität des Windes und durch die nichtlineare Dynamik von Windenergieanlagen ein äußerst interdisziplinäres Forschungsgebiet und verbindet die Fachbereiche Meteorologie, Signalverarbeitung, Fernerkundung, Mechanik und Regelung.

Für dieses Forschungsgebiet wurden in dieser Arbeit wichtige Grundlagen erarbeitet, nicht nur durch die Erforschung möglicher Regelungskonzepte, sondern auch durch die Entwicklung geeigneter Methoden für die Verarbeitung von Lidar-Messdaten. Durch einen integrierten und ganzheitlichen Ansatz konnte der weltweit erste Nachweis der Machbarkeit erbracht werden.

Dieses Ergebnis wurde durch eine zunächst separate Betrachtung der messtechnischen und regelungstechnischen Problematik erreicht. Die Aufgabe der Messtechnik ist es, für die Regelung verwendbare Signale aus den Lidar-Rohdaten zu generieren. Die Regelungstechnik ist dafür verantwortlich, mit diesen Signalen eine Verbesserung für Windenergieanlagen zu erreichen. Beide Bereiche sind stark miteinander vernetzt. Zum einen müssen die vom Messgerät zur Verfügung

gestellten Signale diejenigen Informationen enthalten, welche die Verbesserung der Regelung ermöglichen. Zum anderen muss sich das Regelungssystem kontinuierlich auf die Veränderung der Messqualität einstellen. Außerdem müssen die für den Entwurf der Regelung notwendigen mathematischen Modelle nicht nur den Anforderungen des Regelungskonzepts entsprechen, sondern auch auf die Messbarkeit der Störgröße Wind abgestimmt sein.
Basierend auf diesen Überlegungen behandelt der erste Teil dieser Doktorarbeit die Entwicklung geeigneter Methoden für die Verarbeitung von Lidar-Messdaten. Hier sind Lösungsansätze für zwei Problemstellungen erarbeitet worden. Die erste Problemstellung ergibt sich aus dem Lidar-Messprinzip: Ein Lidar-System misst die Geschwindigkeit von Aerosolen nur in Richtung des ausgesendeten Laserstrahls. Deshalb kann mit einem einzigen Lidar-System das einströmende Windfeld nicht dreidimensional erfasst werden. Deshalb wurden in dieser Arbeit modellbasierte Schätzverfahren entwickelt, welche für charakteristische Größen wie die rotoreffektive Windgeschwindigkeit gute Näherungswerte erreichen. Damit verbunden ist die zweite Problemstellung. Durch das Schätzverfahren, aber auch durch die Evolution des Windfeldes auf dem Weg zum Rotor ergeben sich Unterschiede zwischen den Charakteristiken des Windes, welche vom Lidar-System gemessen werden und den Charakteristiken, welche auf den Rotor wirken. In dieser Arbeit wurde ein analytisches Model für die Korrelation zwischen den Näherungswerten aus der Lidar-Messung und der Reaktion der Anlage entwickelt. Dieses Modell kann zur Optimierung von Scan-Trajektorien und für den Entwurf eines für die lidar-basierte Regelung essentiell wichtigen adaptiven Filter verwendet werden.
Der zweite Teil der Doktorarbeit stellt die entwickelten Regelungskonzepte vor. Alle Regelalgorithmen wurden zunächst unter der Annahme von perfekter Windvorhersage entworfen und dann für realistische Messungen angepasst. Der vielversprechendste Ansatz ist die Vorsteuerung des kollektiven Blattwinkels. Diese Methode unterstützt mit einer Aufschaltung konventionelle Regelungssysteme und ist deshalb sehr für die industrielle Anwendung geeignet. Eine signifikante Reduktion der strukturellen Lasten und eine Verbesserung der Rotordrehzahlregulierung konnte in realistischen Simulationen erreicht und in experimentellen Tests auf zwei Forschungsturbinen bestätigt werden. Des Weiteren wurde eine Vorsteuerungsstrategie entwickelt, welche mit Hilfe des Generatormoments den Energieertrag erhöht. Obwohl mit diesem Regler die Windenergieanlage sehr viel näher am aerodynamischen Optimum betrieben wird, kann neben zusätzlichen Belastungen der Energieertrag nur geringfügig erhöht werden. Zudem wurde eine Vorsteuerung entworfen, welche auf der Systemeigenschaft der „Flachheit" beruht und die Regelung mit Solltrajektorien der Rotordrehzahl und der Turmkopfbewegung ermöglicht. Mit diesem Ansatz können durch eine gleichzeitige Aufschaltung des kollektiven Blattwinkels und des Generatormoments die Turmbewegungen direkt beeinflusst werden. In einer Simulationsstudie konnte gezeigt werden, dass die Turmbelastungen gegenüber der alleinigen Vorsteuerung des kollektiven Blattwinkels weiter reduziert werden können. Allerdings ist das Einstellen der flachheitsbasierten Vorsteuerung deutlich komplexer.

1

Introduction

1.1 Motivation

In recent years, the lidar (light detection and ranging) technology has found its way into wind energy. The main application is still in site assessment, but the possibility to optimize the energy production and reduce the loads by nacelle or spinner based lidar systems is becoming an important issue. This is due to the fact that wind turbines are highly dynamic systems that are excited by stochastic loads from the wind and most of the wind turbine control is designed to deal with variations in this disturbance. However, traditional feedback controllers are only able to react to impacts of wind changes on the turbine dynamics after these impacts have already occurred. Control algorithms with preview information of the wind are promising to provide an improved operational performance over conventional control algorithms with the ultimate aim of increasing the energy yield while keeping the structural loads low. The principle can be depicted by an example from daily life: a person riding, and thus controlling, a bicycle sees obstacles in advance and therefore avoids a crash far before he would feel the impact. In a similar way, lidar measurements in front of the rotor are expected to provide wind preview information and thus lidar-assisted wind turbine control is expected to improve the control performance significantly over conventional feedback controllers.
Due to limitations in the lidar measurement principle, the complexity of the wind, and the nonlinear dynamics of wind turbines, lidar-assisted control is a highly interdisciplinary field of research, including the fields of meteorology, signal processing, mechanics and control.

Figure 1.1: Vision of lidar-assisted control from [1]: Examples of scanning options.

1.2 Related Work

Early work on lidar-assisted control was reported before the start of this PhD project in [1]. In this report, a linear Disturbance Accommodating Controller for individual pitch control was presented which incorporated the signals provided by a lidar simulator scanning the wind field during an aero-elastic simulation and demonstrate the possible improvement in blade load mitigation. Additionally, several lidar scanning options have been proposed, see Figure 1.1.
Since then, this field of investigation has increased significantly and several other researcher achieved promising results for lidar data processing as well as for lidar-assisted blade pitch, generator torque, and yaw control in parallel to this PhD project. In this section, the main achievements are summarized.

1.2.1 Lidar Data Processing

Before the data from a lidar system can be used for lidar-assisted control of wind turbines, the raw lidar data must be processed and transformed into signals that can be used by the control system. The two main important research topics are the reconstruction of wind characteristics and the assessment of the measurement quality.
In order to reconstruct the horizontal inflow angle (equal to yaw misalignment) based on measurements from a spinner mounted lidar system measuring in one plane in front of the rotor, a heuristic method is developed and applied to real data in [2, 3]. In [4], an approach is presented which enables the reconstruction of five wind characteristics (mean wind speed, vertical and horizontal linear shear, and vertical and horizontal inflow angle) based on minimal three measurements in two planes in front of the rotor, a nonlinear model, and assuming Taylor's Frozen Turbulence Hypothesis. In [5], a real-time reconstruction algorithm using a model based on simplified Navier-Stokes equations shows promising results for a two-beam lidar system in a Large Eddy Simulation (LES). Local wind speed and angle-of-attack have been reconstructed from the measurement of a blade-mounted dual-telescope lidar system in [6].

The quality of a single point wind speed measurement is compared to lidar measurements including the effect of range weighting, limitation to line-of-sight direction and wind evolution in [7]. In [8], a model for the correlation between lidar measurement and the blade effective wind speed is derived and used in [9] for an optimal filter design. In [10] it is pointed out, that not only the filtering according to the correlation is important, but also the timing accuracy of the signal provided to the lidar-assisted controller is crucial.

1.2.2 Blade Pitch Control

Modern wind turbines usually pitch their blades out of the wind to regulate the rotational speed and reduce structural loads during high wind speeds. Several feedforward controllers and Model Predictive Controllers (MPCs) using collective or individual blade pitch control are proposed to improve the control performance based on the information from a lidar system.
The feedforward controllers can be used in addition to conventional feedback controller, which is beneficial for industrial applications. In [11, 12] several linear model inverse controllers are proposed for collective pitch control based on the preview of the rotor effective wind speed. The work in [13, 14, 15, 16] shows that either blade effective wind speed preview or preview of the wind shears can be used to assist individual blade pitch control. In [17], linear controllers such as a filtered-x recursive least squares, linear-quadratic, and $\mathcal{H}_\infty$ are designed and tested. The $\mathcal{H}_2$ approach from [18, 19] includes the measurement uncertainties directly in the control design. In [20, 21, 22], the nonlinear controller proposed in this work has been extended with feedback elements.
The MPCs are able to incorporate the wind preview into an optimization problem and thus optimize the control actions using the predicted wind turbine behavior over a finite time horizon. Although the conventional feedback controller is usually replaced and real-time implementation is hard to achieve, a MPC has the advantage that multivariable control, actuator and systems constraints can be taken into account. The work done in the last years can be organized based on the control inputs, the wind preview or the internal model: While in [23], a MPC is proposed for individual pitch control, a MPC is used to adjust the collective pitch alone in [24], or together with the generator torque in [25, 26, 27, 28, 29, 30, 31, 32]. While some work [25, 28] considers perfect wind preview or from an estimator [26, 27], a more realistic preview is used in [23, 24, 29, 30, 31, 32]. Further, linear models are used in [23, 27], linear parameter varying models in [26, 31], and nonlinear models in [25, 24, 29, 28, 30, 32].

1.2.3 Generator Torque Control

For low wind speeds, the rotor speed of modern wind turbines is adjusted using the generator torque. With the wind speed information of a lidar system, a better tracking of the aerodynamic optimum and thus a higher energy capture can be expected.
Some work in this field [33, 34, 35] claim significant improvements. However, the simulation study in [21] reports only minor increase in power production at the expense of unacceptable loads on the rotational shaft. A lidar-assisted torque controller is proposed in [36] which reduced the rotor speed variation without much cost in structural loads in the transition region between partial and full load operation.

1.2.4 Yaw Control

The rotor of modern upwind wind turbines needs to be aligned with the wind direction in order to generate the maximum possible power. Due to the large moment of inertia of the rotor about the yaw axis, the nacelle is aligned with the wind with slow rates and only if the misalignment exceeds a threshold [37]. Traditionally, the yaw misalignment is measured with a wind vane on a single point on the nacelle, where the wind is disturbed by the nacelle geometry and passing blades. Using lidar systems has the advantage that the yaw misalignment can be extracted from multiple measurement points in the undisturbed flow in front of the rotor.
In [2], a simulation study shows that a spinner-mounted lidar system can estimate the 10-minute-mean values with median errors below 3 degrees even during high turbulent wind. In another simulation study, the lidar does not have an obvious advantage over a conventional measurements, but points out that standard 10-minute simulations are too short in order to draw a definitive conclusion [21]. Further, a the simulation study in [38] is carried out based on lidar data measured from a real experiment over several month. For the simulations, the 10-minute-mean wind direction is extracted from a nacelle-mounted lidar system and a conventional sensor, and then a standard yaw controller is simulated for both signals. By assuming a perfect measurement of the lidar system, the maximum achievable increase in energy production of 1.1 % provides an upper limit for the used turbine and site. In a field test experiment, an increase in the energy production of 2.4 % could be observed after correcting on offset in the wind vane measurement based on lidar measurements [39], and the direct use of a lidar system to control the yaw set point was demonstrated in [40].

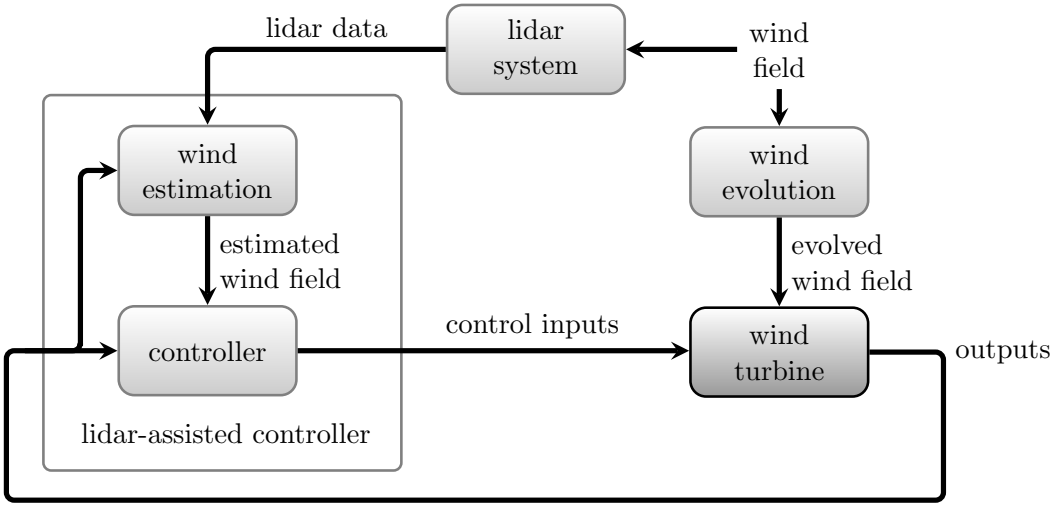

Figure 1.2: Basic control loop of lidar-assisted wind turbine control.

1.3 Research Objectives, Methodology and Organization

The overall goal of the present thesis "Lidar-Assisted Control Concepts for Wind Turbines" is to investigate and evaluate several possible applications of lidar-assisted control and to finally provide a proof-of-concept of the most promising one. Figure 1.2 shows the basic control loop of lidar-assisted wind turbine control: the wind field in front of the turbine is measured by a lidar system and the information is transfered to the lidar-assisted controller. The wind field evolves on its way towards the turbine and causes changes in the measured outputs, such as the rotational speed. The lidar-assisted controller then calculates appropriate control actions from the system outputs and the lidar data.

The main approach in this work is to divide the design of lidar-assisted controller into an estimation and a control problem. The estimation problem deals with the question of how signals useful for control can be extracted from lidar measurements. The control problem deals with the question of how these signals can then be used to improve the performance of wind turbine control. However, these questions are highly correlated with each other: While the data generated by the measurement device must contain useful information to allow for improving the control performance, the control algorithm itself requires continuous adaptation to the quality and information content present in the measurements. Furthermore, the level of detail of the computational models of the wind turbine and the disturbances employed by the control algorithm does not only have to meet the requirements imposed by the chosen control approach, but also needs to be in accordance with the measurement quality. To exemplify, it is not advisable to establish a three-dimensional wind field model interacting with several rotor blade sections, if neither the used control approach can handle this model complexity nor the real three-dimensional wind is measurable with the chosen sensor. In the case of collective blade pitch control, modeling the impact of a one-dimensional rotor effective wind speed will

be better suited for the controller and can be provided by lidar.
After this introduction (Chapter 1), the thesis continues with providing background information in Chapter 2 and presenting the models and simulation tools used in the work in Chapter 3.
Then, the first main part of this thesis will present the work done in the field of processing raw lidar data, addressing the above mentioned estimation problem. There are two important issues which have to be considered, when processing signals for lidar-assisted control from raw lidar data: First, it is mathematically impossible to measure a three-dimensional wind vector with a single nacelle or spinner based lidar system due to the limitation of the line-of-sight wind speed: the wind speed recorded by a lidar system is the speed of the aerosols traveling in the direction of the laser beam. Thus, only one scalar value of the three-dimensional wind vector is measured. Nevertheless, lidar systems can provide a good estimate of wind characteristics such as wind speed, wind direction or shears for control using certain assumptions such as homogeneous flow. These methods will be described in the Chapter 4.
Second, there is a variety of effects, such as the evolution of the wind, the estimation process mentioned above, and measurement uncertainties which makes the wind turbine experience wind loads that differ from the ones expected from the measurements. In general, only the low frequencies can be predicted accurately. Chapter 5 will present an analytic model to calculate the correlation between the lidar estimates and the reaction of the wind turbine using models of wind turbulence, wind evolution and lidar measurements, as well as methods from signal processing. The model can be used to optimize lidar scan configurations and to design an adaptive filter essential for preview control of wind turbines.
In the second main part of the thesis, several controllers are presented, addressing the above mentioned control problem. All controllers are designed first for the case of perfect measurement and then adjusted for realistic measurements. The most promising approach is the collective pitch feedforward controller presented in Chapter 6. The knowledge of the incoming wind speed is translated into an additional control update to assist common collective pitch control. Additional load reduction compared to the state-of-the-art feedback controllers can be achieved. The concept has been successfully tested on two research wind turbines. In Chapter 7 a feedforward control strategy to increase the energy production by tracking optimal inflow conditions is presented. The comparison to existing indirect speed control strategies shows a marginal increase in energy output at the expense of raised fluctuations of the generator torque. Further, a flatness-based feedforward approach is designed in Chapter 8. It allows the calculation of the control action based on trajectories of the rotor speed and tower motion using wind measurements. The trajectories are planned online considering actuator constraints to regulate the rotor speed and minimize tower movements. The feedforward signals of the collective pitch and generator torque update can be combined with conventional feedback controllers.
The thesis concludes with Chapter 9, where conclusions and recommendations for further research are given.

2

Background

An understanding of the wind resource, the lidar systems, and the wind turbines is important to all aspects of this work. In this chapter some background information is given regarding wind turbines (Section 2.1), wind resource (Section 2.2), lidar systems (Section 2.3), and wind turbine control (Section 2.4). This information is then revisited in the corresponding sections in Chapter 3 to describe the work specific to modeling.

2.1 Wind Turbines

This section provides a short general overview of modern wind turbines, their aerodynamics, and their structural dynamics, load analysis, and simulations. The Chapter is mainly based on [41] and [37], where more details can be found.

2.1.1 Development of Modern Wind Turbines

Whereas wind mills have been used for grinding corn and pumping water for more than a thousand years, the use for generating energy started at the end of the 19th century. Before the oil crisis in 1973, several attempts to establish wind turbines as an important source of electrical energy were undertaken worldwide, but were unsuccessful due to the low prices of fossil fuels. One of the pioneers of this time was Ulrich Hütter, who refined the aerodynamics of the rotor blades and started to use glass-fiber composite materials. He introduced wind energy research at the Institut für Flugzeugbau (Institute of Aircraft Design) (IFB), University of Stuttgart, see Figure 2.1 (left), and his work has helped influence the design of current

Figure 2.1: Left: Hütter wind turbine with rated power of 10 kW in front of the IFB building, Stuttgart, Germany. Center: CART3 with rated power of 550 kW at National Renewable Energy Laboratory (NREL), Boulder, USA (foreground). Right: AREVA M5000 with rated power of 5 MW in Bremerhaven, Germany.

wind turbines. The search for alternative energy sources after the oil crisis stimulated the investigation and developments in wind energy, resulting in a still increasing global installed wind power capacity, see Figure 2.2. Today, wind power provides a significant contribution to the energy production and reached 8 % in Germany, and even 33 % in Denmark, of the total electricity consumption [42].

In parallel with this trend, wind turbines also have increased in size over the decades: the Controls Advanced Research Turbine, 3-bladed (CART3) which was used in this thesis research for field testing, was a typical wind turbine at the end of the 20th century with a rotor diameter of around 40 m, see Figure 2.1 (center, foreground). The first lidar measurements for this work have been taken from the nacelle of the AREVA M5000 with a rotor diameter of 116 m, see Figure 2.1 (right). As of 2014, the Vestas V-164 is the world's largest turbine with a rotor diameter of 164 m and rated power of 8 MW.

2.1.2 Aero-Elastic Simulations of Wind Turbines

Wind turbines are usually simulated with aero-elastic simulation tools. These codes have reliable accuracy at the system level [43] and are applied in certification processes.

In this work, the open source tool Fatigue, Aerodynamics, Structures, and Turbulence (FAST) from NREL is used for simulations. It combines subroutines of aerodynamic and structural dynamics. For more details see [44]. The principles of both parts are presented in the next subsections. This background is important to understand the model reduction derived in Chapter 3.

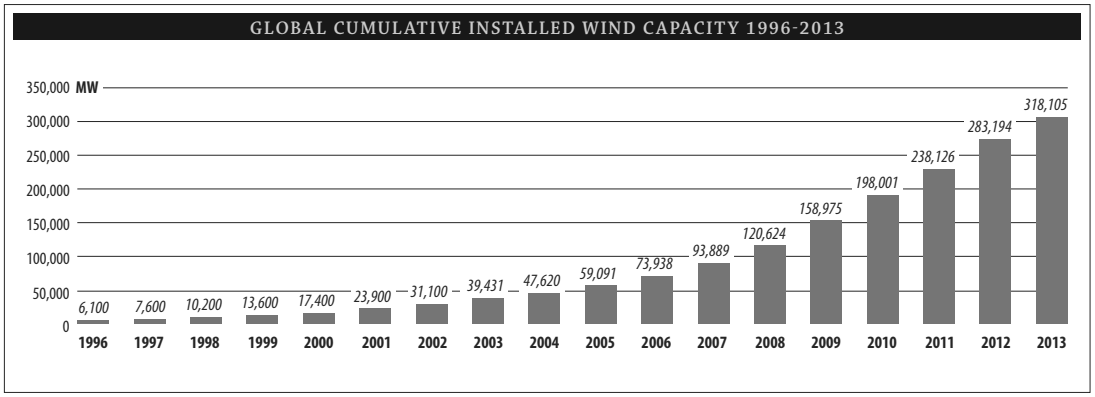

Figure 2.2: Trend of global cumulative installed wind capacity over the last 18 years [42].

Aerodynamics of Wind Turbines

State-of-the art simulation tools usually apply Blade Element Momentum (BEM) theory. Here, two approaches provide equations for the aerodynamic thrust and torque, which when combined can be solved iteratively by assuming that there are no aerodynamic interactions between blade elements [45]. The first method (Momentum Theory) uses a force and momentum balance on an annular stream tube. The second (Blade Element Theory) is based on the lift and drag forces at various sections along the blade.

Momentum Theory models the force balance in a stream tube at a radius r and with a radial width of dr, see Figure 2.3. Three stations are considered: upstream (1), at the rotor (2) and downstream (3). The starting point for the aerodynamic thrust is the force dF_a in the annular stream tube at the rotor defined as the pressure difference Δp_2 multiplied by its area $2\pi r\mathrm{d}r$:

$$\mathrm{d}F_\mathrm{a} = \Delta p_2 \, 2\pi r \mathrm{d}r. \tag{2.1}$$

Further the following set of equations is considered:

$$\Delta p_2 = \frac{1}{2}\rho(u_1^2 - u_3^2) \tag{2.2a}$$

$$a_\mathrm{ax} = \frac{u_1 - u_2}{u_1} \tag{2.2b}$$

$$u_2 = \frac{1}{2}(u_1 + u_3). \tag{2.2c}$$

Equation (2.2a) is based on Bernoulli's equation, where ρ is the air density and u_i is the longitudinal wind speed at station i. Equation (2.2b) defines the axial induction factor a_ax,

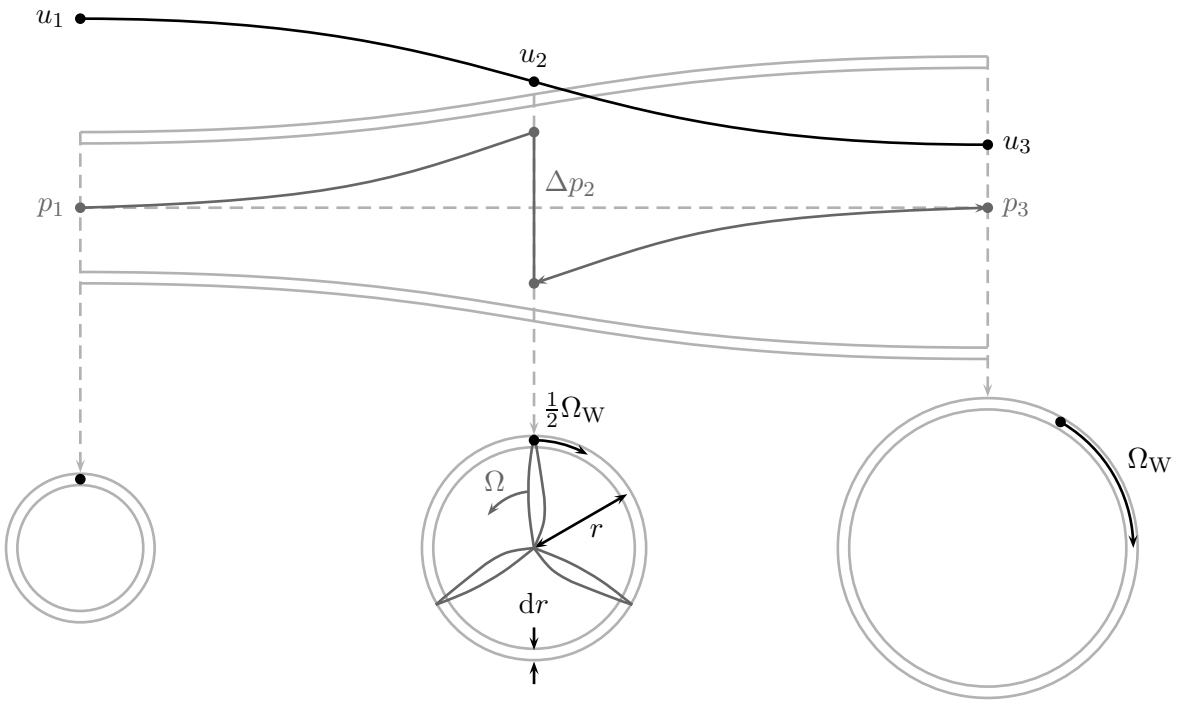

Figure 2.3: Annular stream tube with axial velocity, swirl and pressure distribution, side view (top), cross section (bottom), based on [41, 45].

and (2.2c) is the Froude-Rankine theorem. Combining (2.1) with (2.2), one obtains

$$\mathrm{d}F_\mathrm{a} = \frac{1}{2}\rho u_1^2\, 4a_\mathrm{ax}(1-a_\mathrm{ax})\, 2\pi r \mathrm{d}r. \tag{2.3}$$

In the next step, the momentum balance is modeled. The calculation starts by setting the aerodynamic torque $\mathrm{d}M_\mathrm{a}$ in a circular segment equal to the rate of the angular momentum from the annular stream tube. The rate is then defined as the angular velocity Ω_W of the wake multiplied by the rotating mass flow $\rho u_2 2\pi r \mathrm{d}r$ times the radius squared:

$$\mathrm{d}M_\mathrm{a} = \Omega_\mathrm{W}\, \rho u_2 2\pi r \mathrm{d}r\, r^2. \tag{2.4}$$

With the definition of the angular induction factor

$$a_\mathrm{an} = \frac{\Omega_\mathrm{W}}{2\Omega}, \tag{2.5}$$

where Ω is the rotor speed and (2.2b), one finally obtains

$$\mathrm{d}M_\mathrm{a} = 2\Omega a_\mathrm{an}\, \rho u_1 (1-a_\mathrm{ax}) 2\pi r \mathrm{d}r\, r^2. \tag{2.6}$$

With Blade Element Theory, the lift and drag force normal and parallel to the inflowing wind

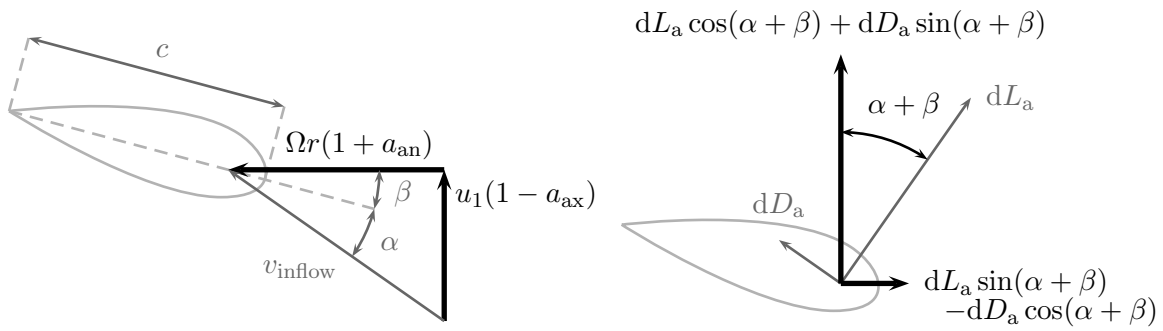

Figure 2.4: Blade element velocities (left) and forces (right), based on [41].

speed v_{inflow} of a blade section with a chord c are

$$\mathrm{d}L_{\mathrm{a}} = \frac{1}{2}\rho v_{\text{inflow}}^2 c_{\mathrm{L}}(\alpha)\, c\, \mathrm{d}r \tag{2.7a}$$

$$\mathrm{d}D_{\mathrm{a}} = \frac{1}{2}\rho v_{\text{inflow}}^2 c_{\mathrm{D}}(\alpha)\, c\, \mathrm{d}r, \tag{2.7b}$$

where $c_{\mathrm{L}}(\alpha)$ and $c_{\mathrm{D}}(\alpha)$ are the lift and drag coefficients depending on the angle of attack α. Here, β is defined as the inclination of the blade segment with respect to the rotor plane, see Figure 2.4. The thrust and torque in each ring are then

$$\mathrm{d}F_{\mathrm{a}} = n_{\mathrm{B}} \left(\mathrm{d}L_{\mathrm{a}} \cos(\alpha+\beta) + \mathrm{d}D_{\mathrm{a}} \sin(\alpha+\beta)\right) \tag{2.8a}$$

$$\mathrm{d}M_{\mathrm{a}} = n_{\mathrm{B}} \left(\mathrm{d}L_{\mathrm{a}} \sin(\alpha+\beta) - \mathrm{d}D_{\mathrm{a}} \cos(\alpha+\beta)\right) r, \tag{2.8b}$$

where n_{B} is the number of blades. From Figure 2.4 one additionally obtains

$$\tan(\alpha+\beta) = \frac{u_1(1-a_{\text{ax}})}{\Omega r(1+a_{\text{an}})} \text{ and } v_{\text{inflow}}^2 = \left(\Omega r(1+a_{\text{an}})\right)^2 + \left(u_1(1-a_{\text{ax}})\right)^2. \tag{2.9}$$

Then the Equations (2.3) and (2.6) are set equal to Equations (2.8a) and (2.8b), respectively. With (2.9) there are 2 equations, in which the remaining unknowns are a_{ax} and a_{an} with given current value of u_1, Ω, ρ, and β and with given blade section properties $c_{\mathrm{L}}(\alpha)$, $c_{\mathrm{D}}(\alpha)$, r, $\mathrm{d}r$, and c. This set of equations can be solved iteratively for each blade section. Finally, combining $\mathrm{d}F_{\mathrm{a}}$ and $\mathrm{d}M_{\mathrm{a}}$ from each section yields the total aerodynamic thrust and torque.
The aerodynamic subroutines of FAST use several corrections to the BEM approach such as tip- and hub-losses [46], which increases the complexity of the procedure.

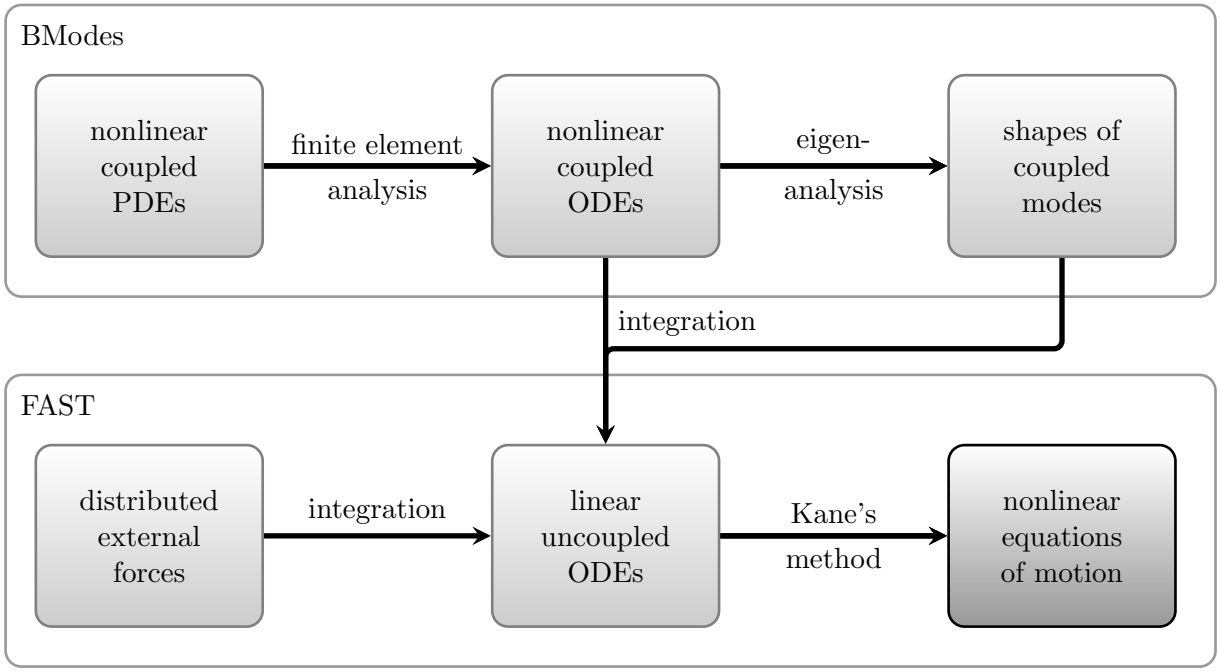

Figure 2.5: Derivation of the nonlinear equations of motion for simulations with FAST.

Structural Dynamics of Wind Turbines

In general, there are two basic approaches to model the structural dynamics of wind turbines: finite element representations and modal analysis [47]. Usually modal models with limited Degrees of Freedom (DOFs) are applied, mainly because of the lower computational effort compared to finite element models.

The equations of the structural dynamics of the FAST code used in this work are derived in a preprocessing step with BModes [48] starting with nonlinear Partial Differential Equations (PDEs) arising from the idealization of tower and blades as Euler-Bernoulli beams, see Figure 2.5. The beams are then discretized in several nodes using finite element analysis, which results in nonlinear coupled Ordinary Differential Equations (ODEs) in nodal coordinates, where the varying structural properties such as mass, stiffness and inertia of tower and blades are considered. These equations are then linearized and coupled modes are obtained from an eigenanalysis.

The preprocessed mode shapes for each mode and the distributed mass and stiffness properties from each beam segment along the span of the flexible bodies are then written into the input file of FAST. The mode shapes $\mu_i(r)$ are polynomials depending on the position r along the beam and are normalized such that at the end of the beam all mode shapes have the value 1.

For the flexibility of the blades and the tower a linear modal representation is used assuming only small deflections [44]. The modal mass m_i, stiffness k_i, damping c_i, and force F_i for each mode i can be calculated by discrete integration over all n_S segments with the distributed mass

m_j, stiffness k_j, damping c_j and forces F_j for each segment j by

$$m_i = \sum_{j=1}^{n_\mathrm{S}} m_j \mu_i^2(r_j) \tag{2.10a}$$

$$k_i = \sum_{j=1}^{n_\mathrm{S}} k_j \mu_i^2(r_j) \tag{2.10b}$$

$$c_i = \frac{d_{\mathrm{s},i} k_i}{\pi f_{0,i}} \text{ with } f_{0,i} = \frac{1}{2\pi}\sqrt{\frac{m_i}{k_i}} \tag{2.10c}$$

$$F_i = \sum_{j=1}^{n_\mathrm{S}} F_j \mu_i(r_j), \tag{2.10d}$$

where $d_{\mathrm{s},i}$ is the structural damping ratio and $f_{0,i}$ the natural frequency of mode i. If considered independent of the other modes, the equation of motion for a single modal coordinate q_i is then

$$m_i \ddot{q}_i + c_i \dot{q}_i + k_i q_i = F_i. \tag{2.11}$$

For each blade, the first mode in the edgewise direction and the first two modes in the flapwise direction are considered. For the tower, the first two modes in the fore-aft and side-side directions are implemented. This is usually justified by the fact that higher-order modes have negligible energy content. Further, the rotor rotation, the first drive train torsional mode, and the nacelle yaw are used in FAST, resulting in 16 DOF for a three-bladed wind turbine. The mode shapes are then superposed for each flexible body. The deflection along the beam during a simulation can be calculated from the actual modal coordinates and the mode shapes. Figure 2.6 shows the flapwise modes together with the blade nodes at a wind speed of 25 m/s of the 5 MW reference turbine presented later in Section 3.1.1.

The modes are then coupled using Kane's method [49], which provides a formalism to derive the equations of motion for interconnected bodies. The resulting system is highly nonlinear due to the coupling of the rotational and structural modes: The tower motion will be different if two blades are in the upper half of the rotor disc or just one. The frequencies of the coupled system are also different from the natural frequencies of the uncoupled and linear component modes: the blade frequency slightly increases with increasing rotor speed because of centrifugal forces. Furthermore, the coupling between the modes varies: the rotor motion is more coupled with the tower side-side motion compared to the fore-aft motion. Eventually, the set of nonlinear equations can be written with the general mass matrix $\boldsymbol{M}$ and the general force vector $\boldsymbol{f}$ as

$$\boldsymbol{M}(\boldsymbol{q}, \boldsymbol{u})\ddot{\boldsymbol{q}} + \boldsymbol{f}(\boldsymbol{q}, \dot{\boldsymbol{q}}, \boldsymbol{u}, \boldsymbol{d}) = \boldsymbol{0}, \tag{2.12}$$

where $\boldsymbol{q}$ is the vector of the modal coordinates, $\boldsymbol{u}$ is the vector of the control inputs, and $\boldsymbol{d}$ is the vector of the disturbances inputs.

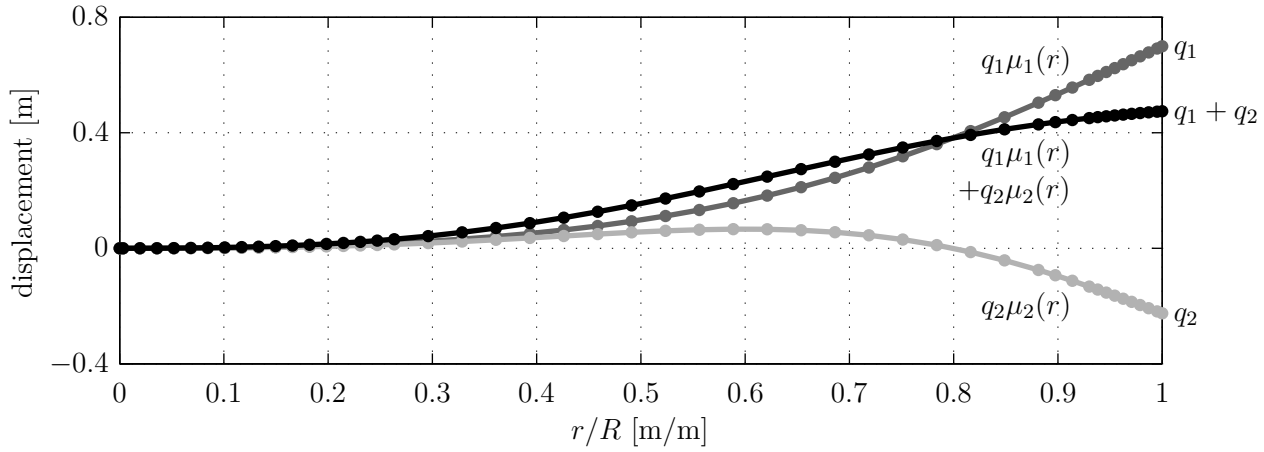

Figure 2.6: Example of a flapwise blade deflections: first mode (dark gray) and second mode (light gray) and resulting blade deflection (black). Dots mark the blade nodes.

2.1.3 Load Analysis

Besides improving the energy yield, another goal of wind turbine control is to reduce the structural loads. Thus, a detailed load analysis is important to evaluate the control performance. The analysis is usually performed by Design Load Cases (DLCs), which are a number of predefined scenarios divided into ultimate and fatigue load calculations.

Design Load Cases

DLCs are part of international standards for the design of wind turbines. The standards of the International Electrotechnical Commission (IEC) [50] are usually applied in the certification process defined for different wind turbine classes depending on the external conditions of the intended site: the annual average wind speeds for Class I, II, and III are 10.0 m/s, 8.5 m/s, and 7.5 m/s, respectively. In the standard, 22 DLCs are described in terms of different combinations of wind conditions based on the wind turbine class and design situations. The most relevant situation for closed-loop controller design is “power production” (DLC 1.x). The other situations such as start up and shut downs (DLC 2.x-5.x) are more relevant for supervisory control design or even without any control action during standstill or transport (DLC 6.x-8.x). The DLCs are divided into 17 ultimate and 5 fatigue cases, where loads are calculated differently.

Ultimate Load Calculations

The analysis of ultimate loads is important to check whether a turbine and its components are able to withstand the maximal loading which may occur during a turbine's lifetime. Therefore, the maximum and minimum value over all relevant load cases is taken for loads of interest. Typically these are the blade root and tower base bending moments or the hub bearing moments. The DLCs for ultimate loads calculations cover a realistic combination of wind conditions and design situations. Normal and extreme wind conditions (worst case with recurrence period of 50 years) are simulated with normal machine states. In contrast, machine fault situations such as control system faults are only simulated with normal wind conditions, because the faults are assumed to be uncorrelated with the 50 year-events.
The ultimate load cases are divided into two types: the stochastic cases, where the wind conditions are defined by stochastic properties such as turbulence models, and the deterministic cases, where the wind conditions are defined by mathematical expressions, for example for an Extreme Operating Gust (EOG). These expressions do not reproduce the behavior of the real wind, although [51] shows that it is possible to integrate these expressions into turbulent wind fields. Simulated lidar measurements under a deterministic wind will not help to understand how lidar data needs to be processed. Therefore, the deterministic wind fields are only considered in this work to test preview control strategies assuming perfect knowledge of the wind.

Fatigue Load Calculations

The analysis of fatigue loads is concerned with dimensioning the turbine to withstand the structural loads accumulated during its lifetime mainly caused by the inhomogeneous wind inflow and the rotating masses. Compared to the ultimate loads, the calculation of fatigue loads is more complicated and several assumptions have to be made. The basic idea here is to condense the effect of all load cycles with different amplitudes and frequencies into one amplitude – the Damage Equivalent Load (DEL), which would cause the same damage, if applied with a specific number of cycles during the turbine's lifetime. This is useful to compare different controller concepts.
To calculate the DEL for a signal of interest like the tower bending moment, the load cycles are classified in a first step. Usually the Rain-Flow-Counting method is used to determine the number $n_{\mathrm{LC},i}$ of load cycles with peak-to-peak amplitude A_i. According to the Palmgren-Miner linear damage hypothesis [41], damages can be then summarized independent of the sequence and thus condensed to a reference load amplitude A_{ref} with an arbitrary number of cycles $n_{\mathrm{LC,ref}}$:

$$A_{\mathrm{ref}}^m n_{\mathrm{LC,ref}} = \sum_i A_i^m n_{\mathrm{LC},i} \Leftrightarrow A_{\mathrm{ref}} = \sqrt[m]{\frac{1}{n_{\mathrm{LC,ref}}} \sum_i A_i^m n_{\mathrm{LC},i}}, \tag{2.13}$$

where m is the material-dependent Wöhler exponent. Within this thesis, $m = 4$ is used for steel (for example for shaft and tower base bending moments) and $m = 10$ for the composite material to determine the blade fatigue loads. The reference number of cycles is chosen to be $n_{\mathrm{LC,ref}} = 2 \times 10^6$. This number is often used, because in this case one can directly determine the notch class for welding [52].
The lifetime-weighted DEL is extrapolated by weighting the reference load amplitude $A_{\mathrm{ref},j}$ from each simulation j according to their relative frequency of occurrence f_j during the turbine's lifetime:

$$\mathrm{DEL} = \sqrt[m]{\sum_j f_j \, A_{\mathrm{ref},j}^m} \text{ with } \sum_j f_j = 1. \tag{2.14}$$

The Weibull distribution (see Section 2.2) is typically applied. Although in a complete fatigue load analysis all 5 fatigue load cases need to be included, here only the power production case is considered (DLC 1.2).

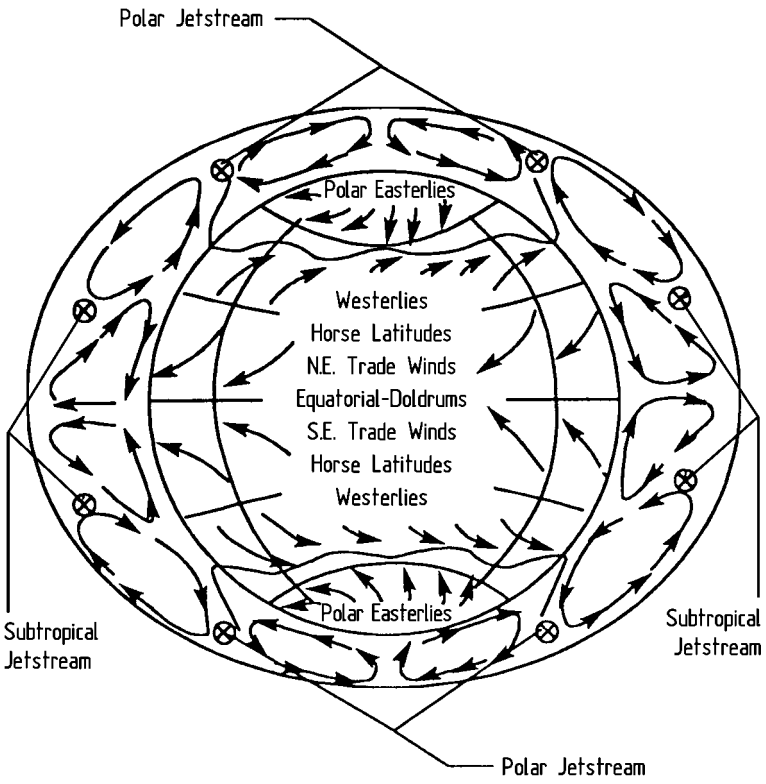

Figure 2.7: Geostrophic wind caused by solar radiation and Coriolis forces [37].

2.2 Wind

The main purpose of lidar-assisted control is to improve the performance of wind turbine control based on the provided knowledge of the wind. Hence, an understanding of the wind resource is vital. This section provides a short overview of general knowledge of the wind mainly based on [41], where more details can be found.

2.2.1 Origin of Wind

Wind is the movement of air masses on a large scale and on earth is mainly caused by solar heating. The absorption of the solar radiation is highly variable, both geographically and temporally, producing great differences in air pressure. The pressure forces together with Coriolis forces caused by the earth's rotation are finally responsible for the geostrophic wind, see Figure 2.7. Although only 2 % of the solar energy is captured in the earth's atmosphere and converted into energy of motion, this amount is one hundred times higher than the global demand for electrical power [37]. Close to the ground, the wind flow is decreased by the friction of the different surface types such as water or forest, and is locally influenced by small-scale topographic conditions such as mountains and valleys.

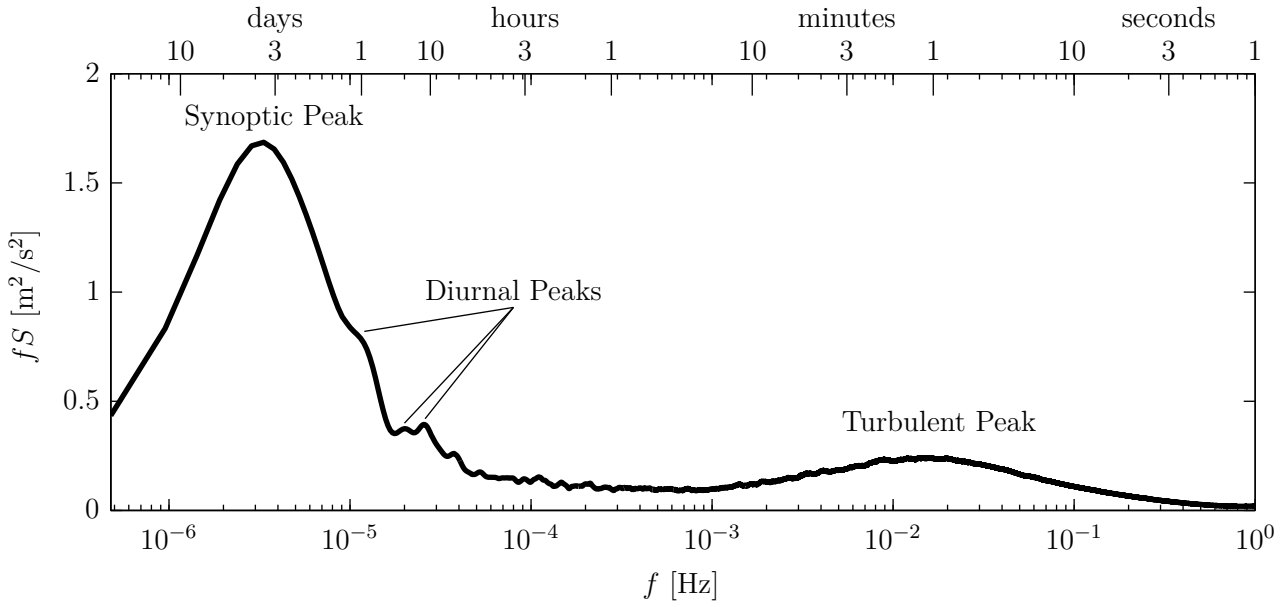

Figure 2.8: Wind spectrum from Bremerhaven measured by a cup anemometer at a height of 44 m, averaged over 4 months.

2.2.2 Description of Wind

Apart from this spatial variability, the description of the temporal changes at a given location is of special interest for the operation of a wind turbine. Figure 2.8 shows a wind speed spectrum S from a measurement campaign in Bremerhaven, Germany over the winter 2009 (for details see [53]).

The first peak in the spectra at around 4 days corresponds to the synoptic scale of typical large-scale weather patterns. The variation between day and night results in a peak at 1 day. The peaks at around 10 and 14 hours are caused by land and sea breezes due to the differential heating and cooling between the shore and the north sea. The wind speed variations with a timescale of minutes or less are known as turbulence. In the case of the considered data, the spectrum multiplied with the frequency f drops before the turbulence region similar to the one presented in [54]. Although the spectral gap between the turbulent and the diurnal peaks might not be present at every geographical location, the daily and the long term synoptic variations are usually treated as distinct from the higher frequency fluctuations of turbulence [41].

Therefore, the wind variation for wind energy applications is traditionally described as a distribution of 10-minute-mean values and turbulence models for a time series of 10 minutes.

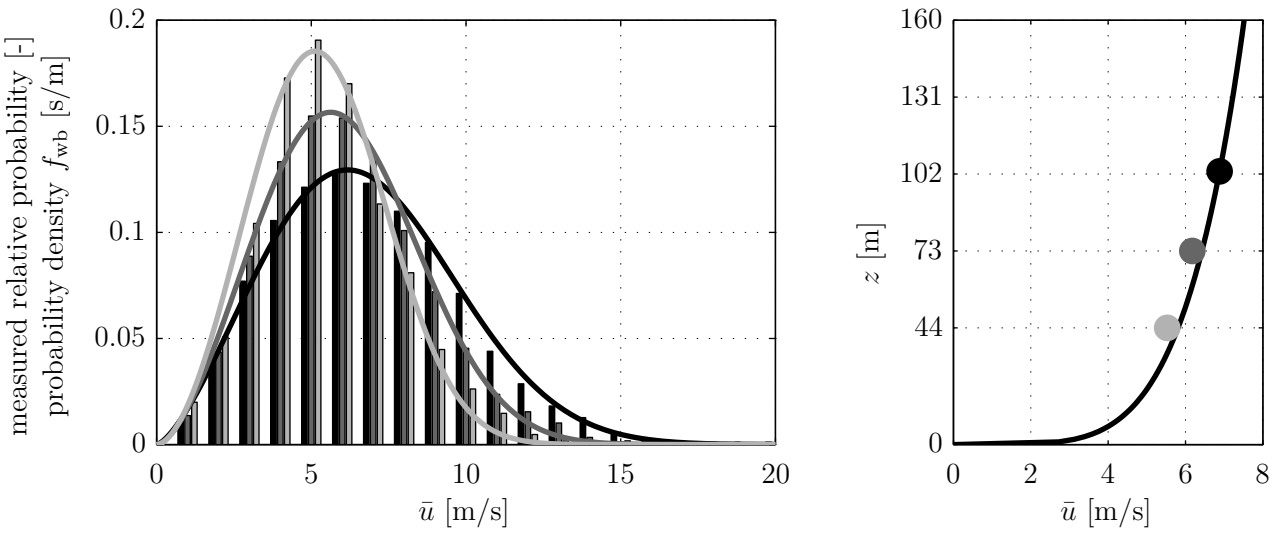

Figure 2.9: Data from Bremerhaven at a height of 44 m (light gray), 73 m (dark gray) and 102 m (black). Left: Measured (bars) and fitted (solid lines) wind distribution. Right: Mean wind speed averaged over the campaign (dots) and exponential wind profile (solid line).

Wind Distribution Model

The variation of the 10-minute-mean wind speed $\bar{u}$ over one year can be parameterized with a probability distribution. Usually, a Weibull distribution is used, which can be characterized with a probability density function

$$f_{\mathrm{WB}}(\bar{u}) = \frac{k_{\mathrm{WB}}}{C_{\mathrm{WB}}} \left(\frac{\bar{u}}{C_{\mathrm{WB}}} \right)^{k_{\mathrm{WB}}-1} \exp\left(- \left(\frac{\bar{u}}{C_{\mathrm{WB}}} \right)^{k_{\mathrm{WB}}} \right), \tag{2.15}$$

where C_{WB} and k_{WB} are the scale and shape parameters.
Figure 2.9 (left) shows a histogram (normalized by the total number of values) from the 10-minute-mean wind speeds of the campaign in Bremerhaven (same data base as Figure 2.8) for each wind speed bin of 1 m/s and for three different heights. The Weibull distributions are fitted to the data and each one shows a good approximation to the histogram.
The parameterization can be used to extrapolate the wind distribution to the hub height of a wind turbine, if only data from lower heights are available. Usually the shape parameter is assumed to be constant as a function of height and the scale parameter is extrapolated with a vertical wind shear model as described in the next subsection.

Vertical Wind Shear Model

Due to the surface roughness, the wind close to the ground is slowed down. The resulting vertical wind profile denotes the average wind speed $\bar{u}$ as a function of height z above the ground. Common models are the logarithmic approximation and the exponential power law approximation. In this work the latter is used as proposed in [50]:

$$\bar{u}(z) = \bar{u}_{\mathrm{H}} \left(\frac{z}{z_{\mathrm{H}}} \right)^{\alpha_{\mathrm{shear}}} \quad \text{with } \alpha_{\mathrm{shear}} = 0.2, \tag{2.16}$$

where $\bar{u}_{\mathrm{H}}$ is the average wind speed at hub height z_{H}. Figure 2.9 (right) shows the averaged profile over the campaign in Bremerhaven.

Wind Turbulence Models

The long term variation of wind is usually described by a distribution of 10-minute-mean values of wind speed and direction. In contrast, one distinguishes in turbulence models between three velocity components of the three-dimensional wind vector: u is the longitudinal, v the lateral, and w the vertical component. The understanding of turbulent flow is a rather complex, ongoing science. There exist several empirical wind turbulence descriptions such as the Kaimal spectra (used in this work) and the von Karman spectra, as well as the more complex models such as the Mann model (see [50] for more details).
In general, the turbulence intensity I_h is defined by the ratio between the standard deviation σ_h and the longitudinal mean wind speed $\bar{u}$:

$$I_h = \frac{\sigma_h}{\bar{u}}, \tag{2.17}$$

where h is the subscript referring to the velocity components (u longitudinal, v lateral, w vertical). The corresponding standard deviations for the Kaimal model are defined in [50] as:

$$\sigma_u = I_{\mathrm{ref}}(0.75\,\bar{u} + 5.6),\ \sigma_v = 0.8\,\sigma_u,\ \sigma_w = 0.5\,\sigma_u, \tag{2.18}$$

where the reference turbulence intensity I_{ref} for a higher, medium, and lower turbulent location is 16 %, 14 %, and 12 %, respectively.
Apart from these statistical values, normalized spectra for each velocity component in a point i are given in the Kaimal model by

$$\frac{f S_{ii,h}}{\sigma_h^2} = \frac{4 f \frac{L_h}{\bar{u}}}{\left(1 + 6 f \frac{L_h}{\bar{u}}\right)^{(5/3)}}, \tag{2.19}$$

where the integral length scales L_h with the turbulence scale parameter $\Lambda_1 = 42\,\mathrm{m}$ for hub

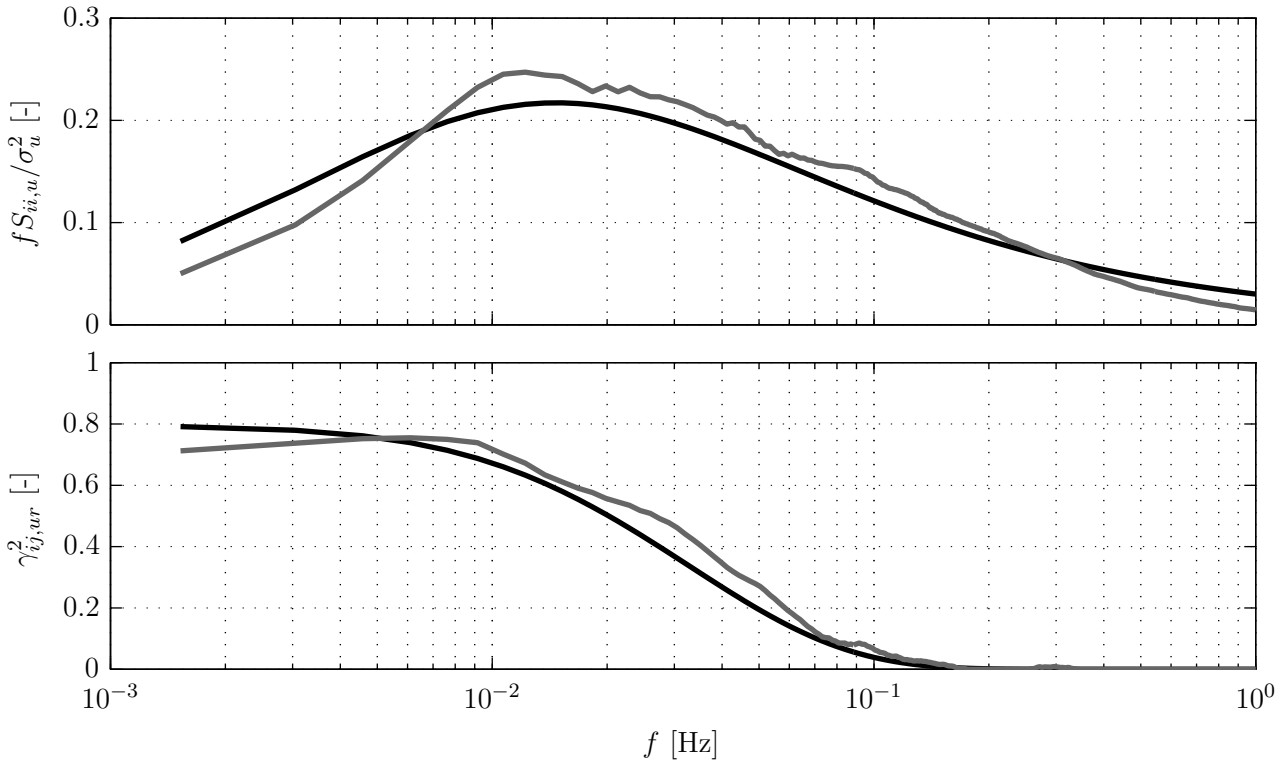

Figure 2.10: Data from Bremerhaven (gray) and Kaimal model (black) for 20 m/s: Normalized longitudinal wind spectrum of the sonic anemometer at a height of 100 m (top) and the longitudinal coherence between the sonic anemometers at a height of 100 m and 73 m (bottom).

heights over 60 m are:

$$L_u = 8.1\,\Lambda_1,\ L_v = 2.7\,\Lambda_1,\ L_w = 0.66\,\Lambda_1. \tag{2.20}$$

The Kaimal model also describes the relationship between the longitudinal velocity component of two spatially separated points as a function of frequency: The coherence $\gamma_{ij,ur}$ of the longitudinal velocity component between two points i and j on a plane perpendicular to the mean wind direction with distance r_{ij} is defined by

$$\gamma_{ij,ur} = \exp\left(-12\sqrt{\left(\frac{f}{\bar{u}}\right)^2 + \left(\frac{0.12}{L_u}\right)^2}\, r_{ij}\right), \tag{2.21}$$

where 0 indicates no correlation and 1 perfect correlation. The Kaimal model assumes no correlation of the other two components for points with a separation of $r_{ij} > 0$.

Figure 2.10 shows an example model of the longitudinal spectrum and coherence for 20 m/s, which again fits well to the real data from the campaign in Bremerhaven.

Wind evolution is here considered by a simple exponential model of coherence, as suggested by [55] and used by [7]. The squared coherence between two points i and j with the longitudinal

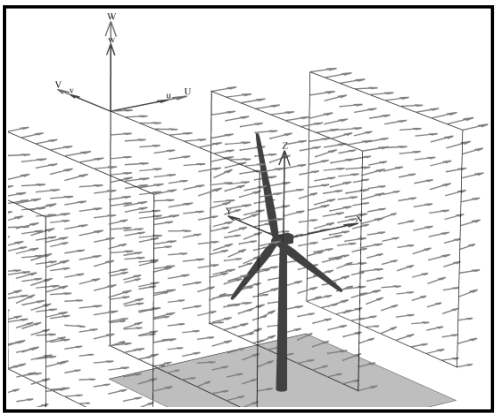

Figure 2.11: TurbSim wind field used for aero-elastic simulations: time variant wind vectors are assigned to a vertical grid [57].

separation $\Delta x_{ij,\mathcal{W}}$ and the dimensionless longitudinal decay parameter α_{ux} is given by

$$\gamma^2_{ij,ux} = \exp\left(-\alpha_{ux}\frac{2\pi f}{\bar{u}}\Delta x_{ij,\mathcal{W}}\right). \tag{2.22}$$

Other approaches such as the one presented by [56] model the wind evolution on physical considerations. The exponential model has been chosen over other models due to its simplicity.

2.2.3 Wind Fields Used for Aero-elastic Simulations

The agreement between the wind description models and the real measurement data justifies the separation into mean values and turbulence spectra. Therefore, simulations of wind turbines are usually carried out in the following way: on the one hand a set of turbulent wind fields with a length of 10 minutes are generated based on the turbulence models and vertical wind shear models for several mean wind speeds. In [50] at least 6 simulations for each mean wind speed from the cut-in to the cut-out wind speed with 2 m/s spacing is recommended to ensure statistical reliability. On the other hand the probability density function of the wind distribution is then used to obtain extrapolated and weighted values such as power, pitch rate and structural loads over the turbine's lifetime.

The wind fields usually used for aero-elastic simulations are time series of three-dimensional wind speed vectors calculated at points on a vertical, two-dimensional grid that is fixed in space. The wind fields for this work are generated with TurbSim [57], which uses a rectangular grid, see Figure 2.11. For the aero-elastic simulations with FAST, the wind field is interpolated along the rotating blades and used to calculate the aerodynamic forces and moments at the rotor using the BEM method as explained in Section 2.1.2. Although the rotor plane is generally not fixed in the longitudinal direction due to displacement of the nacelle or deflection of the rotor blades, the wind field transferred to FAST is independent of these movements.

2.3 Lidar Systems

Lidar (LIght Detection And Ranging) is a remote sensing technology similar to radar (RAdio Detection And Ranging) and has largely contributed to our knowledge of our atmosphere during the last decades. The interactions of the emitted light with the molecules and aerosols allow the observation of atmospheric parameters such as temperature, pressure, humidity, and concentration of gases. Modern lidar technology started with the invention of the laser in the 1960's and one of its first applications was the detection of clouds [58]. Since then, lidar has been used not only in meteorology, but also in a wide range of other applications, such as laser range finders, altimeters, and satellite trackers [59].
The following section concentrates on the use of lidar systems in wind energy applications and the measurement principles underlying these systems. The section is mainly based on [60] and [61].

2.3.1 Lidar in Wind Energy

Although first applications of lidar to wind measurements were explored in the 1980's, the lidar systems of that time were too large, complex, and expensive to be widely used. Lidar technology has become more and more popular for site assessment purposes since 2003, coinciding with the development of a new generation of lidar devices based on components that have been originated from the telecommunications industry.
Lidar systems in wind energy applications are mainly used to measure wind speeds. These systems can be categorized according to their detection, their waveband, and their emission waveform:

- Coherent or direct detection: Systems with coherent detection measure a Doppler shift by comparing the frequency of the original and the backscattered light. The frequency shift can then be translated into a wind speed. Systems with direct detection use cross-correlation of signals backscattered from several measurement points to measure wind speed and direction directly.

- Infra-red or ultra-violet waveband: Depending on the laser source, lidar systems emit infra-red light, which is reflected by aerosols (small particles, dust, salt, water droplets etc.) or ultra-violet light, which is reflected by air molecules.

- Pulsed or continuous waveform: Pulsed lidar systems emit short laser pulses and can measure at various distances simultaneously by relating changes in the backscattered signal over time to changes over space considering the constant speed of light. These distances are often called range gates. Continuous wave systems need to adjust the optical focus to measure at different distances.

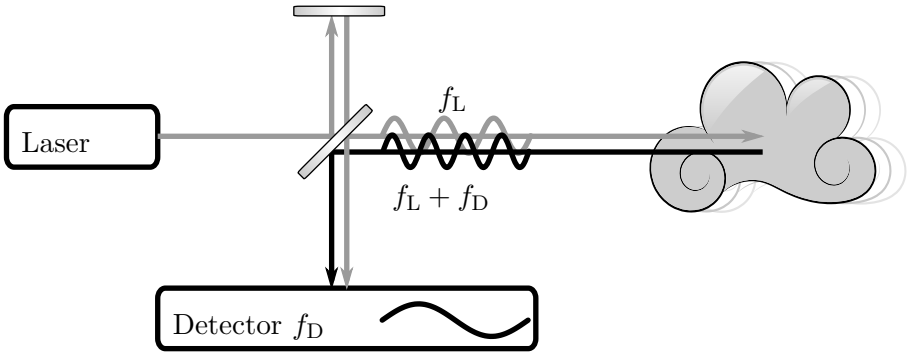

Figure 2.12: Coherent detection of the optical Doppler effect: coherent light from a laser is backscattered from moving aerosols with a Doppler frequency shift, which is detected by mixing the original and the backscattered signal, based on [60].

- Ground-based, nacelle-based, or spinner-based systems: depending on the location of installation, lidar systems have different measurement positions and data processing.

At the beginning of this work, only two systems were commercially available: the continuous wave system ZephIR from the UK company QinetiQ [61] and the pulsed system Windcube from the French company Leosphere [60]. Both are ground-based systems using coherent detection and infra-red lasers developed based on the availability of reliable components from telecommunication. Over the span of this dissertation research, both companies improved their systems and also other coherent systems with an infra-red waveband emerged such as the ground-based system Galion from the Scottish company SgurrEnergy[1], the nacelle-based system Wind Iris from Leosphere's spin-off Avent Lidar Technology[2], the nacelle-based system OCS from the US company BlueScout Technologies[3], and the compact and robust lidar system Whirlwind[4] developed within the German joint research project LIDAR II. While systems using direct detection[5] and ultra-violet lasers[6] are emerging and providing interesting alternatives, the following subsection will concentrate on the measurement principle of systems using coherent detection and infra-red lasers.

2.3.2 Measurement Principle of Doppler Wind Lidar

Lidar systems with coherent detection make use of the optical Doppler effect and compare the original and the backscattered signal to determine the frequency shift [61], see Figure 2.12. Although the details of processing in the used opto-electronics depend on the used waveform and

[1] www.sgurrenergy.com
[2] www.aventlidartechnology.com
[3] Catch The Wind was renamed to BlueScout Technologies and then subsequently disappeared from the market
[4] www.opticsense.eu
[5] SpiDAR from Israeli company Pentalum, www.pentalum.com
[6] Optimizer from US company Opto Atmospherics, www.optoatmospherics.com

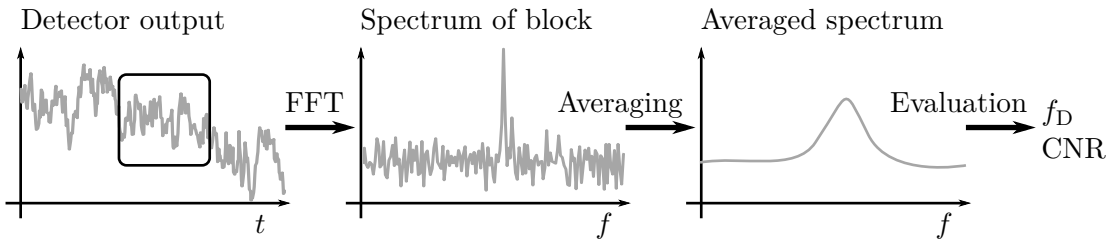

Figure 2.13: Typical lidar signal processing based on [61]: The time signal is split in blocks and an FFT is carried out for each individual block. The spectra are then averaged over a set of blocks and evaluated to obtain the frequency shift f_D and the CNR.

other issues, in principle, the coherent detection is based on following process: a small fraction of the laser beam is separated from the emitted light with frequency f_L by a beam-splitter and superimposed at a second beam-splitter with the backscattered signal with frequency $f_L + f_D$. By processing the signal, the detector is able to determine the frequency shift f_D.
The signal processing is usually done by splitting the detected time signal into several blocks, see Figure 2.13. For each block, a Fast Fourier Transform (FFT) is carried out to obtain the individual spectrum. Then the spectra of the blocks are averaged depending on the used waveform: for pulsed systems the blocks are averaged for the same range gate from different pulses, for continuous wave systems the range is fixed and blocks can be continuously averaged. Finally, the averaged spectrum is evaluated with a peak detection algorithm to obtain the frequency shift f_D and typically a value to rate the quality of the signal such as the Carrier-to-Noise Ratio (CNR).
The frequency shift can then be simply translated into a line-of-sight wind speed v_{los} by

$$v_{los} = \frac{c f_D}{2 f_L} = \frac{\lambda_L f_D}{2}, \tag{2.23}$$

with the speed of light c and the laser wavelength λ_L, which is typically in the order of 1.55 µm. Thus, single lidar systems are only able to provide one-dimensional wind speed measurements compared to sonic anemometers with three-dimensional wind speed measurements. Further, the line-of-sight wind speed measurements from a pulsed lidar system are averaged over a certain volume depending on the pulse length and the FFT windows size [60]. Both effects are described in Section 4.1 in more detail.

2.4 Wind Turbine Control

In general, the wind turbine controller processes its input signals such as generator speed, tower top acceleration, and wind measurements and generates output signals for the actuators such as blade pitch angle, generator torque and yaw [41]. Usually, the control system is divided into a supervisory controller, a real-time closed-loop controller, and a safety control system.

2.4.1 Supervisory Control

The supervisory control is responsible to bring the wind turbine from one operational state (usually standby, start-up, normal operation, shut-down, and stopped) to another. These processes are triggered by sensors exceeding certain values, for example in the case of a shut-down at high wind speeds. They can also be manually started, for example in the case of a shut-down for maintenance. The supervisory control usually is responsible for the majority of the code within an industrial wind turbine controller.
Lidar measurement might also be useful for the supervisory control, for example to bring the wind turbine to a safe operation point, if an extreme wind event is detected. However, the use of lidar for supervisory control is not further considered in this work, because the challenges in designing a good supervisory control lie more in practical implementation than in control theory and more confidence in lidar measurements needs to be obtained first.

2.4.2 Closed-Loop Control

The closed-loop controller is responsible for the normal operation of wind turbines and thus is running most of the time. The primary control goal of the closed-loop controller can be summarized as: to maximize the energy capture while keeping the turbine within its operational limits, such as maximum rotor speed, maximum torque, maximum thrust, or maximum power limited by the generator capacity. To guarantee the operation over the turbine's lifetime (usually 20 years), the structural loads need to be kept within their design limits. In the turbine and controller design process, increase of energy capture is evaluated against higher loads, which usually result in increased material costs. While in the early years of wind energy there have been passive and more robust systems like the "Danish concept" with fixed rotor speed and using the passive stall effect at high wind speeds, in recent years most wind turbines are pitch controlled with variable rotor speed. Traditionally, the closed-loop controller consists of slightly coupled Single-Input Single-Output (SISO) controllers, connecting one sensor with one actuator. The main measurements are the yaw misalignment from a sonic anemometer or a wind vane on the nacelle and the generator speed. The yaw misalignment is used by the yaw controller to adjust the yaw position to orientate the turbine with the main wind direction and

thereby to maximize the energy capture. Due to the high inertia of the nacelle and the normally relatively slow wind direction changes, this controller operates at time scales of several minutes. At a time scale of seconds, the generator speed is used on the one hand by the torque controller to adjust the rotational speed to its optimal value before the rated power is reached. On the other hand, the generator speed is also the input to the collective pitch controller, which regulates the rotational speed to its maximum value if rated power is reached. It is common that the collective pitch and the torque controller are slightly interconnected to guarantee a smooth transition between the operation below rated and at rated power.
Furthermore, modern wind turbines often have additional SISO loops to reduce structural loads on different components [62]:

- Tower vibration damping: The tower top accelerations can be used to generate an additional zero-mean collective blade pitch command to damp the tower oscillation.
- Drive train damper: An additional zero-mean generator torque command based on the generator speed signal is often used to damp vibrations in the torsional drive train motion. These vibrations arise from the coupling of the drive train motion with the edge-wise modes of the blades, which have very little aerodynamic damping.
- Individual Pitch Control (IPC): Based on measurements of the blade root bending moments or of the blade deformations, a zero-mean pitch demand for each blade is added to the collective pitch angle to minimize the tilt and yaw moment of the rotor due to inhomogeneity of the inflowing wind field.

The closed-loop control is further explained in Section 3.4 by means of the used baseline controller. The concepts of lidar-assisted control presented in this work will focus on enhancement of this part of the overall wind turbine controller.

2.4.3 Safety System

The closed-loop and supervisory controller should be capable of running the wind turbine in all conditions covered in their design process. However, if the main controller fails in any unforeseeable situation, the safety system takes over. It usually stops the turbine's operation by pitching the blades to feathering position and disconnecting the generator from the grid, thus overwriting the signals from the main controllers. The safety system needs to be fail-safe and independent from the rest of the control system. It can be activated manually by an emergency button or triggered by overspeeding, by lost connection to the main controller, or by high tower top accelerations caused for example by a structural failure.
Similar to the supervisory control, lidar-assisted control is not applied to this part of the wind turbine controller.

3

Modeling and Simulation Environment

In the previous chapter basic information about wind turbines, wind disturbances, and lidar systems have been given. In this chapter, application specific models are derived, which are later used for the internal model for the design of the wind field reconstruction methods and the lidar-assisted controller presented in this dissertation.

The main issue for the lidar-assisted control application is that not only a model is needed for the controlled system (wind turbine) as is usual for model-based controller design, but also models are vital for the disturbance (wind) and the measurement system (lidar).

Parallel to Chapter 2, wind turbine models are presented first in Section 3.1. In Section 3.2 and 3.3 several models for wind fields and lidar systems are derived for simulation and wind field reconstruction purposes. The baseline feedback controllers used in this work are then explained in Section 3.4. Additionally the simulation environment used in this work is presented in Section 3.5.

Figure 3.1: NREL 5 MW onshore reference turbine (left, [63]), which is based on the Senvion 5M (right, photo by Patrick Jübermann at alpha ventus).

3.1 Wind Turbine Modeling

This section first presents the full nonlinear model which is used for the aero-elastic simulations in this work and then subsequently presents the reduced nonlinear model used for the nonlinear design of the collective pitch and generator torque controllers of Chapters 6 to 8.

3.1.1 Full Nonlinear Model for Aero-Elastic Simulations

Simulations are performed with an aero-elastic model of a 5 MW three-bladed pitch-controlled variable-speed wind turbine designed by NREL as described in [63]. The model implemented in FAST consists of a flexible multi-body system which experiences external forces from aerodynamics as explained in Section 2.1.2. The following 15 DOFs are enabled in the simulation: first and second flapwise and first edgewise blade modes, first and second fore-aft and side-to-side tower bending modes, rotor/generator motion and drive train rotational-flexibility. The yaw DOF and the rotor-teeter DOF also available in FAST are disabled. The FAST model is supplemented with pitch actuator dynamics for each blade described as a linear transfer element from the demanded collective pitch angle θ_c to the collective pitch angle θ:

$$\ddot{\theta} + 2\xi_{PA}\omega_{PA}\dot{\theta} + \omega_{PA}^2\theta = \omega_{PA}^2\theta_c, \tag{3.1}$$

where ω_{PA} is the undamped natural frequency, and ξ_{PA} is the damping factor. This sums up to a total of 36 dynamic states of the aero-elastic model ($15 \times 2 + 3 \times 2$). For basic data see Table C.1.

The nonlinear aero-elastic equations of motion for the modeled wind turbine with the above mentioned modes and disturbances can be written as follows (see [44] and Section 2.1.2)

$$\begin{aligned} \mathbf{0} &= \boldsymbol{M}(\boldsymbol{q}, \boldsymbol{u})\ddot{\boldsymbol{q}} + \boldsymbol{f}(\boldsymbol{q}, \dot{\boldsymbol{q}}, \boldsymbol{u}, \boldsymbol{d}) \\ \boldsymbol{y} &= \boldsymbol{h}\left(\boldsymbol{q}, \dot{\boldsymbol{q}}\right), \end{aligned} \tag{3.2}$$

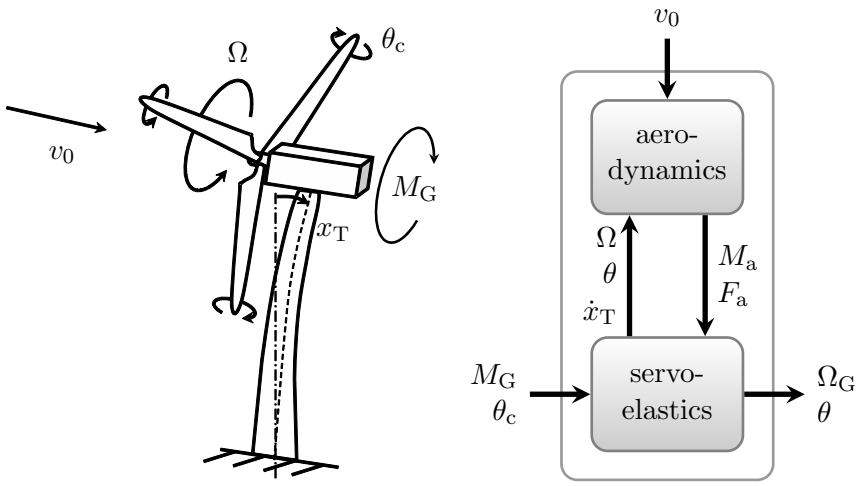

Figure 3.2: Degrees of freedom for the reduced nonlinear model (left). Control and disturbance inputs to the modules of the reduced model (right).

where $\boldsymbol{f}$ and $\boldsymbol{h}$ are nonlinear functions, $\boldsymbol{M}$ is the mass matrix, $\boldsymbol{q}$ is the vector of the considered modal coordinates, $\boldsymbol{u}$ is the vector of the control inputs, $\boldsymbol{d}$ the vector of the disturbance inputs, and $\boldsymbol{y}$ is the vector of the measured outputs.

Aero-elastic simulators, such as FAST, apply the BEM method to compute the impact of the wind field to the turbine model, as explained in Section 2.1.2. The calculation has to be done iteratively and therefore no explicit model equation can be derived to express the impact from each component of the three-dimensional wind field on the wind turbine states. This increases the computational effort in aero-elastic simulations and makes the use of an aero-elastic model unwieldy for controller design. In addition, current remote sensing methods such as lidar are not able to provide a wind field estimate comparable to a generic wind field used in aero-elastic simulations. In the next section, a reduced turbine model is derived from physical fundamentals and the wind field is reduced to a disturbance which is measurable with existing lidar technology.

3.1.2 Reduced Nonlinear Model for Controller Design

For the controller designs described later in this work the full aero-elastic model cannot be used due to the complexity of the iterative calculation of the aerodynamics. Here, the Simplified Low Order Wind turbine (SLOW) model is derived, which is based on [64]. It features several simplifications in a way that it still reproduces reliably the overall dynamic behavior of the system. Figure 3.2 (left) depicts the two considered DOFs: the rotor speed Ω and the tower top displacement x_T. The reduced model is disturbed by the rotor effective wind speed v_0 and controlled by the collective pitch angle θ_c and the generator torque M_G. Only the generator speed Ω_G and the pitch angle θ are considered measurable in this work.

The model consists of a reduced servo-elastic and aerodynamic module, see Figure 3.2 (right).

Servo-elastic subsystem

In the servo-elastic part, the tower fore-aft bending and the rotational motion are considered:

$$J\dot{\Omega} + \frac{M_\mathrm{G}}{i_\mathrm{GB}} = M_\mathrm{a} \tag{3.3a}$$

$$m_\mathrm{eT}\ddot{x}_\mathrm{T} + c_\mathrm{eT}\dot{x}_\mathrm{T} + k_\mathrm{eT}(x_\mathrm{T} - x_\mathrm{0T}) = F_\mathrm{a}. \tag{3.3b}$$

Equation (3.3a) models the rotor dynamics, where M_a is the aerodynamic torque and M_G is the generator torque. The gearbox with the ratio i_GB is assumed loss-free. Further, J is the sum of the moments of inertia about the rotation axis of the hub J_H, blades J_B and the generator J_G:

$$J = J_\mathrm{H} + n_\mathrm{B}J_\mathrm{B} + \frac{J_\mathrm{G}}{i_\mathrm{GB}^2}. \tag{3.4}$$

Equation (3.3b) describes the tower fore-aft dynamics, F_a is the aerodynamic thrust, and x_0T is the static tower top position without the aerodynamic thrust due to the overhanging rotor mass. Further, m_eT, c_eT, and k_eT are the tower equivalent modal mass, structural damping, and bending stiffness, respectively. These values are calculated with Equation (2.10) from the tower mass m_T, nacelle mass m_N, hub mass m_H, blade mass m_B, structural damping ratio $d_\mathrm{s,T}$ and the natural frequency of the first tower fore-aft bending mode $f_\mathrm{0,T}$ from the nonlinear model. According to [65], only a quarter of the tower mass contributes to the oscillating mass:

$$m_\mathrm{eT} = m_\mathrm{N} + m_\mathrm{H} + n_\mathrm{B}m_\mathrm{B} + \frac{1}{4}\, m_\mathrm{T} \tag{3.5a}$$

$$c_\mathrm{eT} = \frac{d_\mathrm{s,T}k_\mathrm{eT}}{\pi f_\mathrm{0,T}} \tag{3.5b}$$

$$k_\mathrm{eT} = m_\mathrm{eT}(2\pi f_\mathrm{0,T})^2. \tag{3.5c}$$

Here, n_B is the number of blades. The pitch actuator and blade dynamics are modeled by a time delay T_B from the demanded collective pitch angle θ_c to the collective pitch angle θ:

$$\theta(t) = \theta_\mathrm{c}(t - T_\mathrm{B}). \tag{3.6}$$

Additionally, the generator speed Ω_G, the low-speed shaft torque M_LSS, and the electrical power P_el are determined with the efficiency of the electro-mechanical energy conversion η_el:

$$\Omega_\mathrm{G} = \frac{\Omega}{i_\mathrm{GB}} \tag{3.7a}$$

$$M_\mathrm{LSS} = \frac{M_\mathrm{G}}{i_\mathrm{GB}} \tag{3.7b}$$

$$P_\mathrm{el} = \eta_\mathrm{el}M_\mathrm{G}\Omega_\mathrm{G}. \tag{3.7c}$$

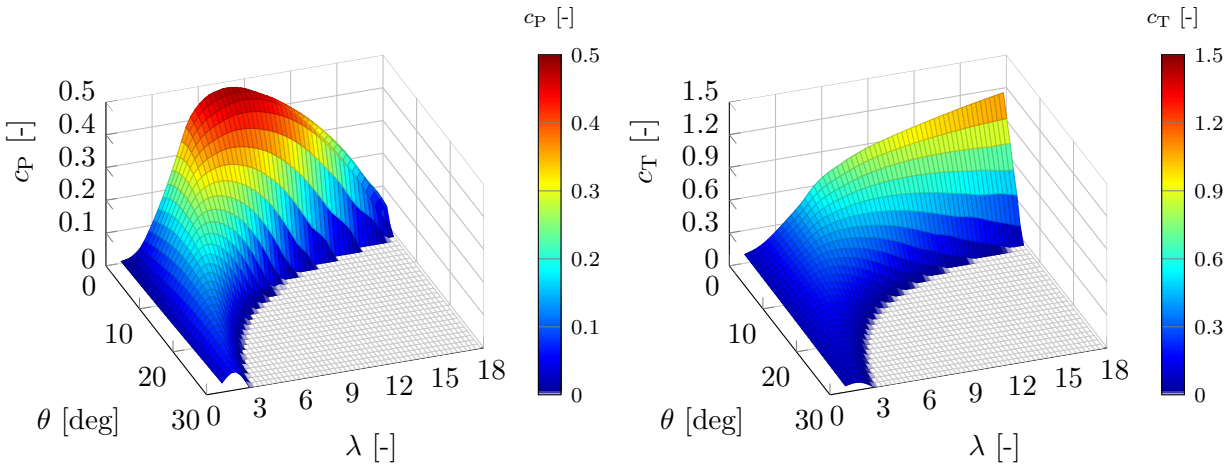

Figure 3.3: Look-up tables of power coefficient (left) and thrust coefficient (right). Negative values are set to zero and discretization of figures is reduced for better illustration.

With the hub height z_H, the tower base fore-aft bending moment $M_{y\mathrm{T}}$ is

$$M_{y\mathrm{T}} = z_\mathrm{H}(c_{\mathrm{eT}}\dot{x}_\mathrm{T} + k_{\mathrm{eT}}x_\mathrm{T}). \tag{3.8}$$

Aerodynamic subsystem

In the aerodynamic part the aerodynamic torque and thrust acting on the rotor with the radius R are

$$M_\mathrm{a} = \frac{1}{2}\rho\pi R^3 \frac{c_\mathrm{P}(\lambda,\theta)}{\lambda} v_\mathrm{rel}^2 \tag{3.9a}$$

$$F_\mathrm{a} = \frac{1}{2}\rho\pi R^2 c_\mathrm{T}(\lambda,\theta) v_\mathrm{rel}^2, \tag{3.9b}$$

where ρ is the air density and λ the tip speed ratio, defined as

$$\lambda = \frac{\Omega R}{v_\mathrm{rel}}, \tag{3.10}$$

and c_P and c_T are the effective power and thrust coefficients, respectively. The two-dimensional look-up tables shown in Figure 3.3 are used, which are calculated from steady-state simulations with the full simulation model. The relative wind speed v_rel is used to model the aerodynamic damping and is defined as the superposition of the tower top speed and the rotor effective wind speed v_0:

$$v_\mathrm{rel} = v_0 - \dot{x}_\mathrm{T}. \tag{3.11}$$

The values of the used parameters can be found in Table C.1.

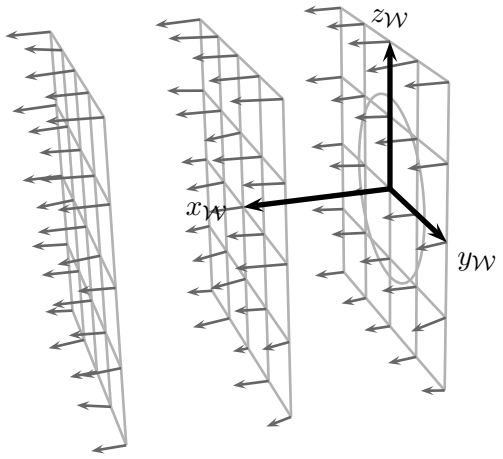

Figure 3.4: Snapshot of the time variant vector field as a general description of wind. Wind speed vectors for aero-elastic simulations are only assigned to the rotor plane, but need to be assigned also to other locations to simulate lidar systems.

3.2 Wind Modeling

As explained in Section 2.2, wind can be mathematically described as a set of three-dimensional wind speed vectors at each point in time and space. For aero-elastic simulations, the wind speed vectors are usually only generated at the rotor plane to calculate the aerodynamic forces and moments. For this work, however, a wind field over the full space in front of the turbine is necessary to simulate lidar systems, see Figure 3.4.

In this section, the coordinate systems used in this work and the general model conceptions of wind fields are introduced. The wind models for the lidar simulations and a reduced model for wind field reconstruction are described.

3.2.1 Wind and Inertial Coordinate System

The wind coordinate system is denoted in this work by the subscript $\mathcal{W}$. It is used to describe the wind flow and is aligned with the mean wind direction regarding the inertial coordinate system, which is denoted here by the subscript $\mathcal{I}$. The direction is defined by the horizontal inflow angle α_h (azimuth or rotation around the $z_\mathcal{I}$-axis) and the vertical inflow angle α_v (elevation or rotation around the rotated $y_\mathcal{I}$-axis), see Figure 3.5. Although all six DOFs could be used in principle, a rotation around the $x_\mathcal{I}$-axis is not considered in this work, but might be useful for very complex terrain.

The origin of the $\mathcal{W}$-system can be set according to the application. For lidar-assisted control, the origin of the $\mathcal{I}$ and the $\mathcal{W}$-system are usually located at the hub of the wind turbine. For ground based lidar systems, a translation to the measurement height can be useful.

If the origins of the $\mathcal{I}$ and the $\mathcal{W}$-system coincide, the transformation of the three wind speed

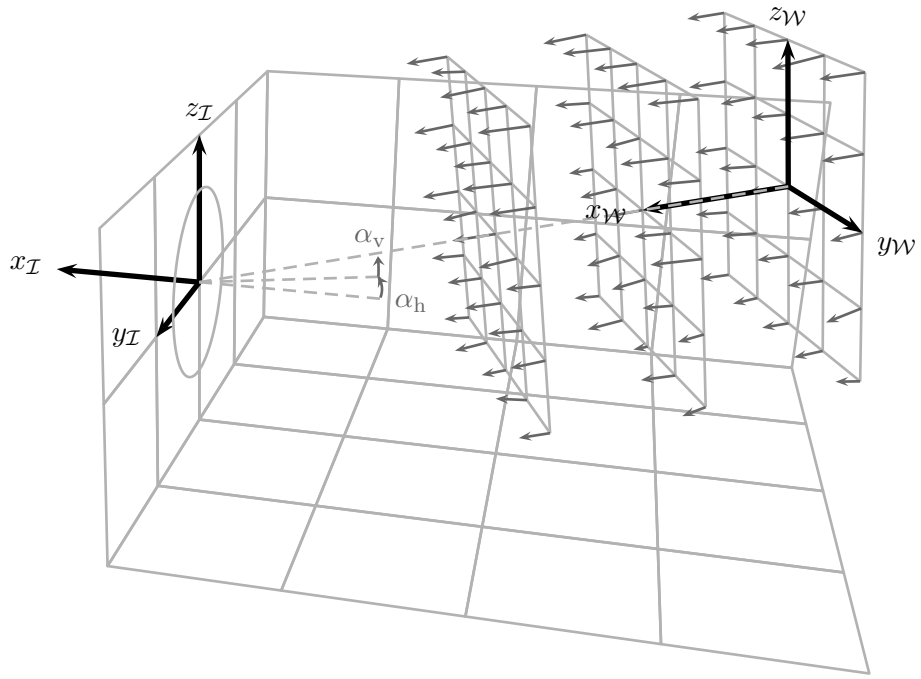

Figure 3.5: Orientation of the wind coordinate system (subscript $\mathcal{W}$) in the inertial coordinate system (subscript $\mathcal{I}$). Rotation order is defined as azimuth $\rightarrow$ elevation ($\alpha_{\mathrm{h}} \rightarrow \alpha_{\mathrm{v}}$).

components $[u_{i,\mathcal{W}}\ v_{i,\mathcal{W}}\ w_{i,\mathcal{W}}]^{\mathrm{T}}$ in a point i from the wind to the inertial coordinate system is then calculated with the rotation matrix $\boldsymbol{T}_{\mathcal{I}\mathcal{W}}$ by

$$\begin{bmatrix} u_{i,\mathcal{I}} \\ v_{i,\mathcal{I}} \\ w_{i,\mathcal{I}} \end{bmatrix} = \underbrace{\underbrace{\begin{bmatrix} \cos(\alpha_{\mathrm{h}}) & -\sin(\alpha_{\mathrm{h}}) & 0 \\ \sin(\alpha_{\mathrm{h}}) & \cos(\alpha_{\mathrm{h}}) & 0 \\ 0 & 0 & 1 \end{bmatrix}}_{T_{\mathrm{azimuth}}} \underbrace{\begin{bmatrix} \cos(\alpha_{\mathrm{v}}) & 0 & \sin(\alpha_{\mathrm{v}}) \\ 0 & 1 & 0 \\ -\sin(\alpha_{\mathrm{v}}) & 0 & \cos(\alpha_{\mathrm{v}}) \end{bmatrix}}_{T_{\mathrm{elevation}}}}_{\boldsymbol{T}_{\mathcal{I}\mathcal{W}}} \begin{bmatrix} u_{i,\mathcal{W}} \\ v_{i,\mathcal{W}} \\ w_{i,\mathcal{W}} \end{bmatrix}. \tag{3.12}$$

The transformation from the inertial to the wind coordinate system is done by

$$\begin{bmatrix} u_{i,\mathcal{W}} \\ v_{i,\mathcal{W}} \\ w_{i,\mathcal{W}} \end{bmatrix} = \boldsymbol{T}_{\mathcal{W}\mathcal{I}} \begin{bmatrix} u_{i,\mathcal{I}} \\ v_{i,\mathcal{I}} \\ w_{i,\mathcal{I}} \end{bmatrix} \text{ with } \boldsymbol{T}_{\mathcal{W}\mathcal{I}} = \boldsymbol{T}_{\mathcal{I}\mathcal{W}}^{-1} = T_{\mathrm{elevation}}^{-1} T_{\mathrm{azimuth}}^{-1}. \tag{3.13}$$

In the majority of this work, the wind turbine is assumed to be perfectly aligned with the mean wind direction. This implies that both inflow angles are zero and the wind coordinate system coincides with the inertial coordinate system. However, for the wind reconstruction in Chapter 4, the three-dimensional wind flowing towards the wind turbine is considered to slowly change its direction. In the next subsections, several wind models in the inertial coordinate system are presented.

3.2.2 Wind Models for Aero-Elastic and Lidar Simulations

As described in Chapter 2, time-variant wind fields defined on a two-dimensional grid are, in general, sufficient to be used for aero-elastic simulations, because only the aerodynamic forces and moments in the rotor plane need to be calculated. These vector fields $[u_{2\mathrm{D}}\ v_{2\mathrm{D}}\ w_{2\mathrm{D}}]^{\mathrm{T}}$ are usually aligned with the inertial coordinate system and assign a three-dimensional wind vector $[u_{i,\mathcal{W}}\ v_{i,\mathcal{W}}\ w_{i,\mathcal{W}}]^{\mathrm{T}}$ to each point i with lateral and horizontal coordinate $y_{i,\mathcal{W}}$ and $z_{i,\mathcal{W}}$ at each time t_i by interpolation. This leads to the following definition:

Definition (Wind model for aero-elastic simulation). *The wind model for aero-elastic simulation assigns a wind speed vector* $[u_{i,\mathcal{I}}\ v_{i,\mathcal{I}}\ w_{i,\mathcal{I}}]^{\mathrm{T}}$ *to each point* i *with coordinates* $[0\ y_{i,\mathcal{I}}\ z_{i,\mathcal{I}}]^{\mathrm{T}}$ *at time* t_i*, with a given vector field* $[u_{2\mathrm{D}}\ v_{2\mathrm{D}}\ w_{2\mathrm{D}}]^{\mathrm{T}}$*, as described by*

$$\begin{bmatrix} u_{i,\mathcal{I}} \\ v_{i,\mathcal{I}} \\ w_{i,\mathcal{I}} \end{bmatrix} = \begin{bmatrix} u_{i,\mathcal{W}} \\ v_{i,\mathcal{W}} \\ w_{i,\mathcal{W}} \end{bmatrix} \text{ with } \begin{bmatrix} u_{i,\mathcal{W}} \\ v_{i,\mathcal{W}} \\ w_{i,\mathcal{W}} \end{bmatrix} = \begin{bmatrix} u_{2\mathrm{D}}(y_{i,\mathcal{W}}, z_{i,\mathcal{W}}, t_i) \\ v_{2\mathrm{D}}(y_{i,\mathcal{W}}, z_{i,\mathcal{W}}, t_i) \\ w_{2\mathrm{D}}(y_{i,\mathcal{W}}, z_{i,\mathcal{W}}, t_i) \end{bmatrix} \text{ and } \begin{bmatrix} y_{i,\mathcal{W}} \\ z_{i,\mathcal{W}} \end{bmatrix} = \begin{bmatrix} y_{i,\mathcal{I}} \\ z_{i,\mathcal{I}} \end{bmatrix}. \tag{3.14}$$

However, for the simulation of lidar systems measuring in front of the rotor plane, time-variant wind fields defined for coordinates outside the rotor plane ($x_{i,\mathcal{I}} \neq 0$) are necessary, see Figure 3.5.

In this work, the method introduced by [1] is used to obtain wind speed vectors for coordinates away from the rotor. Taylor's Frozen Turbulence Hypothesis [66] assumes that the turbulence remains unchanged while traveling with the mean wind speed $\bar{u}$. Hence, the wind at time t_i in the downwind location $[x_{i,\mathcal{W}}\ y_{i,\mathcal{W}}\ z_{i,\mathcal{W}}]^{\mathrm{T}}$ passed by the point $[0\ y_{i,\mathcal{W}}\ z_{i,\mathcal{W}}]^{\mathrm{T}}$ at the rotor disc earlier at time $t_{\mathrm{R},i} = t_i - \frac{x_{i,\mathcal{W}}}{\bar{u}}$. The advantage of this method is that the same wind field can be used for the aero-elastic simulation as well as for the lidar simulations. For $\bar{u}$, the constant mean wind speed at hub height from the wind field can be applied. Thus, the following wind model is defined:

Definition (Wind model for lidar simulation). *The wind model for lidar simulation assigns a wind speed vector* $[u_{i,\mathcal{I}}\ v_{i,\mathcal{I}}\ w_{i,\mathcal{I}}]^{\mathrm{T}}$ *to each point* i *with coordinates* $[x_{i,\mathcal{I}}\ y_{i,\mathcal{I}}\ z_{i,\mathcal{I}}]^{\mathrm{T}}$ *at time* t_i*, with a given wind vector field* $[u_{2\mathrm{D}}\ v_{2\mathrm{D}}\ w_{2\mathrm{D}}]^{\mathrm{T}}$*, with a mean wind speed* $\bar{u}$*, and with given inflow angles* α_{h} *and* α_{v}*, as described by*

$$\begin{bmatrix} u_{i,\mathcal{I}} \\ v_{i,\mathcal{I}} \\ w_{i,\mathcal{I}} \end{bmatrix} = \boldsymbol{T}_{\mathcal{I}\mathcal{W}}(\alpha_{\mathrm{h}}, \alpha_{\mathrm{v}}) \begin{bmatrix} u_{i,\mathcal{W}} \\ v_{i,\mathcal{W}} \\ w_{i,\mathcal{W}} \end{bmatrix} \text{ with } \begin{bmatrix} u_{i,\mathcal{W}} \\ v_{i,\mathcal{W}} \\ w_{i,\mathcal{W}} \end{bmatrix} = \begin{bmatrix} u_{2\mathrm{D}}(y_{i,\mathcal{W}}, z_{i,\mathcal{W}}, t_{\mathrm{R},i}) \\ v_{2\mathrm{D}}(y_{i,\mathcal{W}}, z_{i,\mathcal{W}}, t_{\mathrm{R},i}) \\ w_{2\mathrm{D}}(y_{i,\mathcal{W}}, z_{i,\mathcal{W}}, t_{\mathrm{R},i}) \end{bmatrix},$$

$$t_{\mathrm{R},i} = t_i - \frac{x_{i,\mathcal{W}}}{\bar{u}}, \text{ and } \begin{bmatrix} x_{i,\mathcal{W}} \\ y_{i,\mathcal{W}} \\ z_{i,\mathcal{W}} \end{bmatrix} = \boldsymbol{T}_{\mathcal{W}\mathcal{I}}(\alpha_{\mathrm{h}}, \alpha_{\mathrm{v}}) \begin{bmatrix} x_{i,\mathcal{I}} \\ y_{i,\mathcal{I}} \\ z_{i,\mathcal{I}} \end{bmatrix}. \tag{3.15}$$

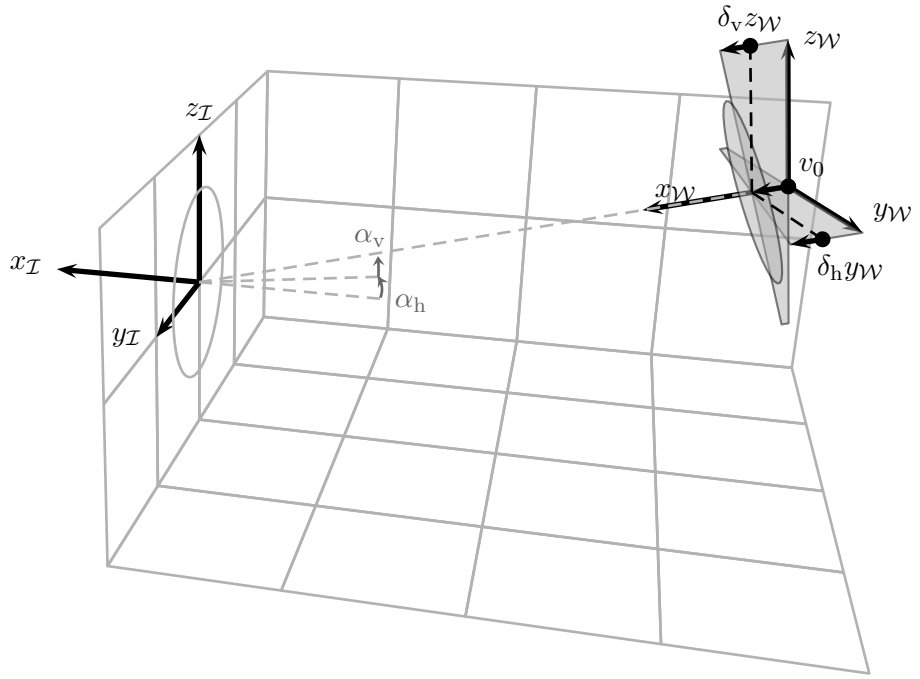

Figure 3.6: Three-dimensional inhomogeneous flow model: the wind vector field is parameterized by a rotor effective wind speed v_0, a linear horizontal and vertical shears δ_h and δ_v, and the horizontal and the vertical inflow angles α_h and α_v.

However, measurements in front of the turbine reveal that the wind field evolves when moving from the point of measurement to the rotor plane [67]. There are several approaches to include the wind evolution in the wind fields used for simulations: in [20, 68] wind component signals are generated at the lidar measurement position using the wind evolution model of [56] in addition to the two-dimensional wind fields used for aero-elastic simulations. Even more realistic three-dimensional time-variant wind fields can be obtained from Computational Fluid Dynamics (CFD) simulations. The advantage of these wind fields is that effects, such as the induction zone, can be included by coupling CFD simulations to aero-elastic simulations [69]. However, these coupled simulations are still computationally very extensive.

3.2.3 Reduced Wind Model for Wind Field Reconstruction

Usually, the following homogeneous flow model is used by commercial lidar systems:

Definition (Homogeneous flow model). *The homogeneous flow model assigns the same wind speed vector* $[u_\mathcal{I}\ v_\mathcal{I}\ w_\mathcal{I}]^\mathrm{T}$ *to each point* i*:*

$$\begin{bmatrix} u_{i,\mathcal{I}} \\ v_{i,\mathcal{I}} \\ w_{i,\mathcal{I}} \end{bmatrix} = \begin{bmatrix} u_\mathcal{I} \\ v_\mathcal{I} \\ w_\mathcal{I} \end{bmatrix}. \tag{3.16}$$

However, this model has some shortcomings as explained later in Chapter 4. Here, an inhomogeneous flow model is proposed that neglects the lateral and vertical wind components $v_{\mathcal{W}}$ and $w_{\mathcal{W}}$ in the $\mathcal{W}$-system. The longitudinal wind component $u_{\mathcal{W}}$ is parameterized by the rotor effective wind speed v_0, the linear horizontal shear δ_h, the linear vertical shear δ_v, the horizontal inflow angle α_h, and the vertical inflow angle α_v (see Figure 3.6). These parameters are denoted in this work as wind characteristics. In the static case, the wind field and the wind characteristics are assumed to be constant for a given period of time:

Definition (Static inhomogeneous flow model). *The static inhomogeneous flow model assigns a wind speed vector* $[u_{i,\mathcal{I}}\ v_{i,\mathcal{I}}\ w_{i,\mathcal{I}}]^\mathrm{T}$ *to each point* i *with coordinates* $[x_{i,\mathcal{I}}\ y_{i,\mathcal{I}}\ z_{i,\mathcal{I}}]^\mathrm{T}$*, with given wind characteristics* v_0*,* δ_h*,* δ_v*,* α_h*, and* α_v*, as described by:*

$$\begin{bmatrix} u_{i,\mathcal{I}} \\ v_{i,\mathcal{I}} \\ w_{i,\mathcal{I}} \end{bmatrix} = \boldsymbol{T}_{\mathcal{I}\mathcal{W}}(\alpha_\mathrm{h}, \alpha_\mathrm{v}) \begin{bmatrix} u_{i,\mathcal{W}} \\ v_{i,\mathcal{W}} \\ w_{i,\mathcal{W}} \end{bmatrix} \text{ with } \begin{bmatrix} u_{i,\mathcal{W}} \\ v_{i,\mathcal{W}} \\ w_{i,\mathcal{W}} \end{bmatrix} = \begin{bmatrix} v_0 + \delta_\mathrm{h} y_{i,\mathcal{W}} + \delta_\mathrm{v} z_{i,\mathcal{W}} \\ 0 \\ 0 \end{bmatrix}$$
$$\text{and } \begin{bmatrix} x_{i,\mathcal{W}} \\ y_{i,\mathcal{W}} \\ z_{i,\mathcal{W}} \end{bmatrix} = \boldsymbol{T}_{\mathcal{W}\mathcal{I}}(\alpha_\mathrm{h}, \alpha_\mathrm{v}) \begin{bmatrix} x_{i,\mathcal{I}} \\ y_{i,\mathcal{I}} \\ z_{i,\mathcal{I}} \end{bmatrix}. \tag{3.17}$$

For lidar-assisted control, it is also beneficial to take the temporal relationship of the wind propagating along the mean wind direction into account. Here, the rotor effective wind speed $v_0(t)$ and the shears $\delta_\mathrm{v}(t)$ and $\delta_\mathrm{h}(t)$ are assumed to be time-dependent and Taylor's Frozen Turbulence Hypothesis is applied. This is similar to model (3.15), which is used for the lidar simulation. With the time-dependent wind characteristics, the following model is defined:

Definition (Dynamic inhomogeneous flow model). *The dynamic inhomogeneous flow model assigns a wind speed vector* $[u_{i,\mathcal{I}}\ v_{i,\mathcal{I}}\ w_{i,\mathcal{I}}]^\mathrm{T}$ *to each point* i *with coordinates* $[x_{i,\mathcal{I}}\ y_{i,\mathcal{I}}\ z_{i,\mathcal{I}}]^\mathrm{T}$ *at time* t_i*, with given time-dependent wind characteristics* $v_0(t)$*,* $\delta_\mathrm{h}(t)$*, and* $\delta_\mathrm{v}(t)$*, with given scalar wind characteristics* α_h *and* α_v*, and with a given mean wind speed* $\bar{u}$*, as described by:*

$$\begin{bmatrix} u_{i,\mathcal{I}} \\ v_{i,\mathcal{I}} \\ w_{i,\mathcal{I}} \end{bmatrix} = \boldsymbol{T}_{\mathcal{I}\mathcal{W}}(\alpha_\mathrm{h}, \alpha_\mathrm{v}) \begin{bmatrix} u_{i,\mathcal{W}} \\ v_{i,\mathcal{W}} \\ w_{i,\mathcal{W}} \end{bmatrix} \text{ with } \begin{bmatrix} u_{i,\mathcal{W}} \\ v_{i,\mathcal{W}} \\ w_{i,\mathcal{W}} \end{bmatrix} = \begin{bmatrix} v_0(t_{\mathrm{R},i}) + \delta_\mathrm{h}(t_{\mathrm{R},i}) y_{i,\mathcal{W}} + \delta_\mathrm{v}(t_{\mathrm{R},i}) z_{i,\mathcal{W}} \\ 0 \\ 0 \end{bmatrix}$$
$$t_{\mathrm{R},i} = t_i - \frac{x_{i,\mathcal{W}}}{\bar{u}}, \text{ and } \begin{bmatrix} x_{i,\mathcal{W}} \\ y_{i,\mathcal{W}} \\ z_{i,\mathcal{W}} \end{bmatrix} = \boldsymbol{T}_{\mathcal{W}\mathcal{I}}(\alpha_\mathrm{h}, \alpha_\mathrm{v}) \begin{bmatrix} x_{i,\mathcal{I}} \\ y_{i,\mathcal{I}} \\ z_{i,\mathcal{I}} \end{bmatrix}. \tag{3.18}$$

The idea behind the wind characteristics is to have signals representing the effect of the wind field on the rotor of a simplified wind turbine. A wind field with the same rotor effective wind

speed v_0 should generate the same aerodynamic torque. In the following subsection, a linear unweighted and a squared weighted case are presented, which will both be used in this work.

3.2.4 Wind Characteristics from Wind Fields

In the linear and unweighted case, it is assumed that the rotor effective wind speed is an average of the wind flowing through the rotor disk. This can be expressed by the integral of the longitudinal wind component over the rotor area with rotor radius R divided by the rotor area:

$$v_0 = \frac{1}{\pi R^2} \int_0^{2\pi} \int_0^R u_{\mathcal{I}} \; r \, \mathrm{d}r \, \mathrm{d}\phi, \tag{3.19}$$

with the polar coordinates $r = \sqrt{y_{\mathcal{I}}^2 + z_{\mathcal{I}}^2}$ and $\phi = \arctan(y_{\mathcal{I}}/z_{\mathcal{I}})$.
For a discrete-dimensional wind field, Equation (3.19) is simplified by a mean over all n_R longitudinal wind components within the rotor disk (Riemann sum):

$$v_0 = \frac{1}{n_\mathrm{R}} \sum_{i=1}^{n_\mathrm{R}} u_{i,\mathcal{I}}. \tag{3.20}$$

In the squared and weighted case, it is assumed that the impact of the longitudinal wind component $u_{\mathcal{I}}$ depends on the contribution to the aerodynamic torque:

$$v_0 = \sqrt{\frac{\int_0^{2\pi} \int_0^R \frac{\partial c_\mathrm{P}}{\partial r}(r) \; u_{\mathcal{I}}^2 \, r \, \mathrm{d}r \, \mathrm{d}\phi}{\int_0^{2\pi} \int_0^R \frac{\partial c_\mathrm{P}}{\partial r}(r) \, r \, \mathrm{d}r \, \mathrm{d}\phi}}. \tag{3.21}$$

The stationary spanwise variation of power extraction $\frac{\partial c_\mathrm{P}}{\partial r}(r)$ with

$$\int_0^R \frac{\partial c_\mathrm{P}}{\partial r}(r) \, \mathrm{d}r = c_{\mathrm{P,max}} \leq c_{\mathrm{P,Betz}} \text{ with } c_{\mathrm{P,Betz}} = \int_0^R \frac{32}{27R^2} r \, \mathrm{d}r = \frac{16}{27} \tag{3.22}$$

can be obtained by modeling tip and root losses following [70] and [41]. Figure 3.7 shows the used weighting function with $c_{\mathrm{P,max}}$ and $r_{\min}$ from Table C.2. This curve is an approximation of the aerodynamics and will differ in aero-elastic simulations from the actual values. However, it still covers the effect of tip and root losses compared to a simple average over the rotor disc. For a discrete wind field, Equation (3.21) is simplified to a weighted sum of all longitudinal

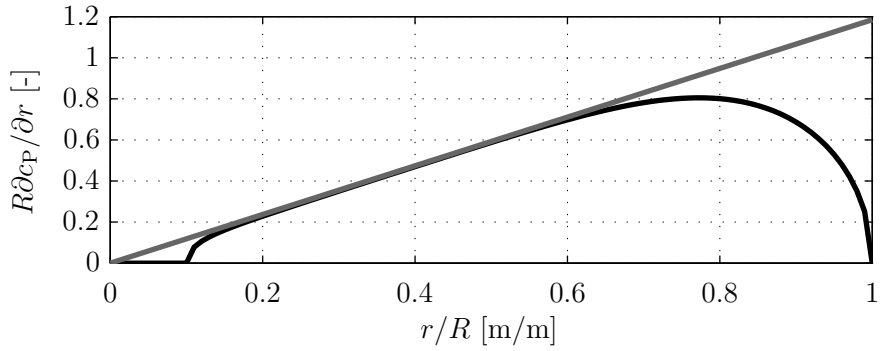

Figure 3.7: Used span-wise variation of power extraction in the presence of tip and root losses (black) and Betz-optimal curve without losses (gray).

wind components within the rotor disc:

$$v_0 = \frac{\sum_{i=1}^{n_\mathrm{R}} c_{\mathrm{P},i}\ u_{i,\mathcal{I}}}{\sum_{i=1}^{n_\mathrm{R}} c_{\mathrm{P},i}}, \tag{3.23}$$

with $c_{\mathrm{P},i} = \frac{\partial c_\mathrm{P}}{\partial r}(r_i)$ evaluated at the distance $r_i = \sqrt{y_{i,\mathcal{I}}^2 + z_{i,\mathcal{I}}^2}$ from the hub.
A linear vertical shear δ_v is chosen for this work instead of a logarithmic or exponential shear, which are often used for the description of averaged vertical wind profiles. One advantage of using linear vertical shear is that it can be directly used as a disturbance input for the reduced wind turbine model. Another advantage is that fitting a wind field with a normal turbulence level to a linear shear is more robust compared to logarithmic or exponential shear models.
In the linear and unweighted case, the shears can be extracted from a two-dimensional wind field using a linear fit. The equations for longitudinal wind components in (3.17) can be arranged in the following form for all n_R points inside the rotor disk and for each time t_i:

$$\underbrace{\begin{bmatrix} u_{1,\mathcal{I}} \\ \vdots \\ u_{n_\mathrm{R},\mathcal{I}} \end{bmatrix}}_{\boldsymbol{m}} = \underbrace{\begin{bmatrix} 1 & y_{1,\mathcal{I}} & z_{1,\mathcal{I}} \\ \vdots & \vdots & \vdots \\ 1 & y_{n_\mathrm{R},\mathcal{I}} & z_{n_\mathrm{R},\mathcal{I}} \end{bmatrix}}_{\boldsymbol{A}} \underbrace{\begin{bmatrix} v_0 \\ \delta_\mathrm{h} \\ \delta_\mathrm{v} \end{bmatrix}}_{\boldsymbol{s}}. \tag{3.24}$$

The wanted vector $\boldsymbol{s}$ can then be obtained by applying the least squares method given that the matrix $\boldsymbol{A}$ represents the linear coefficients and vector $\boldsymbol{m}$ the longitudinal wind components:

$$\min_{\boldsymbol{s}} \left\| \boldsymbol{m} - \boldsymbol{A}\boldsymbol{s} \right\|_2. \tag{3.25}$$

For the rotor effective wind v_0, Equation (3.25) is equivalent to (3.20) due to the linearity.

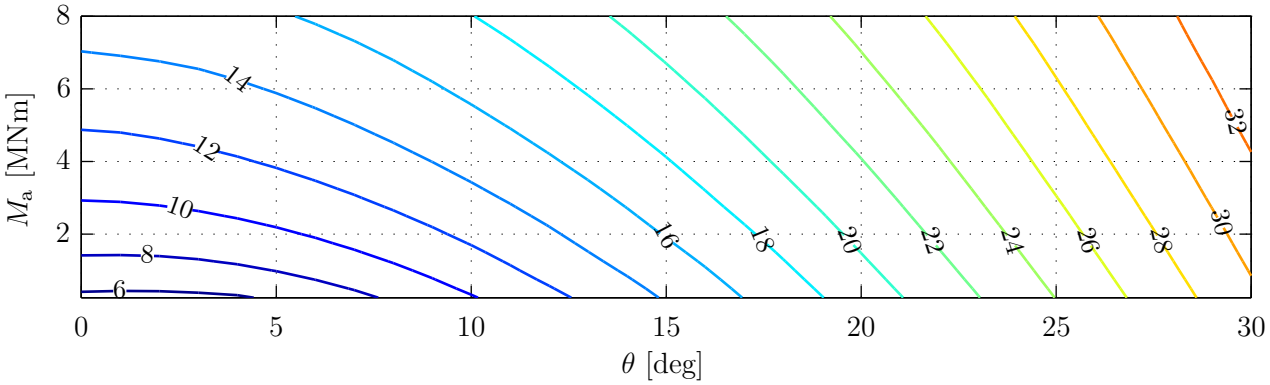

Figure 3.8: Contour lines of rotor effective wind speeds at $\Omega = 12.1\,\text{rpm}$ for the NREL 5 MW turbine.

3.2.5 Wind Characteristics from Turbine Data

The rotor effective wind speed v_0 can be also obtained from turbine data by an estimator similar to the one presented in [71]. Here, the reduced model from Section 3.1.2 is further simplified by neglecting the tower motion. Then, with the equations for the drive train dynamics (3.3a), the aerodynamic torque (3.9a), and the tip speed ratio (3.10), one can obtain the following model

$$J\dot{\Omega} + M_{\text{LSS}} = M_{\text{a}} \tag{3.26a}$$

$$M_{\text{a}} = \frac{1}{2}\rho\pi R^3 \frac{c_{\text{P}}(\lambda,\theta)}{\lambda} v_0^2 \tag{3.26b}$$

$$\lambda = \frac{\Omega R}{v_0}. \tag{3.26c}$$

Here, M_{LSS} is the low-speed shaft torque, which can be either measured directly or calculated from the electrical power (3.7c) or the generator torque:

$$M_{\text{LSS}} = \frac{M_{\text{G}}}{i_{\text{GB}}} = \frac{P_{\text{el}}}{\eta_{\text{el}}\Omega}. \tag{3.27}$$

With measured data of Ω and M_{LSS}, the aerodynamic torque M_{a} can be calculated using Equation (3.26a). Due to numerical issues, Equation (3.26b) is reorganized into:

$$\lambda^3 = \frac{1}{2}\rho\pi R^5 \frac{c_{\text{P}}(\lambda,\theta)}{M_{\text{a}}}\Omega^2. \tag{3.28}$$

Because of the λ-dependency of c_{P}, an explicit expression cannot be found. The equation is solved with a set of M_{a}, Ω and θ, and a three-dimensional look-up table $v_{0\text{R}}(M_{\text{a}},\Omega,\theta)$ is generated (see Figure 3.8), which can then be used to get a time series of $v_{0\text{R}}$ by a three-dimensional interpolation. An adjustment is necessary if c_{P} was determined with an air density different from the measured mean value. This estimator is used for post-processing. More sophisticated estimators such as a Kalman filter [72] might be better suited for online purposes.

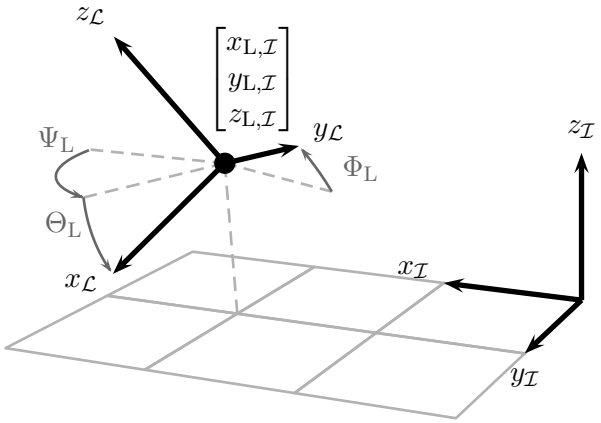

Figure 3.9: Orientation of the lidar coordinate system (subscript $\mathcal{L}$) in the inertial coordinate system (subscript $\mathcal{I}$): Origin of the $\mathcal{L}$-system within the $\mathcal{I}$-system is $[x_{\mathrm{L},\mathcal{I}}\ y_{\mathrm{L},\mathcal{I}}\ z_{\mathrm{L},\mathcal{I}}]^\mathrm{T}$ and rotation order from $\mathcal{L}$ to $\mathcal{I}$ is defined as yaw $\rightarrow$ pitch $\rightarrow$ roll ($\Psi_\mathrm{L} \rightarrow \Theta_\mathrm{L} \rightarrow \Phi_\mathrm{L}$).

3.3 Lidar System Modeling

In this section the lidar coordinate system is defined and the lidar models for idealized point measurements and more realistic volume measurements are presented.

3.3.1 Lidar Coordinate System

The lidar measurements are modeled in the lidar coordinate system, which is denoted in this work by the subscript $\mathcal{L}$. This is necessary, because the lidar system can be installed at different locations other than the origin of the inertial frame or the system can change its position and inclination, for example on the nacelle of an operating wind turbine or on a buoy for offshore applications. All six DOFs are considered, see Figure 3.9. The position of the lidar system within the inertial coordinate system is defined by $[x_{\mathrm{L},\mathcal{I}}\ y_{\mathrm{L},\mathcal{I}}\ z_{\mathrm{L},\mathcal{I}}]^\mathrm{T}$. The rotation follows the convention used in aviation. The translated system is rotated around the z-axis by the yaw angle Ψ_L, around the rotated y-axis by the pitch angle Θ_L, and finally around the rotated x-axis by the roll angle Φ_L.
The transformation from the lidar to the inertial coordinate system is then calculated with the rotation matrix $\boldsymbol{T}_{\mathcal{I}\mathcal{L}}$ by

$$\begin{bmatrix} x_{i,\mathcal{I}} \\ y_{i,\mathcal{I}} \\ z_{i,\mathcal{I}} \end{bmatrix} = \boldsymbol{T}_{\mathcal{I}\mathcal{L}} \begin{bmatrix} x_{i,\mathcal{L}} \\ y_{i,\mathcal{L}} \\ z_{i,\mathcal{L}} \end{bmatrix} + \begin{bmatrix} x_{\mathrm{L},\mathcal{I}} \\ y_{\mathrm{L},\mathcal{I}} \\ z_{\mathrm{L},\mathcal{I}} \end{bmatrix} \quad \text{with}$$

$$\boldsymbol{T}_{\mathcal{I}\mathcal{L}} = \underbrace{\begin{bmatrix} \cos(\Psi_\mathrm{L}) & -\sin(\Psi_\mathrm{L}) & 0 \\ \sin(\Psi_\mathrm{L}) & \cos(\Psi_\mathrm{L}) & 0 \\ 0 & 0 & 1 \end{bmatrix}}_{T_\mathrm{yaw}} \underbrace{\begin{bmatrix} \cos(\Theta_\mathrm{L}) & 0 & \sin(\Theta_\mathrm{L}) \\ 0 & 1 & 0 \\ -\sin(\Theta_\mathrm{L}) & 0 & \cos(\Theta_\mathrm{L}) \end{bmatrix}}_{T_\mathrm{pitch}} \underbrace{\begin{bmatrix} 1 & 0 & 0 \\ 0 & \cos(\Phi_\mathrm{L}) & -\sin(\Phi_\mathrm{L}) \\ 0 & \sin(\Phi_\mathrm{L}) & \cos(\Phi_\mathrm{L}) \end{bmatrix}}_{T_\mathrm{roll}} \tag{3.29}$$

and the transformation back to the lidar coordinate system by

$$\begin{bmatrix} x_{i,\mathcal{L}} \\ y_{i,\mathcal{L}} \\ z_{i,\mathcal{L}} \end{bmatrix} = \boldsymbol{T}_{\mathcal{L}\mathcal{I}} \begin{bmatrix} x_{i,\mathcal{I}} - x_{\mathrm{L},\mathcal{I}} \\ y_{i,\mathcal{I}} - y_{\mathrm{L},\mathcal{I}} \\ z_{i,\mathcal{I}} - z_{\mathrm{L},\mathcal{I}} \end{bmatrix} \text{ with } \boldsymbol{T}_{\mathcal{L}\mathcal{I}} = \boldsymbol{T}_{\mathcal{I}\mathcal{L}}^{-1}. \tag{3.30}$$

3.3.2 Lidar Model for Point Measurement

A lidar system is only able to measure the component of the wind vector in the laser beam direction. Per convention, this value is positive, if the wind is directed towards the laser source. Therefore, the line-of-sight wind speed $v_{\mathrm{los},i}$ measured at point i with coordinates $[x_{i,\mathcal{I}}\ y_{i,\mathcal{I}}\ z_{i,\mathcal{I}}]^{\mathrm{T}}$ can be modeled by a projection of the wind vector $[u_{i,\mathcal{I}}\ v_{i,\mathcal{I}}\ w_{i,\mathcal{I}}]^{\mathrm{T}}$ at point i and the normalized vector of the backscattered laser beam, which mathematically is equivalent to the scalar product of both vectors:

$$v_{\mathrm{los},i} = x_{\mathrm{n},i,\mathcal{I}}\ u_{i,\mathcal{I}} + y_{\mathrm{n},i,\mathcal{I}}\ v_{i,\mathcal{I}} + z_{\mathrm{n},i,\mathcal{I}}\ w_{i,\mathcal{I}}, \tag{3.31}$$

where the normalized laser vector measuring at a distance $r_{\mathrm{L}i}$ from the lidar system is

$$\begin{bmatrix} x_{\mathrm{n},i,\mathcal{I}} \\ y_{\mathrm{n},i,\mathcal{I}} \\ z_{\mathrm{n},i,\mathcal{I}} \end{bmatrix} = \frac{1}{r_{\mathrm{L}i}} \begin{bmatrix} x_{\mathrm{L},\mathcal{I}} - x_{i,\mathcal{I}} \\ y_{\mathrm{L},\mathcal{I}} - y_{i,\mathcal{I}} \\ z_{\mathrm{L},\mathcal{I}} - z_{i,\mathcal{I}} \end{bmatrix} \text{ with } r_{\mathrm{L}i} = \sqrt{x_{i,\mathcal{L}}^2 + y_{i,\mathcal{L}}^2 + z_{i,\mathcal{L}}^2}. \tag{3.32}$$

This model is independent of the used coordinate system. However, it is more convenient to use the $\mathcal{I}$-system. If the lidar system is not fixed in the inertial frame, but moving with $[\dot{x}_{\mathrm{L},\mathcal{I}}\ \dot{y}_{\mathrm{L},\mathcal{I}}\ \dot{z}_{\mathrm{L},\mathcal{I}}]^{\mathrm{T}}$, Equation (3.31) can be adjusted as follows:

$$v_{\mathrm{los},i} = x_{\mathrm{n},i,\mathcal{I}}\ (u_{i,\mathcal{I}} - \dot{x}_{\mathrm{L},\mathcal{I}}) + y_{\mathrm{n},i,\mathcal{I}}\ (v_{i,\mathcal{I}} - \dot{y}_{\mathrm{L},\mathcal{I}}) + z_{\mathrm{n},i,\mathcal{I}}\ (w_{i,\mathcal{I}} - \dot{z}_{\mathrm{L},\mathcal{I}}). \tag{3.33}$$

3.3.3 Lidar Model for Volume Measurement

In Equation (3.31), the measurement is assumed for one single point. However, real lidar systems measure within a probe volume due to the length of the emitted pulse of pulsed lidar systems [60]) or due to the focusing of the laser beam of continuous wave lidar systems [61]. Additionally, the FFT involved in the detection of the frequency shift requires a certain fraction of the backscattered signal, contributing to the averaging effect. Thus, lidar measurements are modeled more realistically considering the overall averaging effect by:

$$v_{\mathrm{los},i} = \int_{-\infty}^{\infty} (x_{\mathrm{n},i,\mathcal{I}}\ u_{a,i,\mathcal{I}} + y_{\mathrm{n},i,\mathcal{I}}\ v_{a,i,\mathcal{I}} + z_{\mathrm{n},i,\mathcal{I}}\ w_{a,i,\mathcal{I}})\, f_{\mathrm{RW}}(a)\, \mathrm{d}a. \tag{3.34}$$

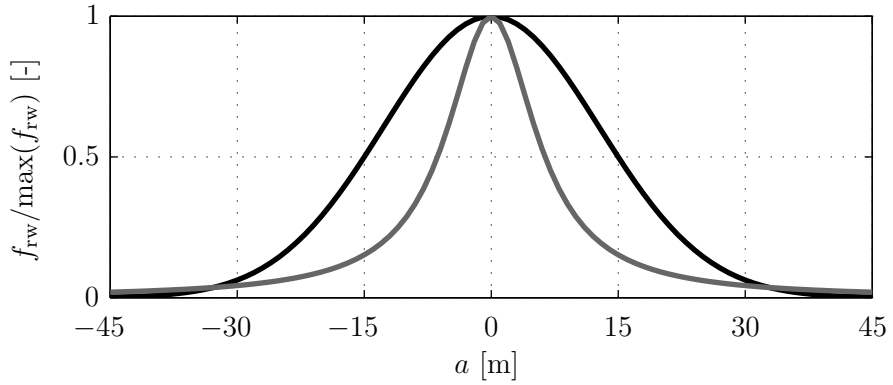

Figure 3.10: Normalized range weighting functions for a pulsed lidar system (black) and a continuous-wave lidar system (gray) at a focus range of 100 m.

The range weighting function $f_{\mathrm{RW}}(a)$ at the distance a to the measurement point depends on the used lidar technology (pulsed or continuous wave). The wind vector $[u_{a,i,\mathcal{I}}\ v_{a,i,\mathcal{I}}\ w_{a,i,\mathcal{I}}]^{\mathrm{T}}$ is an evaluation of the wind field at

$$\begin{bmatrix} x_{a,i,\mathcal{I}} \\ y_{a,i,\mathcal{I}} \\ z_{a,i,\mathcal{I}} \end{bmatrix} = \begin{bmatrix} x_{i,\mathcal{I}} \\ y_{i,\mathcal{I}} \\ z_{i,\mathcal{I}} \end{bmatrix} + a \begin{bmatrix} x_{\mathrm{n},i,\mathcal{I}} \\ y_{\mathrm{n},i,\mathcal{I}} \\ z_{\mathrm{n},i,\mathcal{I}} \end{bmatrix}. \tag{3.35}$$

Again, Equation (3.34) can be adjusted for moving lidar systems similar to Equation (3.33):

$$v_{\mathrm{los},i} = \int_{-\infty}^{\infty} \left(x_{\mathrm{n},i,\mathcal{I}}\ (u_{a,i,\mathcal{I}} - \dot{x}_{\mathrm{L},\mathcal{I}}) + y_{\mathrm{n},i,\mathcal{I}}\ (v_{a,i,\mathcal{I}} - \dot{y}_{\mathrm{L},\mathcal{I}}) + z_{\mathrm{n},i,\mathcal{I}}\ (w_{a,i,\mathcal{I}} - \dot{z}_{\mathrm{L},\mathcal{I}})\right) f_{\mathrm{RW}}(a)\,\mathrm{d}a. \tag{3.36}$$

For the pulsed lidar system considered in this work, a normalized Gaussian shape weighting function is used (see Figure 3.10), following [60]. The function is parameterized by a standard deviation σ_{L} depending on the Full Width at Half Maximum (FWHM) of $W_{\mathrm{L}} = 30\,\mathrm{m}$:

$$f_{\mathrm{RW}}(a) = \frac{1}{\sigma_{\mathrm{L}}\sqrt{2\pi}} \exp\left(-\frac{a^2}{2\sigma_{\mathrm{L}}^2}\right) \text{ with } \sigma_{\mathrm{L}} = \frac{W_{\mathrm{L}}}{2\sqrt{2\ln 2}}. \tag{3.37}$$

Following the considerations of [61], a normalized Lorentzian shape weighting function is used to model the volume measurement of continuous-wave lidar systems. This is given by

$$f_{\mathrm{RW}}(a) = \frac{\Gamma_{\mathrm{L}}/\pi}{a^2 + \Gamma_{\mathrm{L}}^2} \text{ with } \Gamma_{\mathrm{L}} = \frac{\lambda_{\mathrm{L}} r_{\mathrm{L}i}^2}{\pi A_{\mathrm{L}}^2}. \tag{3.38}$$

Here, Γ_{L} is the halfwidth of the weighting function at the -3 dB point depending on the beam radius at the output lens $A_{\mathrm{L}} = 28\,\mathrm{mm}$, the laser wave length λ_{L}, and the focus range $r_{\mathrm{L}i}$. Figure 3.10 shows the function for $r_{\mathrm{L}i} = 100\,\mathrm{m}$.

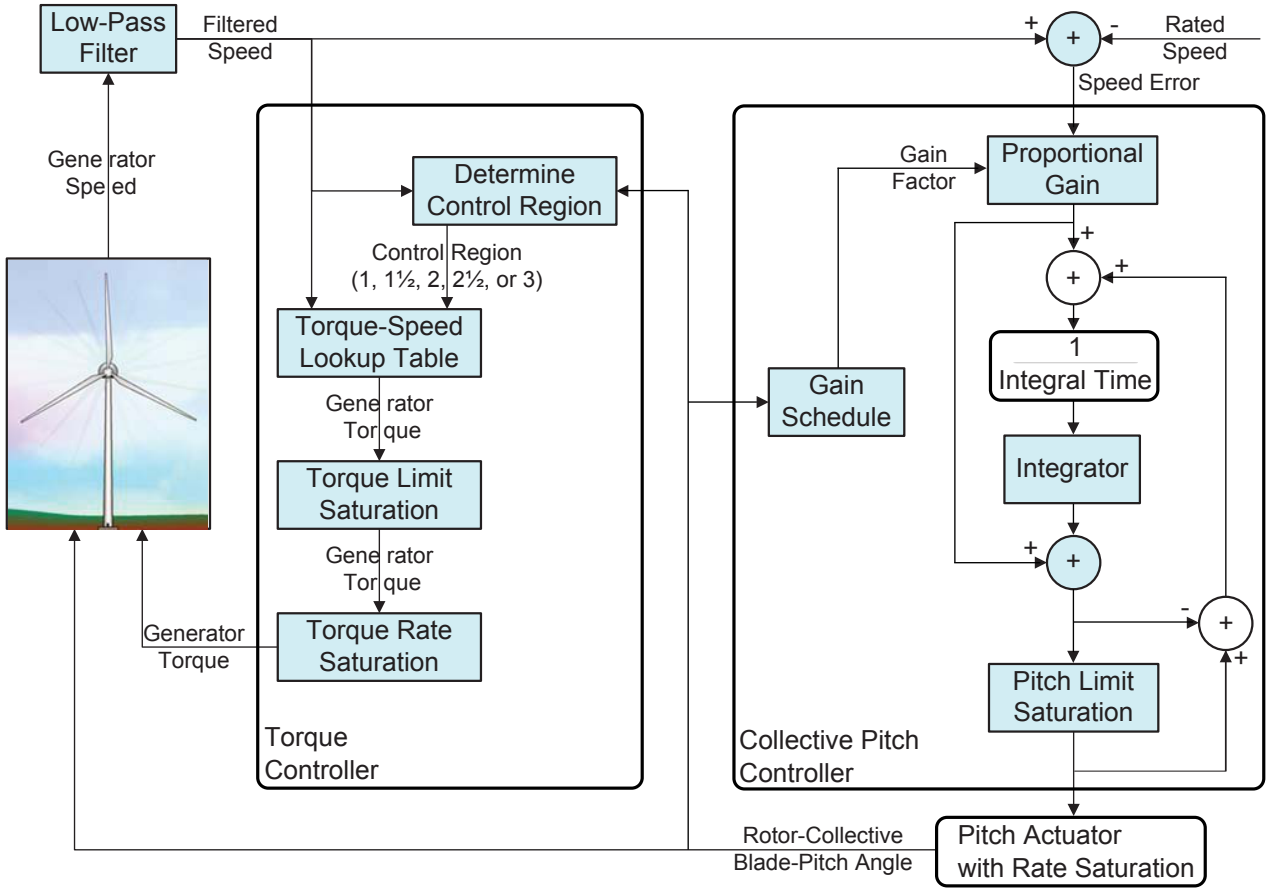

Figure 3.11: Flowchart of the baseline controller for the NREL 5 MW turbine based on [63]. Modifications include the usage of the collective pitch from the added pitch actuator for gain scheduling and determination of the torque control region, the multiplication of the gain factor prior to the integration, and a changed parameterizing and anti-windup strategy of the collective pitch controller.

3.4 Baseline Wind Turbine Controller

The baseline controller is implemented as described in [63] with some minor changes and combines a variable speed generator torque controller and a collective blade pitch controller (see Figure 3.11). Both controllers use the generator speed as the input. The speed signal is filtered using a single-pole low-pass filter with a corner frequency of 0.25 Hz, to mitigate high-frequency excitation of the control systems. The baseline torque and collective pitch controllers are in principle SISO controllers and primarily operate independently of each other. In this section, the basic idea and design process of both controllers are presented. More details can be found in [63]. The used parameters are tabulated in Table C.2.

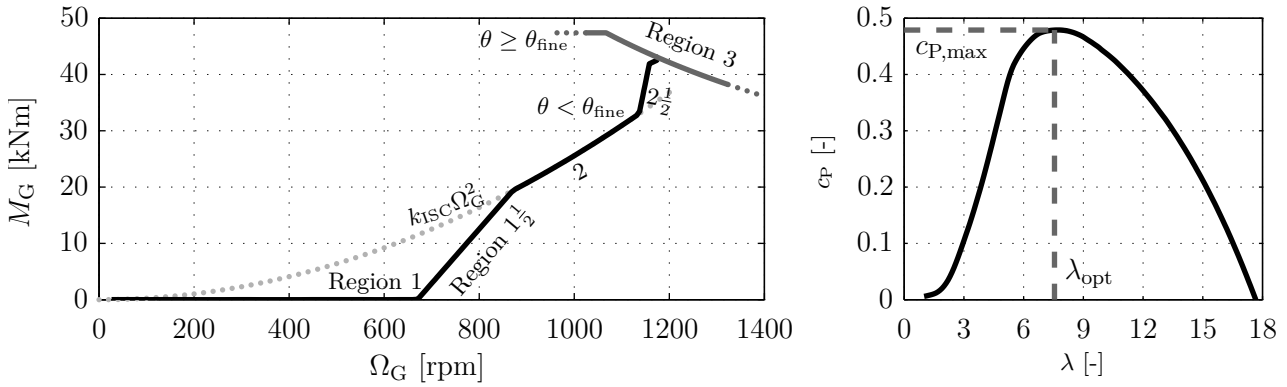

Figure 3.12: Left: Baseline generator torque control for the NREL 5 MW turbine. Right: Power coefficient as a function of tip speed ratio for the NREL 5 MW turbine (solid) and optimal values (dashed).

3.4.1 Baseline Torque Controller

For the torque controller, the operation is divided into several control regions as shown in Figure 3.12 (left).

In region 1, the wind speed is too low to operate the turbine. In region 2, at below rated wind speed, the goal of the torque controller is to maximize the energy yield [41]. Therefore, the turbine has to operate with the rotor blades held at the optimal angle of attack. This maximizes the power coefficient c_P, which, when operating below rated wind speed (fixed blade pitch angles), only depends on λ, see Figure 3.12 (right). The optimal tip speed ratio λ_{opt} can be found at the peak $c_{P,max}$. Thus, the generator torque M_G needs to be adjusted to track the optimal tip speed ratio λ_{opt}. However, λ is not available under normal circumstances. Therefore, a common output feedback controller such as a Proportional-Integral (PI) controller cannot be applied. Normally, nonlinear state feedback controllers are used, measuring the generator or rotor speed. For derivations of state feedback control laws, the rotor motion (3.3a) and the aerodynamic torque (3.9a) of the nonlinear reduced model for below rated wind speed are considered. During steady-state operation, the generator torque needed to maintain the maximum power coefficient $c_{P,max}$ can then be determined by:

$$M_{G,ISC} = \underbrace{\frac{1}{2}\rho\pi R^5 \frac{c_{P,max}}{\lambda_{opt}^3} i_{GB}^3}_{k_{ISC}} \Omega_G^2. \tag{3.39}$$

Equation (3.39) with constant k_{ISC} is known as the Indirect Speed Controller (ISC) and is stable as long as the tip speed ratio resides above a calculable lower limit [73].

The transition regions $1\frac{1}{2}$ and $2\frac{1}{2}$ use a linear function as state feedback and link the region 2 to region 1 and 3, respectively.

In region 3, the torque controller regulates power by simply inverting the equation for the

electrical power (3.7c):

$$M_G = \frac{P_{\text{el,rated}}}{\eta_{\text{el}}\Omega_{\text{G}}} \tag{3.40}$$

The torque controller continues to regulate power as long as the blade pitch angle remains above a certain threshold θ_{fine}. If the pitch angle is below θ_{fine}, the torque controller switches back to region $2\frac{1}{2}$. In [63] no pitch actuator model is implemented. The pitch actuator model in (3.1) allows the use of the actual collective pitch angle for the switching, instead of the demanded pitch angle. Due to the filter effect of the pitch actuator dynamics, switching with high frequency is reduced.

3.4.2 Baseline Collective Pitch Controller

The task of the Collective Pitch Controller (CPC) is to regulate the rotor speed when the turbine operates at rated power. The collective blade pitch angle command is computed using a gain-scheduled PI controller on the speed error between the filtered and the rated generator speed. The gain-scheduling is necessary to account for the increasing sensitivity of the pitch angle. For the same wind change a larger change in the pitch angle is necessary for small pitch angles (for example 0 deg close to rated wind speed) compared to larger pitch angles (for example around 20 deg at the cut-out wind speed). The baseline collective pitch controller is slightly modified. In [63], the gain factor is applied to the integral term after the integration. In this work however, the gain is applied prior to the integration to maintain the basic idea of the "two-degree-of-freedom-control" [74]. It is useful to complete the two main tasks for controllers (reference signal tracking and disturbance compensation) independently by a feedback and a feedforward controller. In the case of using the feedforward for disturbance rejection, the feedback controller should not interfere, if the feedforward controller is able to compensate the disturbance. However, applying the gain after the integration would change the output of the feedback controller and counteract the effects of the feedforward controller. More details are provided in Chapter 6.

Due to the limits of the pitch angle, the PI control needs an integrator anti-windup strategy to avoid saturation of the integral term and the associated drawbacks, such as delayed control reaction and overshooting. In [63], a simple saturation limit for the integrator was used. This is known as "integrator clamping". Here, a more classic approach (often called "back-calculation anti-windup") is used [75].

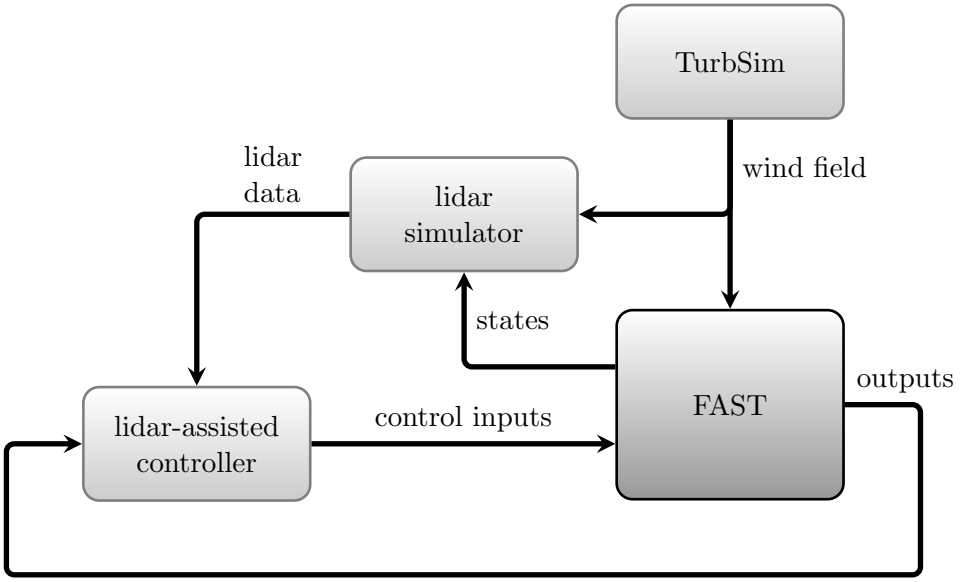

Figure 3.13: Flowchart of the lidar-assisted control simulations.

3.5 Wind Turbine and Lidar Simulator

The WInd Turbine and LIdar Simulator (WITLIS) was first presented in [76] and is implemented in Matlab. In recent years it has been further extended to a toolbox with several scripts not only for the simulation of lidar assisted control, but also for data analysis, since similar calculations have to be done for both simulated and measured lidar data. Although most of the code was developed within this PhD project, it is currently used, extended, and improved by several researchers at Stuttgart Wind Energy (SWE).
A detailed documentation of WITLIS is outside the scope of this work. Only some features important for the understanding of the following chapters will be presented in this section.

3.5.1 Simulated Lidar Measurements

The simulated lidar system scans the same wind field used for aero-elastic simulations (see Figure 3.13), taking into account the movements of the lidar system on the nacelle and the blockage effect of the rotating blades based on the system states of the simulated turbine. The simulator calculates the line-of-sight wind speed and a signal quality flag similar to a real lidar system. The lidar simulator then transfers the raw lidar data to the lidar-assisted controller, where the data is finally processed together with the wind turbine outputs to control the wind turbine.
Therefore, the TurbSim wind field is read into Matlab and linked to the FAST input file prior to the simulation. FAST is then simulated within Simulink with the interface described in [44] together with the lidar simulator and the lidar-assisted controller.

The lidar simulator needs the following inputs:

- Lidar position $[x_{\mathrm{L},\mathcal{I}}\ y_{\mathrm{L},\mathcal{I}}\ z_{\mathrm{L},\mathcal{I}}]^{\mathrm{T}}$ and orientation (Ψ_{L}, Θ_{L}, and Φ_{L}) in the inertial coordinate system.
- Lidar volume weighting function $f_{\mathrm{RW}}(a)$ depending on the lidar system (discretized).
- Trajectory defined by a set of coordinates $[t_i\ x_{i,\mathcal{L}}\ y_{i,\mathcal{L}}\ z_{i,\mathcal{L}}]^{\mathrm{T}}$ of the measurement points from a full scan. For a pulsed lidar system there can be several points with the same time t_i depending on the number of range gates.

During the aero-elastic simulation, the lidar simulator is triggered if the current time t reaches a measurement time t_i:

$$\mathrm{mod}(t, T_{\mathrm{scan}}) \geq t_i, \tag{3.41}$$

where mod() is the modulo operator and T_{scan} the time of a full scan. Then, the following steps are carried out:

1. Update the lidar device position $[x_{\mathrm{L},\mathcal{I}}\ y_{\mathrm{L},\mathcal{I}}\ z_{\mathrm{L},\mathcal{I}}]^{\mathrm{T}}$ and velocity $[\dot{x}_{\mathrm{L},\mathcal{I}}\ \dot{y}_{\mathrm{L},\mathcal{I}}\ \dot{z}_{\mathrm{L},\mathcal{I}}]^{\mathrm{T}}$ based on the current displacement $[x_{\mathrm{T}}\ y_{\mathrm{T}}\ z_{\mathrm{T}}]^{\mathrm{T}}$ and velocity $[\dot{x}_{\mathrm{T}}\ \dot{y}_{\mathrm{T}}\ \dot{z}_{\mathrm{T}}]^{\mathrm{T}}$ of the tower top.
2. Transform the current measurement points from the $\mathcal{L}$ to the $\mathcal{I}$ coordinate system using the coordinate transformation (3.29).
3. Calculate the normalized laser vector $[x_{\mathrm{n},i,\mathcal{I}}\ y_{\mathrm{n},i,\mathcal{I}}\ z_{\mathrm{n},i,\mathcal{I}}]^{\mathrm{T}}$ using Equation (3.32).
4. Check if the laser beam is blocked by a blade with current blade azimuth ψ and blade geometric data. If so, finish simulation and update the line-of-sight wind speed $v_{\mathrm{los},i}$ with a random value and set the current lidar quality flag to false. If not, continue.
5. Calculate the coordinates $[x_{a,i,\mathcal{I}}\ y_{a,i,\mathcal{I}}\ z_{a,i,\mathcal{I}}]^{\mathrm{T}}$ along the laser beam using Equation (3.35).
6. Extract the wind speed vector $[u_{a,i,\mathcal{I}}\ v_{a,i,\mathcal{I}}\ w_{a,i,\mathcal{I}}]^{\mathrm{T}}$ for all points along the laser beam using the wind model for lidar simulation (3.15).
7. Calculate the line-of-sight wind speed $v_{\mathrm{los},i}$ using the measurement equation (3.36) taking into account the velocity of the lidar device. Set the current lidar quality flag to true.

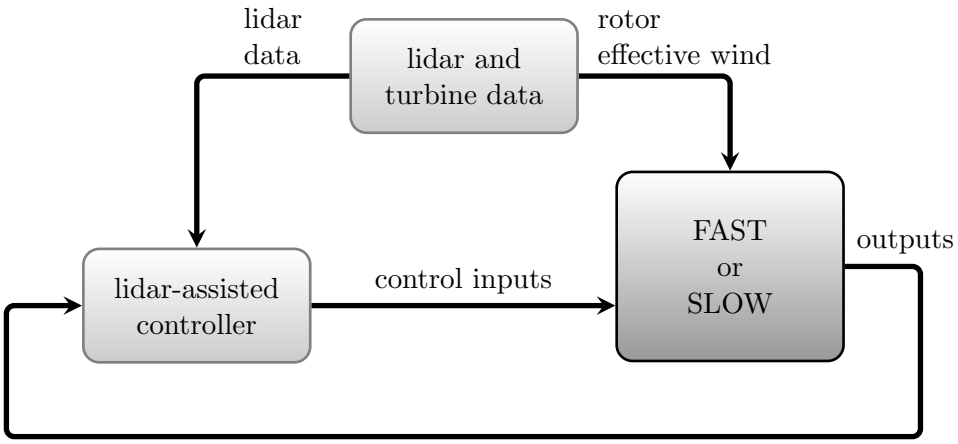

Figure 3.14: Flowchart of hybrid simulations.

3.5.2 Hybrid Simulations

The technique introduced in [77] facilitates a very realistic simulation of lidar-assisted control using simultaneous measured lidar and turbine data. From the turbine data a time series of the rotor effective wind is generated with the estimator from Section 3.2.5. This time series can then either be used as a "hub height wind field" for FAST or as disturbance input v_0 for the SLOW model presented in Section 3.1.2. The raw lidar data can be transfered during the simulation to the lidar-assisted controller. This combination of experiment and simulations is called "hybrid simulations".

The benefits over conventional simulations with lidar simulation and wind evolution models [20] are that effects, such as measurement errors and delays, real wind evolution, and site specific problems, can be included into the simulations. If used along with the same controller enabled during the measurements, the simulated turbine's reaction will be close to the measured turbine data due to the fact that the used estimation of the rotor effective wind speed v_0 is an inverse process to the simulation. If used along with another controller, it can be estimated in a realistic way, which effect the new controller would have produced in this specific situation. Furthermore, the same situation can be repeated and controller parameters can be tuned to achieve better performance.

This technique is used in this work mainly to estimate the effect of the lidar assisted controller as a last test prior to applying it in reality.

4

Wind Field Reconstruction

In this chapter a method is proposed to retrieve wind field information out of lidar data. New techniques are necessary to meet the needs of high resolution data for lidar-assisted control compared to the already widely used application of ground based systems for site assessment. The problem of the limited information of lidar measurements is stated and the basic ideas and problems of model-based wind field reconstruction are presented in Section 4.1. Then an approach is applied and evaluated to ground-based, floating and nacelle-based lidar systems using static wind models in Section 4.2. The approach is then extended in Section 4.3 to provide wind measurements for preview control applications by using dynamic wind models. Finally, Section 4.4 gives a short summary. The chapter is based on [38] and [78].

4.1 Model-Based Approach to Wind Field Reconstruction

In the beginning of this section, experimental data depicts the effect of the limitation of line-of-sight wind speed and volume measurement from a lidar system compared to wind measurements with an ultrasonic anemometer. Then the Doppler Beam Swinging (DBS) technique is explained, which is the state-of-the-art technique to retrieve a three-dimensional wind vector out of the line-of-sight measurement of a ground-based lidar system for site assessment. A simple example shows the shortcomings of this technique. Finally, the basic idea of the model-based approach is presented. The conventional reconstruction methods also use an internal wind model (homogeneous flow). Thus, the intention of this work is not to propose a totally new approach, but to provide a system-theoretical view on wind reconstruction which is useful to improve lidar measurements in situations where the conventional technique fails.

Figure 4.1: SWE scanning lidar system installed on the nacelle of a Nordtank wind turbine. Photo by Andreas Rettenmeier.

4.1.1 Differences between Lidar and Sonic Measurements

Comparison of sonic data from meteorological masts and processed data from ground based lidar systems are usually done by linear regression of 10-minute-mean values [60]. Current lidar systems are able to achieve coefficients of determination of $R^2 > 0.99$ for the processed horizontal wind speed in flat terrain. However, the signals provided by commercial systems are not direct measurements, as explained later in Section 4.1.2. They are calculated based on the assumption of homogeneous flow. This is also the main reason for the lower performance of such systems in complex terrain.
Contrary to comparing processed lidar and sonic data, the following examination focuses on the line-of-sight wind speed in order to demonstrate the two main differences between both measurement principles:

1. On the one hand a sonic anemometer is able to measure a three-dimensional wind vector, while a lidar system is limited to line-of-sight wind speeds.

2. On the other hand a sonic anemometer is measuring within a small volume, which can be considered as a point measurement, while a lidar system is measuring over a probe volume defined by the laser pulse.

For this investigation, the SWE scanning lidar system (see Appendix B) has been installed on the nacelle of a stopped turbine (see Figure 4.1), pointing towards three sonic anemometers installed on different heights on a nearby meteorological mast. Part of this investigation has been presented in [79], where more details of the experimental setup can be found.
The first part of this examination focuses on the difference between line-of-sight and three-dimensional wind speed measurements. For this purpose, the 10-minute-mean values from the three sonic anemometers are projected on the corresponding normalized lidar vector. The

Table 4.1: Linear regression between projected sonic and lidar measurement.

height [m]	16.5	34.5	52.5
slope [-]	1.001	1.020	1.030
offset [m/s]	0.058	-0.016	-0.270
R^2 [-]	0.998	0.999	0.999

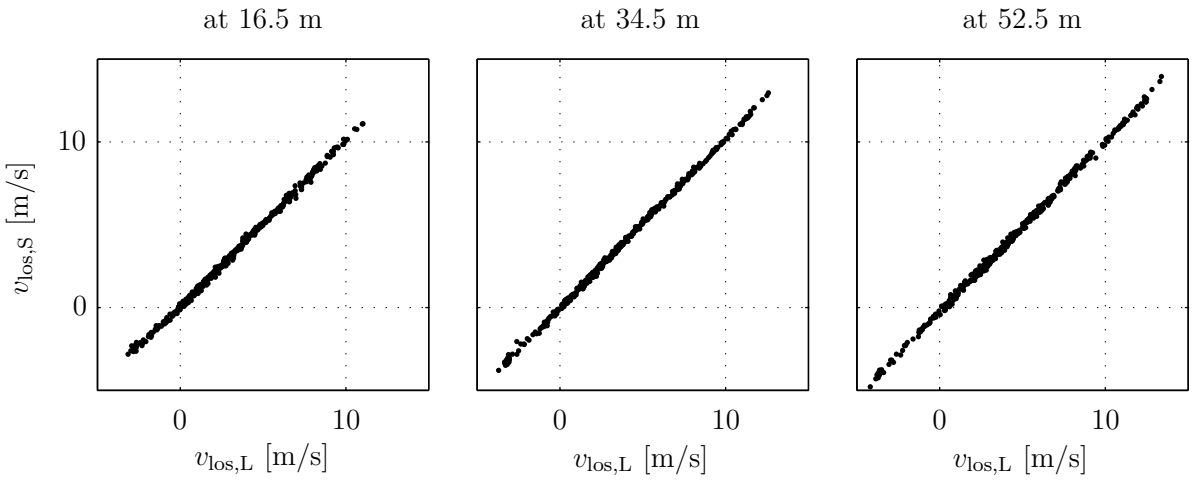

Figure 4.2: Linear regression between projected sonic and lidar measurement.

reduced line-of-sight wind speed for each of the three sonic anemometers is calculated using (3.31):

$$v_{\mathrm{los,S}} = x_{\mathrm{n},i,\mathcal{I}}\, u_{\mathrm{S},\mathcal{I}} + y_{\mathrm{n},i,\mathcal{I}}\, v_{\mathrm{S},\mathcal{I}} + z_{\mathrm{n},i,\mathcal{I}}\, w_{\mathrm{S},\mathcal{I}}, \tag{4.1}$$

with the normalized laser vector $[x_{\mathrm{n},i,\mathcal{I}}\ y_{\mathrm{n},i,\mathcal{I}}\ z_{\mathrm{n},i,\mathcal{I}}]^{\mathrm{T}}$ defined in (3.32) for each height and the wind vector $[u_{\mathrm{S},\mathcal{I}}\ v_{\mathrm{S},\mathcal{I}}\ w_{\mathrm{S},\mathcal{I}}]^{\mathrm{T}}$ measured by the sonic anemometers in the corresponding positions. In the case of the central anemometer, the line-of-sight wind speed is equal to the $u_{\mathrm{S},\mathcal{I}}$ component. The reduced wind speeds $v_{\mathrm{los,S}}$ from the sonic anemometers are then compared to the line-of-sight wind speeds $v_{\mathrm{los,L}}$ from the lidar system. Table 4.1 and Figure 4.2 show that both signals correspond very well. All data of the campaign is used without further filtering. The agreement demonstrates the effect of the first difference between lidar and sonic measurements: After the reduction to line-of-sight wind speed, 10-minute-mean values of the sonic anemometer become directly comparable to the lidar data.

The second part of this examination focuses on the difference between point and volume measurements. For this purpose, 6 h of high resolution data from 11 a.m. to 5 p.m. on December 27, 2011 is analyzed. This period is chosen, because the wind is blowing almost constantly from the meteorological mast towards the lidar system during the 6 h, and the means of the components $v_{\mathrm{S},\mathcal{I}}$ and $w_{\mathrm{S},\mathcal{I}}$ are close to zero. Figure 4.3 shows an excerpt of 10 minutes. The sonic anemometer data is collected at 35 Hz and is reduced again to line-of-sight wind speeds,

while the lidar system measures with 0.5 Hz. Both signals have a similar time progression. However, the sonic data show more variation at higher frequencies. This becomes more obvious comparing the auto-spectra in Figure 4.4.
Due to the special setup of the experiment, it can be assumed that for this wind direction and for the central point, the lidar volume includes all aerosols passing the sonic anemometer. Thus, the spacial filtering effect of the lidar pulse volume measurement can be imitated by a time filter using Taylor's Frozen Turbulence and the Gaussian weighting function (3.37) by

$$v_{\mathrm{los,S,f}}(t) = \int_{-\infty}^{\infty} v_{\mathrm{los,S}}(\tau) f_{\mathrm{RW}}(\bar{u}(t-\tau))\,\mathrm{d}\tau = v_{\mathrm{los,S}}(t) * f_{\mathrm{RW}}(\bar{u}t), \tag{4.2}$$

where $*$ denotes convolution and $\bar{u}$ is the mean wind speed. The filtered sonic signal $v_{\mathrm{los,S,f}}$ is still not exactly the same as the lidar signal (see central plot in Figure 4.3), but more similar than the unfiltered one.
The spectrum of the filtered sonic signal can be calculated from the time signal. Here, the spectrum of the filtered signal is calculated from the spectrum of the unfiltered one in order to explain the relationship of both spectra directly. Based on the convolution theorem the convolution of two functions in the time domain is the product of the Fourier transforms:

$$\mathcal{F}\{v_{\mathrm{los,S}}(t) * f_{\mathrm{RW}}(\bar{u}t)\} = \mathcal{F}\{v_{\mathrm{los,S}}(t)\}\mathcal{F}\{f_{\mathrm{RW}}(\bar{u}t)\}. \tag{4.3}$$

With the auto-spectrum S_{SS} of $v_{\mathrm{los,S}}$ and with the Fourier transform of the normalized Gaussian weighting function with standard deviation σ_{L}

$$\mathcal{F}\{f_{\mathrm{RW}}(\bar{u}t)\} = \exp\left(-\left(\frac{2\pi f}{\bar{u}}\right)^2 \frac{\sigma_{\mathrm{L}}^2}{2}\right) \tag{4.4}$$

the corresponding auto-spectrum can than be calculated by

$$S_{\mathrm{SS,f}} = S_{\mathrm{SS}}\mathcal{F}^2\{f_{\mathrm{RW}}(\bar{u}t)\}. \tag{4.5}$$

It shows a similar drop-off at high frequencies compared to the auto-spectrum of the lidar signal in Figure 4.4. This agreement demonstrates the effect of the second difference between lidar and sonic measurements: After applying the range weighting function also to the sonic data projected on the laser beam direction, the high resolution data of sonic anemometers and lidar systems become comparable.
Eventually, with this investigation, the lidar model described in Section 3.3 is validated by reproducing the main difference between lidar and sonic measurements.

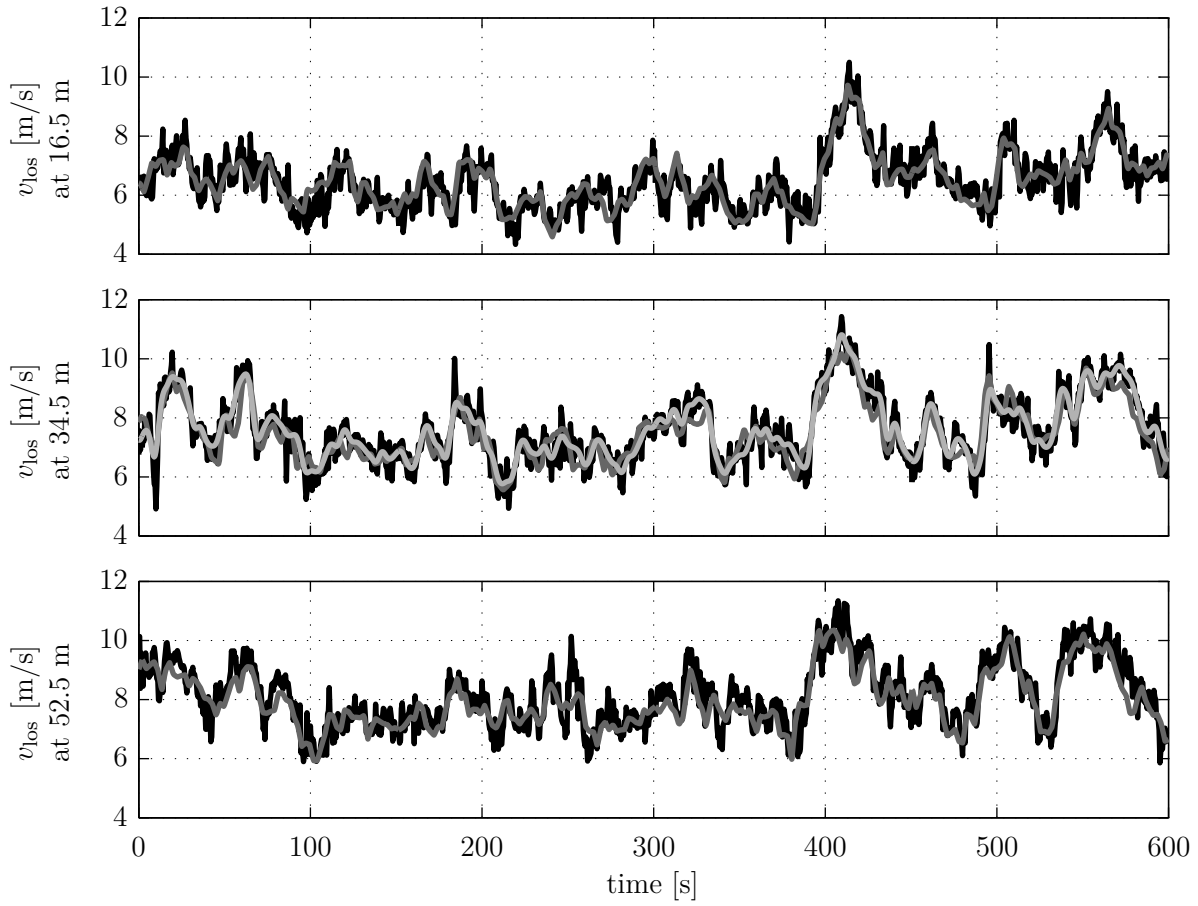

Figure 4.3: Time line of line-of-sight wind speeds. Sonic (black), lidar (dark gray) and filtered sonic (light gray).

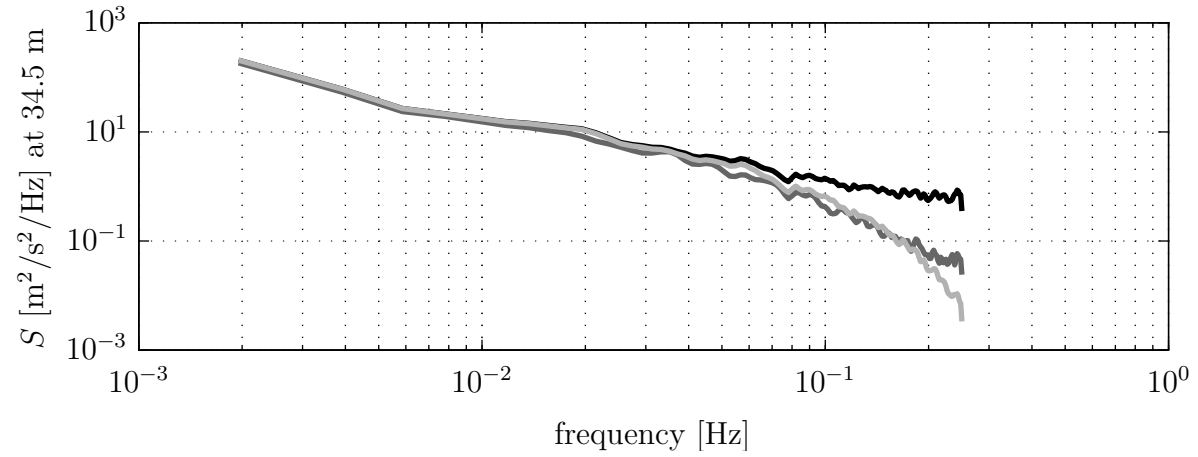

Figure 4.4: Auto-spectra of line-of-sight wind speeds. Sonic (black), lidar (dark gray) and filtered sonic (light gray).

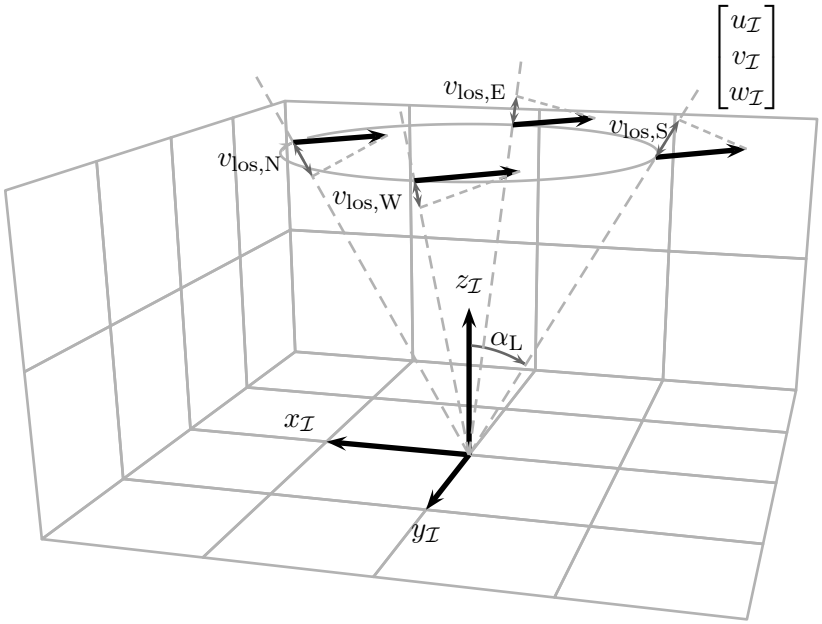

Figure 4.5: Sketch of the DBS scan.

4.1.2 Reconstruction Using the Doppler Beam Swinging Technique

The DBS technique is used in commercial, ground based lidar systems to retrieve wind speed and wind direction. In case of the Windcube [60], the lidar is measuring in the four geographic directions with a half opening angle of α_L, see Figure 4.5. Assuming point measurement (3.31), the four line-of-sight wind speeds are

$$v_{\text{los,N}} = u_{\text{N},\mathcal{I}} \sin\alpha_\text{L} + w_{\text{N},\mathcal{I}} \cos\alpha_\text{L} \tag{4.6a}$$

$$v_{\text{los,W}} = v_{\text{W},\mathcal{I}} \sin\alpha_\text{L} + w_{\text{W},\mathcal{I}} \cos\alpha_\text{L} \tag{4.6b}$$

$$v_{\text{los,S}} = -u_{\text{S},\mathcal{I}} \sin\alpha_\text{L} + w_{\text{S},\mathcal{I}} \cos\alpha_\text{L} \tag{4.6c}$$

$$v_{\text{los,E}} = -v_{\text{E},\mathcal{I}} \sin\alpha_\text{L} + w_{\text{E},\mathcal{I}} \cos\alpha_\text{L}, \tag{4.6d}$$

where $u_{\text{N},\mathcal{I}}$ is the longitudinal wind component in the north (N) direction aligned with the $\mathcal{I}$-Coordinate System and accordingly for the other three directions west (W), south (S), and east (E). This equation system of 4 equations has 8 unknowns and thus it is under-determined and no unique solution exists.

The DBS technique uses the homogeneous flow model (3.16) in each measurement height. Thus, the wind vector $[u_\mathcal{I}\ v_\mathcal{I}\ w_\mathcal{I}]^\text{T}$ in the inertial $\mathcal{I}$-coordinate system is the same for each measurement point i.

With this wind model, (4.6) is simplified to

$$v_{\mathrm{los,N}} = u_{\mathcal{I}} \sin\alpha_{\mathrm{L}} + w_{\mathcal{I}} \cos\alpha_{\mathrm{L}} \tag{4.7a}$$
$$v_{\mathrm{los,W}} = v_{\mathcal{I}} \sin\alpha_{\mathrm{L}} + w_{\mathcal{I}} \cos\alpha_{\mathrm{L}} \tag{4.7b}$$
$$v_{\mathrm{los,S}} = -u_{\mathcal{I}} \sin\alpha_{\mathrm{L}} + w_{\mathcal{I}} \cos\alpha_{\mathrm{L}} \tag{4.7c}$$
$$v_{\mathrm{los,E}} = -v_{\mathcal{I}} \sin\alpha_{\mathrm{L}} + w_{\mathcal{I}} \cos\alpha_{\mathrm{L}}. \tag{4.7d}$$

Now, (4.7) consists of 4 equations for 3 unknowns and in general no solution exists. However, in [60] the following approximation is proposed:

$$u_{\mathrm{DBS},\mathcal{I}} = \frac{v_{\mathrm{los,N}} - v_{\mathrm{los,S}}}{2\sin\alpha_{\mathrm{L}}} \tag{4.8a}$$
$$v_{\mathrm{DBS},\mathcal{I}} = \frac{v_{\mathrm{los,W}} - v_{\mathrm{los,E}}}{2\sin\alpha_{\mathrm{L}}} \tag{4.8b}$$
$$w_{\mathrm{DBS},\mathcal{I}} = \frac{v_{\mathrm{los,N}} + v_{\mathrm{los,W}} + v_{\mathrm{los,S}} + v_{\mathrm{los,E}}}{4\cos\alpha_{\mathrm{L}}}. \tag{4.8c}$$

Note, other approximations can be found. For example, (4.7a)+(4.7c) yields

$$w_{\mathcal{I}} = \frac{v_{\mathrm{los,N}} + v_{\mathrm{los,S}}}{2\cos\alpha_{\mathrm{L}}} \tag{4.9}$$

and (4.7b)+(4.7d) yields

$$w_{\mathcal{I}} = \frac{v_{\mathrm{los},W} + v_{\mathrm{los},E}}{2\cos\alpha_{\mathrm{L}}}. \tag{4.10}$$

Depending on the line-of-sight wind speeds, these two equations can be conflicting. However, the approximation (4.8) minimizes the sum of the squares of the errors made in every equation. This can be proven by arranging (4.7) in following form:

$$\underbrace{\begin{bmatrix} v_{\mathrm{los,N}} \\ v_{\mathrm{los,W}} \\ v_{\mathrm{los,S}} \\ v_{\mathrm{los,E}} \end{bmatrix}}_{\boldsymbol{m}} = \underbrace{\begin{bmatrix} \sin\alpha_{\mathrm{L}} & 0 & \cos\alpha_{\mathrm{L}} \\ 0 & \sin\alpha_{\mathrm{L}} & \cos\alpha_{\mathrm{L}} \\ -\sin\alpha_{\mathrm{L}} & 0 & \cos\alpha_{\mathrm{L}} \\ 0 & -\sin\alpha_{\mathrm{L}} & \cos\alpha_{\mathrm{L}} \end{bmatrix}}_{\boldsymbol{A}} \underbrace{\begin{bmatrix} u_{\mathcal{I}} \\ v_{\mathcal{I}} \\ w_{\mathcal{I}} \end{bmatrix}}_{\boldsymbol{s}}. \tag{4.11}$$

The Moore-Penrose pseudoinverse $\boldsymbol{A}^{+}$ of matrix $\boldsymbol{A}$ is

$$\boldsymbol{A}^{+} = \begin{bmatrix} \frac{1}{2\sin\alpha_{\mathrm{L}}} & 0 & \frac{-1}{2\sin\alpha_{\mathrm{L}}} & 0 \\ 0 & \frac{1}{2\sin\alpha_{\mathrm{L}}} & 0 & \frac{-1}{2\sin\alpha_{\mathrm{L}}} \\ \frac{1}{4\cos\alpha_{\mathrm{L}}} & \frac{1}{4\cos\alpha_{\mathrm{L}}} & \frac{1}{4\cos\alpha_{\mathrm{L}}} & \frac{1}{4\cos\alpha_{\mathrm{L}}} \end{bmatrix}. \tag{4.12}$$

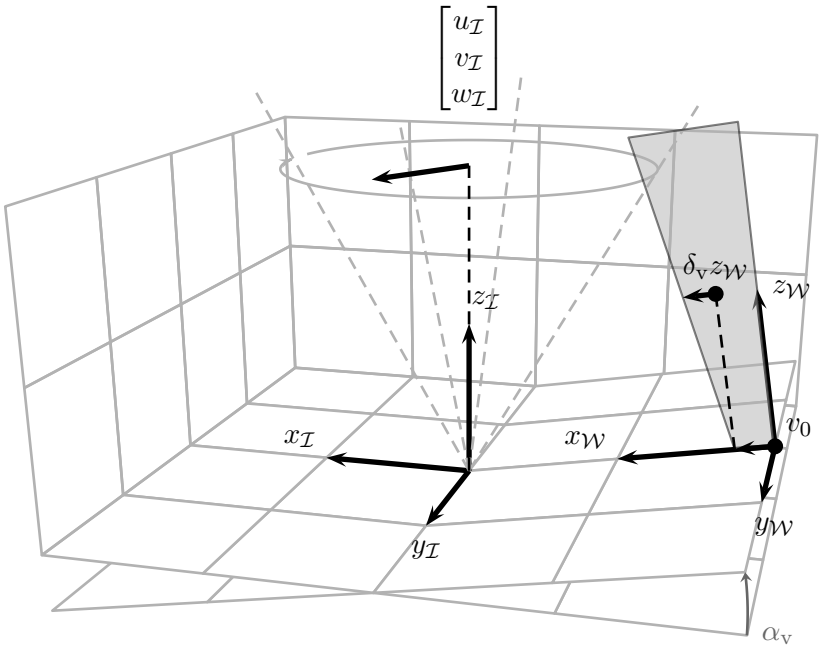

Figure 4.6: Sketch of the DBS scan in sloped terrain.

The solution of the linear least squares problem

$$\min_{\boldsymbol{s}} \|\boldsymbol{m} - \boldsymbol{A}\boldsymbol{s}\|_2 \tag{4.13}$$

is (4.8) or rewritten in other variables

$$\boldsymbol{s} = \boldsymbol{A}^{+}\boldsymbol{m}. \tag{4.14}$$

This proves that the approximation minimizes the 2-norm of the estimation error.
This consideration also explains that the wind speed and direction signals provided by commercial lidar systems are not direct measurements, but estimates based on the homogeneous wind flow model.

Shortcomings of the DBS Technique

The DBS technique yields very good results in flat terrain [60]. However, the assumed wind model of homogeneous flow in each measurement height becomes more and more inappropriate with increasing complexity of the terrain. For flow over a hill, this has been pointed out in [80]. In this subsection, the error made on a sloped terrain is investigated to motivate the model-based wind field reconstruction. In this example, the wind is flowing downhill on a slope with an inclination of α_v passing the lidar, see Figure 4.6. It is assumed that the wind with a linear vertical shear of δ_v and an effective wind speed of v_0 is attached to this slope and thus homogeneous flow can be assumed on each height in the $\mathcal{W}$-system. The wind in each point

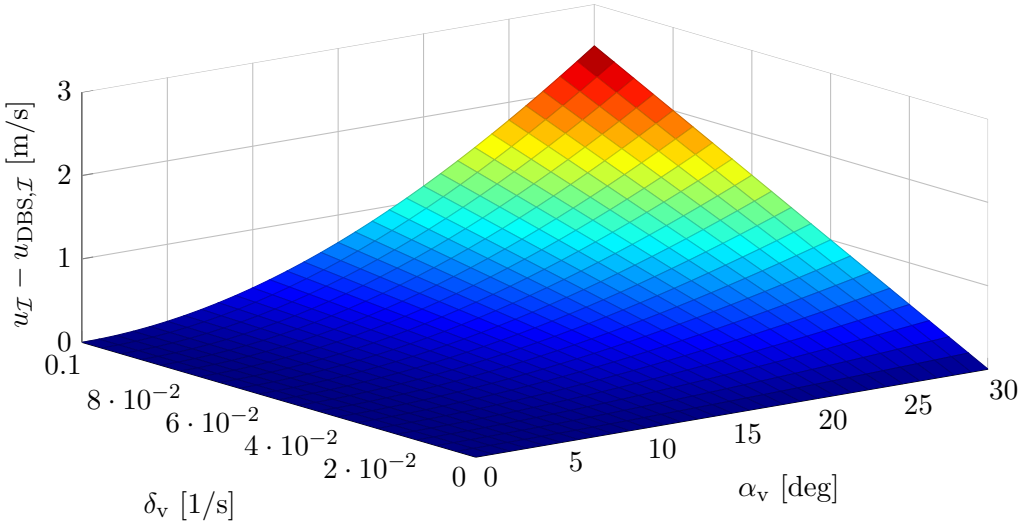

Figure 4.7: Absolute error in the longitudinal wind speed component using the DBS technique in sloped terrain depending on the linear vertical shear δ_v and the vertical inflow angle α_v for a measurement height of 100 m.

i in the $\mathcal{I}$-system can be described using the static inhomogeneous wind model (3.17) with $\alpha_\mathrm{h} = \delta_\mathrm{h} = 0$:

$$\begin{bmatrix} u_{i,\mathcal{I}} \\ v_{i,\mathcal{I}} \\ w_{i,\mathcal{I}} \end{bmatrix} = T_\mathrm{elevation} \begin{bmatrix} u_{i,\mathcal{W}} \\ v_{i,\mathcal{W}} \\ w_{i,\mathcal{W}} \end{bmatrix} \quad \text{with} \quad \begin{bmatrix} u_{i,\mathcal{W}} \\ v_{i,\mathcal{W}} \\ w_{i,\mathcal{W}} \end{bmatrix} = \begin{bmatrix} v_0 + \delta_\mathrm{v} z_{i,\mathcal{W}} \\ 0 \\ 0 \end{bmatrix}$$
$$\text{and} \quad \begin{bmatrix} x_{i,\mathcal{W}} \\ y_{i,\mathcal{W}} \\ z_{i,\mathcal{W}} \end{bmatrix} = T_\mathrm{elevation}^{-1} \begin{bmatrix} x_{i,\mathcal{I}} \\ y_{i,\mathcal{I}} \\ z_{i,\mathcal{I}} \end{bmatrix}. \tag{4.15}$$

With this model and given values for α_v, v_0, and δ_v, the wind speed vector at each location can be determined. Here, the model is used to simulate the measurements of a ground-based lidar system. In a first step, the wind speed vectors in the 4 measurement points are calculated with the coordinates and (4.15). In a second step, the 4 line-of-sight wind speeds are computed with the measurement equations (4.6). In the last step, (4.8) is used to obtain the 3 wind speed components based on the DBS technique.

The standard DBS technique is based on the assumption of homogeneous flow on each height in the $\mathcal{I}$-system, which in this case is not correct, because the wind is attached to the sloped terrain and thus homogeneous on each height in the $\mathcal{W}$-system. The correct wind vector $[u_\mathcal{I}\ v_\mathcal{I}\ w_\mathcal{I}]^\mathrm{T}$ in the point $[0\ 0\ z_\mathcal{I}]^\mathrm{T}$ centered above the lidar system can be obtained with the wind model (4.15).

Figure 4.7 illustrates the resulting error for a measurement height of $z_\mathcal{I} = 100\,\mathrm{m}$. At a linear vertical shear of $\delta_\mathrm{v} = 0.04\,\frac{1}{\mathrm{s}}$, corresponding to the exponential power law approximation (2.16)

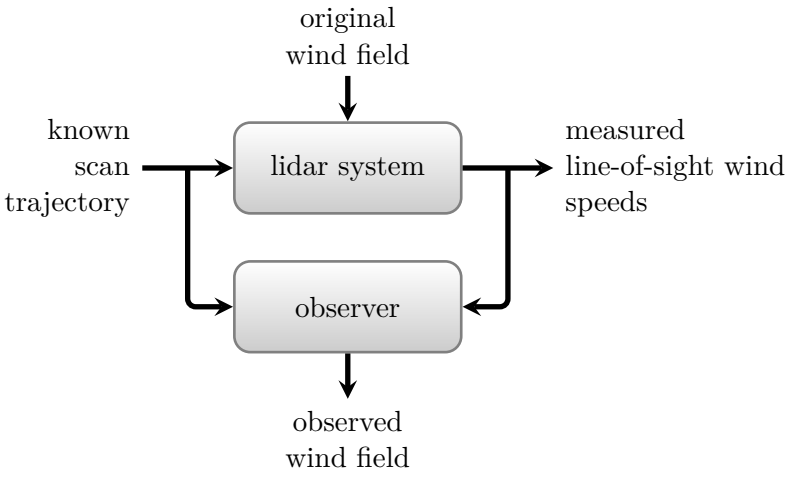

Figure 4.8: System theoretical view on lidar measurements and wind field reconstruction.

at this height, and a sloped terrain of $\alpha_\mathrm{v} = 30\,\mathrm{deg}$, the error reaches 1 m/s, which is a severe value for site assessment. The error in the longitudinal component can be calculated by comparing the correct wind speed $u_\mathcal{I}$ and the wind speed $u_{\mathrm{DBS},\mathcal{I}}$ from the DBS technique. After some minor basic arithmetic operations, the error results in

$$u_\mathcal{I} - u_{\mathrm{DBS},\mathcal{I}} = \delta_\mathrm{v} z_\mathcal{I} \sin^2 \alpha_\mathrm{v}. \tag{4.16}$$

Similar to the error made in the flow over a hill, this error is independent of the lidar measurement angle α_L and the absolute wind speed v_0.
This simple example demonstrates which problem occurs, if the internal model of the reconstruction algorithm (in this case homogeneous flow parallel to the lidar orientation) is different from the external model (in this case homogeneous flow attached to a sloped terrain). The intention of the model-based wind field reconstruction is to overcome this discrepancy as explained in more details in the following sections.

4.1.3 Basic Idea of Model-Based Wind Field Reconstruction

The basic idea of model-based wind field reconstruction is to retrieve useful information of the wind field from the lidar measurements depending on the application. But this system theoretical view also gives a framework to evaluate and optimize the level and the reliability of the reconstructed wind information, which will be explained in this section.
A lidar system can be described in a system theoretical way (see Figure 4.8): All known settings such as the scan trajectory can be considered as inputs to the system. All unknown influences to the measurements are the disturbances and the measurements themselves are the outputs of the system. In system theory, a disturbance observer can be used to reconstruct the disturbances from the system inputs and outputs, if observability is given. Robustness analysis

determines, how well this is done in the presence of model and measurement uncertainties. Whereas observability and robustness for dynamic systems are complex, for static systems they can be simplified to the questions of whether a unique disturbance can be found which caused the measured output with given input and how sensitive it is to uncertainties. For this purpose, a model of the system is needed (either analytically or from CFD), similar to a simulation model and the observation can be considered to be the inverse of a simulation.

Based on the simple lidar model (3.31), it is impossible to reconstruct the local wind vector, since there is only one equation for the three unknowns $u_{\mathcal{I}}$, $v_{\mathcal{I}}$ and $w_{\mathcal{I}}$. Observability can be restored by changing the wind model. One possibility is to assume that the wind vector in 3 measurement points is the same. This yields 3 equations for 3 unknowns. The wind model has to be chosen according to the application, and the quality of the results depends on the validity of the model. In the following sections, this will be illustrated by the application of this basic idea to ground based, floating and nacelle based lidar systems.

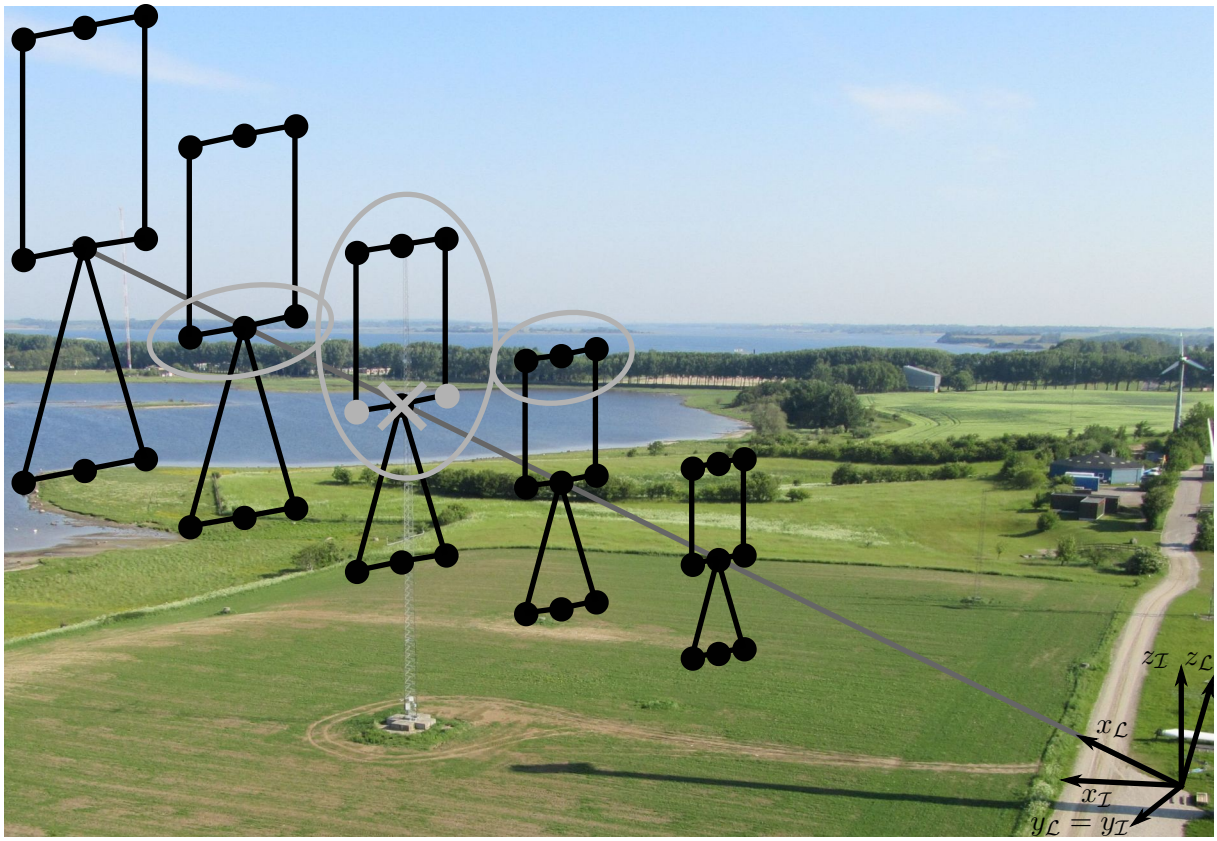

Figure 4.9: Measurement campaign at Risø Campus. The wind vector in the center (cross) is reconstructed using the measurement at the points marked with gray dots for the investigation in flat terrain or inside the ellipses for the investigation in complex terrain. Photo by Andreas Rettenmeier.

4.2 Static Wind Field Reconstruction

In this section the wind field is reconstructed based on the line-of-sight wind speeds only. In contrast to the dynamic wind field reconstruction in Section 4.3, the propagation of the wind field over time is not considered.

4.2.1 Application to Ground Based Lidars

In this first example the SWE scanning lidar system (see Appendix B) was installed at the Risø Campus tilted by $\Theta_\mathrm{L} = 25\,\mathrm{deg}$, scanning the wind close to a met mast with a 3x3 grid trajectory on 5 horizontal planes within 2 s, see Figure 4.9. The center points of the third measurement plane were located close to the ultrasonic anemometers installed on the met mast. For the following investigations, all 10-minute-mean values are used, including low wind speeds and wind directions orthogonal to the main measurement direction.
More details on the experimental setup can be found in [79].

Reconstruction in Flat Terrain

If the tilt angle Θ_L is known, the wind can be reconstructed in the $\mathcal{I}$-coordinate system, assuming that the wind is homogeneous in planes parallel to the ground. The measurement points are transformed from the $\mathcal{L}$ to the $\mathcal{I}$-coordinate system by (3.29). Furthermore, the origin of the $\mathcal{L}$- and the $\mathcal{I}$-coordinate system are set equal.
In a first step, the sonic longitudinal and the vertical wind speed measurements of the center sonic anemometer is compared to the lidar data reconstructed from the two measurement points next to the anemometer, see dots in Figure 4.9. Similar to (3.16), $u_\mathcal{I}$ and $v_\mathcal{I}$ is assumed to be constant in each measurement point i, but here $w_\mathcal{I}$ is neglected:

$$\begin{bmatrix} u_{i,\mathcal{I}} \\ v_{i,\mathcal{I}} \\ w_{i,\mathcal{I}} \end{bmatrix} = \begin{bmatrix} u_\mathcal{I} \\ v_\mathcal{I} \\ 0 \end{bmatrix}. \tag{4.17}$$

This wind model of homogeneous flow is combined with the lidar measurement model (3.31) and the line-of-sight wind speeds of the two points with the distances $r_{\mathrm{L}1}$ and $r_{\mathrm{L}2}$ from the lidar system and next to the center anemometer are simulated by the set of linear equations

$$\underbrace{\begin{bmatrix} v_{\mathrm{los},1} \\ v_{\mathrm{los},2} \end{bmatrix}}_{\boldsymbol{m}} = \underbrace{\begin{bmatrix} \frac{x_{1,\mathcal{I}}}{r_{\mathrm{L}1}} & \frac{y_{1,\mathcal{I}}}{r_{\mathrm{L}1}} \\ \frac{x_{2,\mathcal{I}}}{r_{\mathrm{L}2}} & \frac{y_{2,\mathcal{I}}}{r_{\mathrm{L}2}} \end{bmatrix}}_{\boldsymbol{A}} \underbrace{\begin{bmatrix} u_\mathcal{I} \\ v_\mathcal{I} \end{bmatrix}}_{\boldsymbol{s}}. \tag{4.18}$$

The two-dimensional wind can then be reconstructed simply by a matrix inversion

$$\boldsymbol{s} = \boldsymbol{A}^{-1}\boldsymbol{m}. \tag{4.19}$$

This example shows why observations can be considered to be inverse to simulations. The notation as a linear equation system shows that the reconstruction can be done independently of the shape of the scan. Circular scans normally used for lidar measurements are not necessary. However, matrix A needs to be invertible.
The results of the investigation are shown in Figure 4.10 (top) and Table 4.2. A higher correlation between the sonic anemometer and the lidar system is achieved for the longitudinal component $u_\mathcal{I}$ compared to the lateral component $v_\mathcal{I}$. Due to the values in the inverted matrix $\boldsymbol{A}^{-1}$, measurement errors in the line-of-sight wind speeds have more effect on $v_\mathcal{I}$. An appropriate measure for robustness can be defined in the following way: The condition number of $\boldsymbol{A}$ describes the worst case factor which transfers relative errors from measurement vector $\boldsymbol{m}$ to the vector of the searched variables $\boldsymbol{s}$. This approach can be used to optimize the setup of lidar measurements: in this case the condition number could have been reduced from 5.23 to 1, by measuring closer to the met mast, setting $x_{1,\mathcal{I}} = x_{2,\mathcal{I}} = y_{1,\mathcal{I}} = -y_{2,\mathcal{I}}$.

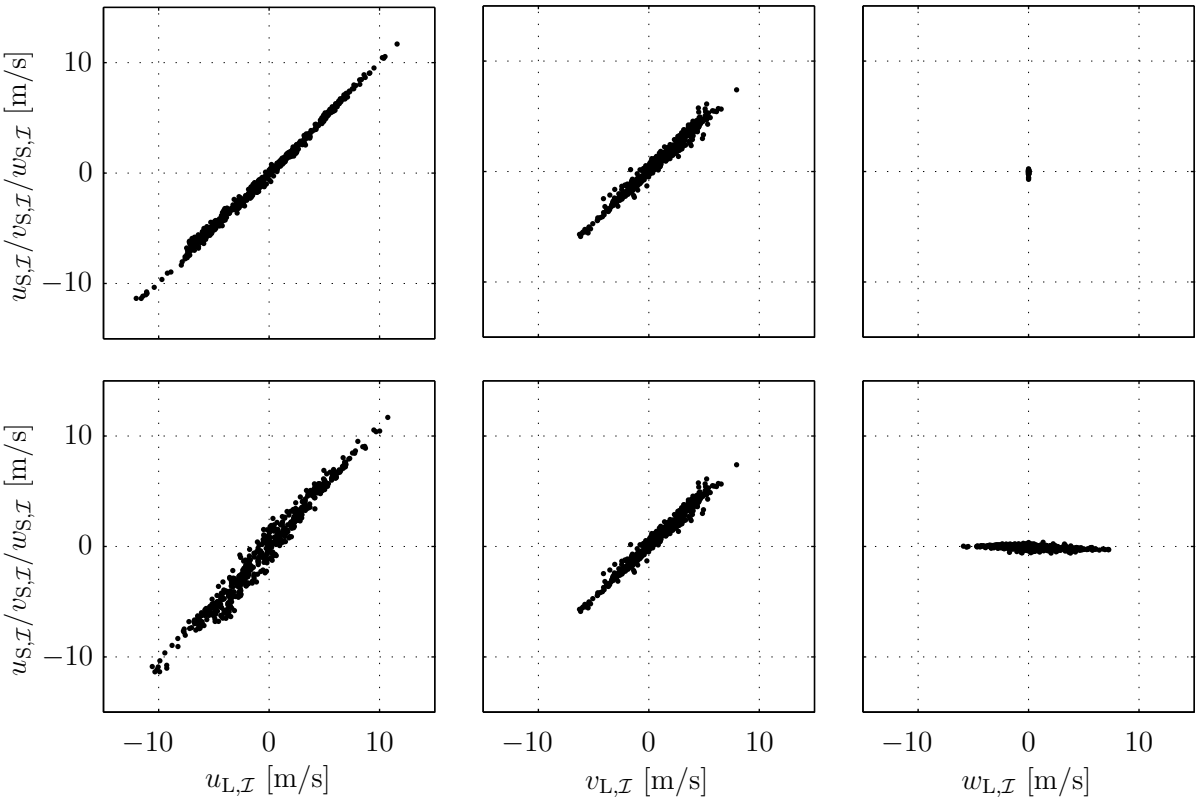

Figure 4.10: Regression between lidar and sonic anemometer measurements in the inertial coordinate system. For the 2D homogeneous flow model (top) and the 3D homogeneous flow model (bottom).

In a second step, the wind model of three-dimensional homogeneous flow (3.16) used in the DBS technique is considered. A third measurement is added to have the number of linear equations equal to the number of unknowns:

$$\underbrace{\begin{bmatrix} v_{\mathrm{los},1} \\ v_{\mathrm{los},2} \\ v_{\mathrm{los},3} \end{bmatrix}}_{\boldsymbol{m}} = \underbrace{\begin{bmatrix} \frac{x_{1,\mathcal{I}}}{r_{\mathrm{L}1}} & \frac{y_{1,\mathcal{I}}}{r_{\mathrm{L}1}} & \frac{z_{1,\mathcal{I}}}{r_{\mathrm{L}1}} \\ \frac{x_{2,\mathcal{I}}}{r_{\mathrm{L}2}} & \frac{y_{2,\mathcal{I}}}{r_{\mathrm{L}2}} & \frac{z_{2,\mathcal{I}}}{r_{\mathrm{L}2}} \\ \frac{x_{3,\mathcal{I}}}{r_{\mathrm{L}3}} & \frac{y_{3,\mathcal{I}}}{r_{\mathrm{L}3}} & \frac{z_{3,\mathcal{I}}}{r_{\mathrm{L}3}} \end{bmatrix}}_{\boldsymbol{A}} \underbrace{\begin{bmatrix} u_{\mathcal{I}} \\ v_{\mathcal{I}} \\ w_{\mathcal{I}} \end{bmatrix}}_{\boldsymbol{s}} . \tag{4.20}$$

If the measurement point close to the sonic anemometer is added, the matrix $\boldsymbol{A}$ is not invertible, because the $x_{\mathcal{I}}$ and $z_{\mathcal{I}}$ of all three points are equal and thus the first and third column are linearly dependent. This can be avoided and observability can be restored by choosing the measurement point above the sonic anemometer. However, the $w_{\mathcal{I}}$ component still cannot be observed satisfactorily applying the inversion (4.19), see Figure 4.10 (bottom) and Table 4.2. Furthermore, the reconstruction of the $u_{\mathcal{I}}$ component is negatively affected.

The insufficient results can be assigned to the uncertainties in the wind model. Due to the vertical shear, the assumption of a homogeneous wind vector in all measurement points is unrealistic. Simply neglecting the vertical wind component yields better results for flat terrain.

Table 4.2: Linear regression between sonic and reconstructed lidar measurements in the inertial coordinate system.

	2D homogeneous flow (4.17), 2 points			3D homogeneous flow (3.16), 3 points		
	$u_\mathcal{I}$	$v_\mathcal{I}$	$w_\mathcal{I}$	$u_\mathcal{I}$	$v_\mathcal{I}$	$w_\mathcal{I}$
slope [-]	1.000	0.933	∞	1.112	0.933	-0.034
offset [m/s]	0.006	0.043	-0.076	-0.039	0.043	-0.068
R^2 [-]	0.998	0.975	0.000	0.970	0.975	0.207

Reconstruction in Complex Terrain

The investigation above used the knowledge of the tilt angle Θ_L and assumed that the flow is homogeneous in planes parallel to the ground. At least two measurement points in each plane are necessary to reconstruct the two-dimensional wind vector in that plane. In a more complex terrain this assumption is not always useful, see Section 4.1.2: the wind will be parallel to a linear slope at lower heights, but parallel to the surface of the earth at higher heights. In a further investigation, the knowledge of the tilt angle is not used and the wind is reconstructed in the $\mathcal{L}$-coordinate system, by including the vertical wind shear in the wind model. Using more than one focus distance to distinguish between shears and inflow angles was proposed in [38] and tested in simulations in [4], ignoring the drift of the shear due to the flow angle.
Here, the 3D inhomogeneous flow model (3.17) is used, which parameterizes the wind speed vector by the effective wind speed v_0, by the horizontal and the vertical shears δ_h and δ_v, and by the horizontal and the vertical inflow angles α_h and α_v. For a given set of the wind characteristics v_0, α_h, α_v, δ_h, δ_v, the lidar measurement in each point i can be simulated by combining the wind model (3.17) with the lidar measurement model (3.31):

$$v_{\mathrm{los},i} = \frac{x_{i,\mathcal{W}}}{r_{\mathrm{L}i}}(v_0 + \delta_\mathrm{h} y_{i,\mathcal{W}} + \delta_\mathrm{v} z_{i,\mathcal{W}}) \text{ with } \begin{bmatrix} x_{i,\mathcal{W}} \\ y_{i,\mathcal{W}} \\ z_{i,\mathcal{W}} \end{bmatrix} = \boldsymbol{T}_{\mathcal{W}\mathcal{I}}(\alpha_\mathrm{h}, \alpha_\mathrm{v}) \begin{bmatrix} x_{i,\mathcal{L}} \\ y_{i,\mathcal{L}} \\ z_{i,\mathcal{L}} \end{bmatrix} \tag{4.21}$$

In this case $\boldsymbol{T}_{\mathcal{W}\mathcal{I}}$ is used, because the $\mathcal{L}$-system coincides with the $\mathcal{I}$-system. For several measurement points this forms a nonlinear set of equations and an inversion to obtain the wind characteristics from a given set of line-of-sight wind speeds is not directly possible. Here, a numerical inversion for the nonlinear equations can be achieved by solving the least squares minimization problem for n_P measurement points

$$\min_{v_0,\alpha_\mathrm{h},\alpha_\mathrm{v},\delta_\mathrm{h},\delta_\mathrm{v}} \sum_{i=1}^{n_\mathrm{P}} \left(v_{\mathrm{los},i} - \frac{x_{i,\mathcal{W}}}{r_{\mathrm{L}i}}(v_0 + \delta_\mathrm{h} y_{i,\mathcal{W}} + \delta_\mathrm{v} z_{i,\mathcal{W}}) \right)^2 . \tag{4.22}$$

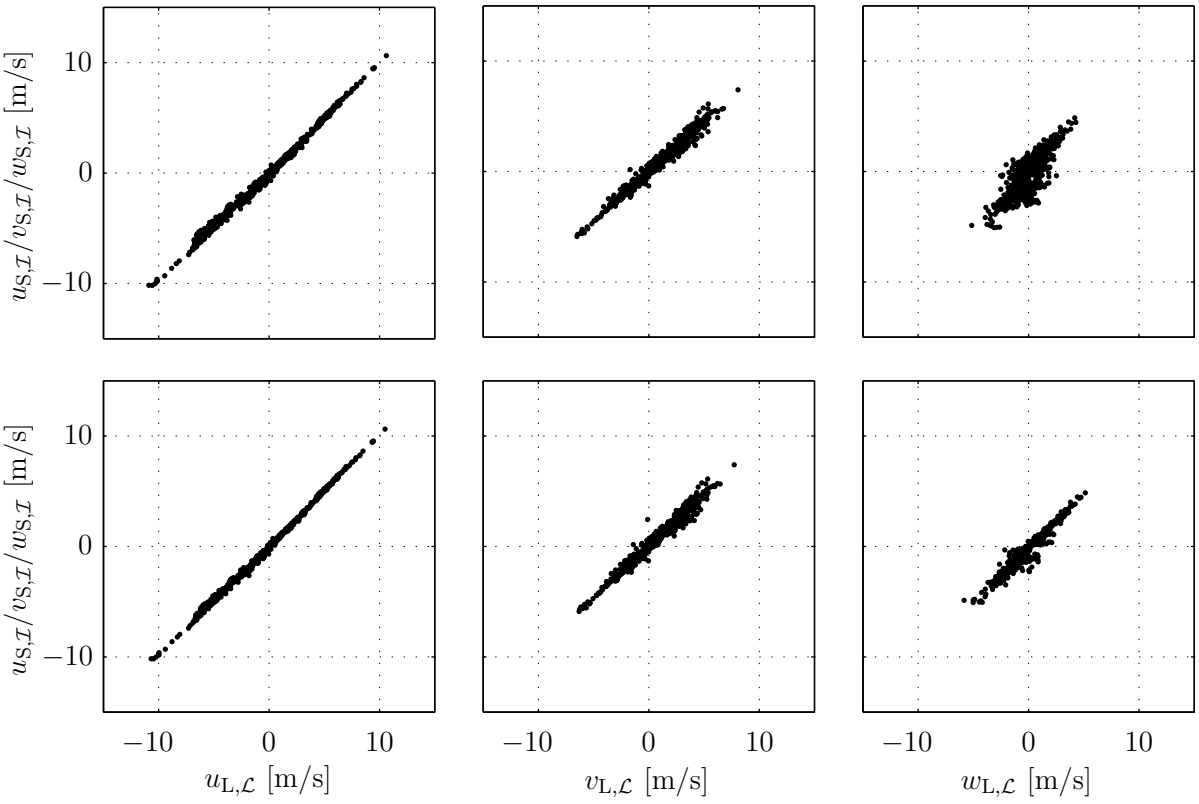

Figure 4.11: Regression between lidar and sonic anemometer measurements in the lidar coordinate system. For the 3D homogeneous flow model (top) and the 3D inhomogeneous flow model (bottom).

Finally, the wind vector in lidar coordinates can be calculated with the found wind characteristics and the flow model (3.17).

The linear model (3.16), which only accounts for the sloped inflow, and the nonlinear model (3.17) neglecting δ_h are applied to the data using $n_\mathrm{P} = 12$ points (see Figure 4.9) and the least squares method. The coefficient of determination can be improved significantly for the $w_\mathcal{I}$ component, see Table 4.3. Figure 4.11 shows that it is possible to enhance the measurement of the 3D wind vector in the presence of vertical shear, but it is necessary to investigate under which conditions observability is given and how higher robustness can be obtained.

Table 4.3: Linear regression between sonic and reconstructed lidar measurements in the inertial coordinate system.

	3D homogeneous flow (3.16), 12 points			3D inhomogeneous flow (3.17), 12 points		
	$u_\mathcal{L}$	$v_\mathcal{L}$	$w_\mathcal{L}$	$u_\mathcal{L}$	$v_\mathcal{L}$	$w_\mathcal{L}$
slope [-]	0.969	0.900	1.059	0.986	0.929	0.968
offset [m/s]	0.021	0.008	-0.339	0.030	0.020	-0.241
R^2 [-]	0.996	0.974	0.699	0.998	0.971	0.951

4.2.2 Application to Floating Lidar Systems

Floating lidars are a promising option to replace expensive floating met masts for the evaluation of offshore wind resources and wind farm projects. The wave motion disturbs the measurement, which is why several attempts have been made to compensate the effect either by stabilization of the floating platform with active or passive hardware solutions or by software solutions [81]. Here, a software solution is proposed, which uses a model-based wind field reconstruction approach. For this purpose, simplified motions of a floating lidar are derived and simulated, and then the simulation model is inverted to reconstruct the wind field. The approach is tested first with a constant wind field to validate the method and then with a turbulent wind field to investigate the robustness.

Simplified Motion of a Floating Lidar System

The height η of the waves propagating in $x_\mathcal{I}$-direction is defined according to the Airy Wave Theory [41]:

$$\eta(x_\mathcal{I}, t) = \frac{h_\eta}{2} \cos\left(k_\eta x_\mathcal{I} - \frac{2\pi}{T_\mathrm{WP}} t\right), \tag{4.23}$$

where h_η is the wave peak-to-peak amplitude, k_η is the angular wavenumber, and T_WP is the wave period. For deep water, wavenumber and wave period are connected through the dispersion relationship

$$k_\eta = \frac{4\pi^2}{T_\mathrm{WP}^2 g}, \tag{4.24}$$

where g is the acceleration by gravity. For this investigation $T_\mathrm{WP} = 5\,\mathrm{s}$ and $h_\eta = 4\,\mathrm{m}$ are chosen. In a simplified simulation it is assumed that the lidar is mounted on a raft-like floating platform, is only able to change its vertical position ($x_{\mathrm{L},\mathcal{I}} = y_{\mathrm{L},\mathcal{I}} = 0$), and follows the wave surface, resulting in two DOF out of six. The vertical movement results in

$$\begin{aligned} z_{\mathrm{L},\mathcal{I}}(t) &= \eta(0,t) = \frac{h_\eta}{2} \cos\left(-\frac{2\pi}{T_\mathrm{WP}} t\right), \\ \dot{z}_{\mathrm{L},\mathcal{I}}(t) &= \frac{h_\eta \pi}{T_\mathrm{WP}} \sin\left(-\frac{2\pi}{T_\mathrm{WP}} t\right). \end{aligned} \tag{4.25}$$

The pitch angle Θ_L (rotation around $y_\mathcal{I}$ axis) of the floating lidar following the wave surface is obtained by the negative gradient in $x_\mathcal{I}$-direction:

$$\tan(\Theta_\mathrm{L}(t)) = -\left.\frac{\partial \eta}{\partial x_\mathcal{I}}\right|_{x_\mathcal{I}=0,t} = \frac{h_\eta k_\eta}{2} \sin\left(-\frac{2\pi}{T_\mathrm{WP}} t\right). \tag{4.26}$$

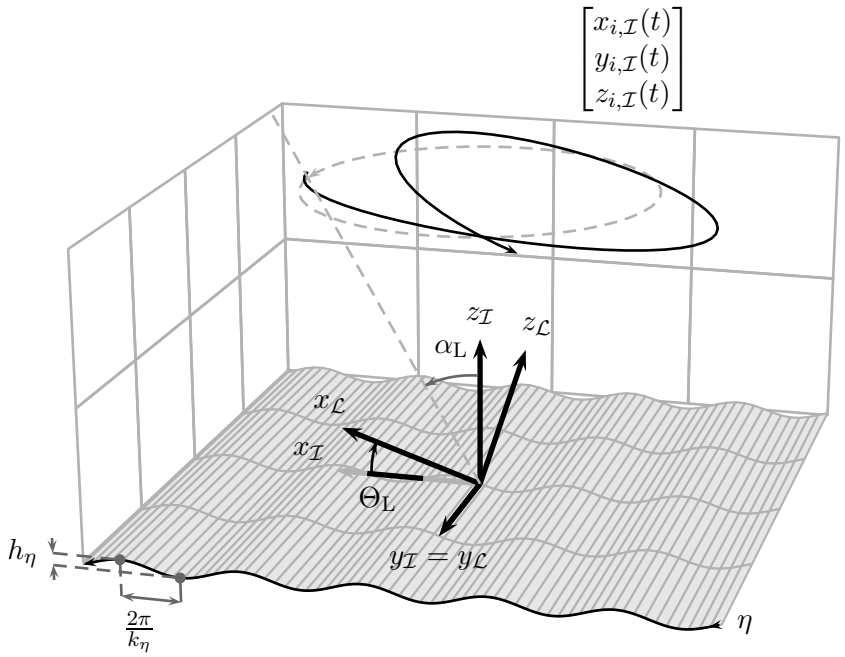

Figure 4.12: Floating lidar simulation: the path of the focus point with waves (solid) differs from the one at calm sea (dashed).

Figure 4.12 illustrates the motion of the floating lidar system at the highest inclination of $\Theta_{\mathrm{L}} = -17.8\,\mathrm{deg}$. With a hydrodynamic simulation, the missing translational and rotational degrees of freedom could be considered in a similar way. However, this is beyond the scope of this work.

Simulation of a Floating Lidar System

For this investigation a continuous-wave lidar is simulated, focusing at $z_{i,\mathcal{L}} = 100\,\mathrm{m}$ and measuring $n_{\mathrm{P}} = 50$ points per second on a circular scan with a half opening angle of $\alpha_{\mathrm{L}} = 30\,\mathrm{deg}$, resulting in a constant focus length of $r_{\mathrm{L}i} = 115.47\,\mathrm{m}$. The moving measurement of the floating lidar system considering the displacement, velocity, and the inclination is simulated with the lidar simulator described in Section 3.5. Here, the simulator scans a static inhomogeneous wind field as defined in (3.17) and a turbulent wind field as defined in (3.15). For the scanning of the constant wind field no weighting function is used, for the turbulent wind field the weighting function (3.38) typical for continuous-wave lidar systems is applied. As a worst case scenario for both simulations, a wind-wave-misalignment of 180 deg is used by propagating the waves against the $x_{\mathcal{I}}$ direction, because having $\dot{z}_{\mathrm{L},\mathcal{I}}(t)$ and $\Theta_{\mathrm{L}}(t)$ in phase opposition yields the highest error for the Velocity Azimuth Display (VAD)-technique. Figure 4.13 shows the measurement path of the focus point during one wave period.

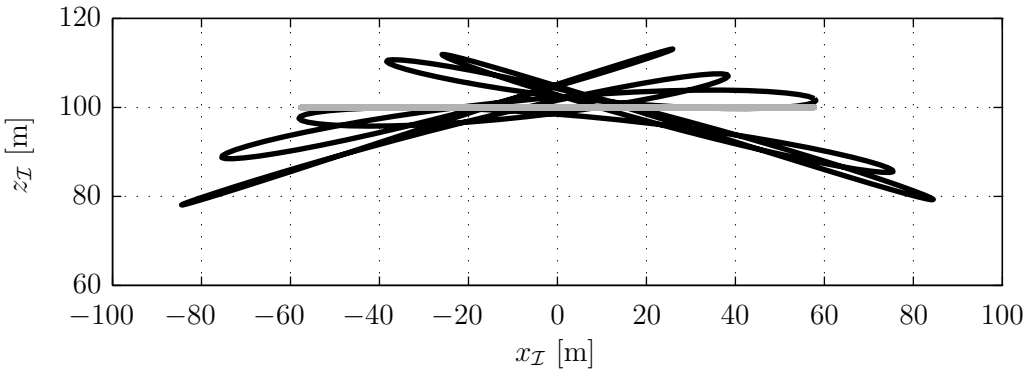

Figure 4.13: Path of the measurement points of a floating lidar system with waves (black) and at calm sea (gray).

Wind Field Reconstruction of a Floating Lidar System

The standard VAD-technique uses the homogeneous flow model (3.16) to fit the line-of-sight wind speeds to a sinusoidal curve and thus can be considered mathematically identical with the DBS-technique when using a circular scan. The VAD-technique assumes that the lidar system is aligned with the inertial coordinate system and is located at its origin. Thus, the wind vector is obtained by inverting

$$\underbrace{\begin{bmatrix} v_{\mathrm{los},1} \\ \vdots \\ v_{\mathrm{los},50} \end{bmatrix}}_{\boldsymbol{m}} = \underbrace{\begin{bmatrix} \frac{x_{1,\mathcal{L}}}{r_{\mathrm{L}i}} & \frac{y_{1,\mathcal{L}}}{r_{\mathrm{L}i}} & \frac{z_{1,\mathcal{L}}}{r_{\mathrm{L}i}} \\ \vdots & \vdots & \vdots \\ \frac{x_{50,\mathcal{L}}}{r_{\mathrm{L}i}} & \frac{y_{50,\mathcal{L}}}{r_{\mathrm{L}i}} & \frac{z_{50,\mathcal{L}}}{r_{\mathrm{L}i}} \end{bmatrix}}_{\boldsymbol{A}} \underbrace{\begin{bmatrix} u_\mathcal{I} \\ v_\mathcal{I} \\ w_\mathcal{I} \end{bmatrix}}_{\boldsymbol{s}} \tag{4.27}$$

with the linear least squares method (4.19). This description of the VAD technique in coordinates rather than in trigonometry shows the problem and guides to a solution: conventional wind reconstruction uses the non-transformed lidar coordinates and thus is not an inverse to the simulation and hence it is not possible to find a correct solution.

This error can be reduced with the model-based approach, when the lidar displacement, velocity, and inclination are known. Similar to (4.22), the wind characteristics effective wind speed v_0, horizontal inflow angle α_h, and vertical linear shear δ_v are found by minimizing the error between the measured $v_{\mathrm{los},i}$ and the estimated $\hat{v}_{\mathrm{los},i}$ with the 3D-inhomogeneous flow model (3.17):

$$\min_{v_0,\alpha_\mathrm{h},\delta_\mathrm{v}} \sum_{i=1}^{50} \left(v_{\mathrm{los},i} - \hat{v}_{\mathrm{los},i}\right)^2 . \tag{4.28}$$

Due to the flat offshore surface, the vertical inflow angle α_v and the horizontal linear shear δ_h are assumed to be zero. Here, the minimization problem is solved for each set of $n_\mathrm{P} = 50$ points with the high-resolution data.

Table 4.4: Mean values for the simulations of a floating lidar.

	3D homogeneous flow (3.16), floating			3D inhomogeneous flow (3.17), floating			3D homogeneous flow (3.16), fixed		
	$u_{\mathcal{I}}$	$v_{\mathcal{I}}$	$w_{\mathcal{I}}$	$u_{\mathcal{I}}$	$v_{\mathcal{I}}$	$w_{\mathcal{I}}$	$u_{\mathcal{I}}$	$v_{\mathcal{I}}$	$w_{\mathcal{I}}$
constant wind	9.08	0.00	-0.01	10.00	0.00	0.00	10.00	0.00	0.00
turbulent wind	9.22	0.00	0.01	10.01	0.00	0.00	10.07	-0.03	0.02

The following steps have to be carried out iteratively:

1. Transformation of the 50 lidar measurements from the $\mathcal{L}$ to the $\mathcal{I}$ and then to the $\mathcal{W}$ system using (3.29) and (3.13) with a given horizontal inflow angle α_{h} and the lidar displacement and inclination at each measurement point.

2. Calculation of the wind speed vector in the $\mathcal{W}$ system using (3.17) and a given effective wind speed v_0 and vertical linear shear δ_{v}.

3. Transformation of the wind speed vector from the $\mathcal{W}$ to the $\mathcal{I}$ coordinate system using (3.12).

4. Calculation of the 50 normalized backscattered laser vectors using (3.32) using the lidar displacement at each measurement point.

5. Calculation of the 50 line-of-sight wind speeds $\hat{v}_{\mathrm{los},i}$ using (3.33) and the lidar velocity in each measurement point.

6. Update of the optimization variables (v_0, α_{h}, and δ_{v}) based on the optimization criterion (root mean square error between the measured $v_{\mathrm{los},i}$ and the estimated $\hat{v}_{\mathrm{los},i}$) and an optimization algorithm.

These steps are repeated until the optimization criterion reaches an acceptable threshold. Here, the `fsolve` function of the Matlab Optimization Toolbox is used.

Results for a Floating Lidar System in Constant Wind

In the first simulation a constant wind field with mean wind speed of $\bar{u} = 10\,\mathrm{m/s}$ at 100 m and a vertical shear of $\delta_{\mathrm{v}} = 0.04\,\frac{1}{\mathrm{s}}$ corresponding to the exponential power law approximation (2.16) at this height is used. A lidar point measurement is used to have the simulation model equal to the reconstruction model. Figure 4.14 shows that the conventional VAD reconstruction has a periodic error, leading to an underestimation of around 9 %, see Table 4.4, due to the non-linearity of the movement (see Figure 4.13). Figure 4.14 and Table 4.4 depict that for constant wind, there is no error using the model-based approach with the inhomogeneous flow model, which is the same result when using the VAD-technique with the homogeneous flow model for a fixed lidar. This investigation validates the proposed method.

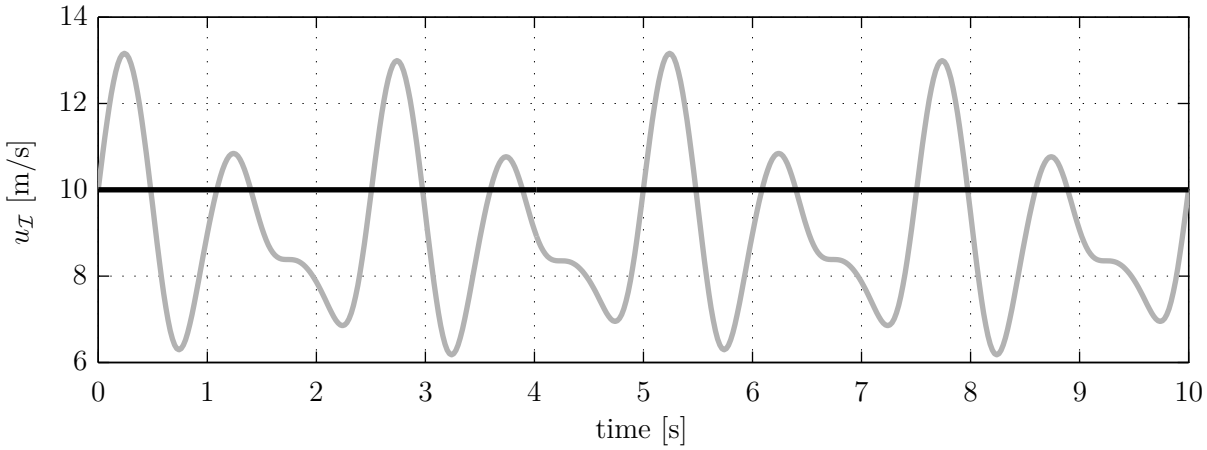

Figure 4.14: Reconstruction of a constant wind field of a floating lidar: With VAD-technique (gray) and the model-based approach (black).

Results for a Floating Lidar System in Turbulent Wind

In a second simulation, a turbulent wind field with a mean wind speed of 10 m/s, a turbulence intensity of 21 %, and a shear according to IEC standards is used. Furthermore, the weighting function for continuous-wave lidar systems is applied. As a reference, the wind field is also scanned by a fixed lidar with no waves.

In Figure 4.15 it can be seen that the conventional reconstruction has a non-zero-mean error (around 8 % over the simulation of 10 minutes, see Table 4.4), while the model-based reconstruction methods are closer to the fixed lidar and the error is insignificant.

This investigation shows that the proposed method is robust enough to deal with uncertainties in the lidar model (volume measurement instead of point measurement) and the wind model (turbulent wind field instead of inhomogeneous flow wind field).

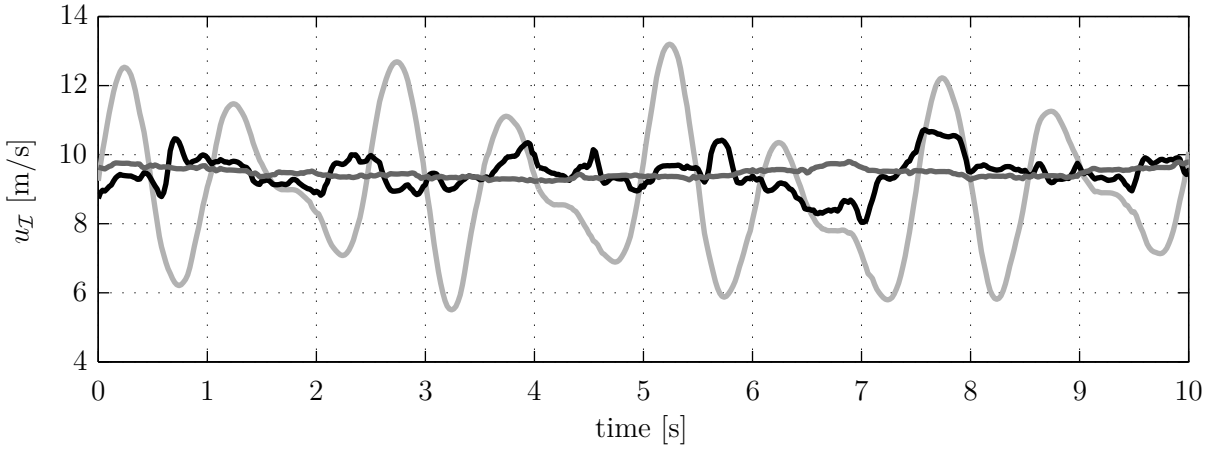

Figure 4.15: Reconstruction of a turbulent wind field of a floating lidar: With VAD-technique (light gray) and the model-based approach (black). Reconstruction of the same wind field of a fixed lidar using the VAD-technique (dark gray).

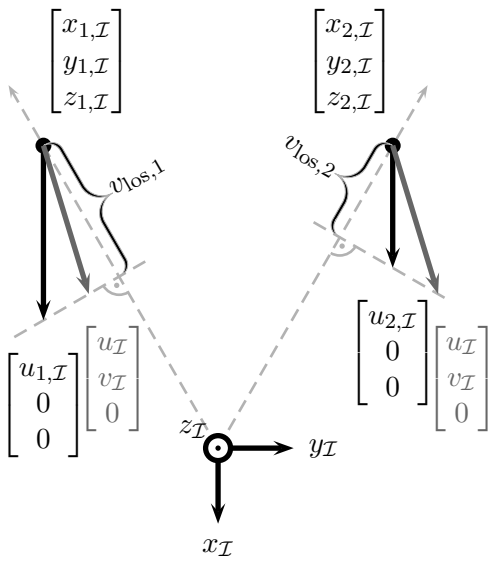

Figure 4.16: The Cyclops Dilemma: Using only line-of-sight wind speeds causes an ambiguity in wind field reconstruction: The assumption of perfect alignment yields horizontal shear (black) and the assumption of homogeneous flow yields misalignment (gray).

4.2.3 Application to Nacelle Lidar Systems

Similar to ground-based and floating lidar systems, it is not possible to measure a three-dimensional wind vector with a single nacelle-based or spinner-based lidar system due to the limitation to the line-of-sight wind speed. But with one of the following simple assumptions, the wind vector can be reconstructed:

1. no vertical and no horizontal wind component

2. no vertical component and homogeneous flow

In Figure 4.16, the effect of both assumptions is shown. In this example, the lidar is situated at the origin of the $\mathcal{I}$-coordinate system. The 3D vectors in the locations $[x_{1,\mathcal{I}}\ y_{1,\mathcal{I}}\ z_{1,\mathcal{I}}]^{\mathrm{T}}$ and $[x_{2,\mathcal{I}}\ y_{2,\mathcal{I}}\ z_{2,\mathcal{I}}]^{\mathrm{T}}$ (measured at the same height) are reconstructed from the line-of-sight wind speeds $v_{\mathrm{los},1}$ and $v_{\mathrm{los},2}$, which can be modeled with (3.31) and the focus length $r_{\mathrm{L}i} = \sqrt{x_{i,\mathcal{I}}^2 + y_{i,\mathcal{I}}^2 + z_{i,\mathcal{I}}^2}$ by

$$v_{\mathrm{los},i} = -\frac{x_{i,\mathcal{I}}}{r_{\mathrm{L}i}} u_{i,\mathcal{I}} - \frac{y_{i,\mathcal{I}}}{r_{\mathrm{L}i}} v_{i,\mathcal{I}} - \frac{z_{i,\mathcal{I}}}{r_{\mathrm{L}i}} w_{i,\mathcal{I}}. \tag{4.29}$$

The first assumption ($\hat{v}_{i,\mathcal{I}} = \hat{w}_{i,\mathcal{I}} = 0$) simplifies (4.29) to

$$v_{\mathrm{los},1} = -\frac{x_{1,\mathcal{I}}}{r_{\mathrm{L1}}}\hat{u}_{1,\mathcal{I}} \quad \text{and} \quad v_{\mathrm{los},2} = -\frac{x_{2,\mathcal{I}}}{r_{\mathrm{L2}}}\hat{u}_{2,\mathcal{I}}. \tag{4.30}$$

The wind vectors in both measurement points can then be estimated by

$$\begin{bmatrix}\hat{u}_{1,\mathcal{I}}\\ \hat{v}_{1,\mathcal{I}}\\ \hat{w}_{1,\mathcal{I}}\end{bmatrix} = \begin{bmatrix}-\frac{r_{\mathrm{L1}}}{x_{1,\mathcal{I}}}v_{\mathrm{los},1}\\ 0\\ 0\end{bmatrix} \quad \text{and} \quad \begin{bmatrix}\hat{u}_{2,\mathcal{I}}\\ \hat{v}_{2,\mathcal{I}}\\ \hat{w}_{2,\mathcal{I}}\end{bmatrix} = \begin{bmatrix}-\frac{r_{\mathrm{L2}}}{x_{2,\mathcal{I}}}v_{\mathrm{los},2}\\ 0\\ 0\end{bmatrix}, \tag{4.31}$$

representing a horizontal shear.

The second assumption (two-dimensional homogeneous flow (4.17): $\hat{u}_{1,\mathcal{I}} = \hat{u}_{2,\mathcal{I}} = \hat{u}_{\mathcal{I}}$, $\hat{v}_{1,\mathcal{I}} = \hat{v}_{2,\mathcal{I}} = \hat{v}_{\mathcal{I}}$, $\hat{w}_{i,\mathcal{I}} = 0$) simplifies (4.29) to

$$\begin{bmatrix}v_{\mathrm{los},1}\\ v_{\mathrm{los},2}\end{bmatrix} = \underbrace{\begin{bmatrix}-\frac{x_{1,\mathcal{I}}}{r_{\mathrm{L1}}} & -\frac{y_{1,\mathcal{I}}}{r_{\mathrm{L1}}}\\ -\frac{x_{2,\mathcal{I}}}{r_{\mathrm{L2}}} & -\frac{y_{2,\mathcal{I}}}{r_{\mathrm{L2}}}\end{bmatrix}}_{\boldsymbol{A}} \begin{bmatrix}\hat{u}_{\mathcal{I}}\\ \hat{v}_{\mathcal{I}}\end{bmatrix} \tag{4.32}$$

and the longitudinal and lateral wind speed component is obtained by

$$\begin{bmatrix}\hat{u}_{\mathcal{I}}\\ \hat{v}_{\mathcal{I}}\end{bmatrix} = \boldsymbol{A}^{-1}\begin{bmatrix}v_{\mathrm{los},1}\\ v_{\mathrm{los},2}\end{bmatrix}, \tag{4.33}$$

representing a cross-flow.

A dilemma ("Cyclops Dilemma", introduced in [82]) exists, if the lidar should be used for yaw and cyclic pitch control at the same time: If the first assumption is used to calculate the inhomogeneous inflow, perfect alignment is assumed. If the second assumption is used to obtain the misalignment, homogeneous flow is assumed. The estimation error for both cases will be different depending on how well the assumption fits to the real wind conditions. For example, with the first assumption the estimated longitudinal wind speeds will be (integrating (4.29) into (4.31)):

$$\hat{u}_{1,\mathcal{I}} = u_{1,\mathcal{I}} + \frac{y_{1,\mathcal{I}}}{x_{1,\mathcal{I}}}v_{1,\mathcal{I}} + \frac{z_{1,\mathcal{I}}}{x_{1,\mathcal{I}}}w_{1,\mathcal{I}} \quad \text{and} \quad \hat{u}_{2,\mathcal{I}} = u_{2,\mathcal{I}} + \frac{y_{2,\mathcal{I}}}{x_{2,\mathcal{I}}}v_{2,\mathcal{I}} + \frac{z_{2,\mathcal{I}}}{x_{2,\mathcal{I}}}w_{2,\mathcal{I}}. \tag{4.34}$$

This effect is often referred to as "cross contamination". If the real wind is equal to the homogeneous flow (3.16), this effect can be canceled out by the average over a symmetric scan (e.g., $y_{1,\mathcal{I}} = -y_{2,\mathcal{I}}$, $z_{1,\mathcal{I}} = z_{2,\mathcal{I}} = 0$):

$$\hat{u} = \frac{1}{2}(\hat{u}_{1,\mathcal{I}} + \hat{u}_{2,\mathcal{I}}) = u_{\mathcal{I}}. \tag{4.35}$$

However, this is not true, if the real wind is equal to the inhomogeneous flow (3.17). Similar to the ground-based systems, the static inhomogeneous flow model (3.17) can be used in the estimation to distinguish between shear and inflow angle. Measurements in several distances in front of the turbine are then necessary to solve a minimization problem similar to (4.22). However, static wind field reconstruction methods need a large averaging time to provide robust results and all measurements must be treated equally independent of their time of measurement. Since the signals for control need to be right in time before the wind reaches the turbine, those methods are not promising for control applications. Nevertheless, nacelle lidar systems can provide a good estimate of wind characteristics for control using dynamic wind models taking into account the time of measurement as will be presented in the next section.

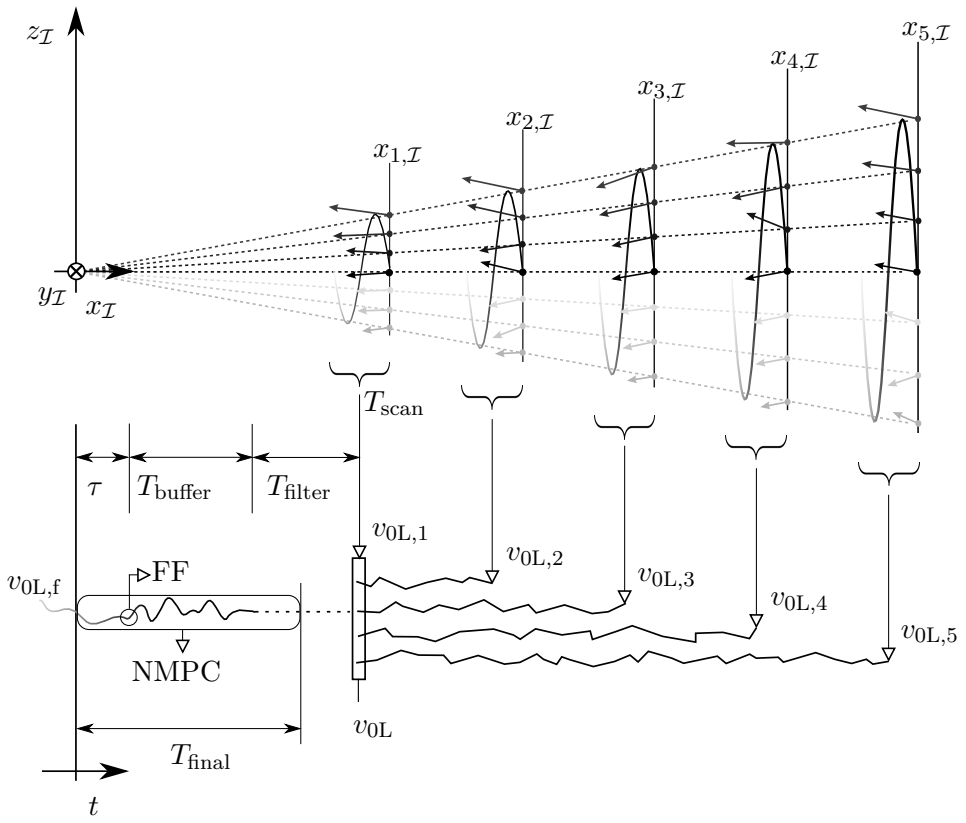

Figure 4.17: Scope of the dynamic wind reconstruction: The line-of-sight wind speeds are measured at fixed distances, corrected, averaged over the last trajectory, time shifted, and combined to form a preview of the rotor effective wind speed. The signal is filtered and then transferred to Feedforward (FF) controllers (Chapters 6, 7, 8) or an Nonlinear Model Predictive Controller (NMPC) [29].

4.3 Dynamic Wind Field Reconstruction

In the previous section about static wind field reconstruction, the estimation of the wind characteristic is made based on the line-of-sight wind speeds alone, and no temporal relationship of measurements along the stream line is included in the model. However, the estimation process can be improved and adapted to the needs for lidar-assisted control by extending the wind field model by Taylor's Frozen Turbulence Hypothesis, which is a very simple temporal relation.

Although the methods presented in this section are basically independent of the position of the lidar system (ground or nacelle), the rotor effective wind speed (4.3.1) and shear (4.3.2) are reconstructed from the nacelle.

4.3.1 Dynamic Reconstruction of Rotor Effective Wind Speed

The knowledge of the rotor effective wind speed is useful to improve the performance of the collective pitch and the torque controller.
When perfect alignment with the wind direction and no wind shears are assumed, the dynamic inhomogeneous flow wind model (3.18) is reduced to:

$$\begin{bmatrix} u_{i,\mathcal{I}} \\ v_{i,\mathcal{I}} \\ w_{i,\mathcal{I}} \end{bmatrix} = \begin{bmatrix} v_0(t_{\mathrm{R},i}) \\ 0 \\ 0 \end{bmatrix} \text{ with } t_{\mathrm{R},i} = t_i - \frac{x_{i,\mathcal{I}}}{\bar{u}}. \tag{4.36}$$

Thus, the lidar estimate of the rotor effective wind speed $v_{0\mathrm{L}}$ could be estimated at each measurement point i with the lidar point measurement model (3.31) from the line-of-sight wind speed $v_{\mathrm{los},i}$ by

$$v_{0\mathrm{L}}(t_i) = \frac{v_{\mathrm{los},i}}{x_{\mathrm{n},i,\mathcal{I}}}. \tag{4.37}$$

However, if various measurement points are distributed over the rotor area, the estimate can be improved by combining all measurements into one signal. In the case of a pulsed lidar system with n_{D} measurement distances and n_{P} measurement points at each measurement distance j, a signal $v_{0\mathrm{L},j}$ can be generated by summarizing all n_{P} points of the last full scan by

$$v_{0\mathrm{L},j}(t_i) = \frac{1}{n_{\mathrm{P}}} \sum_{i=1}^{n_{\mathrm{P}}} \frac{v_{\mathrm{los},ij}}{x_{\mathrm{n},i,\mathcal{I}}}. \tag{4.38}$$

The obtained time series $v_{0\mathrm{L},j}$ are then time-shifted according to Taylor's Frozen Turbulence Hypothesis (see Figure 4.17), which assumes that the turbulent wind field moves with the mean wind speed $\bar{u}$: The time to reach the first focus distance is assumed to be $(x_{j,\mathcal{I}} - x_{1,\mathcal{I}})/\bar{u}$. The lidar estimate of the rotor effective wind speed $v_{0\mathrm{L}}$ is then calculated by

$$v_{0\mathrm{L}}(t_i) = \frac{1}{n_{\mathrm{D}}} \sum_{j=1}^{n_{\mathrm{D}}} v_{0\mathrm{L},j}(t_i - \frac{x_{j,\mathcal{I}} - x_{1,\mathcal{I}}}{\bar{u}}). \tag{4.39}$$

The wind speed preview $v_{0\mathrm{L}}$ is filtered by a low-pass filter, and the time delay introduced by the filter has to be considered as explained in Section 5.5. The purpose of the filtering and the time-shifting is to have the filtered lidar estimate $v_{0\mathrm{L,f}}$ in magnitude and phase as close as possible to the rotor effective wind speed v_0.

4.3.2 Dynamic Reconstruction of Rotor Effective Wind Shears

The knowledge of the rotor effective wind shears is used in [83] to improve the performance of the individual pitch controller.
Horizontal and vertical inflow angles are neglected and thus the inertial ($\mathcal{I}$) and the wind coordinate system ($\mathcal{W}$) coincide. The following reduced version of the dynamic inhomogeneous flow wind model (3.18) is used:

$$\begin{bmatrix} u_{i,\mathcal{I}} \\ v_{i,\mathcal{I}} \\ w_{i,\mathcal{I}} \end{bmatrix} = \begin{bmatrix} v_0(t_{\mathrm{R},i}) + \delta_{\mathrm{h}}(t_{\mathrm{R},i}) y_{i,\mathcal{I}} + \delta_{\mathrm{v}}(t_{\mathrm{R},i}) z_{i,\mathcal{I}} \\ 0 \\ 0 \end{bmatrix} \text{ with } t_{\mathrm{R},i} = t_i - \frac{x_{i,\mathcal{I}}}{\bar{u}}. \tag{4.40}$$

Similar to Section 4.3.1, the estimate of the horizontal and vertical shear (δ_{hL} and δ_{vL}) can be obtained at time t_i together with the rotor effective wind speed estimate $v_{0\mathrm{L}}$ over all n_{P} points of the last full scan. Therefore, the lidar point measurement model (3.31) is combined with the reduced dynamic inhomogeneous flow wind model (4.40):

$$\underbrace{\begin{bmatrix} v_{\mathrm{los},1} \\ \vdots \\ v_{\mathrm{los},n_{\mathrm{P}}} \end{bmatrix}}_{\boldsymbol{m}} = \underbrace{\begin{bmatrix} x_{\mathrm{n},1,\mathcal{I}} & x_{\mathrm{n},1,\mathcal{I}}\, y_{1,\mathcal{I}} & x_{\mathrm{n},1,\mathcal{I}}\, z_{1,\mathcal{I}} \\ \vdots & \vdots & \vdots \\ x_{\mathrm{n},n_{\mathrm{P}},\mathcal{I}} & x_{\mathrm{n},n_{\mathrm{P}},\mathcal{I}}\, y_{n_{\mathrm{P}},\mathcal{I}} & x_{\mathrm{n},n_{\mathrm{P}},\mathcal{I}}\, z_{n_{\mathrm{P}},\mathcal{I}} \end{bmatrix}}_{\boldsymbol{A}} \underbrace{\begin{bmatrix} v_{0\mathrm{L}}(t_i) \\ \delta_{\mathrm{hL}}(t_i) \\ \delta_{\mathrm{vL}}(t_i) \end{bmatrix}}_{\boldsymbol{s}}. \tag{4.41}$$

Again, the searched values $\boldsymbol{s}$ can be obtained from the measured data $\boldsymbol{m}$ by applying the least squares method or by multiplying with the Moore-Penrose pseudoinverse $\boldsymbol{A}^{+}$ of matrix $\boldsymbol{A}$.
In the case of a pulsed lidar system with more than one measurement distance, the estimates from each distance can be shifted in time and combined similar to Section 4.3.1.

4.4 Summary and Possible Extensions for Wind Field Reconstruction

In this chapter, a system-theoretical view on wind field reconstruction based on lidar measurements and its application to wind field reconstruction are presented.

Conventional techniques for site assessment use the same wind model in all situations, which causes problems in complex terrain or on floating platforms, although detailed simulation models exist. These models can be used for wind reconstruction under certain constraints. For site assessment, usually only averages over ten minutes are required and thus static models without any temporal relationship are sufficient to reconstruct the wind field. The model-based wind field reconstruction is first evaluated with real measurements for a ground based lidar. By including a more detailed model, the reconstruction of the wind vector can be significantly improved. Secondly, the model-based approach is applied to floating lidar simulations. By including the inclination information and the vertical shear into the model, the measurement error caused by the motion can be compensated. For nacelle based systems the limitation to line-of-sight wind speeds complicates the simultaneous estimation of horizontal shear and wind direction.

For control purposes, real-time preview information about the inflowing wind field is beneficial. Thus, the wind field needs to be reconstructed much faster than for the site assessment, and including the temporal information is necessary. Therefore, the model-based wind field reconstruction is extended by dynamic wind models. Here, Taylor's Frozen Turbulence Hypothesis is used, which assumes that the wind field propagates with the mean wind speed. With this assumption the measurements from several measurement distances can be combined to estimate wind characteristics such as the rotor effective wind speed and wind shears.

For testing lidar-assisted individual pitch control on real wind turbines, the shears and the inflow angles need to be integrated into the estimation process. The following idea came up during the writing of this thesis and was elaborated in [84]: For pulsed lidar systems, the measurements from all measurement distances can be integrated into one single optimization problem by defining several stages behind and in front of the turbine within the wind ($\mathcal{W}$) coordinate system, see Figure 4.18. For each stage j the wind is reduced to a corresponding rotor effective wind speed $v_{0,j}$ and a linear horizontal and vertical shear $\delta_{\mathrm{h},j}$ and $\delta_{\mathrm{v},j}$. With Taylor's Frozen Turbulence Hypothesis, each measured line-of-sight wind speed can be allocated to a certain stage. The optimization problem can then be defined as a minimization of the accumulated difference between the measured line-of-sight wind speeds and the ones resulting from the wind field model-based on the optimization variables (inflow angle α_{h}, α_{v} as well as rotor effective wind speed $v_{0,j}$ and a linear horizontal and vertical shear $\delta_{\mathrm{h},j}$ and $\delta_{\mathrm{v},j}$ for each stage j). With weights, one can account for the higher uncertainty of past measurements. With this approach not only the rotor effective wind speed and the wind shears can be estimated, but also the

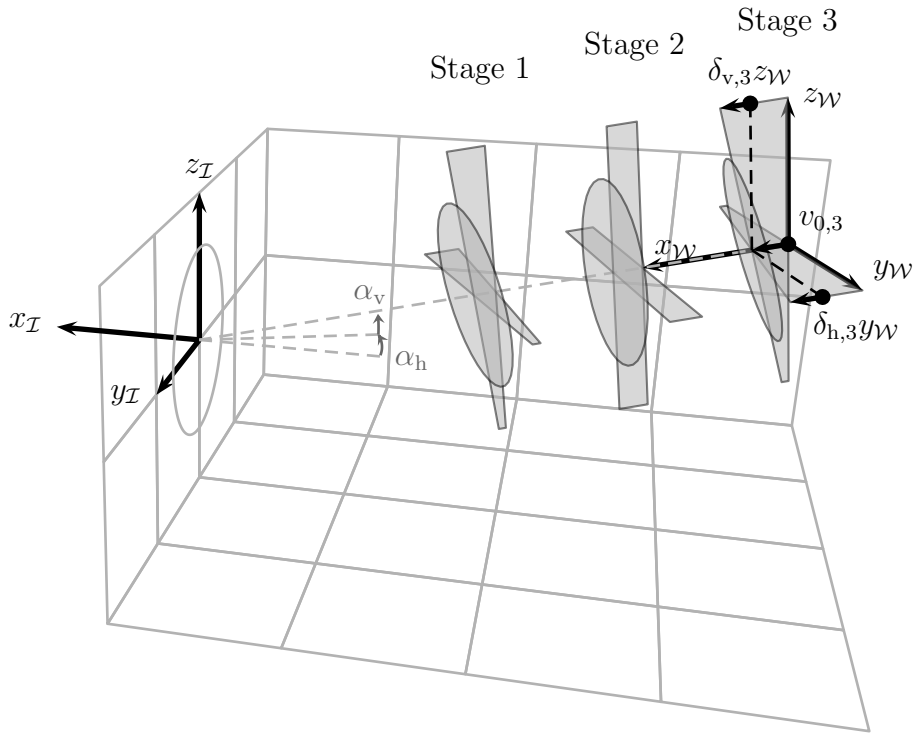

Figure 4.18: Multi-stage dynamic inhomogeneous wind field model: The wind field model consists of various stages with corresponding effective wind speeds, linear vertical and horizontal shears and is rotated with the horizontal and vertical inflow angle (α_{h} and α_{v}).

inflow angles.

Another important improvement of the dynamic wind field reconstruction is to include other, more realistic dynamic models such as differential equations which would enable estimation techniques such as Kalman filters that are often used for dynamic systems [5].

5

Correlation between Lidar Systems and Wind Turbines

For lidar assisted control, it is crucial to know the correlation between the wind speed preview provided by a nacelle- or spinner-based lidar system and the wind speed affecting the turbine. If on the one side the assumed correlation is overestimated, the uncorrelated frequencies of the preview will cause unnecessary control action, inducing undesired loads. On the other side the benefits of the lidar-assisted controller will not be fully exhausted, if correlated frequencies are filtered out.

However, there are several interacting effects which determine how well the wind speed is predicted. This chapter presents a method to model the correlation between lidar systems and wind turbines using Kaimal wind spectra. The correlation is expressed by the magnitude squared coherence γ^2_{RL} between the rotor effective wind speed measured by the lidar and that sensed by the turbine's rotor, defined as

$$\gamma^2_{\mathrm{RL}} = \frac{|S_{\mathrm{RL}}|^2}{S_{\mathrm{RR}} S_{\mathrm{LL}}}, \tag{5.1}$$

where S_{RL}, S_{RR}, and S_{LL} are the cross-spectrum between both signals and the auto-spectrum of the signal from the turbine and the lidar, respectively. The derived model accounts for different measurement configurations and spatial averaging of the lidar system, different rotor sizes, and wind evolution. The method is compared to real measurement data with promising results. In addition, an example depicts how the model can be used to optimize the configuration or the scanning pattern of a lidar system for a given turbine to improve the correlation. Furthermore,

an adaptive filter for the rotor effective wind speed used in the Chapters 6 to 8 is designed by fitting a linear filter to the magnitude of the modeled transfer function

$$|G_{\mathrm{RL}}| = \left| \frac{S_{\mathrm{RL}}}{S_{\mathrm{LL}}} \right|. \tag{5.2}$$

Related work has been done by Eric Simley. In [7], single point wind speed is compared to lidar measurements including the effect of range weighting, limitation to line-of-sight direction and wind evolution. In [8], a similar model to the one presented in this work is derived, extending the idea to the correlation between lidar measurement and the blade effective wind speed. In [9], an alternative way to obtain an appropriate filter based on the modeled correlation is presented.

This Chapter is organized as follows. Section 5.1 provides the basic idea. In Section 5.2 and in Section 5.3, the model for a perfect staring and a real scanning lidar is derived, which is evaluated with field testing data in Section 5.4. The model is used in Section 5.5 to design an adaptive filter and in Section 5.6 to optimize a lidar system. A summary and a proposal for extensions are given in Section 5.7.

This chapter extends the work published in [85].

5.1 Motivation of Correlation Model

The auto- and cross-spectra necessary to determine the correlation between lidar measurements and turbine reaction can be calculated by a simulation study in the time domain, see Figure 5.1. Therefore, the wind components $u_{\mathcal{W}}, v_{\mathcal{W}}, w_{\mathcal{W}}$ on a spatial and temporal grid $(y_{\mathcal{W}}, z_{\mathcal{W}}, t)$ have to be generated using a discrete inverse Fourier transformation (iFFT) based on wind spectral models. In the case of the Kaimal turbulence model, these are the auto-spectra $S_{ii,h}$ for each wind speed component of each grid point and the squared coherence $\gamma^2_{ij,u}$ between the longitudinal component of the ith and the jth grid point. See Section 2.2 for more details. Then, the wind field has to be scanned by a lidar simulator to obtain the line-of-sight wind speeds and wind field reconstruction algorithms have to be applied to obtain the lidar estimate of the rotor effective wind speed $v_{0\mathrm{L}}$. Furthermore, the rotor effective wind speed v_0 has to be calculated based on simulated turbine data or directly from the wind field. In the last step, the auto- and cross-spectra can be estimated with a FFT and the estimate of the transfer function G_{RL} and the squared coherence γ^2_{RL} are determined by (5.2) and (5.1). Due to the properties of the discrete FFT which will be discussed in Section 5.2, the estimate of the coherence and the transfer function improves with the length of the wind field and the simulation. Finally, one would need an endless wind field and simulation to get exact values.

To avoid this issue, the method proposed in this chapter calculates the cross- and auto-spectra

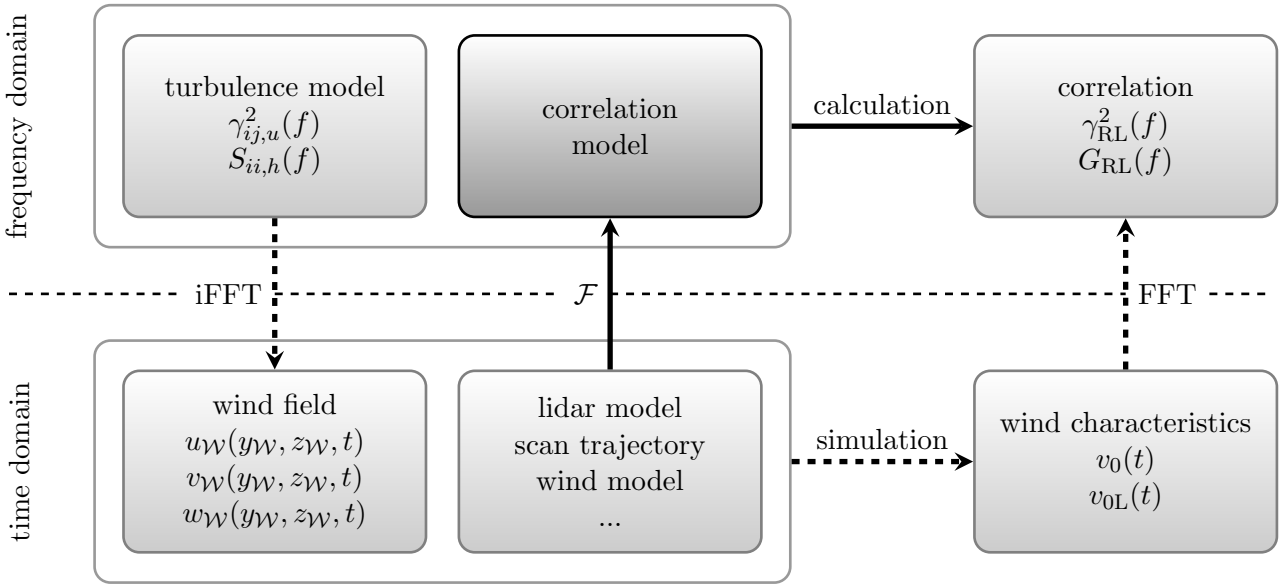

Figure 5.1: Basic idea of the correlation model: The correlation between a lidar system and a turbine's reaction is directly calculated in the frequency domain with the Fourier transform of equations for the simulation and the turbulence model (solid) – instead of generating a wind field, time domain simulation, and estimating the correlation (dashed).

directly from the wind turbulence model and the Fourier transform of the measurement equations and reconstruction method, see Figure 5.1. However, a purely analytic model is only achieved for a basic set-up. Therefore, partial discretization (here denoted "semi-analytic") is also necessary to model more realistic set-ups.

5.2 Correlation of a Perfect Staring Lidar System

The auto- and cross-spectra S_{LL}, S_{RR}, and S_{RL} are necessary to model the correlation between a lidar system and a turbine as expressed by the coherence (5.1) and the transfer function (5.2). For a perfect staring lidar system, the spectra are calculated fully analytically and semi-analytically. They are derived based on the Kaimal wind spectrum (2.19) and coherence (2.21). However, any other wind turbulence models can be used in principle.
The auto-spectra of the rotor effective wind speed v_0 and the lidar estimate $v_{0\mathrm{L}}$ and the cross-spectrum between them is defined – omitting all scaling constants and mean operators – by

$$\begin{aligned} S_{\mathrm{RR}} &= \mathcal{F}\{v_0\}\mathcal{F}^*\{v_0\} \\ S_{\mathrm{RL}} &= \mathcal{F}\{v_0\}\mathcal{F}^*\{v_{0\mathrm{L}}\} \\ S_{\mathrm{LL}} &= \mathcal{F}\{v_{0\mathrm{L}}\}\mathcal{F}^*\{v_{0\mathrm{L}}\}, \end{aligned} \tag{5.3}$$

where $\mathcal{F}\{\}$ and $\mathcal{F}^*\{\}$ are the Fourier transform and its complex conjugate, respectively [86].

5.2.1 Determination of Lidar Auto-spectrum

Ignoring the filtering effect of a lidar and assuming Taylor's Frozen Turbulence Hypothesis [66] to be fully valid (no wind evolution), the lidar estimate of the rotor effective wind speed is considered equal to the longitudinal wind velocity u_{H} at the hub:

$$v_{0\mathrm{L}} = u_{\mathrm{H}}. \tag{5.4}$$

Therefore, the spectrum of a perfect staring lidar system is simply modeled with the longitudinal Kaimal auto-spectrum (2.19) by

$$S_{\mathrm{LL}} = \mathcal{F}\{u_{\mathrm{H}}\}\mathcal{F}^*\{u_{\mathrm{H}}\} = S_{\mathrm{HH}} = S_{ii,u} = \frac{4\sigma_u^2 \frac{L_u}{\bar{u}}}{\left(1 + 6f\frac{L_u}{\bar{u}}\right)^{(5/3)}}. \tag{5.5}$$

5.2.2 Determination of Rotor Auto-spectrum

With the definition of the rotor effective wind speed (3.19), the rotor averaged spectrum S_{RR} can be derived by

$$\begin{aligned} S_{\mathrm{RR}} &= \mathcal{F}\left\{\frac{1}{\pi R^2}\int_0^{2\pi}\int_0^{R} u_{\mathcal{I}}\; r\,\mathrm{d}r\,\mathrm{d}\phi\right\}\mathcal{F}^*\left\{\frac{1}{\pi R^2}\int_0^{2\pi}\int_0^{R} u_{\mathcal{I}}\; r\,\mathrm{d}r\,\mathrm{d}\phi\right\} \\ &= \frac{1}{(\pi R^2)^2}\int_0^{2\pi}\int_0^{R}\int_0^{2\pi}\int_0^{R} \underbrace{\mathcal{F}\{u_{i,\mathcal{I}}\}\mathcal{F}^*\{u_{j,\mathcal{I}}\}}_{S_{ij,u}}\; r_i\; r_j\,\mathrm{d}r_i\,\mathrm{d}\phi_i\,\mathrm{d}r_j\,\mathrm{d}\phi_j. \end{aligned} \tag{5.6}$$

To obtain the cross-spectrum $S_{ij,u}$ of the longitudinal wind speed component between a point i and j, the coherence of the longitudinal velocity component (2.21) between two points with distance r_{ij} is rewritten as

$$\gamma_{ij,ur} = \exp\left(-\kappa\; r_{ij}\right) \text{ with } \kappa = 12\sqrt{\left(\frac{f}{\bar{u}}\right)^2 + \left(\frac{0.12}{L_u}\right)^2}. \tag{5.7}$$

Here, κ is the frequency-dependent lateral decay parameter. With the definition of coherence

$$\gamma_{ij,ur}^2 = \frac{|S_{ij,u}|^2}{S_{ii,u}S_{jj,u}} \tag{5.8}$$

and the assumption that there is no phase shift between the longitudinal wind speed component in point i and j and with $S_{ii,u} = S_{jj,u}$, the cross-spectrum is obtained by

$$S_{ij,u} = |S_{ij,u}| = \gamma_{ij,ur}S_{ii,u} = \exp\left(-\kappa\; r_{ij}\right) S_{ii,u}. \tag{5.9}$$

With (5.9), the explicit solution of (5.6) can be found as

$$S_{\mathrm{RR}} = \frac{2S_{ii,u}}{(R\kappa)^3}\left(L_1(2R\kappa) - I_1(2R\kappa) - \frac{2}{\pi} + R\kappa\left(-2L_{-2}(2R\kappa) + 2I_2(2R\kappa) + 1\right)\right), \tag{5.10}$$

where L are modified Struve functions[1] and I are modified Bessel functions of the first kind[2]. Details of this calculation can be found in Appendix C.4.

5.2.3 Determination of Cross-spectrum

Similar to (5.6), the cross-spectrum between the staring lidar system and the rotor is

$$\begin{aligned} S_{\mathrm{RL}} &= \mathcal{F}\left\{\frac{1}{\pi R^2}\int_0^{2\pi}\int_0^{R} u_{\mathcal{I}}\; r\,\mathrm{d}r\,\mathrm{d}\phi\right\}\mathcal{F}^*\left\{u_{\mathrm{H}}\right\} \\ &= \frac{1}{\pi R^2}\int_0^{2\pi}\int_0^{R} S_{\mathrm{H}j,u}\; r_j\,\mathrm{d}r_j\,\mathrm{d}\phi_j, \end{aligned} \tag{5.11}$$

where $S_{\mathrm{H}j,u}$ is the cross-spectrum of the longitudinal wind component between the hub and the point j. Assuming that the lidar signal $u_{\mathcal{I}}$ is time-shifted to the rotor, the cross-spectrum can be replaced similar to (5.9) by the coherence and auto-spectrum and then (5.11) is solved by

$$S_{\mathrm{RL}} = \frac{2S_{ii,u}}{R^2\kappa^2}\left(1 - \frac{R\kappa + 1}{\exp(R\kappa)}\right). \tag{5.12}$$

5.2.4 Determination of Coherence and Transfer Function

Finally, the transfer function G_{RL} and the squared coherence γ^2_{RL} can be calculated based on the cross- and auto-spectra of (5.5), (5.10), and (5.12) using (5.2) and (5.1).
With the definition of the wavenumber

$$k = \frac{2\pi f}{\bar{u}}, \tag{5.13}$$

the coherence and transfer function are independent of the mean wind speed $\bar{u}$. Figure 5.2 shows both for the NREL 5 MW reference turbine.
The model is compared to the coherence and transfer function obtained from a time domain simulation. As illustrated in Figure 5.1, a wind field needs to be generated and scanned to

[1] See `www.mathworld.wolfram.com/ModifiedStruveFunction.html`.
[2] See `www.mathworld.wolfram.com/ModifiedBesselFunctionoftheFirstKind.html`.

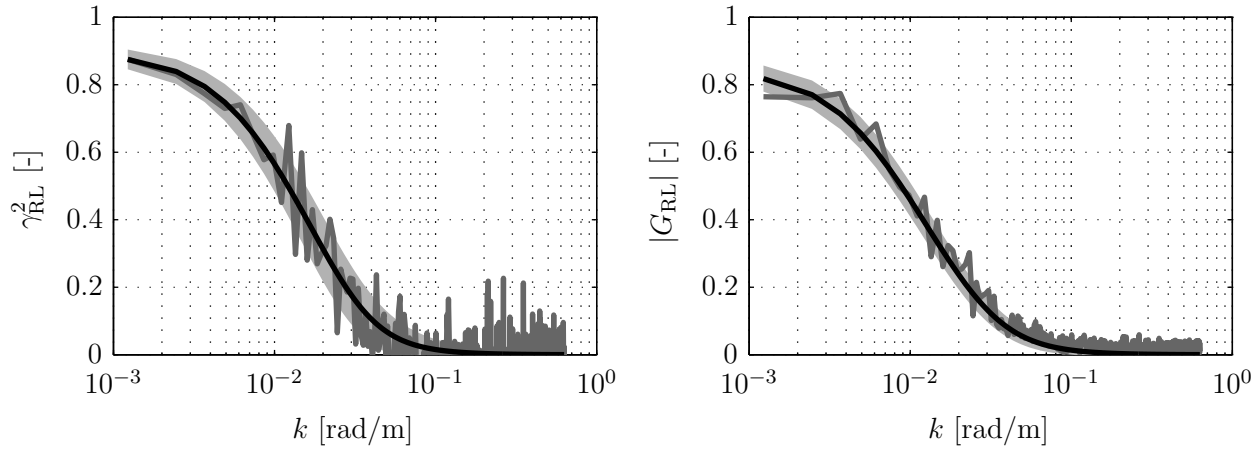

Figure 5.2: Coherence (left) and transfer function (right) between a perfect staring lidar and a turbine with a rotor diameter of 126 m. From model (black) and from estimation (dark gray) with $\pm\sigma(\hat{\gamma}^2_{\mathrm{RL}})$ and $\pm\sigma(|\hat{G}_{\mathrm{RL}}|)$ confidence bounds (light gray).

extract the signals for the rotor effective wind speed v_0 and its lidar estimate $v_{0\mathrm{L}}$. Here, a large TurbSim wind field with a time step of 0.25 s based on the Kaimal turbulence model with $n_{\mathrm{R}} = 777$ points distributed equally over the rotor area with 4 m separation is used (for details see Table C.3). A time length of 8192 s is chosen to obtain a good estimation of the correlation. The rotor effective wind speed v_0 is obtained by using the average of all longitudinal wind speed components (3.20). Its lidar estimate $v_{0\mathrm{L}}$ in this case is equal to the longitudinal wind speed at hub height.

The process of estimating the coherence and the transfer function from time signals is quite complex and is here briefly explained to show the limitations and adjusting possibilities. First, the two signals are divided into $n_{\mathrm{C}} = 32$ data chunks of the same length (here 1024 data points). Then, the coherence and the transfer function are estimated using Welch's averaged periodogram method[3]:

$$\hat{\gamma}^2_{\mathrm{RL,biased}} = \frac{\left|\sum_{i=1}^{n_{\mathrm{C}}} V_{0\mathrm{L},i} V^*_{0,i}\right|^2}{\sum_{i=1}^{n_{\mathrm{C}}} |V_{0,i}|^2 \sum_{i=1}^{n_{\mathrm{C}}} |V_{0\mathrm{L},i}|^2} \tag{5.14a}$$

$$\hat{G}_{\mathrm{RL}} = \frac{\sum_{i=1}^{n_{\mathrm{C}}} V_{0\mathrm{L},i} V^*_{0,i}}{\sum_{i=1}^{n_{\mathrm{C}}} |V_{0\mathrm{L},i}|^2}, \tag{5.14b}$$

[3]Done using no overlap and a rectangular window with `mscohere` and `tfestimate` of The MathWorks Inc., Matlab R2013b, Natick, USA (2013).

where $V_{0,i}$ and $V_{0\mathrm{L},i}$ are the FFTs of the signals v_0 and $v_{0\mathrm{L}}$ from the data chunk i. The bias of the coherence is then corrected using the approach proposed in [87].

$$\hat{\gamma}^2_{\mathrm{RL}} = \hat{\gamma}^2_{\mathrm{RL,biased}} - \left(\frac{1}{n_{\mathrm{C}}}(1-\gamma^2_{\mathrm{RL}})^2\right). \tag{5.15}$$

Although the spectra are averaged over several chunks, the random error in both estimates is still visible. Based on [86], the standard deviation of the random error can be calculated by

$$\sigma(\hat{\gamma}^2_{\mathrm{RL}}) = \sqrt{\frac{2\gamma^2_{\mathrm{RL}}(1-\gamma^2_{\mathrm{RL}})^2}{n_{\mathrm{C}}}} \tag{5.16a}$$

$$\sigma(|\hat{G}_{\mathrm{RL}}|) = \sqrt{\frac{(1-\gamma^2_{\mathrm{RL}})|G_{\mathrm{RL}}|^2}{2\gamma^2_{\mathrm{RL}} n_{\mathrm{C}}}}. \tag{5.16b}$$

The estimates and the corresponding $\pm\sigma$-confidence bounds are shown in Figure 5.2. The agreement not only validates the analytic approach, but also demonstrates the advantage: with the proposed model the correlation between lidar measurements and the rotor effective wind speed can be directly calculated without the inaccuracy involved in the spectra estimation process. By dividing the signals in more data chunks, the bias and the random error can be decreased. However, there will be less data points per chunk and thereby the frequency resolution will degrade (here the sampling frequency is $f_{\mathrm{s}} = \frac{1}{512}$ Hz). It has to be mentioned that usually the segments are weighted with cosine windows (e.g., von Hann or Hamming functions) to decrease the spectral leakage (smearing of spectral content due to the finite length of the FFT) and overlapped to recover the information lost by the windowing.

5.2.5 Comparison to Semi-analytical Approach

These calculations above show that a fully analytic approach is already very complicated for the simplest lidar set-up when the integration has to be done "by hand". However, to evaluate several more realistic lidar set-ups, a simpler and automated approach is important. For this purpose, a semi-analytic approach is developed to avoid the integration necessary for the derivation of the correlation model. Here, the basic idea is to discretize and linearize the equations where possible before applying the Fourier transformation. Using the linearity property of the Fourier transform, all spectra can be finally calculated by sums and products of wind spectra and coherences.

The determination of the auto-spectrum S_{RR} and the cross-spectrum S_{RL} can be simplified by

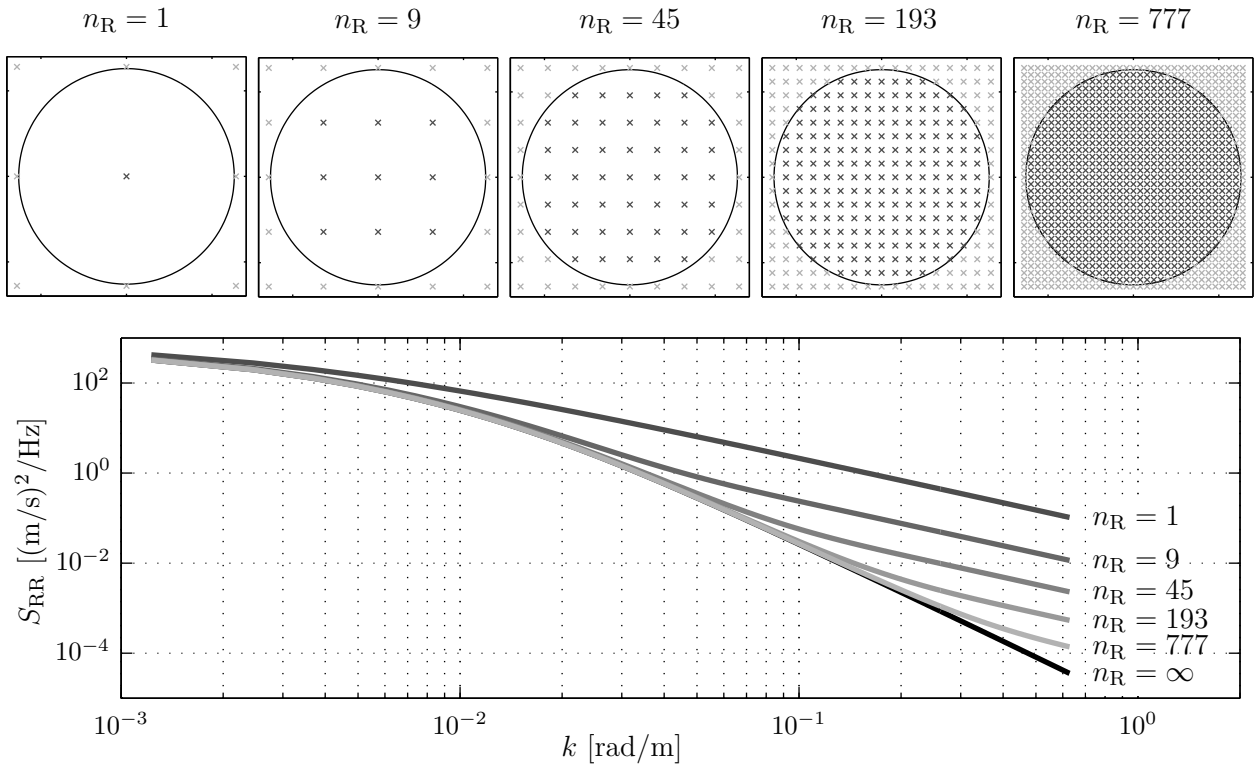

Figure 5.3: Auto-spectrum of the rotor effective wind speed (rotor diameter 126 m) with the analytical model (black) and several semi-analytical models (shades of gray).

using the discrete definition of the rotor effective wind speed (3.20):

$$\begin{aligned} S_\mathrm{RR} &= \mathcal{F}\left\{\frac{1}{n_\mathrm{R}}\sum_{i=1}^{n_\mathrm{R}} u_{i,\mathcal{I}}\right\}\mathcal{F}^*\left\{\frac{1}{n_\mathrm{R}}\sum_{i=1}^{n_\mathrm{R}} u_{i,\mathcal{I}}\right\} &&= \frac{S_{ii,u}}{n_\mathrm{R}^2}\sum_{i=1}^{n_\mathrm{R}}\sum_{j=1}^{n_\mathrm{R}}\gamma_{ij,ur} \\ S_\mathrm{RL} &= \mathcal{F}\left\{\frac{1}{n_\mathrm{R}}\sum_{i=1}^{n_\mathrm{R}} u_{i,\mathcal{I}}\right\}\mathcal{F}^*\left\{u_\mathrm{H}\right\} &&= \frac{S_{ii,u}}{n_\mathrm{R}}\sum_{j=1}^{n_\mathrm{R}}\gamma_{\mathrm{H}j,ur}. \end{aligned} \tag{5.17}$$

The transfer function G_RL and the squared coherence γ^2_RL can be calculated with (5.17) in a straightforward manner and the differences compared to using (5.10) and (5.12) decrease with increasing n_R. In Figure 5.3, Cartesian grids with grid resolutions of 64, 32, 16, 8, and 4 m are used, resulting in averages over $n_\mathrm{R} = 1$, 9, 45, 193, and 777 grid points within the rotor disc. The figure shows that the semi-analytic spectra are approaching the analytic one ($n_\mathrm{R} = \infty$) as the number of grid points increases. The point of divergence from the analytical model to a trend parallel to the single-point-spectrum ($n_\mathrm{R} = 1$) can be roughly doubled by halving the distance between the grid points.

The advantage of the semi-analytic model is that a weighting considering tip and root losses (3.23) can be easily implemented, only slightly increasing the complexity of the model.

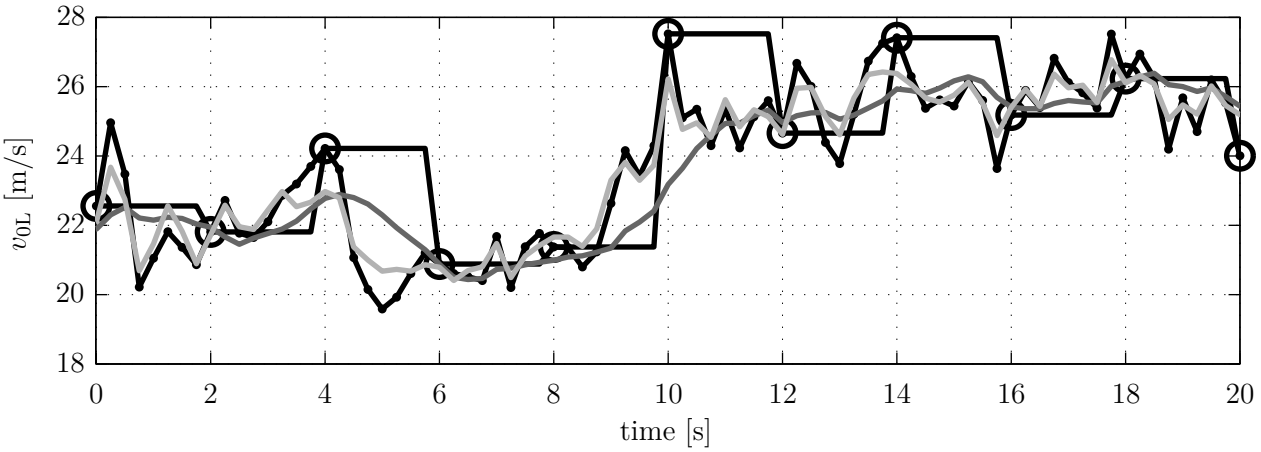

Figure 5.4: Excerpt of lidar simulations (see Section 5.3.1–5.3.3 for details): Staring lidar with point measurement equal to the longitudinal wind speed component (black with dots), staring lidar with point measurement and time averaging (dark gray), staring lidar with spatial averaging due to pulse volume (light gray), and staring lidar with point measurement at discrete times (black with circles).

5.3 Correlation of a Real Scanning Lidar System

For a real scanning lidar system, the following effects are integrated into the semi-analytic model: temporal averaging (Section 5.3.1), spatial averaging (Section 5.3.2), discrete scanning (Section 5.3.3), wind reconstruction (Section 5.3.4), and wind evolution (Section 5.3.5). These effects will make the calculation of the auto-spectrum S_{LL} of the lidar estimate more complex, but the main idea of the approach can still be used: The measured wind can be considered as a sum of signals and due to the linearity of the Fourier transformation, the spectra can be calculated by sums and products of wind spectra and coherences.

In the following subsections, all of the above mentioned effects will be explained separately, and simple examples will be given. The wind speed components are given in the wind ($\mathcal{W}$) coordinate system, where the wind spectra are defined. For each effect (except wind evolution), the analytic model is compared to an estimated spectrum based on the lidar simulator from Section 3.5 scanning a wind field with a time length of 8192 s (for details see Table C.3). An excerpt of these simulations is depicted in Figure 5.4.

The spectrum of a real scanning lidar system is a combination of all these effects.

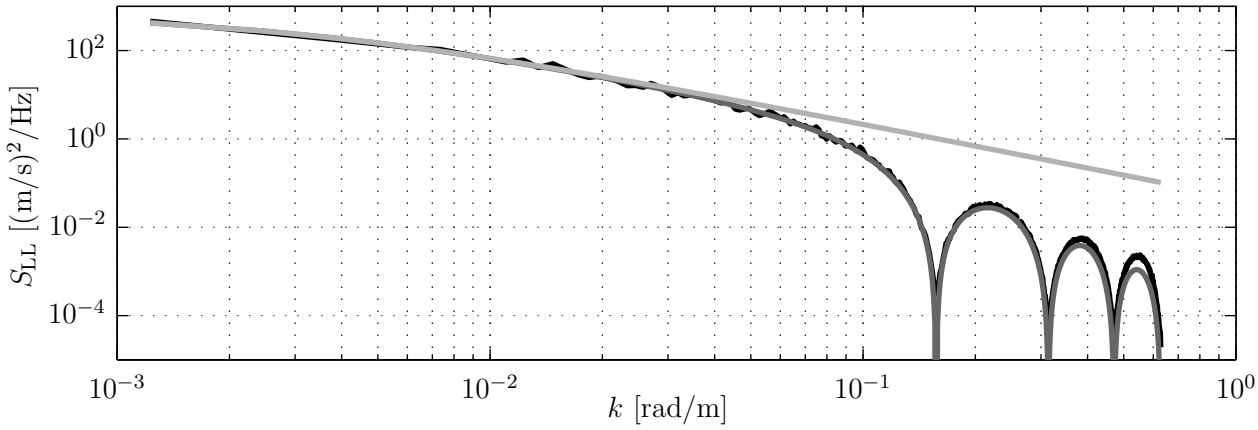

Figure 5.5: Effect of temporal averaging: Auto-spectrum of the longitudinal wind component (light gray) and of the temporal averaged lidar measurement calculated directly with the analytical model (dark gray) and estimated from the signal of the simulation (black).

5.3.1 Temporal Averaging

Lidar systems need to average spectra over a certain time to determine the Doppler frequency shift, see Section 2.3. This can be modeled by a running average. For example, the point measurement of a staring lidar system aligned with the mean wind direction and with measurement acquisition time T_{ACQ} is represented by:

$$\begin{aligned} v_{0\mathrm{L}}(t) &= \int_{-\infty}^{\infty} u_{\mathcal{W}}(\tau)\mathrm{rect}\left(\frac{(t-\tau)-T_{\mathrm{ACQ}}/2}{T_{\mathrm{ACQ}}}\right)\mathrm{d}\tau \\ &= u_{\mathcal{W}}(t) * \mathrm{rect}\left(\frac{t-T_{\mathrm{ACQ}}/2}{T_{\mathrm{ACQ}}}\right), \end{aligned} \tag{5.18}$$

where rect() is the rectangular function defined at time t as

$$\mathrm{rect}(t) = \begin{cases} 1, & |t| \leq \frac{1}{2} \\ 0, & |t| > \frac{1}{2} \end{cases} \tag{5.19}$$

and $*$ denotes convolution, which is translated by the Fourier transformation to a multiplication of the individual Fourier transforms. With the normalized cardinal sine function defined as

$$\mathrm{sinc}(f) = \frac{\sin(\pi f)}{\pi f} \tag{5.20}$$

at the frequency f, the resulting auto-spectrum is

$$S_{\mathrm{LL}} = \mathcal{F}\{v_{0\mathrm{L}}\}\mathcal{F}^*\{v_{0\mathrm{L}}\} = \mathrm{sinc}^2(fT_{\mathrm{ACQ}})S_{ii,u}. \tag{5.21}$$

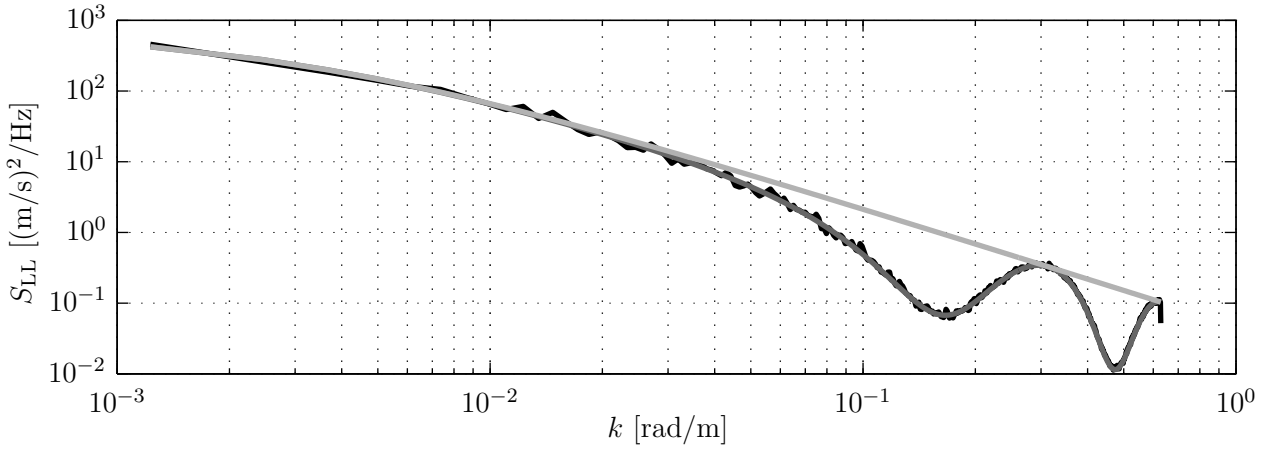

Figure 5.6: Effect of spatial averaging: Auto-spectrum of the longitudinal wind component (light gray) and of the pulsed lidar measurement with a discretized range weighting function calculated directly with the analytical model (dark gray) and estimated from the signal of the simulation (black).

Figure 5.4 shows the effect for a lidar measurement with an acquisition time $T_{\mathrm{ACQ}} = 2\,\mathrm{s}$. The averaged signal (dark gray) is delayed compared to the original one (black with dots) by $T_{\mathrm{ACQ}}/2 = 1\,\mathrm{s}$. The estimated auto-spectrum in Figure 5.5 using Welch's averaged periodogram method agrees well with the calculated auto-spectrum based on (5.21). This validates the overall approach: Instead of the time consuming process of generating wind fields, simulating lidar measurements, and only then estimating the spectra, the proposed method is able to calculate directly the spectra with less computational effort.

5.3.2 Spatial Averaging

Due to the pulse length (for pulsed systems) or the optical focusing (for continuous wave systems) and the data processing, real lidar systems average the wind speeds along the laser beam according to a weighting function f_{RW}, see Section 3.3. For pulsed systems it can be assumed that f_{RW} depends only on the distance a from the measurement point. For continuous wave systems there is an additional dependency on the distance from the lidar. With the weighting function $f_{\mathrm{RW}}(a)$ it is possible to calculate the line-of-sight wind speed of each measurement point i by a spatial integral, see Equation (3.34). With Taylor's Frozen Turbulence Hypothesis this could be translated into an integral over time similar to (4.2) and then the spectrum could be calculated analytically by a convolution with the Fourier transform $\mathcal{F}\{f_{\mathrm{RW}}\}$ of the weighting function similar to (5.21), depending on the wavenumber k. However, here a discretized approach is used that is consistent with the overall semi-analytic approach. For this purpose, the weighting function is evaluated at discrete distances and the spatial separations are treated similar to the time delays of a temporal filter.

If, for example, a discrete weighting function with the values f_{RW1}, f_{RW2}, and f_{RW3} is used for

a staring lidar aligned with the mean wind direction, the measurement can be modeled by

$$v_{0\mathrm{L}} = \frac{f_{\mathrm{RW}1} u_{1,\mathcal{W}} + f_{\mathrm{RW}2} u_{2,\mathcal{W}} + f_{\mathrm{RW}3} u_{3,\mathcal{W}}}{f_{\mathrm{RW}1} + f_{\mathrm{RW}2} + f_{\mathrm{RW}3}}, \tag{5.22}$$

where $u_{1,\mathcal{W}}$, $u_{2,\mathcal{W}}$, and $u_{3,\mathcal{W}}$ are the longitudinal wind at the distances a_1, $a_2 = 0$, and $a_3 = -a_1$ from the measurement point. By treating the spatial shift as a delay in the wavenumber domain similar to a temporal shift, the resulting spectrum is represented with the imaginary unit i:

$$\begin{aligned} S_{\mathrm{LL}} =& \mathcal{F}\{v_{0\mathrm{L}}\}\mathcal{F}^*\{v_{0\mathrm{L}}\} = \frac{S_{ii,u}}{(f_{\mathrm{RW}1} + f_{\mathrm{RW}2} + f_{\mathrm{RW}3})^2} \\ & \big(f_{\mathrm{RW}1}^2 + f_{\mathrm{RW}1} f_{\mathrm{RW}2} \exp(\mathrm{i}ka_1) + f_{\mathrm{RW}1} f_{\mathrm{RW}3} \exp(2\mathrm{i}ka_1) \\ & + f_{\mathrm{RW}2} f_{\mathrm{RW}1} \exp(-\mathrm{i}ka_1) + f_{\mathrm{RW}2}^2 + f_{\mathrm{RW}2} f_{\mathrm{RW}3} \exp(\mathrm{i}ka_1) \\ & + f_{\mathrm{RW}3} f_{\mathrm{RW}1} \exp(-2\mathrm{i}ka_1) + f_{\mathrm{RW}3} f_{\mathrm{RW}2} \exp(-\mathrm{i}ka_1) + f_{\mathrm{RW}3}^2 \big) . \end{aligned} \tag{5.23}$$

Figure 5.4 shows the effect for a lidar measurement with $a_1 = 20\,\mathrm{m}$ and the Gaussian range weighting function (3.37). Due to the mean wind speed of $\bar{u} = 20\,\mathrm{m/s}$, the resulting signal (light gray) is a weighted sum of the original signal (black with dots) at the current time, and at 1 s before and after the current time. Due to the symmetry of the range weighting function, there is no time delay for the spatial averaged signal relative to the original signal, in contrast to the time averaged signal. Again, the estimated spectrum from the signal follows the spectrum from the analytic model in Figure 5.6. If more discretization points for the range weighting function are used, the spectrum will monotonously drop down similar to Figure 4.4, where the spectrum (4.5) is based on the Fourier transform of the range weighting function.

5.3.3 Discrete Scanning

Real lidar systems with only one laser source measuring in different points have to scan sequentially. Thus the lidar measurement in a certain measurement point is only available in certain time points. If the lidar estimate of the rotor effective wind speed is calculated from an average over the last full scan as described in Section 4.3.1, the values of previous time points need to be available at the current time. This can be achieved by buffering the values. Following the considerations in [8] and personal communications with Eric Simley, a staring lidar point measurement evaluating the longitudinal wind component only after each full scan (T_{scan}) and then holding the value, is described by

$$v_{0\mathrm{L}} = \Bigg(u_{\mathcal{W}}(t) \underbrace{\sum_{h=-\infty}^{\infty} \delta(t - hT_{\mathrm{scan}})}_{\Delta(t)} \Bigg) * \mathrm{rect}\left(\frac{t - T_{\mathrm{scan}}/2}{T_{\mathrm{scan}}} \right), \tag{5.24}$$

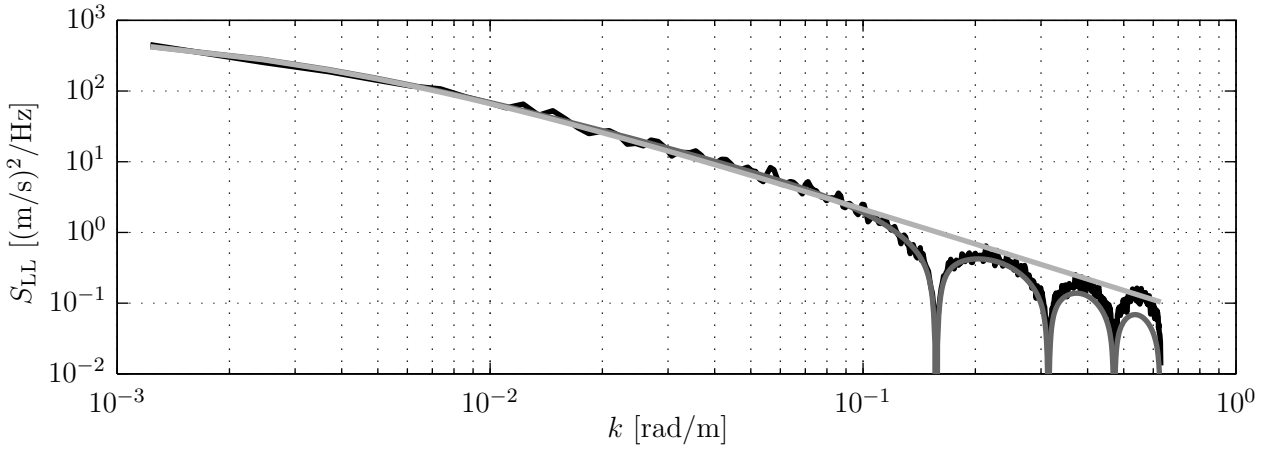

Figure 5.7: Effect of discrete scanning: Auto-spectrum of the longitudinal wind component (light gray) and of the lidar measurement only evaluated at discrete time points calculated directly with the analytical model (dark gray) and estimated from the signal of the simulation (black).

where $\delta()$ is the Dirac delta function with

$$\delta(t) = \begin{cases} \infty, & t = 0 \\ 0, & t \neq 0 \end{cases} \quad \text{with} \int_{-\infty}^{\infty} \delta(t)\mathrm{d}t = 1. \tag{5.25}$$

For each part of the sum, the multiplication of the signal $u_{\mathcal{W}}(t)$ with the Dirac delta function $\delta(t - hT_{\mathrm{scan}})$ yields a signal, which at the time $t = hT_{\mathrm{scan}}$ has the value of $u_{\mathcal{W}}(t)$ at this time multiplied with ∞ and which is zero for all other times. Due to this selective effect, the infinite sum of the Dirac delta functions is denoted as Dirac comb $\Delta(t)$. The convolution with the rectangular function then produces a signal, which holds the value $u_{\mathcal{W}}(hT_{\mathrm{scan}})$ from the time $t = hT_{\mathrm{scan}}$ to $t = hT_{\mathrm{scan}} + T_{\mathrm{scan}}$ due to the unity integral of the Dirac delta function. Finally, the sum generates the signal of a lidar measurement at discrete times while holding the value until the next measurement is performed.
For the analytic model, the following points need to be considered:

- A multiplication is translated by the Fourier transformation into a convolution and a convolution into a multiplication.

- The Fourier transform of the Dirac comb is again a Dirac comb:

$$\mathcal{F}\{\Delta(t)\} = \Delta(f) = \sum_{h=-\infty}^{\infty} \delta\left(f - \frac{h}{T_{\mathrm{scan}}}\right). \tag{5.26}$$

- Since convolution of a function $g(f)$ with a delta function $\delta\left(f - \frac{h}{T_{\mathrm{scan}}}\right)$ corresponds to shifting the function by $\frac{h}{T_{\mathrm{scan}}}$, the convolution with the Dirac comb is equivalent to an

infinite sum of shifted functions:

$$(\Delta * g)(f) = \sum_{h=-\infty}^{\infty} g\left(f - \frac{h}{T_{\text{scan}}}\right). \tag{5.27}$$

- Different frequency components of the signals $u_{\mathcal{W}}$ are uncorrelated [8].

With these considerations, the auto-spectrum for discrete lidar measurements is

$$\begin{aligned} S_{\text{LL}} &= \mathcal{F}\{v_{0\text{L}}\}\mathcal{F}^*\{v_{0\text{L}}\} \\ &= (\mathcal{F}\{u_{\mathcal{W}}\} * \mathcal{F}\{\Delta\})\mathcal{F}\{\text{rect}\}(\mathcal{F}^*\{u_{\mathcal{W}}\} * \mathcal{F}^*\{\Delta\})\mathcal{F}^*\{\text{rect}\} \\ &= \left(\sum_{h=-\infty}^{\infty} \mathcal{F}\{u_{\mathcal{W}}\}\left(f - \frac{h}{T_{\text{scan}}}\right) \sum_{h=-\infty}^{\infty} \mathcal{F}^*\{u_{\mathcal{W}}\}\left(f - \frac{h}{T_{\text{scan}}}\right)\right)(\mathcal{F}\{\text{rect}\}\mathcal{F}^*\{\text{rect}\}) \\ &= \sum_{h=-\infty}^{\infty} S_{ii,u}\left(f - \frac{h}{T_{\text{scan}}}\right)\text{sinc}^2(fT_{\text{scan}}). \end{aligned} \tag{5.28}$$

Figure 5.4 shows the effect for a lidar measurement, where a measurement is taken every $T_{\text{scan}} = 2\,\text{s}$ and held. The resulting signal (black with circles) is thus equivalent to the original signal (black with dots) at multiples of T_{scan}.
Again, the analytic model in Figure 5.7 can reproduce the estimated spectrum. Due to the wind field's discretization time of 0.25 s, the signal is band limited to the Nyquist frequency of $f_{\text{max}} = 2\,\text{Hz}$. Thus in this case, the infinite sum in (5.28) can be limited to those values of h, where $|(f - \frac{h}{T_{\text{scan}}})| \leq f_{\text{max}}$ holds.

5.3.4 Wind Field Reconstruction

If the lidar beam is not perfectly aligned with the mean wind direction, the line-of-sight will be not only determined by the longitudinal wind speed component, but also by the lateral and vertical wind speed components, as described by the lidar point measurement model (3.31).
As discussed in Chapter 4, assumptions are necessary to reconstruct the rotor effective wind speed. The reconstruction method together with measurements not aligned with the mean wind direction yield a distortion of the rotor effective wind speed estimate by the lateral and vertical wind components.
Considering for example a lidar system measuring simultaneously two horizontal points ($z_{\text{n},i,\mathcal{W}} = 0$), the line-of-sight wind speeds are

$$\begin{aligned} v_{\text{los},1} &= x_{\text{n},1,\mathcal{W}}\ u_{1,\mathcal{W}} + y_{\text{n},1,\mathcal{W}}\ v_{1,\mathcal{W}} \\ v_{\text{los},2} &= x_{\text{n},2,\mathcal{W}}\ u_{2,\mathcal{W}} + y_{\text{n},2,\mathcal{W}}\ v_{2,\mathcal{W}}. \end{aligned} \tag{5.29}$$

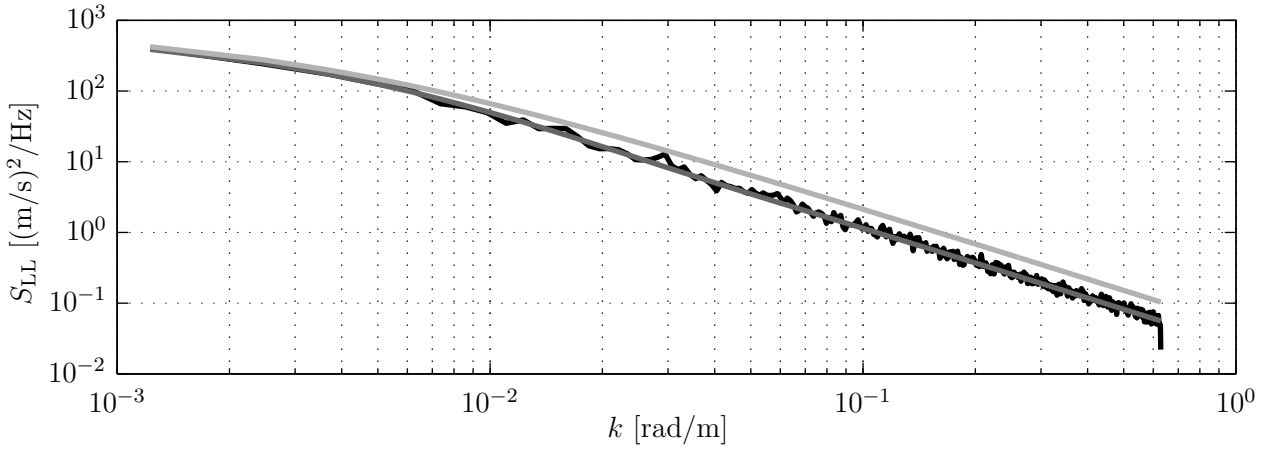

Figure 5.8: Effect of wind reconstruction: Auto-spectrum of the longitudinal wind component (light gray) and a lidar estimate of the rotor effective wind speed from simultaneous measurement of two points based on the analytical model (dark gray) and from a simulation (black).

Assuming that the lidar system is aligned with the mean wind direction, the rotor effective wind speed can be estimated by a mean over both line-of-sight wind speeds corrected by $x_{\mathrm{n},i,\mathcal{W}}$:

$$v_{0\mathrm{L}} = \frac{1}{2}\left(\frac{v_{\mathrm{los},1}}{x_{\mathrm{n},1,\mathcal{W}}} + \frac{v_{\mathrm{los},2}}{x_{\mathrm{n},2,\mathcal{W}}}\right) = \frac{1}{2}\left(u_{1,\mathcal{W}} + \frac{y_{\mathrm{n},1,\mathcal{W}}}{x_{\mathrm{n},1,\mathcal{W}}} v_{1,\mathcal{W}} + u_{2,\mathcal{W}} + \frac{y_{\mathrm{n},2,\mathcal{W}}}{x_{\mathrm{n},2,\mathcal{W}}} v_{2,\mathcal{W}}\right). \tag{5.30}$$

With the coherence $\gamma_{ij,ur}$ from (5.9), the resulting spectrum is

$$S_{\mathrm{LL}} = \frac{1}{4}\left(S_{ii,u}\left(2 + 2\gamma_{ij,ur}\right) + S_{ii,v}\left(\frac{y_{\mathrm{n},1,\mathcal{W}}^2}{x_{\mathrm{n},1,\mathcal{W}}^2} + \frac{y_{\mathrm{n},2,\mathcal{W}}^2}{x_{\mathrm{n},2,\mathcal{W}}^2}\right)\right). \tag{5.31}$$

In Figure 5.8, the spectrum from the analytical model agrees well with the simulation for the two points measured at $x_{1,\mathcal{W}} = x_{2,\mathcal{W}} = 80\,\mathrm{m}$ and $y_{1,\mathcal{W}} = -y_{2,\mathcal{W}} = 20\,\mathrm{m}$.

5.3.5 Wind Evolution

Wind evolution is considered here by the simple exponential model of coherence $\gamma_{ij,ux}$ (2.22). If, for example, a second point at $\Delta x_{ij,\mathcal{W}}$ downwind is added to the perfect staring lidar system (5.4), the rotor effective wind speed estimate can be calculated by shifting the measurement downwind in time considering Taylor's Frozen Turbulence Hypothesis:

$$v_{0\mathrm{L}} = \frac{1}{2}\left(u_{1,\mathcal{W}}(t) + u_{2,\mathcal{W}}(t - \Delta x_{ij,\mathcal{W}}/\bar{u})\right). \tag{5.32}$$

Due to wind evolution, the resulting spectrum is

$$S_{\mathrm{LL}} = \frac{1}{4} S_{ii,u}\left(2 + 2\gamma_{ij,ux}\right). \tag{5.33}$$

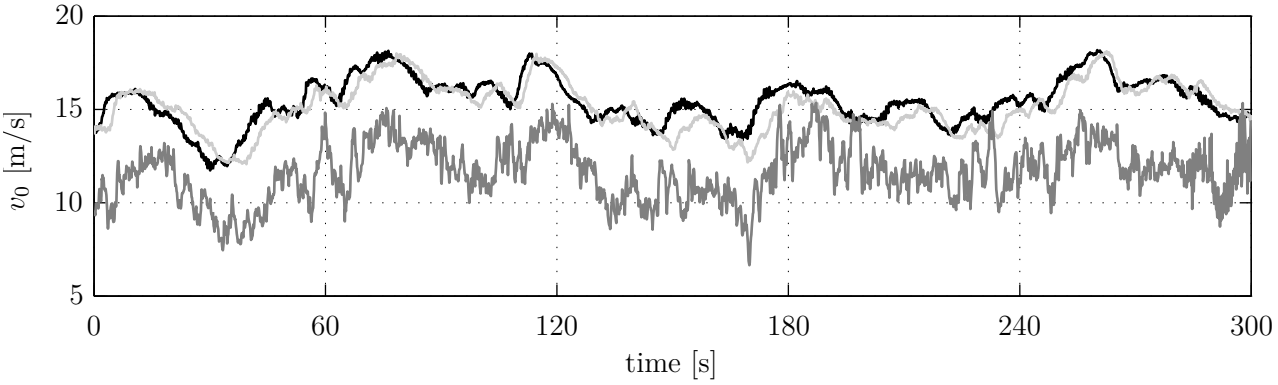

Figure 5.9: Wind speed from the nacelle anemometer (dark gray) and rotor effective wind speed estimates from the CART2 (light gray) and the scanning lidar system (black).

5.4 Evaluation with Real Data

The analytic and the semi-analytic model are both evaluated with real data from the field testing of lidar-assisted control. Here, a scanning lidar system from the University of Stuttgart was installed at the National Wind Technology Center on the nacelle of the Controls Advanced Research Turbine, 2-bladed (CART2) with a rotor diameter of $D = 42.7\,\mathrm{m}$ and a hub height of 36.8 m.

The signals necessary for this correlation study are obtained from lidar and turbine data, see Appendix A.1 for more details. The rotor effective wind speed v_0 is estimated from measured turbine data by the nonlinear estimator from Section 3.2.5 and estimated from the lidar data using the dynamic wind field reconstruction from Section 4.3. For the lidar system a circular trajectory with $n_\mathrm{P} = 6$ focus points in $n_\mathrm{D} = 5$ focus distances equally distributed between $1D$ and $2D$ and a scan time of $T_\mathrm{scan} = 1.33\,\mathrm{s}$ was used. Figure 5.9 shows both signals from the considered 5 min period together with the wind speed measured with the anemometer on the nacelle. The lidar provides a preview signal which coincides with the wind speed estimate from the turbine for low frequencies. The anemometer measures a lower wind speed due to its position behind the rotor, which extracts energy from the wind. With the comparison between the analytic and semi-analytic model, it can be confirmed that the lack of correlation for high frequencies is caused by the combination of the effects described in Section 5.3.

Here, the correlation is compared with respect to the transfer function, which will be used later in Section 5.5 to design filters to filter out uncorrelated frequencies.

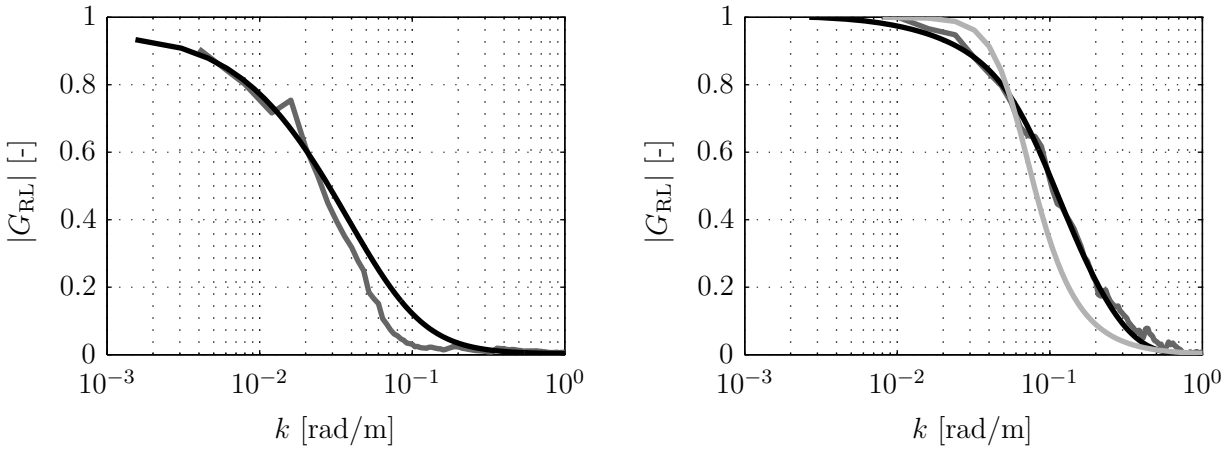

Figure 5.10: Transfer function of the nacelle anemometer (left) and the scanning lidar system (right) to the CART2: From model (black) and from estimation (dark gray). Fitted filter (light gray).

5.4.1 Evaluation of the Analytic Model

The analytic model for a perfect scanning lidar is calculated based on the equations (5.5), (5.10) and (5.12) for the auto- and cross-spectra using the rotor diameter $D = 42.7\,\mathrm{m}$.
The analytic model cannot be evaluated with a real lidar system, because wind evolution and volume measurement will be always present. Therefore, the signal of an anemometer installed on the nacelle is used. The transfer function between the wind speed measured by the anemometer and the rotor effective wind speed from turbine data is estimated using Welch's averaged periodogram method as described in Section 5.2 using overlapping Hamming windows. Although the estimation process is very sensitive due to the small amount of available data, Figure 5.10 (left) shows that the estimated transfer function fits quite well to the analytic transfer function. The maximum coherent wavenumber $\hat{k}$ defined at $-3\,\mathrm{dB}$ of this setup is $0.018\,\mathrm{rad/m}$.

5.4.2 Evaluation of the Semi-Analytic Model

For the semi-analytic model, the auto-spectrum S_{RR} of the rotor effective wind speed v_0 is obtained from (5.17) by averaging over the longitudinal wind components in $n_{\mathrm{R}} = 357$ points distributed equally over the rotor area with 2 m separation. The separation distance is chosen as a compromise between accuracy and computational effort.
The auto-spectrum S_{LL} of the scanning lidar is calculated using the equations from Section 5.3. The volume measurement of the pulsed lidar system is considered by a Gaussian shape weighting function (3.37) discretized at $n_{\mathrm{RW}} = 5$ equally distributed points with a distance of 10 m. The weighting function in this case is beneficial for the determination of the rotor effective wind speed, because more information is collected over the rotor disk. Furthermore, the dimensionless longitudinal decay parameter $\alpha_{ux} = 0.4$ is roughly estimated with a staring lidar system

measuring from a wind turbine based on [67]. The modeled S_{LL} is calculated by a sum of spectra arising from the combinations of the Fourier transforms from $3n_{\mathrm{P}}n_{\mathrm{D}}n_{\mathrm{RW}} = 450$ signals of the u, v and w wind speed components in $v_{0\mathrm{L}}$. Note that most of the combinations do not contribute to S_{LL}, since in the wind turbulence model used, coherence is only defined for the longitudinal component.

The cross-spectrum S_{RL} is then calculated by a combination of the Fourier transforms of the 357 longitudinal wind speed components from v_0 and the 150 longitudinal wind components from $v_{0\mathrm{L}}$.

Figure 5.10 (right) shows good agreement with the data. Similar agreement on a lower coherence level was achieved in field testing with a commercial lidar system and the CART3 [88]. Based on this model, a filter depending on the mean wind speed $\bar{u}$ was fitted with a maximum coherent wavenumber of $\hat{k} = 0.06\,\mathrm{rad/m}$. This filter will be further explained in Section 5.5.

5.5 Adaptive Filter Design

As mentioned in the introduction (Chapter 1), the approach taken in this work is to design lidar-assisted controllers assuming perfect knowledge of the incoming wind characteristics, addressing a pure control problem. The goal of the wind estimation process is then to provide signals as close as possible to the disturbances experienced by the turbine. In a first step of this estimation process, the methods presented in Chapter 4 reconstruct characteristics of the wind field such as wind speed, shears and direction from the line-of-sight wind speeds of a lidar system. However, the reconstructed wind characteristics only carry a limited information of the ones arriving at the rotor due to several effects described above. In general, only low frequencies can be well captured by lidar systems. Thus, in a second step all uncorrelated frequencies need to be filtered out to avoid wrong and harmful control action. Additionally, the information is available ahead in time and needs to be synchronized with the disturbance impact on the rotor. Both tasks (filtering and timing) are performed by the adaptive filter presented in this section. This section in mainly based on [89].

5.5.1 Fitting the Magnitude

The transfer function G_{RL} describes the relationship between the lidar estimate of the rotor effective wind speed $v_{0\mathrm{L}}$ and the real rotor effective wind speed v_0. Thus, a filter perfectly fitting to the transfer function G_{RL} would perfectly match $v_{0\mathrm{L}}$ to v_0. Due to the limited DOF, continuous standard filters such as a Butterworth filter are not able to perfectly fit an arbitrary transfer function G_{RL}. The filter design is also hindered by the fact that the transfer function will change for a given lidar scan trajectory: For most of the effects explained above, the resulting transfer function is parametrized by the wavenumber k and thus changes with mean wind speed $\bar{u}$. Additionally, the wind evolution is likely to depend on more external conditions such as atmospheric stability. In [9] a filter is calculated, which corresponds to a discretized transfer function in an optimal way. Thus, such an optimal filter adjusted to the current mean wind speed and external conditions should provide the best solution.

In this work a different approach is proposed: Due to its simplicity in implementation, a Butterworth filter is fitted to the magnitude of the transfer function G_{RL} for a given mean wind speed. The filter coefficients are then adjusted online for changing mean wind speeds.

The fit to the Butterworth filter is done by the following procedure: First, the transfer function $G_{\mathrm{RL}}(k)$ is calculated for a given turbine and lidar configuration with the analytical model and a mean wind speed $\bar{u}$ above rated wind speed. Alternatively, $G_{\mathrm{RL}}(k)$ can be obtained from lidar and turbine data. In a next step, the maximum coherent wavenumber $\hat{k}$ defined at $-3\,\mathrm{dB}$ ≈ 0.7 below the static value is determined from the transfer function G_{RL}. Then, depending

on which fits better to G_{RL}, a first or second-order Butterworth filter is chosen

$$G_{\mathrm{filter}}(s) = \frac{\omega_{\mathrm{cutoff}}}{s + \omega_{\mathrm{cutoff}}} \text{ or } G_{\mathrm{filter}}(s) = \frac{\omega_{\mathrm{cutoff}}^2}{s^2 + s\sqrt{2}\omega_{\mathrm{cutoff}} + \omega_{\mathrm{cutoff}}^2}, \tag{5.34}$$

where the cut-off-frequency is calculated by

$$\omega_{\mathrm{cutoff}} = 2\pi f_{\mathrm{cutoff}} = \hat{k}\bar{u}. \tag{5.35}$$

Figure 5.10 shows additionally a second-order filter fitted to the correlation model for the SWE scanning lidar system and the CART2. This filter can be directly used for simulation, since the mean wind speed is determined by the chosen wind field. Thus, the filter parameter will be calculated prior to the simulation for a given mean wind speed and stay constant during the simulation.
However, the mean wind speed changes on real applications and thus the filter is discretized, such that the filter parameter can be adjusted online in a discrete control system. This is done by "Tustin's method" [90]. For the first-order filter

$$G_{\mathrm{filter}}(z) = \frac{b_0 + b_1 z^{-1}}{a_0 + a_1 z^{-1}} \tag{5.36}$$

the filter coefficients are calculated by

$$\begin{aligned} b_0 &= \omega_{\mathrm{cutoff}} & a_0 &= \omega_{\mathrm{cutoff}} + \frac{2}{\Delta t} \\ b_1 &= \omega_{\mathrm{cutoff}} & a_1 &= \omega_{\mathrm{cutoff}} - \frac{2}{\Delta t}. \end{aligned} \tag{5.37}$$

For the second-order filter

$$G_{\mathrm{filter}}(z) = \frac{b_0 + b_1 z^{-1} + b_2 z^{-2}}{a_0 + a_1 z^{-1} + a_2 z^{-2}} \tag{5.38}$$

the filter coefficients are calculated by

$$\begin{aligned} b_0 &= (\omega_{\mathrm{cutoff}}\Delta t)^2 & a_0 &= (\omega_{\mathrm{cutoff}}\Delta t)^2 + 2\sqrt{2}\omega_{\mathrm{cutoff}}\Delta t + 4 \\ b_1 &= 2(\omega_{\mathrm{cutoff}}\Delta t)^2 & a_1 &= 2(\omega_{\mathrm{cutoff}}\Delta t)^2 - 8 \\ b_2 &= (\omega_{\mathrm{cutoff}}\Delta t)^2 & a_2 &= (\omega_{\mathrm{cutoff}}\Delta t)^2 - 2\sqrt{2}\omega_{\mathrm{cutoff}}\Delta t + 4. \end{aligned} \tag{5.39}$$

These simple equations can be implemented easily on real hardware and can in principle deal with changes in the mean wind speed $\bar{u}$ and the maximum coherent wavenumber $\hat{k}$. For details, see Section 6.4.
In addition to the fit of the magnitude, the timing needs to be corrected (see Section 5.5.2).

5.5.2 Adjusting the Phase

Due to the lidar measurement in front of the rotor, the wind information is in principle available with a certain preview time. How much preview is necessary to improve the control performance depends on the used controller: For the collective pitch feedforward controller (Chapter 6), the filtered signal of the rotor effective wind speed has to be transfered to the control system only with a small preview time τ before the wind reaches the turbine to compensate the pitch actuator dynamics. The direct speed controller presented in Chapter 7 needs no preview at all. Other control strategies such as nonlinear model predictive control ([29]) can incorporate longer previews. Therefore, the filtered signal has to be synchronized with the wind reaching the rotor plane with an adaptive buffer time T_{buffer}, see Figure 4.17, to provide the necessary preview time τ considering all delaying effects.
The corresponding buffer time is obtained from the following considerations: All measurement distances $v_{0\text{L},j}$ are shifted to the first one by (4.39) and then averaged. With Taylor's Frozen Turbulence Hypothesis, the wind travels during the time T_{Taylor} from the first measurement distance to the turbine. The averaged signal is filtered and thus retarded by the filter delay T_{filter}. Additionally, all $v_{0\text{L},j}$ are delayed by $T_{\text{scan}}/2$ due to the averaging over the full trajectory. Thus, the buffer time is calculated by

$$T_{\text{buffer}} = T_{\text{Taylor}} - \frac{1}{2}T_{\text{scan}} - T_{\text{filter}} - \tau. \tag{5.40}$$

The Butterworth filter described above has nonlinear phase and thus frequency-dependent time delays. Here, two methods are presented to calculate the delay introduced by these filters:

1. The filter delay T_{filter} can be approximated by the time delay of the filters at a certain frequency $\omega_{\text{delay}} = 2\pi f_{\text{delay}}$. For the first-order filter this is calculated by

$$T_{\text{filter}} = \frac{\arctan(\omega_{\text{n}})}{\omega_{\text{delay}}} \text{ with } \omega_{\text{n}} = \frac{\omega_{\text{delay}}}{\omega_{\text{cutoff}}}. \tag{5.41}$$

   For the second-order Butterworth filter, the filter delay is

$$T_{\text{filter}} = \frac{\arctan(\frac{\sqrt{2}\omega_{\text{n}}}{1-\omega_{\text{n}}^2})}{\omega_{\text{delay}}}. \tag{5.42}$$

   The frequency is then chosen close to the relevant frequency for the lidar-assisted control approach. This method was used during the field testing of collective pitch feedforward control (see Section 6.4). During this campaign, the peak frequency of the rotor speed spectra $f_{\text{delay}} = 0.1\,\text{Hz}$ was chosen, since the main intention of the feedforward controller was to minimize the rotor speed variation. This method is independent of the filtered signal and easy to implement online for changing mean wind speed, but neglects that

frequencies other than f_{delay} are delayed with different delay times.

2. The second method calculates the overall delay of the signal based on its auto-spectrum. The overall delay is defined as the peak of the cross-correlation. For this purpose, the lidar estimate of the rotor effective wind speed $v_{0\text{L}}$ is considered as a finite sum of sinusoids for n_{F} discrete frequencies f_i with a discretization of Δf. Since the auto-spectrum S_{LL} in each f_i is known, all possible $v_{0\text{L}}$ are represented by

$$v_{0\text{L}} = \bar{u} + \sum_{i=1}^{n_{\text{F}}} a_i \sin(2\pi f_i t + \Phi_i), \tag{5.43}$$

where Φ_i is the phase angle of the sinusoid i and

$$a_i = \sqrt{2\Delta f S_{\text{LL}}(f_i)} \tag{5.44}$$

is the amplitude. If $v_{0\text{L}}$ is filtered by the first-order low pass filter (5.34), then the filtered signal is again a finite sum of sinusoids

$$v_{0\text{L,f}} = \bar{u} + \sum_{i=1}^{n_{\text{F}}} a_{\text{f},i} \sin(2\pi f_i (t - \Delta t_{\text{f},i}) + \Phi_i), \tag{5.45}$$

where the modified amplitude $a_{\text{f},i}$ and the time shift $\Delta t_{\text{f},i}$ for the ith sinusoid are

$$\begin{aligned} a_{\text{f},i} &= \frac{a_i}{\sqrt{1 + \left(\frac{f_i}{f_{\text{cutoff}}}\right)^2}} \\ \Delta t_{\text{f},i} &= \frac{\arctan(\frac{f_i}{f_{\text{cutoff}}})}{2\pi f_i} \end{aligned} \tag{5.46}$$

From these considerations, the cross-correlation $R_{\text{LL,f}}$ between $v_{0\text{L}}$ and $v_{0\text{L,f}}$ can then be calculated over the time τ_{f} independently of the phase angles Φ_i by

$$\begin{aligned} R_{\text{LL,f}}(\tau_{\text{f}}) &= \lim_{T\to\infty} \frac{1}{T} \int_0^T v_{0\text{L}}(t) v_{0\text{L,f}}(t + \tau_{\text{f}}) \, \mathrm{d}t \\ &= \sum_{i=1}^{n_{\text{F}}} \frac{a_{\text{f},i} \; a_i}{2} \cos(2\pi f_i (\tau_{\text{f}} - \Delta t_{\text{f},i})). \end{aligned} \tag{5.47}$$

Thus, for each auto-spectrum S_{LL} and each cutoff frequency f_{cutoff}, the filter delay T_{filter} can be found as the time to the peak of the cross-correlation $R_{\text{LL,f}}$, which is a simple sum of time-shifted cosines with variable amplitudes. This method is used in this work for the simulations.

5.6 Lidar System Optimization

For lidar systems used for control it is crucial to provide a signal of the rotor effective wind, which is on the one hand sufficiently correlated to the wind speed affecting the turbine to improve the control performance. On the other hand, the signals must be provided with enough preview to filter out the uncorrelated frequencies which will cause unnecessary control action, inducing undesired loads.
However, there are several interacting effects which determine how well the wind speed is predicted. The approach presented above models the correlation between lidar systems and wind turbines using Kaimal wind spectra. The derived model accounts for different measurement configurations and spatial averaging of the lidar system, different rotor sizes, and wind evolution.
One of the advantages of the correlation model is that the correlation can be calculated directly with relatively low computational effort. This can be exploited to optimize the scan configuration of lidar systems by simply calculating the correlation for several scan parameters and then choosing the best. In principle, nonlinear solvers could be applied to this optimization problem to converge faster and closer to the optimum. Here, a brute force optimization is done to display the impact of all variables.
In this section, a scan trajectory of the SWE scanning lidar system (see Appendix B for details) is optimized for measuring the rotor effective wind speed from the nacelle of the NREL 5 MW Reference wind turbine (see Appendix C.1 for details). The optimal trajectory will then be used in the remainder of this work. First, the optimization problem is set up in Section 5.6.1 and then the results are presented in Section 5.6.2.

5.6.1 Constrained Optimization Problem

An optimization problem consists typically of a cost function (what should be optimized), optimization variables (which parameter can be changed), and constraints (which conditions have to be fulfilled).
In the case of finding an optimal configuration for a lidar system, the cost function depends on the application. In this case, the lidar system should provide a signal of the rotor effective wind speed for collective pitch feedforward control, which is correlated to the rotor effective wind speed felt by the turbine in an optimal sense. This trajectory will be also used for the simulations for the other controllers for the sake of simplicity and consistency, although other trajectories might be better suited.
There are several possibilities, how to define the “optimal sense”. Measures in the time domain such as the mean square error proposed by [9] or the correlation coefficient proposed by Fiona Dunne in personal communication are very useful measures under simulation conditions. Those

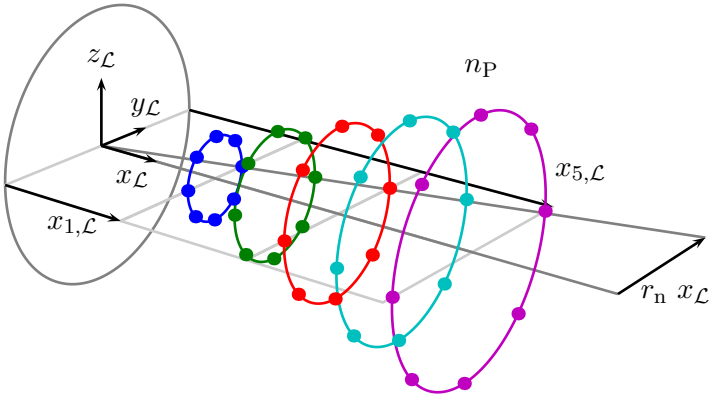

Figure 5.11: Variables for the trajectory optimization.

measures are also simple to determine from field testing data. However, they sum up effects over all frequencies. This is problematic, because real signals of the rotor effective wind speed estimated from turbine or lidar data often differ from simulated ones in that real signals include noise from the measurements or the lidar movements. With frequency-based measures one can focus on the relevant frequency range and thus avoid these effects. But frequency-based measures are unfavorably more difficult to determine. In [85], the maximum coherent wavenumber is proposed, defined by the pole location of a first-order low-pass filter whose magnitude best fits the transfer function G_RL. However, less filtering does not automatically lead to better correlation. Better suited is a certain level of the magnitude squared coherence as proposed in [67] and [10], where it is named "coherence bandwidth". Here, the coherence bandwidth is used as the measure of optimality and is defined as the wavenumber $k_{0.5}$, where the magnitude squared coherence γ^2_RL reaches the level of 0.5.
The choice of the optimization variables depends on the flexibility of the lidar system. In the case of the SWE scanning lidar system, a circular trajectory has been chosen due to simplicity and is parametrized by the following variables, see Figure 5.11:

- n_P: number of points on a circle
- r_n: radius of the circle normalized by its distance from the rotor
- $x_{1,\mathcal{L}}$: position of the first circle

The constraints in the present optimization problem can be divided into constraints of the lidar system itself and constraints from the requirements from the applications. The constraints for the SWE scanning lidar system are:

- Due to mechanical constraints, the radius r_n has to be between 0 and 0.5 (corresponding to the range of 0 deg to 26.6 deg).
- The acquisition time is chosen to $T_\mathrm{ACQ} = 0.2\,\mathrm{s}$ and thus the scan time is $T_\mathrm{scan} = n_\mathrm{P} T_\mathrm{ACQ}$.

- Based on the experience gathered during the testing of the SWE scanning lidar system in Bremerhaven (see [53] for more details), this acquisition time allows measurements up to $1.5\,D = 189\,\mathrm{m}$. Since the trajectory will be used for simulations, where wind evolution is not included, larger distances will be beneficial for the trajectory to minimize the cross-contamination effect from the lateral and vertical wind speed components. Thus, for this trajectory optimization the last distance is fixed to $x_{5,\mathcal{L}} = 1.5\,D$.

- The lidar system is unable to measure at ranges much shorter than 40 m. Therefore, for the minimum measurement distance $x_{1,\mathcal{L}}$ is limited to $0.3\,D = 37.8\,\mathrm{m}$.

Apart from these lidar-system-specific constraints, controller-specific requirements need to be fulfilled as well. For the collective pitch feedforward controller, the filtered signal of the rotor effective wind speed has to be transferred to the control system only with a small prediction time τ before the wind reaches the turbine to compensate the pitch actuator dynamics. For the used NREL 5 MW reference wind turbine this is $\tau = 0.2\,\mathrm{s}$. In order to provide the signal in time, the buffer time (5.40) needs to be non-negative. The maximum coherent wavenumber $\hat{k}$ and the corresponding T_{buffer} can be determined for each setting of the optimization variables and a given mean wind speed $\bar{u}$.
Finally, the optimization problem can be formulated:

$$\begin{aligned} \max_{n_\mathrm{P}, r_\mathrm{n}, x_{1,\mathcal{L}}} \quad & k_{0.5} \\ \text{such that: } & T_{\mathrm{buffer}} \geq 0 \\ & 0.5 \geq r_\mathrm{n} \geq 0 \\ & x_{1,\mathcal{L}} \geq 0.3\,D \\ & x_{5,\mathcal{L}} = 1.5\,D \\ & T_{\mathrm{scan}} = n_\mathrm{P} T_{\mathrm{ACQ}}. \end{aligned} \tag{5.48}$$

5.6.2 Optimal Trajectory

The optimization problem (5.48) can be solved with solvers for nonlinear problems. Here, a brute force optimization is done to display the impact of all variables.
The coherence bandwidth $k_{0.5}$ and the buffer time T_{buffer} are calculated for the following variations, see Figure 5.12 and 5.13 (each grid point represents a set of variables):

- The number of points n_P is set to 4, 8, and 12.

- The radius r_n is chosen from 0.2 to 0.4 in steps of 0.05.

- The first distance $x_{1,\mathcal{L}}$ varies from $0.3\,D$ to $0.7\,D$ in steps of $0.1\,D$.

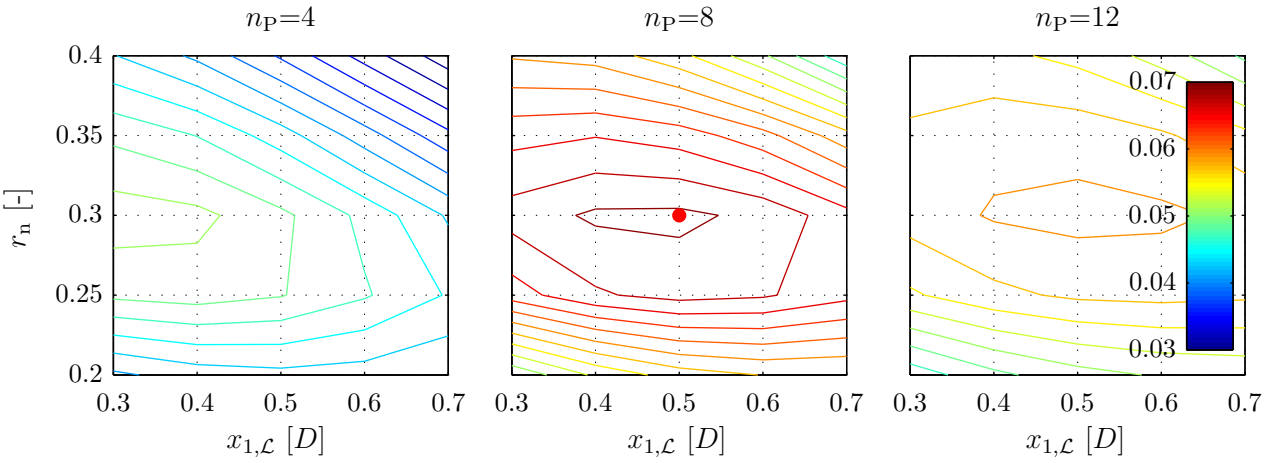

Figure 5.12: Coherence bandwidth as a function of optimization variables. Optimal solution (•).

In total, 75 different setups are evaluated. For all calculations, the following additional parameters are used:

- The prediction time is chosen as $\tau = 0.2\,\mathrm{s}$ (see considerations in previous subsection).
- A spacing of 4 m is used for the Cartesian grid to calculate S_{RR} and S_{RL}.
- Tip and root losses are considered in S_{RR} and S_{RL} linearly as in (3.23).
- All coherences, auto- and cross-spectra are calculated for $n_{\mathrm{F}} = 512$ frequencies with a discretization of $\Delta f = \frac{1}{256}$ Hz.
- A mean wind speed of $\bar{u} = 20\,\mathrm{m/s}$ is chosen.
- A first-order filter is chosen, since it fits better at lower frequencies compared to the second-order filter.

Only focusing on the coherence bandwidth in Figure 5.12, the optimal setup (•) is the circle with 8 measurement points, a normalized radius of 0.3 (corresponding to a half opening angle of 16.7 deg), and the first distance $x_{1,\mathcal{L}}$ at $0.5D = 63\,\mathrm{m}$. For the constrained optimization, only the buffer time needs to be non-negative to provide enough time for filtering. The other constraints are fulfilled by choosing the optimization variables. Since the buffer time in Figure 5.13 for this setup is $T_{\mathrm{buffer}} = 1.65\,\mathrm{s}$, it fulfills all constraints. This scan configuration is displayed in Figure 5.11. Figure 5.14 shows the auto-spectrum of the optimal scan. The analytic spectrum fits well to the one obtained from a simulation with the wind field and lidar simulator used in Section 5.3. This confirms that the analytic correlation model is able to reproduce complex scan patterns. Similar good agreement is achieved for the coherence and the transfer function as shown in Figure 5.15.
The optimal scan trajectory and the first-order filter with $\hat{k} = 0.07\,\mathrm{rad/m}$ will be used for the simulations in the next chapters.

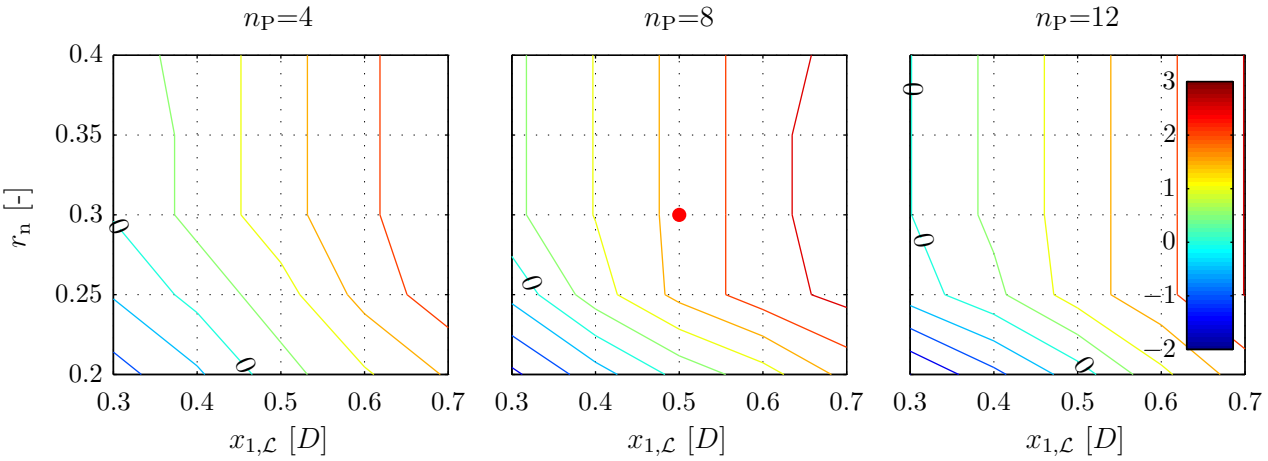

Figure 5.13: Buffer time as a function of optimization variables. Optimal solution (●).

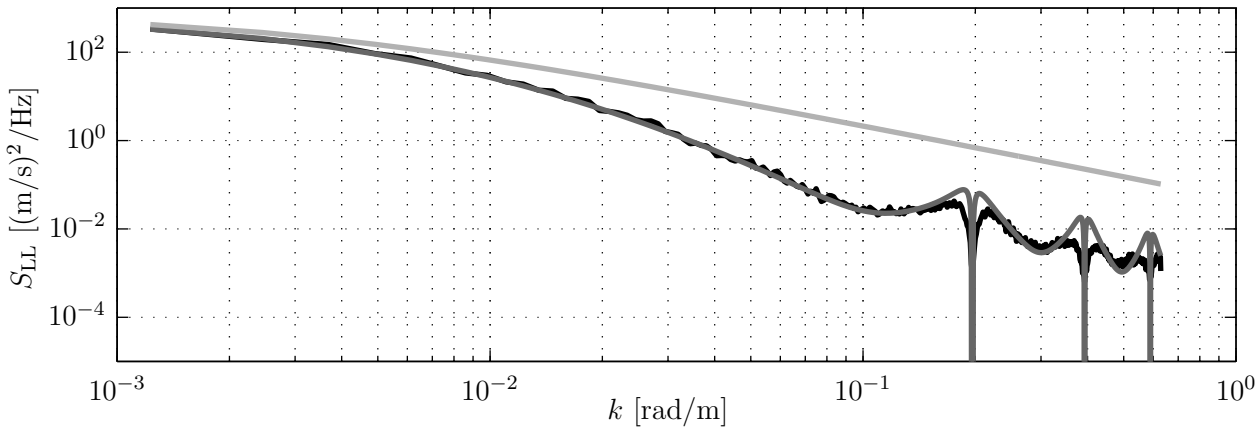

Figure 5.14: Auto-spectrum of the longitudinal wind component (light gray) and a lidar estimate of the rotor effective wind speed from the optimized trajectory based on the analytical model (dark gray) and from a simulation (black).

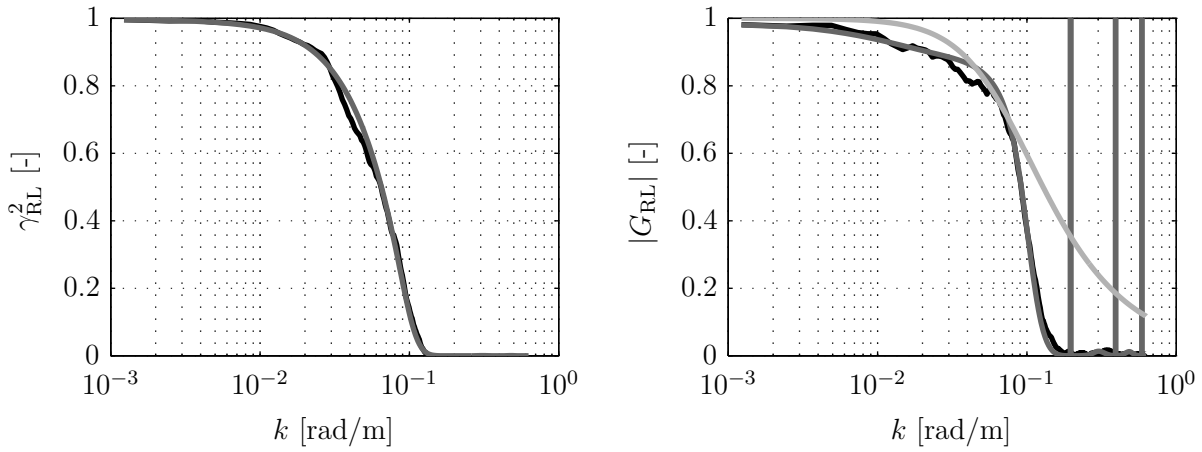

Figure 5.15: Coherence (left) and transfer function (right) between the lidar estimate of the rotor effective wind speed and the real rotor effective wind speed: based on the analytical model (dark gray) and from a simulation (black). Fitted filter (light gray).

5.7 Summary and Possible Extensions of the Correlation Model

This chapter presents a model to estimate the correlation of the rotor effective wind speed between a lidar system and a wind turbine, considering different rotor diameters, spatial averaging, different scanning patterns and wind evolution, which are responsible in combination for the level of correlation.
Each effect is verified by simulated lidar measurements and the full model is evaluated with data from a field testing campaign. The modeled and measured coherence show very good agreement.
The derived model is modular and all changes can be applied in a straightforward manner which makes it usable for following applications:

1. The correlation of real or simulated lidar measurements can be checked. With the model, a measurement problem could be identified in the field testing presented in Section 6.4, since the correlation was below the one calculated with the correlation model.

2. The correlation model can be used to optimize the configuration or scan pattern of lidar systems by formulating and solving a constrained optimization problem. The scan configuration is optimized such that it provides a wind speed signal, which on the one hand exhibits a high correlation to the wind speed affecting the turbine in order to improve the control performance. On the other hand, the problem considers that the signal needs to be transfered to the control system with enough preview to filter out the uncorrelated frequencies, which have negative impacts on structural loads. As a measure of the correlation, the coherence bandwidth is used, which is the wavenumber, where the magnitude squared coherence decreases to a value of 0.5. This is done in this chapter for the SWE scanning lidar system and the 5 MW reference wind turbine. The optimal scan configuration is used for the simulations performed in this work.

3. With the correlation model an adaptive filter can be designed, which filters out all uncorrelated frequencies for a given rotor diameter and a given lidar system. In this chapter, the filter is designed for the previously optimized scan and will be used to provide a feedforward signal for the controllers in this work.

The model was in principle developed to be able to test the lidar assisted collective pitch control on a real turbine. The model could be extended in future work in the following ways:

- For lidar-assisted individual pitch control, an estimation of either the blade effective wind speeds or the linear vertical and horizontal shears is necessary. Further work should be done to apply the correlation models to shear estimates, to be able to optimize scan patterns, and to design corresponding filters. A correlation model for the blade effective wind speed has been presented in [8].

- The adaptive filter in its current state is only changing online with changing mean wind speed. The maximum coherent wavenumber is determined either by a correlation study or by calculations using the presented correlation model. To guarantee a safe operation under changing lidar measurement quality or other effects changing the correlation, the filter needs to be adapted also online to the current correlation. Initial work in this field has been presented in [91].

- In this work the Kaimal spectra model is used, which has the advantage of simplicity. However, no coherence is defined for the lateral and vertical wind speed components. Using more realistic models might be worth considering, although this will increase the computational effort.

- In a similar way, using more sophisticated wind evolution models considering for example atmospheric stability would make the results even more realistic.

- Recent advances in wind field reconstruction use dynamic wind models and advanced estimation techniques [84, 5]. However, including these methods into the presented correlation model might be very complicated. Future investigation could try to incorporate wind reconstruction and adaptive filtering in one single algorithm similar to the Kalman filter, which is often used for estimation of dynamic systems based on noisy data.

6

Collective Pitch Feedforward Control

The collective pitch feedforward controller is the most promising approach of all lidar-assisted controllers presented in this thesis due to its potential, robustness, and simplicity of implementation. The approach is based on the work in [89, 92, 83]. Related work in this field can generally be divided into complex linear controllers derived from linearized wind turbine models and simpler, but nonlinear feedforward controllers. In [11, 12] several model inverse controllers are proposed. In [17], several linear controllers such as a filtered-x recursive least squares, linear-quadratic, and $\mathcal{H}_\infty$ are designed and tested. These linear controllers are designed in general at one linearization point and for perfect wind preview and will not cancel out all wind speed changes over the entire full load region. However, more advanced linear feedforward controllers such as the $\mathcal{H}_2$ approach in [18] have the advantage that the measurement uncertainties can be directly included in the control design. Contrary to these controllers, the approach proposed in this work is based on a reduced nonlinear model and adds a feedforward update to a baseline collective pitch controller. It is designed for the entire full load region and is able to almost perfectly cancel out the wind disturbance to the rotor speed assuming perfect wind preview. It is combined with an adaptive filter, if used with simulated lidar measurements or in real applications. Similar controllers have been proposed in [21] and [22].

This chapter is organized as follows: In Section 6.1 the lidar-assisted collective pitch feedforward controller is derived. The controller is then evaluated by simulations using perfect wind preview and simulated lidar measurements in Section 6.2 and 6.3. A proof of concept from a field test is given in Section 6.4. Finally, a summary and possible extensions are presented in Section 6.5.

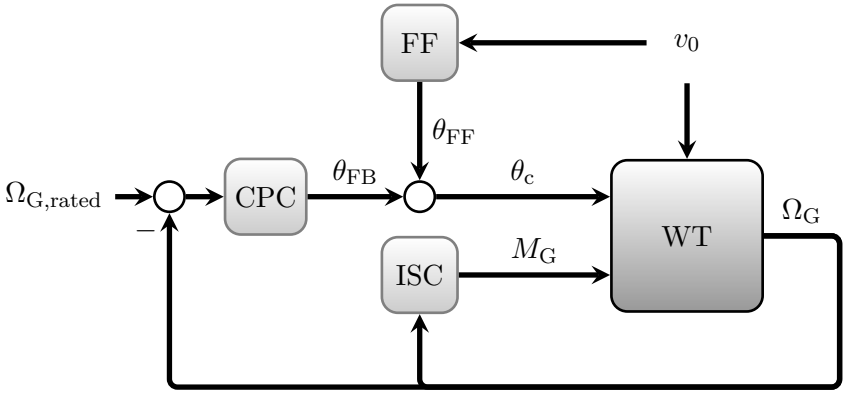

Figure 6.1: Feedback control loops and collective pitch feedforward control loop assuming perfect wind preview.

6.1 Collective Pitch Feedforward Controller Design

The main control goal of the CPC as described in Section 3.4.2 is to maintain the rated generator speed $\Omega_{\mathrm{G,rated}}$ in the presence of changing wind speed v_0 by adjusting the blade pitch angle demand θ_{c}, see Figure 6.1. The ISC additionally adjusts the generator torque M_{G} to maintain constant electrical power, if the generator speed differs from its rated value. The combination of the CPC and the ISC is referred to as "Feedback (FB)" in this work.

The basic idea of the "two-degrees-of-freedom-control" [74] is to complete the two main tasks for controllers (reference signal tracking and disturbance compensation) independently by a feedback and a feedforward controller and both controllers should not obstruct each other. For example, it would be possible to calculate an update to the generator torque to cancel out wind speed changes and to maintain constant generator speed. However, this would yield changing electrical power and thus interfere with the control goal of the ISC.

Here, the feedforward controller is designed such that changes from the wind speed v_0 to the generator speed Ω_{G} are compensated by an additional blade pitch angle θ_{FF}. In this case, the feedforward controller is not counteracting the control action of the CPC and ISC.

6.1.1 Collective Pitch Feedforward Controller for Perfect Wind Preview

For the design of the collective pitch feedforward controller, perfect knowledge of the rotor effective wind speed v_0 is assumed in a first step.

Feedforward controllers for disturbance rejection are well described for linear systems in the basic control literature, see for example [93]. The full nonlinear system (3.2) can be linearized and written in the form

$$\Omega_{\mathrm{G}}(s) = G_{\Omega_{\mathrm{G}}\theta_{\mathrm{c}}}\ \theta_{\mathrm{c}}(s) + G_{\Omega_{\mathrm{G}}M_{\mathrm{G}}}\ M_{\mathrm{G}}(s) + G_{\Omega_{\mathrm{G}}v_0}\ v_0(s), \tag{6.1}$$

where $\Omega_\mathrm{G}(s)$, $M_\mathrm{G}(s)$, $\theta_\mathrm{c}(s)$, and $v_0(s)$ are the Laplace transforms of $\Omega_\mathrm{G}(t)$, $M_\mathrm{G}(t)$, $\theta_\mathrm{c}(t)$, and $v_0(t)$, respectively. Further, $G_{\Omega_\mathrm{G}\theta_\mathrm{c}}$, $G_{\Omega_\mathrm{G}M_\mathrm{G}}$, and $G_{\Omega_\mathrm{G}v_0}$ are the corresponding transfer functions. With the linearized controller transfer functions G_CPC, G_ISC, and G_FF, the control inputs are

$$\begin{aligned} \theta_\mathrm{c}(s) &= -G_\mathrm{CPC}\ \Omega_\mathrm{G}(s) + G_\mathrm{FF}\ v_0(s) \\ M_\mathrm{G}(s) &= G_\mathrm{ISC}\ \Omega_\mathrm{G}(s). \end{aligned} \tag{6.2}$$

Incorporating these in (6.1) yields the following equation of the overall closed-loop control system:

$$\Omega_\mathrm{G}(s) = \frac{G_{\Omega_\mathrm{G}v_0} + G_{\Omega_\mathrm{G}\theta_\mathrm{c}}G_\mathrm{FF}}{1 + G_{\Omega_\mathrm{G}\theta_\mathrm{c}}G_\mathrm{CPC} - G_{\Omega_\mathrm{G}M_\mathrm{G}}G_\mathrm{ISC}} v_0(s). \tag{6.3}$$

The dynamic, linear feedforward controller canceling out all effects from v_0 to Ω_G can then be obtained by

$$G_\mathrm{FF} = -G^{-1}_{\Omega_\mathrm{G}\theta_\mathrm{c}} G_{\Omega_\mathrm{G}v_0}. \tag{6.4}$$

Depending on the included states in the linearization, this involves approximation by advanced inversion techniques such as non-causal series expansion, if $G_{\Omega_\mathrm{G}\theta_\mathrm{c}}$ contains non-minimum phase zeros, see [12]. In either case, the resulting feedforward controller will be designed only for the linearization point and will not perfectly cancel out all wind speed changes over the entire full load region.

Here, a static but nonlinear feedforward controller is proposed. Instead of a linearized full aero-elastic model, the SLOW model is used for the controller design. If the tower movement is neglected, the wind turbine model is reduced by using (3.3a), (3.9a), and (3.10) to:

$$J\dot{\Omega} + \frac{M_\mathrm{G}}{i_\mathrm{GB}} = M_\mathrm{a}(\Omega, \theta, v_0). \tag{6.5}$$

With this model, it can be shown that if M_G is used to control electrical power, then the aerodynamic torque needs to be held at its rated value to maintain constant rotor speed:

$$\begin{aligned} &\Omega{=}\Omega_\mathrm{rated} \\ \Leftrightarrow\ &M_\mathrm{a}(\Omega_\mathrm{rated}, \theta, v_0){=}\frac{M_\mathrm{G,rated}}{i_\mathrm{GB}}. \end{aligned} \tag{6.6}$$

This can be achieved for changing v_0 by adjusting the pitch angle using the static pitch curve $\theta_\mathrm{ss}(v_0)$. This curve is obtained by steady-state simulations, see Figure 6.2 (left). Since the pitch actuator and the delay introduced by the blades is modeled in (3.6) with a delay, the

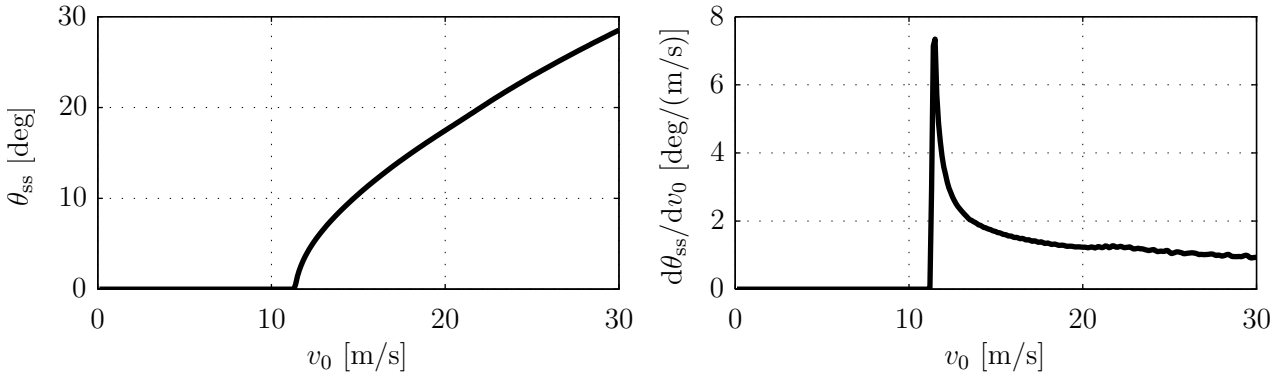

Figure 6.2: Static pitch curve (left) and its derivative (right) for the 5 MW reference wind turbine.

feedforward controller needs to apply the static pitch curve with a preview time $\tau = T_B$:

$$\theta_{FF}(t) = \theta_{ss}(v_0(t+\tau)). \tag{6.7}$$

Finally, following adjustment is made: Instead of adding the pitch angle θ_{FF} to the output θ_{FB} of the feedback controller, a feedforward pitch rate $\dot{\theta}_{FF}$ is added to the input of the integrator included in the feedback controller. The advantages of this adjustment are:

- The feedforward controller can be switched on and off without the need of adjusting the feedback controller. If for example no wind speed preview is available, $\dot{\theta}_{FF}$ can simply be set to zero. As soon as a wind speed preview is measurable again, $\dot{\theta}_{FF}$ can be transfered to the feedback controller without any further steps. In the case of adding θ_{FF}, the integrator of the feedback controller needs to have the actual value of θ_{FF} added to its current states as soon as no wind speed preview exists and the new value of θ_{FF} needs to be subtracted from its current state, when the preview is available again.
- Advanced or industrial controllers often have state-dependent lower pitch limits and more complicated anti-windup techniques [94]. Using $\dot{\theta}_{FF}$ instead of θ_{FF} simplifies the integration of the feedforward controller.

Although in principle mathematically identical with the direct derivative, $\dot{\theta}_{FF}$ is calculated by

$$\dot{\theta}_{FF}(t) = \dot{v}_0(t+\tau)\frac{d\theta_{ss}}{dv_0}(v_0(t+\tau)). \tag{6.8}$$

The function $\frac{d\theta_{ss}}{dv_0}(v_0)$ is displayed in Figure 6.2 (right). This is done, since $\dot{v}_0$ is often already available as a state of the adaptive filter (see Section 5.5). Furthermore, $\frac{d\theta_{ss}}{dv_0}(v_0)$ can be limited close to rated wind speed allowing a pitch rate still proportional to $\dot{v}_0$, which is beneficial for load reduction similar to the retuning of the feedback controller as shown in [83]. However, this is outside the scope of this thesis.

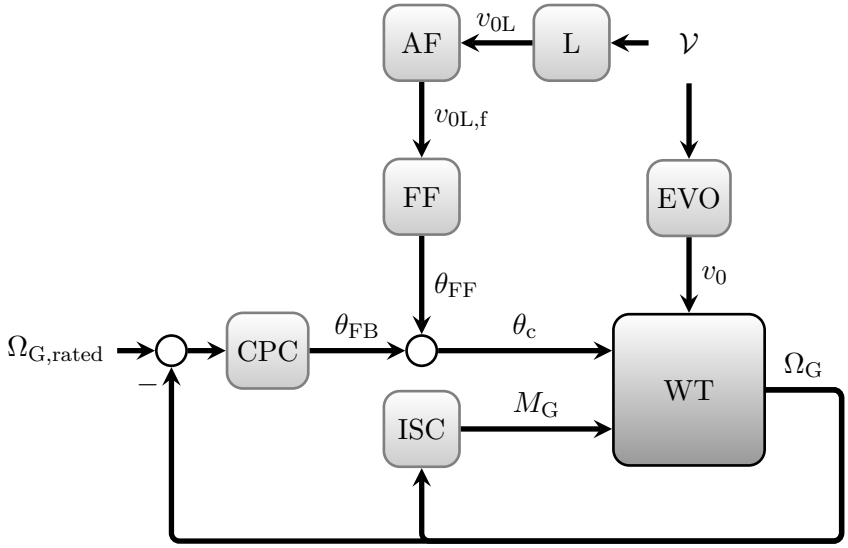

Figure 6.3: Feedback control loops and collective pitch feedforward control loop assuming realistic wind preview.

6.1.2 Collective Pitch Feedforward Controller for Realistic Wind Preview

In reality, the rotor effective wind speed v_0 cannot be measured perfectly. As depicted in Figure 6.3, while the lidar system measures in a three-dimensional wind field $\mathcal{V}$, it is only able to yield an estimate of the rotor effective wind speed v_{0L} due to the limitations which were discussed in Chapter 4. The wind field also evolves from the place of measurement to the rotor. Similar to (6.3), the closed-loop transfer function in the linear case is

$$\Omega_G(s) = \frac{G_{\Omega_G v_0} G_{EVO} + G_{\Omega_G \theta_c} G_{FF} G_{AF} G_L}{1 + G_{\Omega_G \theta_c} G_{CPC} - G_{\Omega_G M_G} G_{ISC}} \mathcal{V}(s), \tag{6.9}$$

where $\mathcal{V}(s)$ is the Laplace transform of $\mathcal{V}(t)$ and G_{EVO}, G_{AF}, and G_L are the linearized transfer functions of the wind evolution, the Adaptive Filter (AF), and the lidar system, respectively. In the linear case, a full compensation of the effect from the rotor effective wind speed to the generator speed would be theoretically still possible with the feedforward controller (6.4) and the filter

$$G_{AF} = G_{EVO}\, G_L^{-1} = G_{v_0 v_{0L}}, \tag{6.10}$$

if those transfer functions would be known and G_L would be invertible. Practically, this is very unlikely, because on the one hand information is lost by parts of the lidar measurement process such as the volume measurement, which cannot be restored. On the other hand, the wind evolution process is quite complex to model.
Nonetheless, (6.10) shows that the AF needs to fit the lidar estimate v_{0L} to the rotor effective wind speed v_0. This is done by the filter proposed in Section 5.5.

6.2 Simulations Using Perfect Wind Preview

In a first simulation study, the collective pitch feedforward controller is tested assuming perfect wind preview as described in Section 6.1.1. For this purpose, the reduced SLOW model (see Section 3.1.2) and the full aero-elastic FAST model (see Section 3.1.1) are disturbed by an EOG at 13 m/s and 25 m/s according to [50].
In the case of the SLOW model, no perfect cancellation can be expected, since the tower fore-aft mode was not included in the controller design model. However, the overshoot of the rotor speed (deviation from $\Omega_{\text{rated}} = 12.1\,\text{rpm}$) can be reduced almost to zero compared to the feedback controller, see Figure 6.4 (left) and 6.5 (left). For the EOG at 13 m/s a reduction of 97.0 % is achieved and at 25 m/s a reduction of 99.4 %, see Table 6.1 and 6.2.
Additionally, the maximum tower base fore-aft bending moment $M_{y\text{T}}$ is reduced by 47.1 % at 13 m/s and by 71.1 % at 25 m/s. This shows that the collective pitch feedforward control is also able to reduce the impact of the changing wind speed to the tower fore-aft movement, although it has not been included in the controller design. This is not trivial, since holding the aerodynamic torque constant does not automatically result in constant thrust. However, for the gust at 13 m/s the tower top displacement x_{T} is significantly reduced over the feedback controller and for 25 m/s x_{T} can be almost held constant at its steady state. Since the tower top movement interferes with the rotor motion through (3.11), the collective pitch feedforward controller achieves better speed regulation at higher wind speeds.
If the much more detailed FAST model is used, the proposed feedforward controller still can achieve almost perfect cancellation of the effect from v_0 to Ω, see Figure 6.4 (right) and 6.5 (right). Table 6.1 and 6.2 show that the deviation from the rated rotor speed $\Delta\Omega$ and the maximum tower base fore-aft bending moment $M_{y\text{T}}$ are reduced by similar values.
Finally, these results can be summarized by:

- The reduced wind turbine model with only 3 dynamic states (rotor speed, tower top displacement, and tower top speed) is able to sufficiently reproduce over the entire full load region the behavior of the full aero-elastic simulation model with 36 dynamic states and an iterative calculation of the aerodynamics.

- With perfect wind preview, the proposed static nonlinear feedforward controller is able to almost perfectly cancel out the effect from the rotor effective wind to the rotor speed over the entire full load region and for the full aero-elastic model.

- Additionally, the tower movement and thus the tower base bending moment can be reduced. This works better for higher wind speeds.

Table 6.1: Maximum values of the reaction to an EOG at 13 m/s in the case of perfect wind preview using the 5 MW reference wind turbine (see Figure 6.4).

	SLOW		FAST	
	$\Delta\Omega$ [rpm]	$M_{y\mathrm{T}}$ [MNm]	$\Delta\Omega$ [rpm]	$M_{y\mathrm{T}}$ [MNm]
FB	2.01	120.6	2.18	128.3
FB+FF	0.06	63.8	0.07	65.9
$\frac{\mathrm{FB+FF}}{\mathrm{FB}}$ [%]	3.0	52.9	3.0	51.3

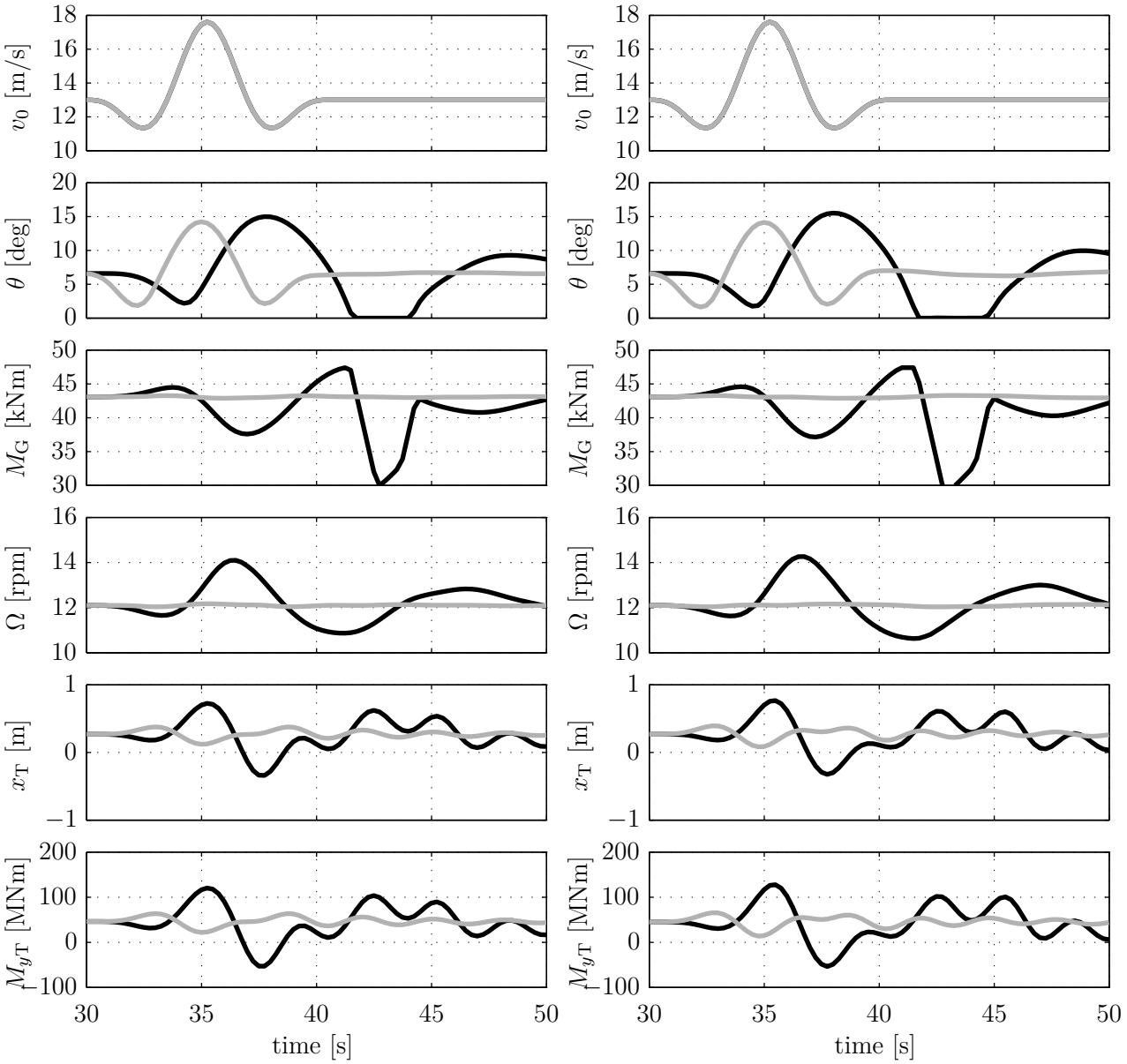

Figure 6.4: Reaction to an EOG at 13 m/s in the case of perfect wind preview using the 5 MW reference wind turbine. Simulated with reduced SLOW model (left) and full FAST model (right): Feedback controller only (black) and with additional feedforward (gray).

Table 6.2: Maximum values of the reaction to an EOG at 25 m/s in the case of perfect wind preview using the 5 MW reference wind turbine (see Figure 6.5).

	SLOW		FAST	
	$\Delta\Omega$ [rpm]	$M_{y\mathrm{T}}$ [MNm]	$\Delta\Omega$ [rpm]	$M_{y\mathrm{T}}$ [MNm]
FB	2.81	97.0	2.91	99.0
FB+FF	0.02	28.1	0.03	26.9
$\frac{\mathrm{FB+FF}}{\mathrm{FB}}$ [%]	0.6	28.9	0.9	27.2

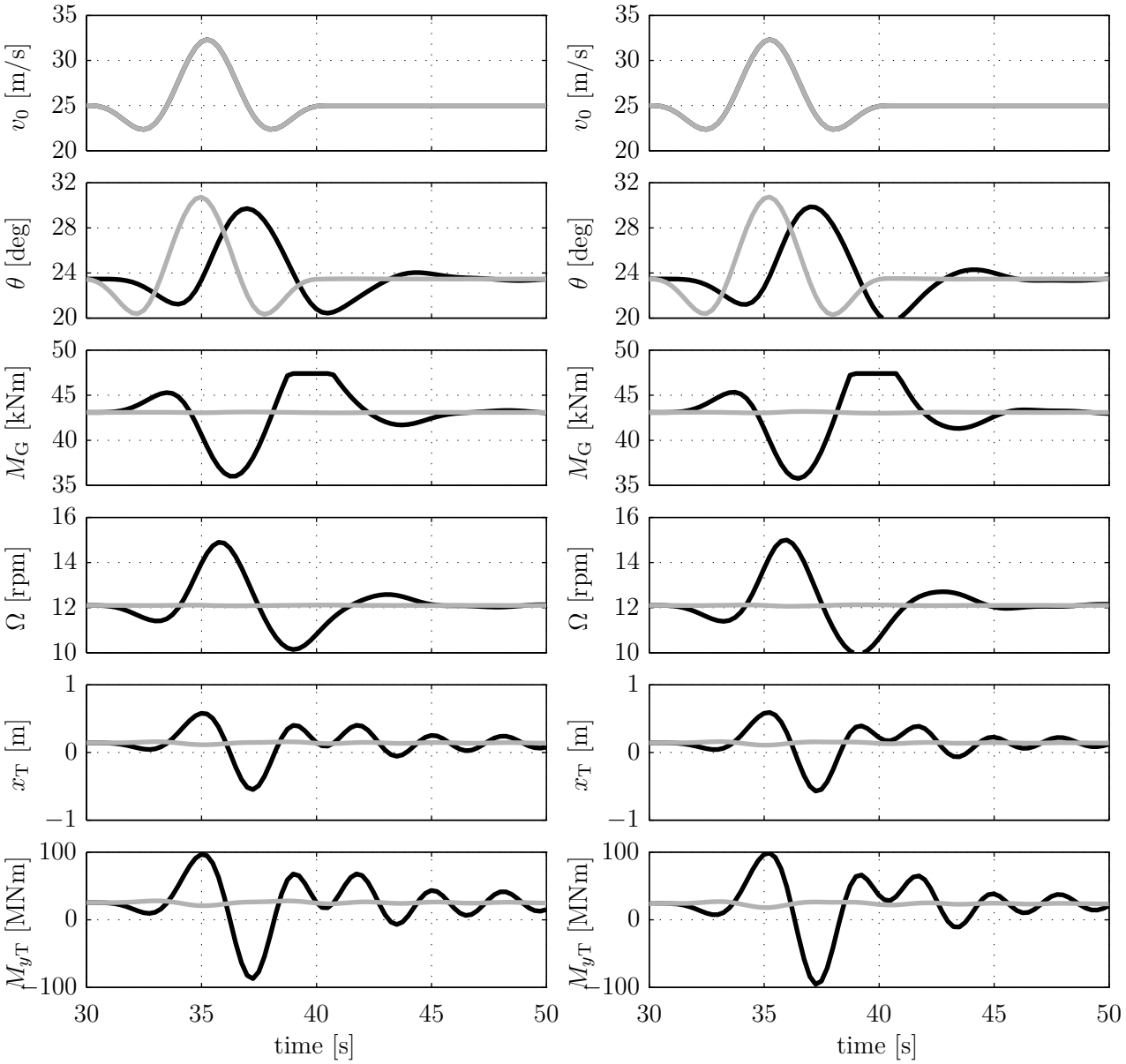

Figure 6.5: Reaction to an EOG at 25 m/s in the case of perfect wind preview using the 5 MW reference wind turbine. Simulated with reduced SLOW model (left) and full FAST model (right): Feedback controller only (black) and with additional feedforward (gray).

6.3 Simulations Using Simulated Lidar Measurements

The previous simulation study with perfect wind preview leads one to conclude that the collective pitch feedforward controller is sufficiently robust against model uncertainties. Although the feedforward controller is designed based on a static nonlinear model, it is able to maintain the rotor speed variation of the full nonlinear simulation model close to zero.

In a second simulation study, the robustness against measurement uncertainties of the wind preview is investigated by using the lidar simulator described in Section 3.5. As discussed in Section 6.1, an adaptive filter is necessary to fit the lidar estimate of the rotor effective wind speed to the real rotor effective wind speed. The filter depends on the mean wind speed and cancels out all uncorrelated frequencies and thus avoids unnecessary and harmful control action.

For this investigation, a lifetime of the 5 MW reference wind turbine is simulated as proposed in [50]. According to DLC 1.2, a set of 11 turbulent wind fields with turbulence class "A" and a length of 3660 s are generated with TurbSim[57] with mean wind speeds from 4 m/s to 24 m/s in steps of 2 m/s. For details see Table C.4. With these wind fields, the 5 MW reference wind turbine is simulated for 3630 s using the FAST model. The first 30 s of each simulation are ignored to avoid falsification of the results due to initialization effects of the FAST model. The results such as DELs and STandard Deviations (STDs) are weighted using a Weibull distribution with the scale parameter $C_{\mathrm{WB}} = 12\,\mathrm{m/s}$ and the shape parameter $k_{\mathrm{WB}} = 2$. The simulations are done first with the feedback controller only (CPC and ISC, see Figure 6.3) and then with the feedback controller augmented by the feedforward controller, the adaptive filter, and the lidar simulator (CPC, ISC, FF, AF, and L). For the lidar simulation, the optimized trajectory from Section 5.6 and the dynamic wind field reconstruction from Section 4.3 are used. Wind evolution is neglected for simplicity. Figure 6.6 illustrates 300 s out of the 3630 s simulation with mean wind speed $\bar{u} = 18\,\mathrm{m/s}$. In the upper part of the figure the rotor effective wind speed v_0 extracted from the wind field using (3.20) and its lidar estimate $v_{0\mathrm{L}}$ are displayed. The preview and the uncorrelated higher frequencies in $v_{0\mathrm{L}}$ can be observed. The resulting collective pitch angle θ and the generator torque M_{G} using the combined feedback and feedforward controller are smoother compared to the control action of the feedback controller alone. Several times a transition to below rated operation can be avoided (in Figure 6.6 at $t = 2116$, 2187, and 2205 s). Thus, the variation in the rotor speed Ω can be significantly reduced, even though not fully compared to the simulations in Section 6.2 due to the imperfect wind preview. Additionally, the variation in the tower top displacement x_{T} and the resulting tower base fore-aft bending moment $M_{y\mathrm{T}}$ are reduced, especially where a transition to below rated operation is avoided.

The effect of the feedforward controller can be observed clearly in the Power Spectral Densities (PSDs) of Figure 6.7. The lidar-assisted controller can significantly reduce the influence of the wind disturbance to the rotor speed at low frequencies. Since the adaptive filter has a cut-off-

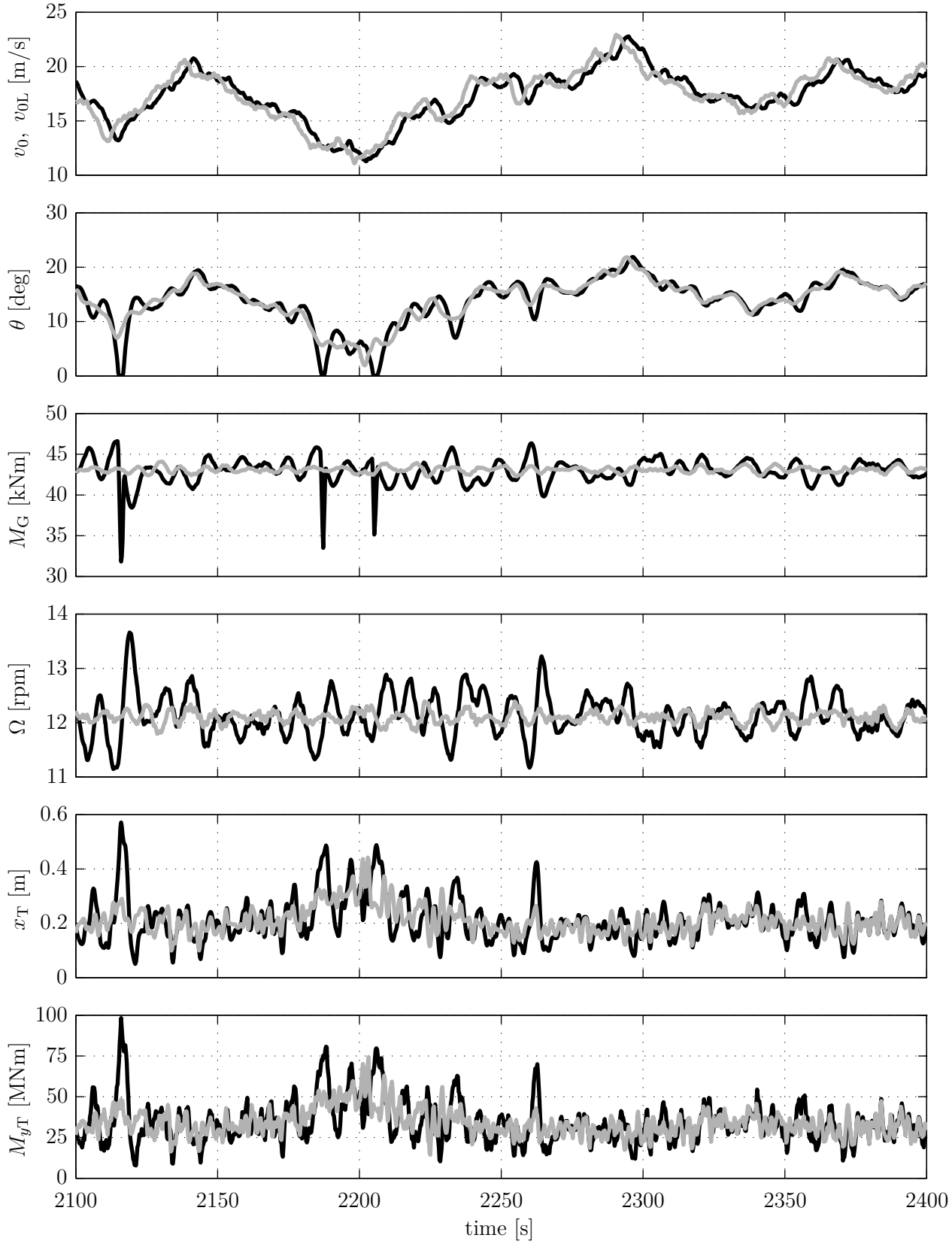

Figure 6.6: Reaction to a turbulent wind field with mean wind speed of 18 m/s using the FAST model of the 5 MW reference wind turbine (illustrative 5 min excerpt). Top: rotor effective wind speed (black) and its lidar estimate (gray). Rest: Feedback controller only (black) and with additional feedforward (gray) using simulated lidar measurements.

Table 6.3: Comparison of the results for the 1 h simulation at 18 m/s using the feedback controller alone (FB) and using the combined feedback and feedforward controller (FB+FF).

	DEL($M_{y\mathrm{T}}$) [MNm]	DEL(M_{LSS}) [MNm]	DEL(M_{oop1}) [MNm]	STD(Ω) [rpm]	STD($\dot{\theta}$) [deg/s]	STD(P_{el}) [MW]	EP [MWh]
FB	98.0	3.02	14.75	0.330	0.797	0.0616	4.9977
FB+FF	67.0	2.74	12.62	0.108	0.505	0.0231	5.0000
$\frac{\mathrm{FB+FF}}{\mathrm{FB}}$[%]	68.4	90.8	85.6	32.7	63.3	37.4	100.046

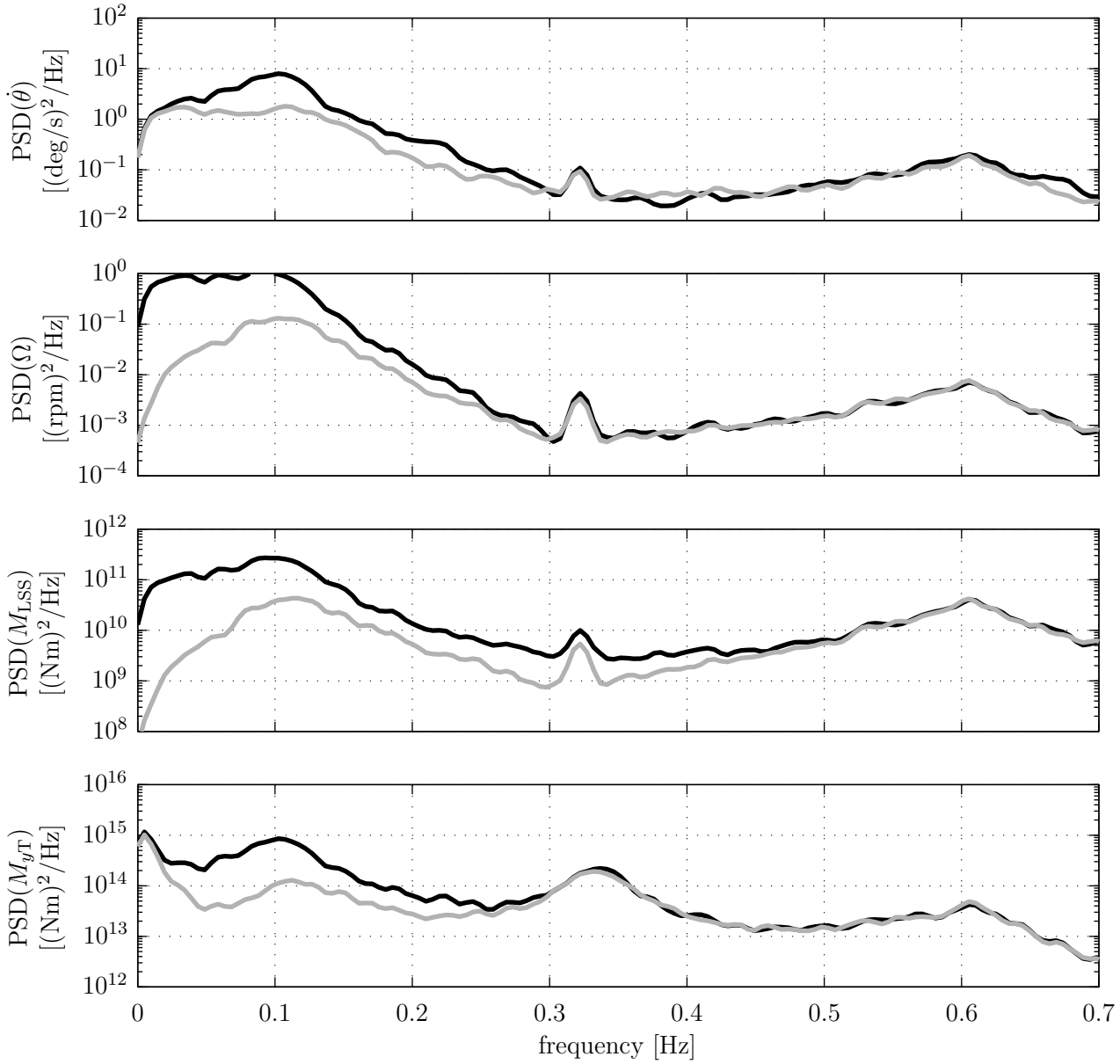

Figure 6.7: PSDs for the 1 h simulation at 18 m/s: Feedback controller only (black) and with additional feedforward (gray).

frequency at $f_{\text{cutoff}} = \hat{k}\bar{u}/(2\pi) = 0.201\,\text{Hz}$, the improvement minimizes above this frequency and no reduction is achieved at the damped eigenfrequency of the tower (0.322 Hz) and the three-per-revolution (3P) frequency (0.605 Hz). No large improvements can be expected above the one-per-revolution (1P) frequency (0.202 Hz) with collective pitch control in general.
In addition, the collective pitch rate $\dot{\theta}$, the low-speed shaft torque M_{LSS}, and the tower base fore-aft bending moment $M_{y\text{T}}$ are significantly reduced in this region. Since the steady states of the tower and the collective pitch angle are changing with the mean wind speed, no reduction is possible at frequencies close to 0 Hz. Table 6.3 summarizes the results of the 1 h simulation at 18 m/s. For the calculation of the DELs, a reference number of cycles $n_{\text{LC,ref}} = 2 \times 10^6$ is used. Further, a Wöhler exponent of $m = 4$ is assumed for the fatigue load calculation of the tower base fore-aft bending moment and the low-speed shaft torque. For M_{oop1}, the out-of-plane blade root bending moment of blade 1, a Wöhler exponent of $m = 10$ is applied. See Section 2.1.3 for more details. Besides the above mentioned load reduction on the tower base (over 30 %), additional load reduction on shaft and blade root (almost 10 % and 15 %, respectively) is achieved. The reductions of the rotor speed error and pitch rate expressed by the corresponding STDs are almost 70 % and 40 %, respectively. As a result of the reduced rotor speed error, the power variation is also decreased by over 60 %. Due to the avoidance of operations below rated power, the Energy Production (EP) can also be slightly improved.
However, the wind turbine will not operate at 18 m/s during its full lifetime, which is traditionally assumed to be 20 years. Based on the above mentioned Weibull distribution and the used discretization ($\bar{u}$ from 4 m/s to 24 m/s in steps of 2 m/s), the probability is only 5.68 %. Thus, each result of the individual simulations is weighted with its probability. For the STDs this is done by simple multiplication, for the DELs using the corresponding Wöhler exponent, see Equation (2.14). In Figure 6.8, the lifetime weighted results are plotted over the mean wind speed $\bar{u}$. Additionally, the difference between the EP over the lifetime using the feedback controller alone and the EP adding the feedforward controller is shown. No improvements at all can be achieved for the simulations with mean wind speed between 4 m/s and 8 m/s, because rated wind speed is not reached. For all other simulations, the collective pitch feedforward controller provides only positive effects (reduction of STDs and DELs, and increase in EP).
Finally, Table 6.4 expresses the overall potential. The DELs on tower base, shaft, and blade root are still reduced by approximately 20 %, 5 %, and 10 %. Since the turbine has variable rotor speed and power, the reduction of the variation in these quantities is less significant (about 10 % and 2 %) compared to the reduction in the pitch rate (still close to 30 %). The increased energy yield achieved by improved performance close to the rated wind speed is also positive.
These results confirm that the collective pitch feedforward control is very promising even under realistic conditions. Including wind evolution as done for example in [20] and [68] or other lidar systems is expected to quantitatively but not qualitatively change these results. The field testing in the next section will confirm the positive effects.

Table 6.4: Comparison of the lifetime-weighted results for the DLC1.2 simulations using the feedback controller alone (FB) and using feedback and feedforward controller (FB+FF).

	DEL(M_{yT}) [MNm]	DEL(M_{LSS}) [MNm]	DEL(M_{oop1}) [MNm]	STD(Ω) [rpm]	STD($\dot{\theta}$) [deg/s]	STD(P_{el}) [MW]	EP [GWh]
FB	85.3	2.85	13.12	0.579	0.447	0.5134	547.2914
FB+FF	69.7	2.68	11.71	0.513	0.312	0.5045	548.7218
$\frac{\text{FB+FF}}{\text{FB}}$[%]	81.7	94.1	89.3	88.5	69.7	98.3	100.261

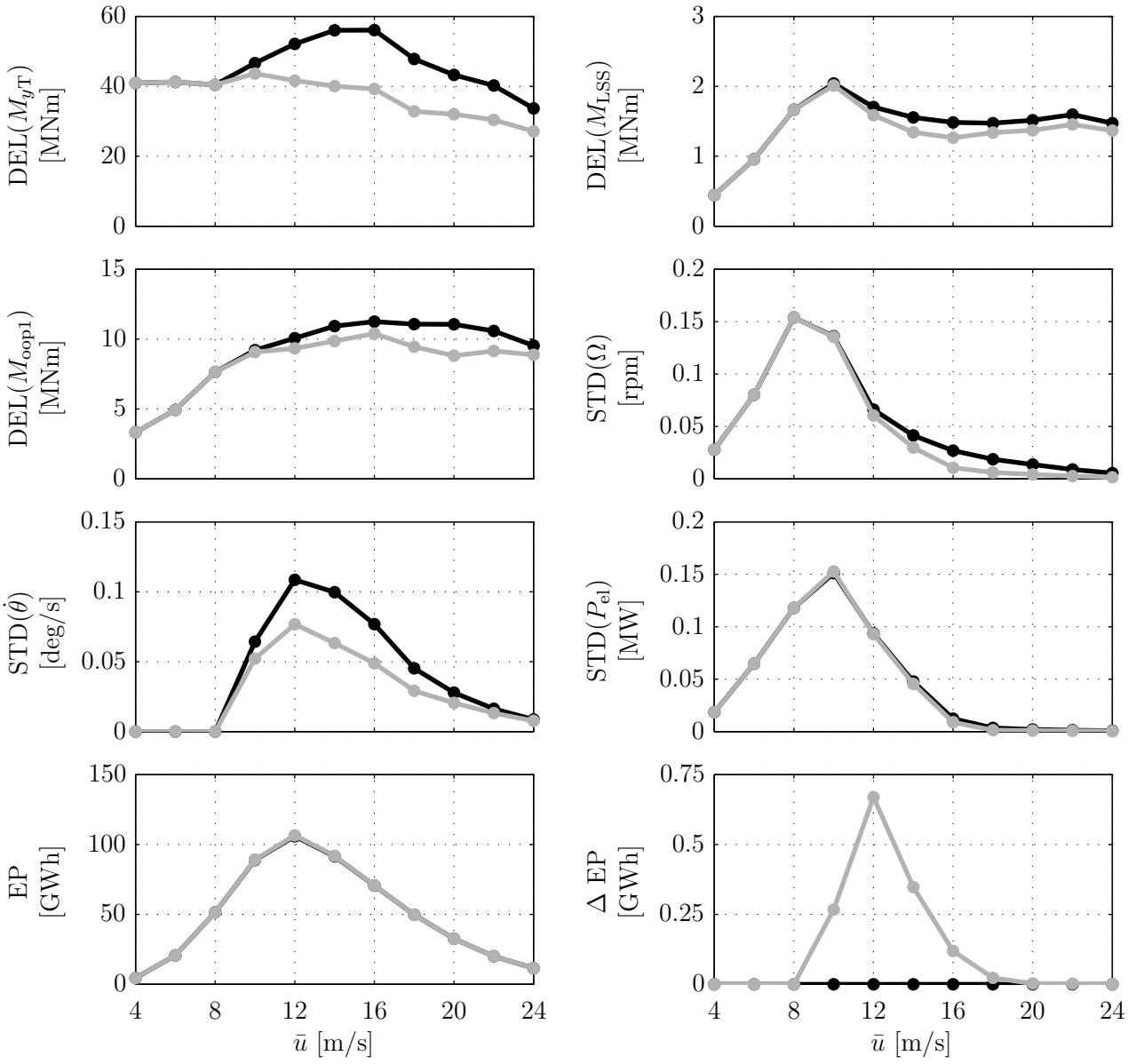

Figure 6.8: Lifetime-weighted results for the DLC1.2 simulations plotted over the mean wind speed: Feedback controller only (black) and with additional feedforward (gray).

Figure 6.9: The CART2 with the SWE scanning lidar system and the CART3 with a commercial lidar system at the National Wind Technology Center (NWTC) during the field testing (February 2012).

6.4 Field Testing

This section presents the results from a field test of the collective pitch feedforward controller described in the previous sections. From March to August 2012, two independent test campaigns were performed in cooperation with NREL, SWE, and the lidar manufacturer BlueScout Technologies at the NWTC, see Figure 6.9.

The results of both campaigns have been published in [88] and [95]. Although the collected data has been limited, both campaigns can be considered as a "proof-of-concept", since the results are consistent with the simulations: The generator speed variation can be reduced if the lidar estimate of the rotor effective wind speed is filtered according to the correlation between the lidar system and the reaction of the turbine.

This section focuses on the field testing on the CART2 and is organized as follows. In Section 6.4.1, the lidar data processing and the controllers used are outlined. The correlation of the lidar and the turbine is described in Section 6.4.2. Section 6.4.3 presents the measured results and a simulation study based on the data. More details of the test environment can be found in Appendix A.1.

6.4.1 Controller Design

This subsection gives a short overview of the reconstruction of the rotor effective wind speed from the lidar data and the feedback and feedforward controller.

Feedback Controller for the CART2

The baseline feedback controller is a slightly modified standard wind turbine controller. The torque controller uses a normal $k_{\mathrm{ISC}}\Omega_{\mathrm{G}}^2$ law in region 2 and a constant torque is applied in region 3. The pitch controller is called a PI/ID type controller, which is a PI controller with an additional integrated derivative term. The design and motivation for this control law are provided in [96]. In practice, the controller performs similarly to a normal PI controller. Both the torque and pitch controller follow the standard practice of feeding back only the generator speed measurement to the controller. The controller includes several additional elements including roll-off filters, notch filters at certain resonance and disturbance frequencies, and finally a tower-resonance avoidance scheme. The baseline controller has been used as a reference in a number of past studies. For example, it is used as the baseline controller with which to compare a state-space IPC controller in [97].

Lidar Data Processing and Feedforward Controller for the CART2

For this campaign, circular trajectories with 6 focus points in 5 focus distances equally distributed between $x_{1,\mathcal{L}} = 1D = 42.7\,\mathrm{m}$ and $x_{5,\mathcal{L}} = 2D = 85.3\,\mathrm{m}$ were used based on an optimization study similar to the one in Section 5.6. The SWE scanning lidar system was operated in different scan modes (see Appendix B for more details.) The duration of one scan for the "BangBang" mode is $T_{\mathrm{scan}} = 1.33\,\mathrm{s}$ and for the "StartStop" mode is $T_{\mathrm{scan}} = 2.42\,\mathrm{s}$. For the acquisition of one measurement, 2000 pulses with an average duration of $T_{\mathrm{ACQ}} = 0.144\,\mathrm{s}$ are used. For each distance, data points with bad synchronization or low CNR are removed. For the remaining data points, the longitudinal wind component is reconstructed assuming lateral and vertical wind components to be zero and by averaging over the last trajectory as described in Section 4.3.
The wind speed preview $v_{0\mathrm{L}}$ is then filtered with an adaptive filter (2nd order) as described in Section 5.5 using a 180 s moving average of $v_{0\mathrm{L}}$ to determine the mean wind speed $\bar{u}$. The filtered rotor effective wind speed is then transferred to the collective pitch feedforward controller, which has been implemented as described in Section 6.1.

Table 6.5: Overview of evaluated data from the NREL CART2 campaign.

Block ID	Start Time	End Time	FFoff-sections	FFon-sections high	FFon-sections low	$\hat{k}$ [rad/m]	Yaw [deg]	Scan mode
0	03-30 15:05:47	03-30 15:15:47	0	0	0	0.06	246	BangBang
1	04-13 15:39:29	04-13 16:34:29	8	0	0	<0.01	307	BangBang
2	05-17 01:18:28	05-17 01:28:28	0	0	6	0.02	296	StartStop
3	06-05 23:20:59	06-05 23:30:59	0	6	0	0.06	148	BangBang
4a	07-25 04:06:12	07-25 04:11:12	5	3	0	0.06	250	BangBang

6.4.2 Correlation Study

This subsection describes how the maximum coherent wavenumber $\hat{k}$ and the prediction time τ for the adaptive filter and the timing of the signal were identified before applying the feedforward control. For this purpose, the measured rotor effective wind speed $v_{0\mathrm{L}}$ from the lidar is compared to an estimate from turbine data. In the beginning of the campaign, the correlation decayed due to the collision of the laser beam with hard targets. This problem was solved during the campaign by improved data processing.

Identification of the Filter Parameters

Before applying the lidar feedforward update to the CART2, the maximum coherent wavenumber $\hat{k}$ and the prediction time τ have been identified based on the lidar and CART2 data of Block 0 using the "BangBang" scanning mode, (see Table 6.5 and Figure 6.10).
Figure 6.11 depicts the measured transfer functions between the v_0 and the wind speeds $v_{0\mathrm{L,i}}$ from the different measurement distances (shades of gray) as well as the transfer function between v_0 and $v_{0\mathrm{L}}$ which is a combination of all measurement distances (cyan). The figure shows that on the one hand all distances used alone would require more filtering than the combination, while the first and the last distance have the lowest $\hat{k}$. This motivates the use of pulsed lidar systems, because the averaged signal over several focus distances requires less filtering and thus smaller time delays. On the other hand the figure shows the chosen filter. The maximum coherent wavenumber was identified with $\hat{k} = 0.06\,\mathrm{rad/m}$. This is close to the expected value based on the analytic correlation model as elaborated in Section 5.4.
Based on the measured cross correlation in Figure 6.12 between v_0 and the wind speeds $v_{0\mathrm{L,i}}$, the preview time was adjusted to a negative value $\tau = -0.6\,\mathrm{s}$ such that predicted previews met the measured ones. The figure also shows that the second distance is the best correlated in terms of the peak cross correlation, which is equal to the cross correlation coefficient of the synchronized signals. Again, the combination of all distances improves the correlation.

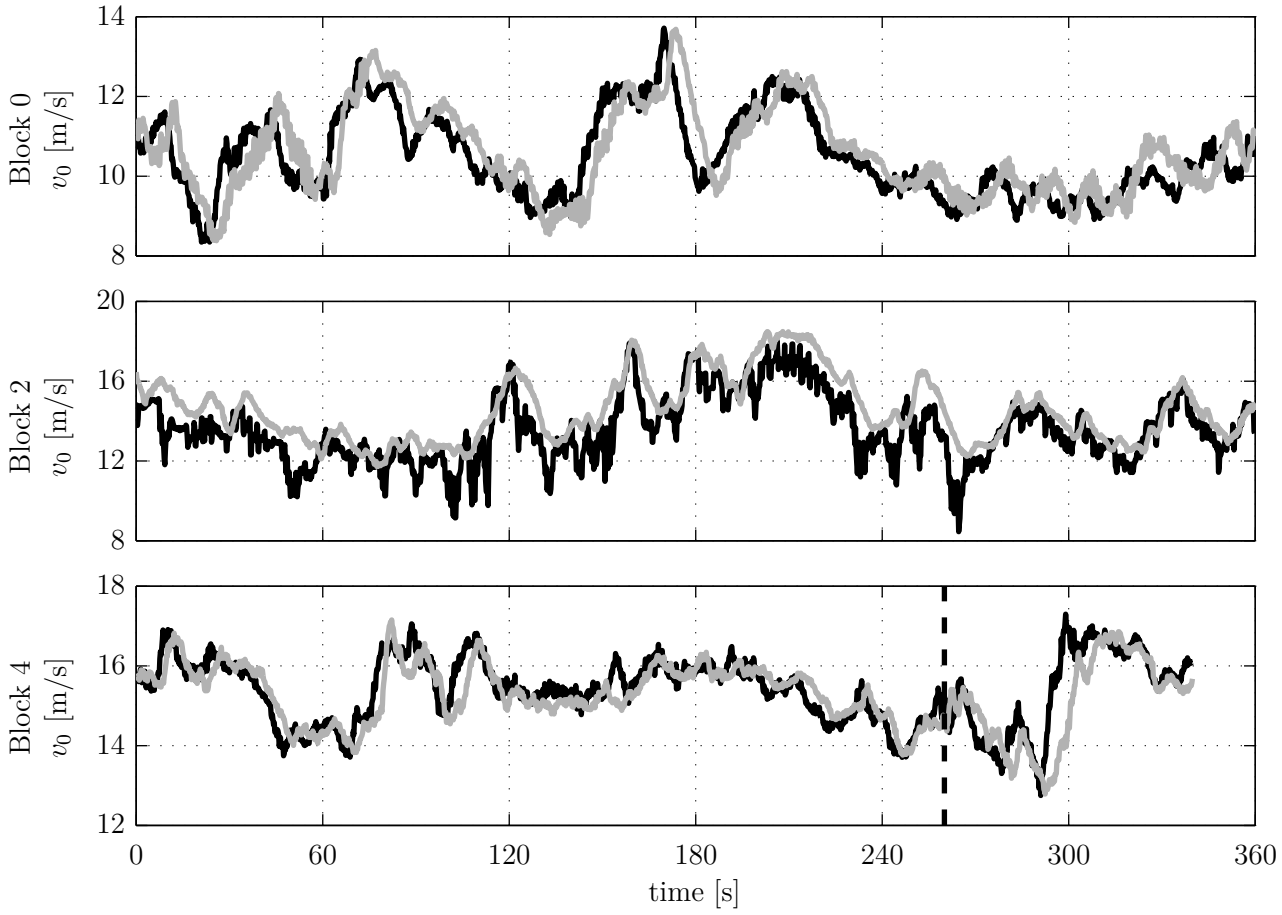

Figure 6.10: Rotor effective wind speed estimates from the turbine (gray) and the lidar (black). Block 4a ends at the dashed line.

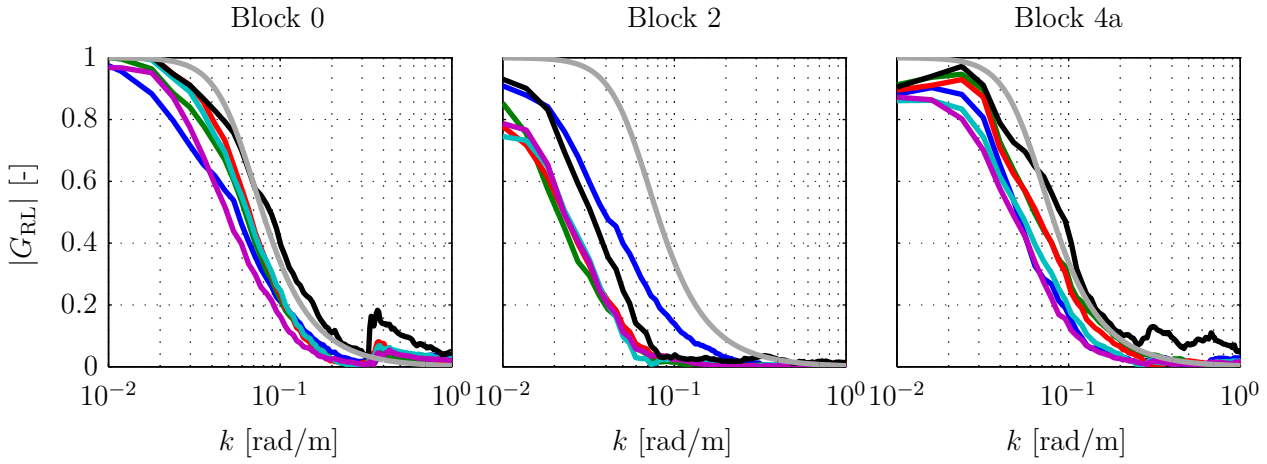

Figure 6.11: Transfer function between the turbine and the lidar: the first to the last distance (colors see Figure 6.13b) and the resulting v_{0L} (black). The gray line shows the used filter.

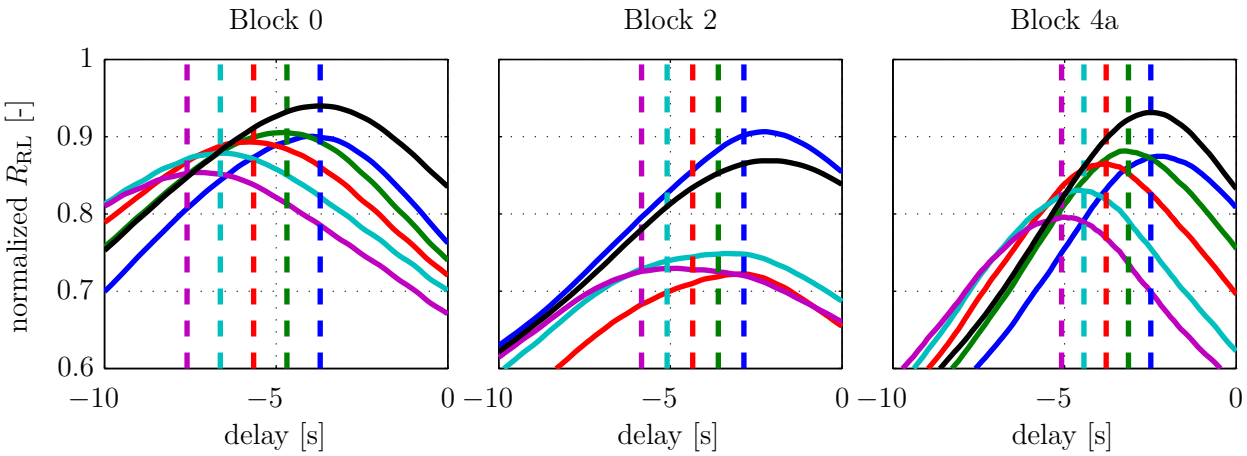

Figure 6.12: Cross correlation between the turbine and the lidar: the first to the last distance (colors see Figure 6.13b) and the resulting v_{0L} (black). The vertical lines indicate the predicted preview.

Hard Target Problem

During the next period of high wind speeds (Block 1), a lower correlation was discovered ($\hat{k} < 0.01\,\mathrm{rad/m}$) and the feedforward controller was not applied. A detailed investigation of the data revealed values of v_{los} around 0 m/s, typical for an impact with a hard target. It was assumed due to the position in the trajectory (see Figure 6.13b) and the yaw dependency that the met mast and the guy wires were responsible. Figure 6.13a shows an example of the v_{los} data distribution over the CNR of a 10 min raw data file. Impact with the rotating blades can be easily identified by a lower CNR limit, depending on the trajectory, the number of averaged pulses, and the aerosol concentration. Here −18 dB was used. This cannot be done for the hard target issue, because the CNR value are distributed along the CNR range of the normally reliable data. Due to the high occurrence of this issue, using only data with high v_{los} was not considered. Instead, two strategies were used:

1. Use the "StartStop" mode and remove all data online with a CNR value above −5 dB, because it was assumed that with this modification the probability of an impact can be minimized and the CNR will be maximized in the case of an impact. This implies that the correlation is supposed to be lower due to the slower trajectory.

2. Cut off the FFT spectra at bin 15. The peak detection algorithm is then able to find the second minor peak, see Figure 6.13c. This implies that v_{los} below 6 m/s cannot be detected.

The first approach was applied in Block 2 with enabled feedforward controller (see Figure 6.10) without significant improvements. With the second approach, the hard target problem was not observed in the rest of the campaign, independent on the yaw direction. For Blocks 3 and 4a, a maximum coherent wavenumber close to $\hat{k} = 0.06\,\mathrm{rad/m}$ and a prediction time $\tau = -0.6\,\mathrm{s}$

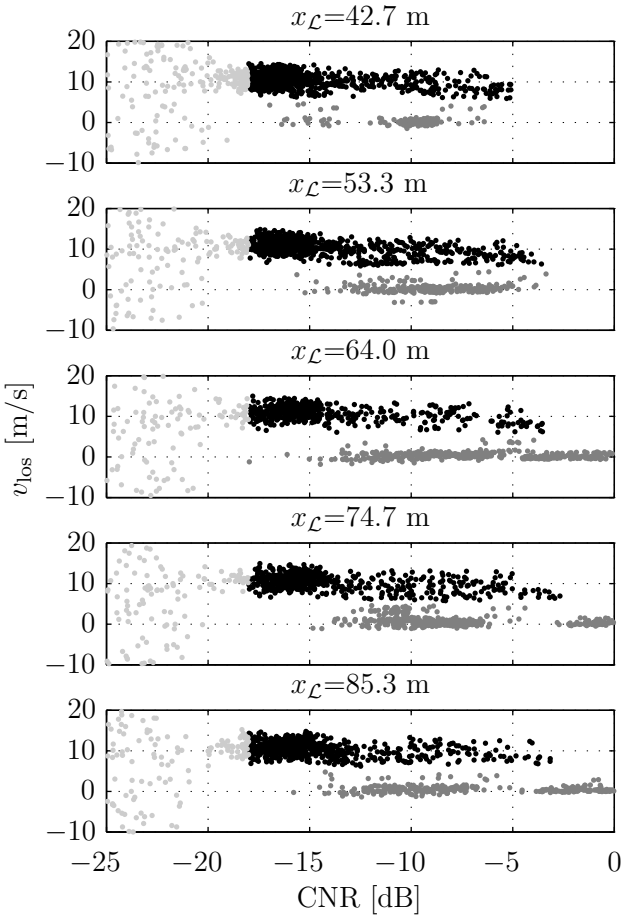

(a) Distribution of CNR over line-of-sight wind speed: Correct data (black), disturbed data by blade impact (light gray) and met mast (dark gray).

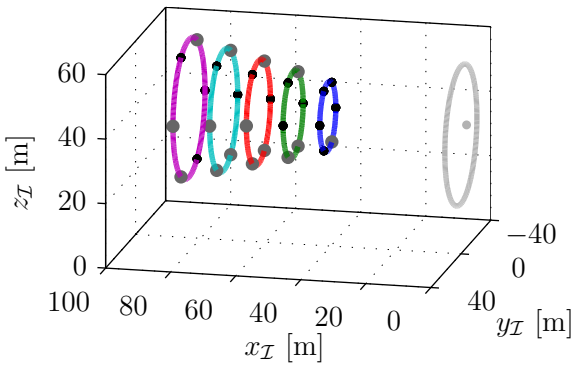

(b) Circular scan with points with hard targets (dark gray).

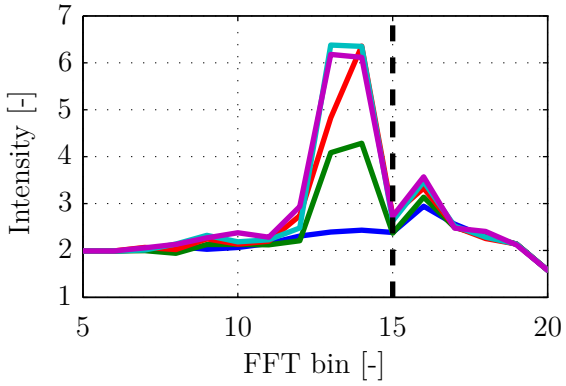

(c) Averaged spectra from the first to the last distance. Colors see Figure 6.13b.

Figure 6.13: The hard target problem during Block 1.

could be again detected and the transfer function as well as the cross correlation show a similar behavior compared to Block 0, see Figure 6.11 and 6.12. But at $t \approx 300\,\mathrm{s}$ after the end of Block 4a, the lidar detects a gust with a higher preview. The average wind speed $\bar{u}$ is calculated by a moving average over 180 s. The investigation in [10] proves that the control performance can be improved by a shorter average time.

Due to problems with the data acquisition system of the turbine and the short wind season, no more than the 4 blocks of significant data were collected during the campaign. For further analysis, the data with positive pitch angles from Blocks 1 to 4a are divided into sections of 32 s with the feedforward controller on with high and low correlation (FFon high/low) and sections when only the feedback controller was running (FFoff), see Table 6.5.

6.4.3 Field Testing Results

The results of the campaign are first examined in the time domain and then evaluated by spectral analysis. Then, the data from turbine and lidar are used to re-simulate the situation to check if better results would have been possible by tuning the filter and the feedback controller.

Time Domain

Figure 6.14 shows the smooth enabling of the feedforward controller by changing the FF switch g_{FF} from 0 to 1, which is multiplied with the pitch rate update $\dot{\theta}_{\mathrm{FF}}$. Some reduction of the generator speed error can be observed and the pitch angle follows the feedforward pitch angle θ_{FF} for most of the time. As described above, the lidar detects the gust at $t \approx 300\,\mathrm{s}$ too early. However, in this case the feedforward controller reduced the generator speed overshoot when reaching rated speed compared to similar cases when using the feedback controller alone. This shows that further investigation is also necessary to improve the feedforward control close to rated wind speed.
Besides the primary control goal to reduce the standard deviation of the generator speed, also some general loads of the turbine, namely the flapwise root bending moment of the first blade M_{flp1} and the tower base bending moment M_{T} are evaluated and the results are shown in Table 6.6. DELs are calculated based on a rainflow counting with reference number of cycles 2×10^6 for 20 years lifetime and with a Wöhler exponent of 4 and 10, typical for steel and composite material, respectively. For the sections with high correlation, the feedforward controller is able to reduce the standard deviation of the generator speed by about 30 % and the tower loads by 10 %. However, for the sections with low correlation, the feedforward controller increases the standard deviation of the generator speed by about 30 % and the tower loads by about 20 %. The blade loads are reduced in both cases by about 10 %. Although the collected data yields only a limited evaluable amount of data, the shown results are considered to be still indicative because the wind conditions of the evaluated sections are comparable. As shown in Figure 6.15, the turbulence intensities I measured by the met mast are distributed over the mean wind speed $\bar{u}$ similarly for the evaluated sections. Further findings can be gathered by the frequency domain analysis in the next subsection.

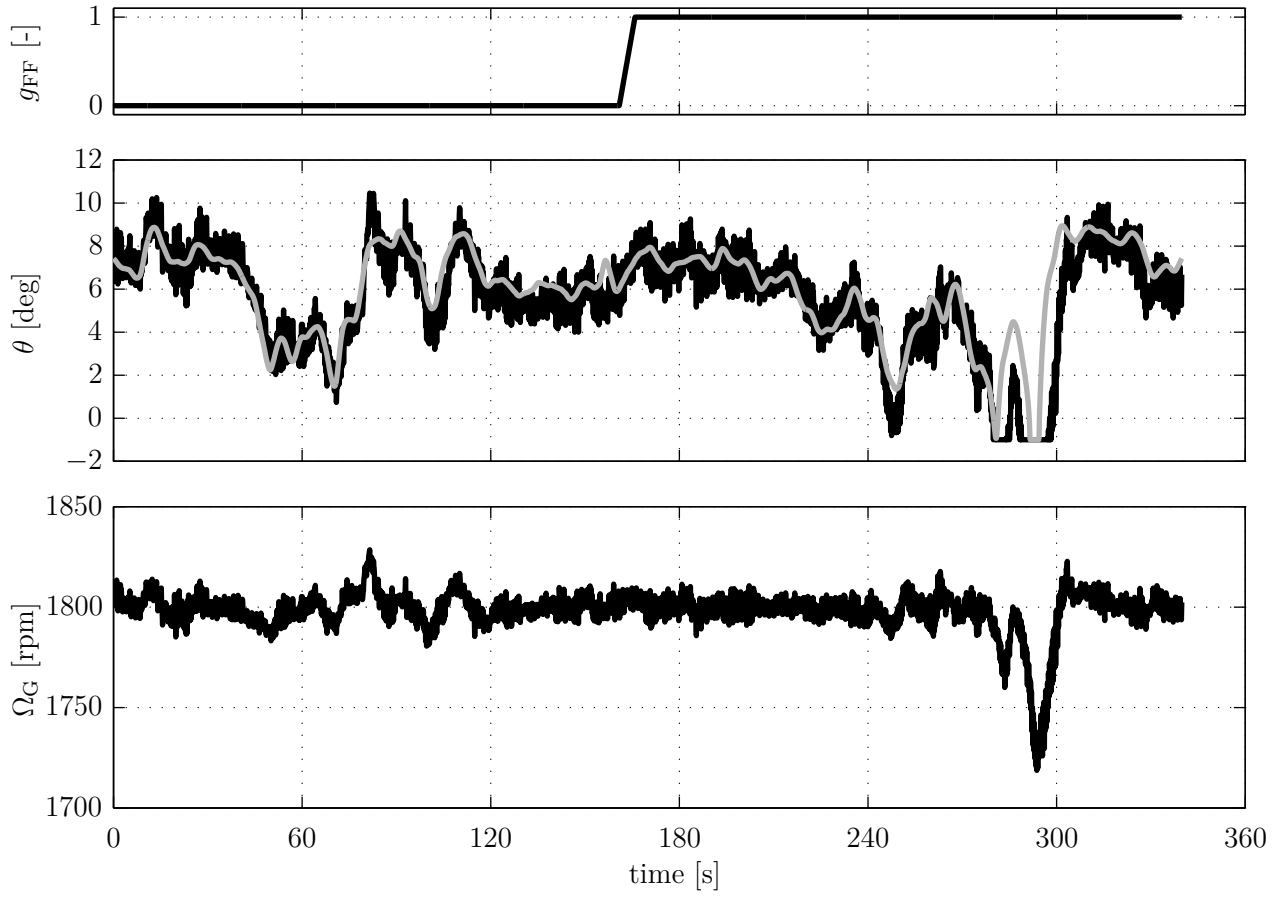

Figure 6.14: FF switch, the measured pitch angle (black) and the feedforward pitch angle (gray) and the generator speed for Block 4.

Table 6.6: Standard deviation of the generator speed and DELs for tower base bending moment and flapwise blade root bending moment of blade 1.

	$\sigma(\Omega_G)$ [rpm]	DEL(M_T) [kNm]	DEL(M_{flp1}) [Nm]
FFoff	6.89	4.85	435
FFon high	4.74	4.38	380
FFon low	8.77	5.79	404

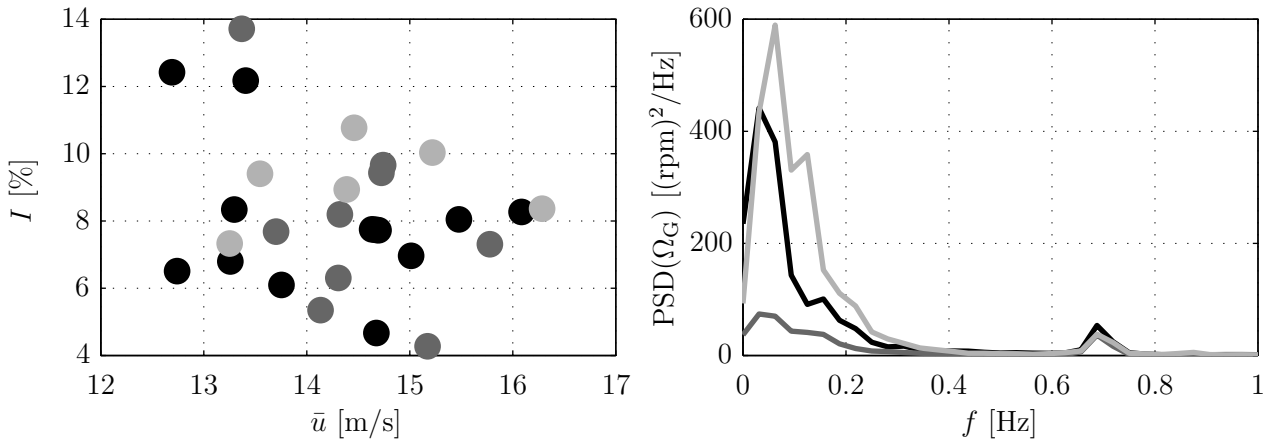

Figure 6.15: Distribution of turbulence intensity over mean wind speed (left) and PSD of generator speed (right): FFoff(black), FFon high (dark gray), FFon low (light gray).

Frequency Domain

Figure 6.15 shows the PSD of the generator speed for the different cases. Due to the linear scale, the area below the PSD corresponds to the square of the standard deviation. In the case of high correlation lower standard deviation is obtained by a reduction of the PSD at low frequencies, e.g., the peak at the 1P-frequency (0.695 Hz) is not affected by the feedforward controller. The PSD of the FFon case with low correlation starts to be above the PSD of the FFoff case at frequencies of 0.0625 Hz which corresponds at a mean wind speed of $\bar{u} = 14\,\mathrm{m/s}$ to a wavenumber of 0.028 rad/m. This value is above the maximum coherent wavenumber $\hat{k} = 0.02\,\mathrm{rad/m}$. Therefore, the increment of the generator speed variations is caused by wrong pitch action of the feedforward controller due to the uncorrelated wind speed measurements. The PSD of the tower base bending moment M_T and flapwise blade root bending moment M_flp1 are illustrated in Figure 6.16. Although the data base is small, some general observations fit to the considerations above: The PSD again is mainly affected by the feedforward controller at low frequencies: For highly correlated lidar measurements, the PSD is decreased and for low correlation the PSD is above the FFoff case.

Hybrid Simulations

The results above showed that the lidar-assisted feedforward controller was only able to improve the control performance in the case where the correlation between the lidar measurement and the turbine's reaction corresponded to the correlation which was predicted and used in the filter design. The following simulation study investigates if the filter used was close to the optimum and if further improvements could have been achieved by re-tuning of the feedback controller as proposed in [83, 20]. The first 300 s of the rotor effective wind speed v_0 and the lidar estimate $v_{0\mathrm{L}}$ from Block 4 (see Figure 6.10) is used for the hybrid simulation technique

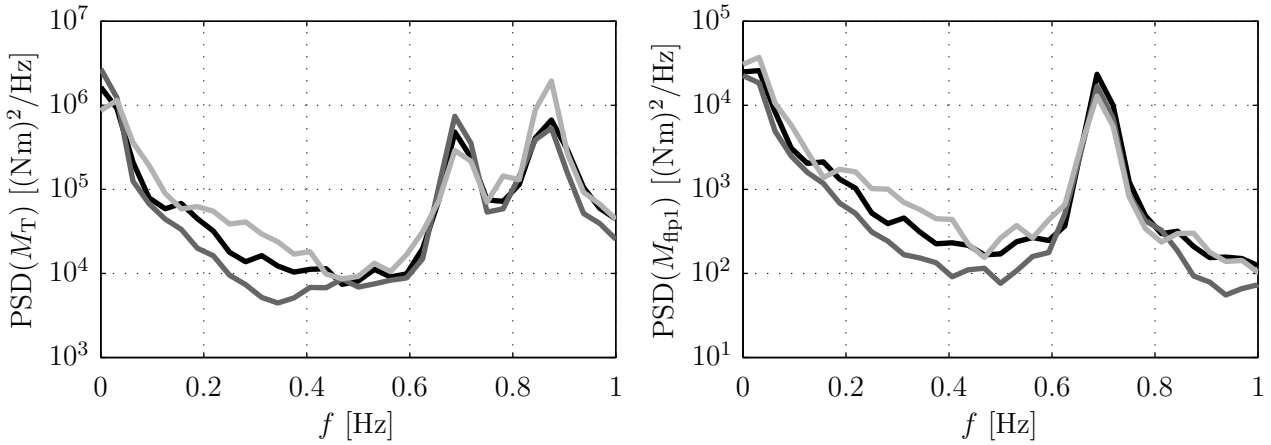

Figure 6.16: PSD of tower base bending moment and flapwise blade root bending moment: FFoff(black), FFon high (dark gray), FFon low (light gray).

described in Section 3.5.2. An aero-elastic wind turbine model of the CART2 is disturbed by v_0 as a coherent hub height wind speed. The turbine is controlled by the same feedback controller and in the case of no further changes, the simulation produces a similar reaction of the turbine, because the estimation described in Section 3.2.5 is based on an inversion of the reduced model. In a first step, the simulation is repeated with the feedforward controller and different values for the maximum coherent wavenumber $\hat{k}$ and the prediction time τ. 10 values are equally distributed between 0.03 rad/m and 0.12 rad/m for $\hat{k}$ and 13 values between -1.2 s and 1.2 s for τ, resulting in 130 simulations. The top part of Figure 6.17 shows that the parameters used in the field testing (black marker) are close to the optimal values for the reduction of the generator speed standard deviation STD(Ω_G). However, for the DEL of the tower base bending moment M_T and the flapwise blade root bending moment M_{flp1}, more load reduction is achieved in simulations with larger prediction times and less filtering (higher $\hat{k}$). Similar effects have been reported in [15].

In a second step, the 130 simulations are repeated with a relaxed feedback controller. Both the proportional and the integral gain are reduced by 1/3 based on the experience gathered in [83]. The lower part of Figure 6.17 depicts that on the one hand, the loads can be further reduced at the cost of higher standard deviation of the generator speed. On the other hand, the shape of the relative improvement of $\sigma(\Omega_G)$ over the parameters $\hat{k}$ and τ is similar for the combination with the baseline and the re-tuned feedback controller. This confirms the measurement problem ("How can we obtain a signal similar to the rotor effective wind speed from the lidar measurements?") and the control problem ("How can we improve the control performance knowing the rotor effective wind speed?") of lidar-assisted control can be solved independently from each other: The adaptive filter is solving the measurement problem best, if it is fitted to the current correlation between the lidar and turbine's reaction. This is not affected by re-tuning the feedback controller.

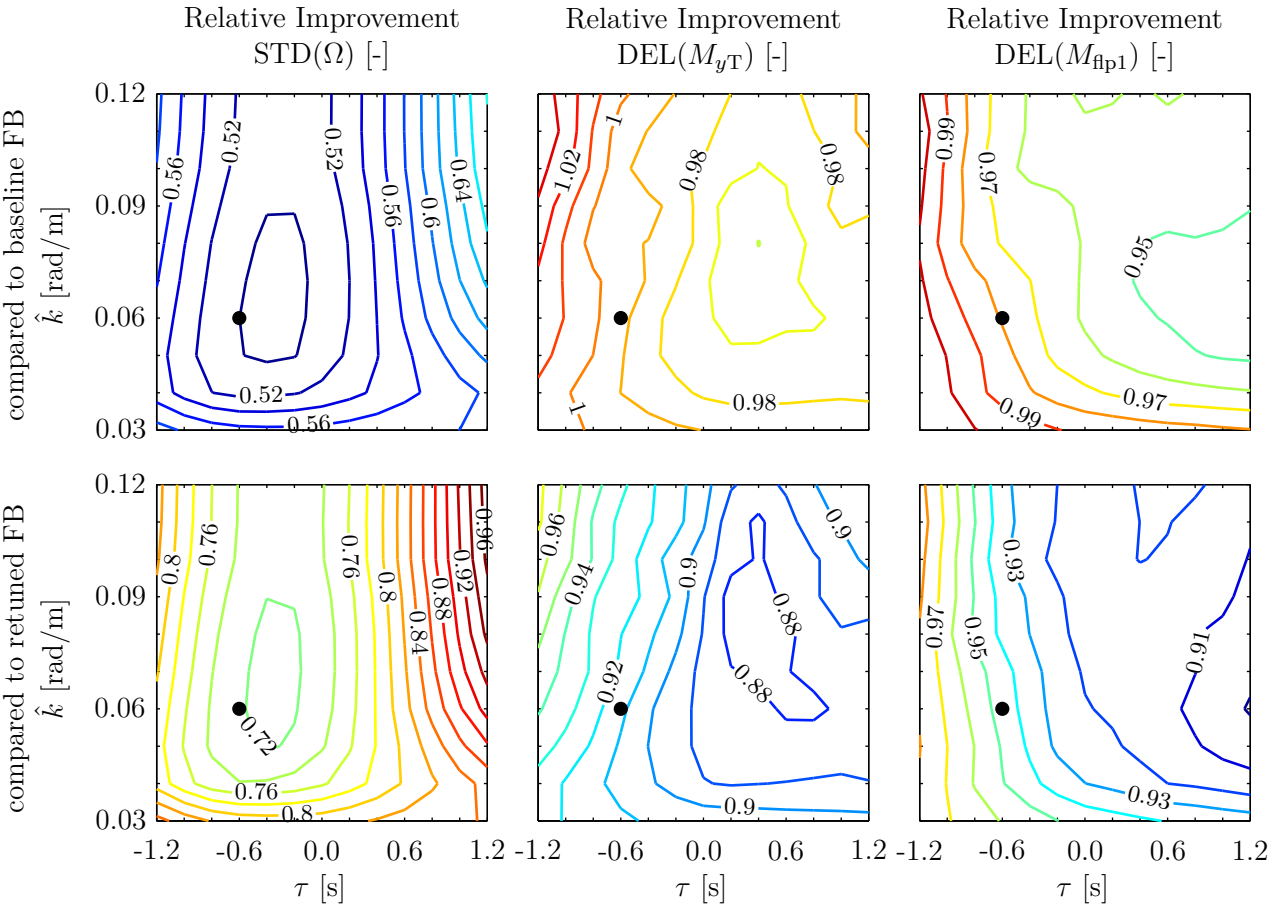

Figure 6.17: Results from simulation study using v_0 and v_{0L} of Block 4 and aero-elastic CART2 model: Relative improvement with different feedforward parameters over baseline (top) and re-tuned (bottom) feedback controller. Black marker: used parameters in field testing.

6.5 Summary and Possible Extensions for Collective Pitch Control

In this chapter a collective pitch feedforward controller has been presented.

The controller is first designed assuming perfect wind preview using a reduced nonlinear wind turbine model. Under these assumptions, the controller is able to almost perfectly cancel out the effect from the rotor effective wind to the rotor speed over the entire full load region and for the full aero-elastic model. This also indirectly reduces the impact on other states and thus decreases the structural loads of the turbine.

The promising results are then confirmed with a detailed load analysis extrapolating the effects on the lifetime of a wind turbine. For this purpose, the 5 MW reference turbine is simulated using a full aero-elastic model and a set of turbulent wind fields. The same wind fields are scanned with a realistic lidar simulator. The rotor effective wind speed is then reconstructed from the lidar data and filtered by an adaptive filter to provide a signal to the feedforward controller, which is as close as possible to the real rotor effective wind speed. The reduction in damage equivalent loads on tower base bending, shaft torsion, and blade root bending moment can be estimated to be approximately 20 %, 5 %, and 10 %, respectively. Additionally, the blade pitch activity can be decreased by about 30 % based on the standard deviation of the pitch rate. These effects are very promising to help to reduce the operation and maintenance cost of already installed wind turbines. From a longer term perspective, the reduction in structural loads, rotor speed variation, and pitch activity can be exploited by redesigning wind turbines to further reduce the cost of wind energy. Although further research is necessary to investigate how these benefits relate to a commercial application, the estimated increase in energy production of over 1.4 GWh due to improved control performance close to rated power is already in the vicinity needed to pay off directly the investment of a commercial lidar system.

In a next step, field testing results have been presented which confirm that the improved control performance can be achieved also under real conditions. In cooperation with NREL, a scanning lidar system has been integrated in a control system of a mid-scale wind turbine and was able to improve the rotor speed regulation. Although only limited data could be collected, the data shows that it is important to filter the data according to the correlation of the turbine and the lidar system. In the case of low correlation, which was due to initially not considering the impact of the laser beam with the met mast and guy wires, the feedforward controller was not beneficial to the turbine. In the case of high correlation, the standard deviation of the rotor speed has been reduced by 30 % and 10 % lower structural loads on the tower base have been observed. However, in the case of low correlation, which was due to the impact with the met mast and guy wires, an increase in the generator speed variations can be seen, due to the erroneous pitch action by the feedforward controller. This confirms that it is possible to assisted wind turbine controllers with lidar measurements, but the measurement signal has

to be carefully filtered to have a beneficial effect. Furthermore, a simulation study using the simultaneously measured turbine and lidar data confirms that a filter fitted to the correlation yields the best results and that loads can be further reduced by relaxing the feedback controller independent from the filter design.
The collective pitch feedforward controller will on the one hand benefit from further improvement in the field of lidar data processing as discussed in Sections 4.4 and 5.7. On the other hand, there are several possibilities for future research regarding the pure control part:

- The benefit gained in rotor speed variation can be transformed in further load reduction by relaxing the feedback controller gains as for example stated in [89] and [21]. Further investigations are necessary to quantify this effect and to provide a method to tune the controller based on the quality of the lidar measurements. The approach presented in [9] which calculates the standard deviation of turbine states based on the measurement coherence might be very useful.

- The collective pitch controller aims to directly reduce the rotor speed variation and only indirectly addresses the turbine loads. More advanced Multiple-Input Multiple-Output (MIMO) controllers such as NMPC provide the possibility to penalize tower movements and thus reduces tower bending loads directly. However, these controllers replace existing feedback controllers, rely on estimated turbine states, and are computational more complex. Therefore, these concepts might not be robust enough for real applications. Thus, further investigations are necessary to design nonlinear, robust, and simple feedforward controllers, which reduce the structural loads similar to these advanced controllers without their drawbacks. A first attempt is made by the flatness-based approach presented in Chapter 8.

- For the collective pitch feedforward controller, the control problem is solved independently of the measurement problem. This is done by first designing the controller under the assumption of perfect knowledge of the rotor effective wind speed and then the adaptive filter is responsible to fit the lidar estimate to a signal that is representative of the real signal. Approaches addressing both problems together like the one presented by [18] in combination with nonlinear methods might provide a more consistent solution.

- In this work, feedforward and feedback is strictly separated based on the "two-degree-of-freedom" idea and since it also facilitated the field testing. However, further research is necessary to investigate the benefit of the approaches which calculate the collective pitch feedforward-update based on measured turbine data such as the current pitch angle, as presented in [21] and [22].

7

Direct Speed Control

The main purpose of variable speed control for wind turbines below rated wind speed is to maximize the electrical power extraction [41]. Therefore, the turbine has to operate with the rotor blades held at the optimal angle of attack. Maximum power extraction is achieved by adjusting the generator torque M_{G} and thereby tracking the optimal tip speed ratio λ_{opt}. This chapter explains how tracking λ_{opt} can be improved by using the knowledge of the incoming wind and it is an extension to [38, 77].

Unfortunately, the findings in this chapter show that while the tracking of the optimal tip speed ratio is possible, it is not reasonable due to increased loads for marginal benefit. These findings coincide with the results in [21]. However, other work in this field, for example [33, 34, 35] claim significant improvements.

This chapter is organized as follows: In Section 7.1 the lidar-assisted torque controller is derived and its potential is theoretically estimated in Section 7.2. Simulations using perfect wind preview, simulated lidar measurements, and real turbine and lidar data in Sections 7.3 to 7.5 show that tracking the optimal tip speed ratio can be significantly improved. However, the energy yield is only marginal and additional shaft loads cannot be avoided. This effect is consistent with the theoretical potential. A summary of the chapter and a proposal for extensions are given in Section 7.6.

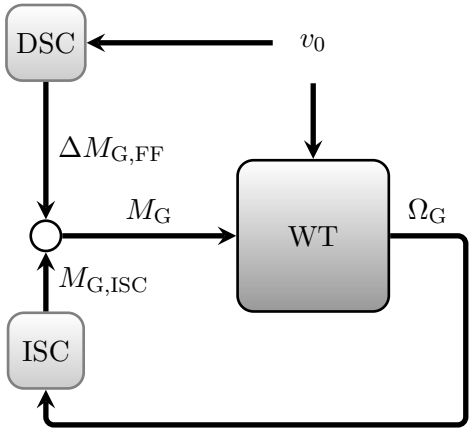

Figure 7.1: Torque control loop for below rated operation and additional feedforward update assuming perfect wind measurement.

7.1 Direct Speed Controller Design

The main control goal of the baseline torque controller as described in Section 3.4.1 is to maintain constant power in above rated wind conditions and to maximize the energy yield in below rated wind conditions. This is done by operating with the rotor blades held at the optimal angle of attack and consequently with the optimal power coefficient. The power coefficient for the 5 MW reference wind turbine is displayed in Figure 3.12 and in below rated wind speed depends only on λ, since the pitch angle is set to 0 deg. The optimal tip speed ratio λ_{opt} can be found at the peak $c_{\mathrm{P,max}}$. Thus, the aerodynamic optimum can be achieved by tracking λ_{opt} by adjusting the generator torque M_{G} as shown in Figure 7.1. Nonlinear state feedback controllers are commonly used in wind energy to control λ indirectly, measuring the generator speed Ω_{G}. Therefore, the baseline torque controller is also known as the Indirect Speed Controller (ISC). If the rotor effective wind speed v_0 is known, the tip speed ratio λ can be controlled directly, and therefore the proposed controller is considered as the Direct Speed Controller (DSC). Similar to Section 6.1, the controller design is split into two subsections. In a first step, the controller is design assuming perfect knowledge of the incoming wind speed and in the second step, realistic wind preview is considered.

7.1.1 Direct Speed Controller for Perfect Wind Preview

For the design of the direct speed controller, perfect knowledge of the rotor effective wind speed v_0 is assumed in a first step. The basic idea of the proposed DSC is to keep the ISC feedback law (3.39) and to find a feedforward update as illustrated in Figure 7.1 to compensate for changes in the wind speed similar to the one used for collective pitch control in Chapter 6.
The advantages of this structure are:

- The baseline controller can be kept. This is important especially for industrial application.

- The stability behavior of the speed control loop is not modified.
- If no wind preview is available, the feedforward part can be simply set to zero and the feedback can continue to operate without further adjustments.
- The feedforward update can be multiplied with a gain to smoothly enable the lidar-assisted control during testing or in the transition to region 2.

For the design of the feedforward controller the rotor speed error ε is introduced

$$\varepsilon = \Omega - \Omega_{\mathrm{opt}}, \tag{7.1}$$

where the optimal rotor speed Ω_{opt} is defined as

$$\Omega_{\mathrm{opt}} = \frac{\lambda_{\mathrm{opt}} v_0}{R}. \tag{7.2}$$

Using the drive train dynamics (3.3a) from the reduced model and (7.2), the dynamics of the error ε can be described by:

$$\dot{\varepsilon} = \dot{\Omega} - \dot{\Omega}_{\mathrm{opt}} = \frac{1}{J}\left(M_{\mathrm{a}} - \frac{M_{\mathrm{G}}}{i_{\mathrm{GB}}}\right) - \frac{\lambda_{\mathrm{opt}}}{R}\dot{v}_0. \tag{7.3}$$

With the proposed DSC

$$M_{\mathrm{G}} = M_{\mathrm{G,ISC}} \underbrace{-i_{\mathrm{GB}} J \frac{\lambda_{\mathrm{opt}}}{R}\dot{v}_0}_{\Delta M_{\mathrm{G,FF}}} \tag{7.4}$$

the error dynamics become

$$\begin{aligned}\dot{\varepsilon} &= \frac{1}{J}\left(M_{\mathrm{a}} - \frac{M_{\mathrm{G,ISC}}}{i_{\mathrm{GB}}}\right) \\ &= \frac{1}{2}\rho\pi R^5 \left(\frac{c_{\mathrm{P}}}{\lambda^3} - \frac{c_{\mathrm{P,max}}}{\lambda_{\mathrm{opt}}^3}\right)\Omega^2.\end{aligned} \tag{7.5}$$

Similar to [73], it can be shown that $\dot{\varepsilon} < 0$ if $\varepsilon > 0$ and $\dot{\varepsilon} > 0$ if $\varepsilon < 0$ as long as the tip speed ratio resides above a calculable lower limit. In the nominal case, changes in the wind will be perfectly compensated by the feedforward part $\Delta M_{\mathrm{G,FF}}$. For the non-nominal case, caused by inaccurate measurements or model uncertainties, the feedback part $M_{\mathrm{G,ISC}}$ compensates deviations from optimal operation.

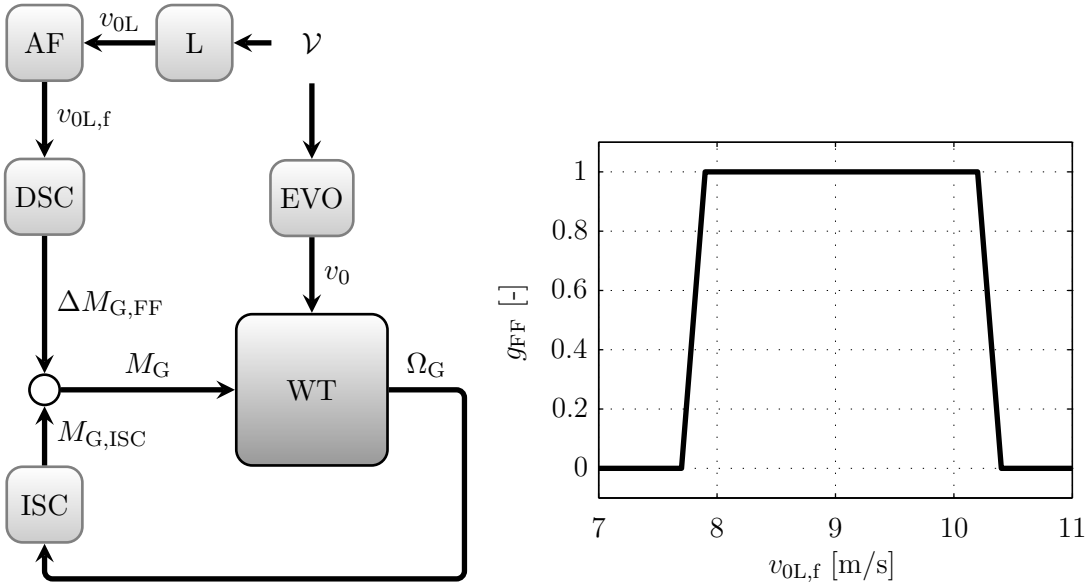

Figure 7.2: Left: Torque control loop for below rated operation and additional feedforward update assuming realistic wind preview. Right: gain to enable the feedforward update only in region 2 and to have a smooth transition.

7.1.2 Direct Speed Controller for Realistic Wind Preview

In the previous subsection, perfect knowledge of the rotor effective wind speed v_0 is required for the DSC. However, the lidar technology is only able to provide an estimate v_{0L} as pointed out in Chapter 4. The lidar measures in front of the wind turbine within the wind field $\mathcal{V}$ which will evolve on its way towards the rotor as illustrated in Figure 7.2 (left).
Similar to the adjustment of the collective pitch feedforward controller in Section 6.1, the adaptive filter proposed in Section 5.5 is used to fit the lidar estimate v_{0L} to the rotor effective wind speed v_0.
Additionally, the DSC is enabled with a gain function g_{FF} depending on the estimated and filter wind speed $v_{0L,f}$:

$$\Delta M_{G,FF} = -g_{FF}(v_{0L,f})\; i_{GB} J \frac{\lambda_{opt}}{R} \dot{v}_0. \tag{7.6}$$

The function is depicted in Figure 7.2 (right) and is set to 1 in region 2 (from 7.9 to 10.2 m/s) and 0 outside region 2 with linear ramps in between the sections starting at 7.7 m/s and ending at 10.4 m/s, for a smooth transition.
Higher-order error dynamics can be chosen and extended DSCs can be found as proposed in [77] and [98]. However, this entails additional feedback of the generator speed and is not further considered in this work.

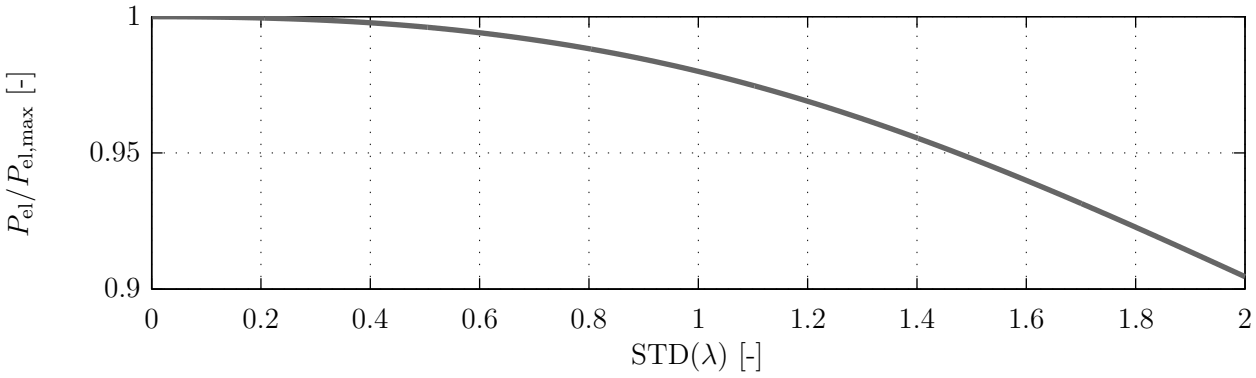

Figure 7.3: Relative power extraction for the 5 MW reference wind turbine depending on the variation of the tip speed ratio.

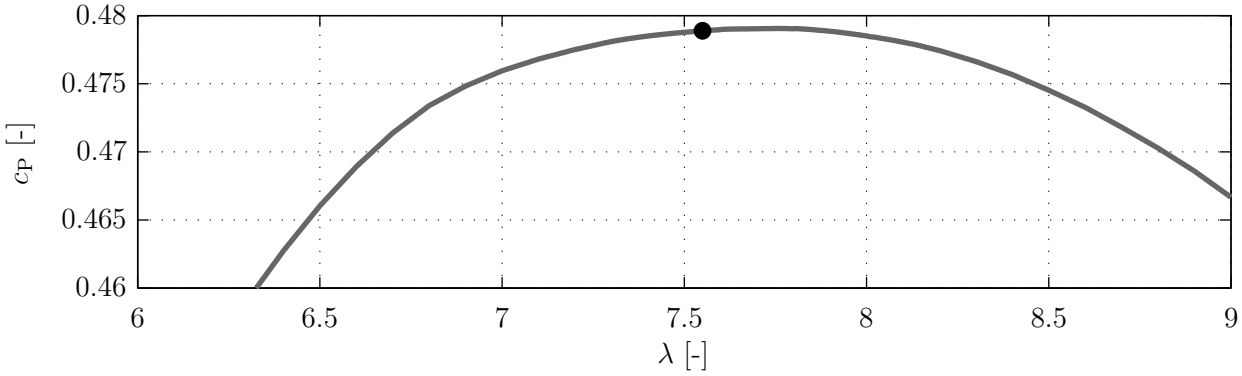

Figure 7.4: Position of the optimal tip speed ratio λ_{opt} from [63] on the power coefficient curve.

7.2 Potential of Direct Speed Control

The increase in energy production is obtained by improving the accuracy of tracking the optimal tip speed ratio λ_{opt}. Therefore, the fluctuation of the tip speed ratio can be used as a measure for the potential of energy optimization. Assuming the distribution of the tip speed ratio $\varphi_{\lambda_{opt};STD(\lambda)}$ to be Gaussian with mean λ_{opt} and with a standard deviation of STD(λ) (see Section 7.5 regarding this assumption), the generated power can be estimated by

$$P_{el}(\mathrm{STD}(\lambda)) = P_{el,max} \int_{-\infty}^{\infty} \varphi_{\lambda_{opt};\mathrm{STD}(\lambda)}\ c_P(\lambda)\ \mathrm{d}\lambda, \tag{7.7}$$

where $P_{el,max}$ is the maximum value which is obtained, if the tip speed ratio is always λ_{opt} and thus the power coefficient is constant $c_{P,max}$.

In Figure 7.3, this potential is quantified for the 5 MW reference wind turbine. This curve is very flat for low STD(λ) since λ_{opt} chosen in [63] is not exactly the maximum of the c_P curve (see Figure 7.4). Under this consideration, an improvement of 10 % as claimed in [35] would be possible, if the STD(λ) could be reduced from around 2 to 0.

7.3 Simulations Using Perfect Wind Preview

In a first simulation study, the DSC is tested assuming perfect wind preview as in Section 7.1.1. Additionally, the filter for the generator speed and the limits on the torque and torque rate are disabled. Then the reduced SLOW model (see Section 3.1.2) and the full aero-elastic FAST model (see Section 3.1.1) are disturbed by a coherent gust similar to [50], but only with a 1 m/s amplitude (minimum to maximum). The simulation results are plotted in Figure 7.5.
In the case of the SLOW model, the ISC reacts to wind speed changes slowly because the rotor speed varies slowly, see Figure 7.5 (left). During the transition of the gust, the tip speed ratio departs from the optimum λ_{opt}, resulting in a suboptimal angle of attack at the rotor blades and thereby reducing power extraction from the wind. As opposed to this, the DSC using a perfect wind preview can maintain the optimal operation of the turbine by holding the tip speed ratio much closer to λ_{opt} compared to the ISC. The small deviations are due to the model differences, since the DSC is designed based on the reduced model (neglecting the tower movements). A reduction of 96.5 % in the deviation from λ_{opt} is achieved over the controller without wind preview, see Table 7.1.
However, the generator torque M_{G} has to vary substantially to achieve the tracking of the optimal tip speed ratio and even is reaching negative values, extracting electrical power from the grid. Only marginal increase in the energy production (0.0431 %) is achieved over the simulation of 60 s.
Additionally, the maximum low-speed shaft torque M_{LSS} is increased by over 200 %.
If the more detailed FAST model is used, the proposed feedforward controller still can achieve almost perfect cancellation of the effect from v_0 to λ, see Figure 7.5 (right). Table 7.1 shows that the deviation from the optimal tip speed ratio λ_{opt} and the maximum moment M_{LSS} have similar values. The energy production is only increased by 0.0220 %.
Finally, these results can be summarized by:

- With perfect wind preview, the proposed direct speed controller is able to almost perfectly cancel out the effect from the rotor effective wind to the tip speed ratio, even for the full aero-elastic model.
- The direct speed controller provides an update to the generator torque of the baseline torque controller. The generator torque reaches negative values already for a wind acceleration of around $\dot{v}_0 = 0.8\,\text{m/s}^2$.
- However, no significant increase in power can be achieved.
- Similar to the results using the collective pitch feedforward controller in Section 6.2, the reduced model also sufficiently reproduces the behavior of the full aero-elastic model in below rated operation.

Table 7.1: Maximum values of the reaction to a small gust at 9 m/s in the case of perfect wind preview using the 5 MW reference wind turbine (see Figure 7.5).

	SLOW		FAST	
	$\Delta\lambda$ [-]	M_{LSS} [MNm]	$\Delta\lambda$ [-]	M_{LSS} [MNm]
ISC	0.533	2.56	0.543	2.59
DSC	0.019	5.67	0.038	5.38
$\frac{\mathrm{DSC}}{\mathrm{ISC}}$ [%]	3.5	221.5	7.0	207.4

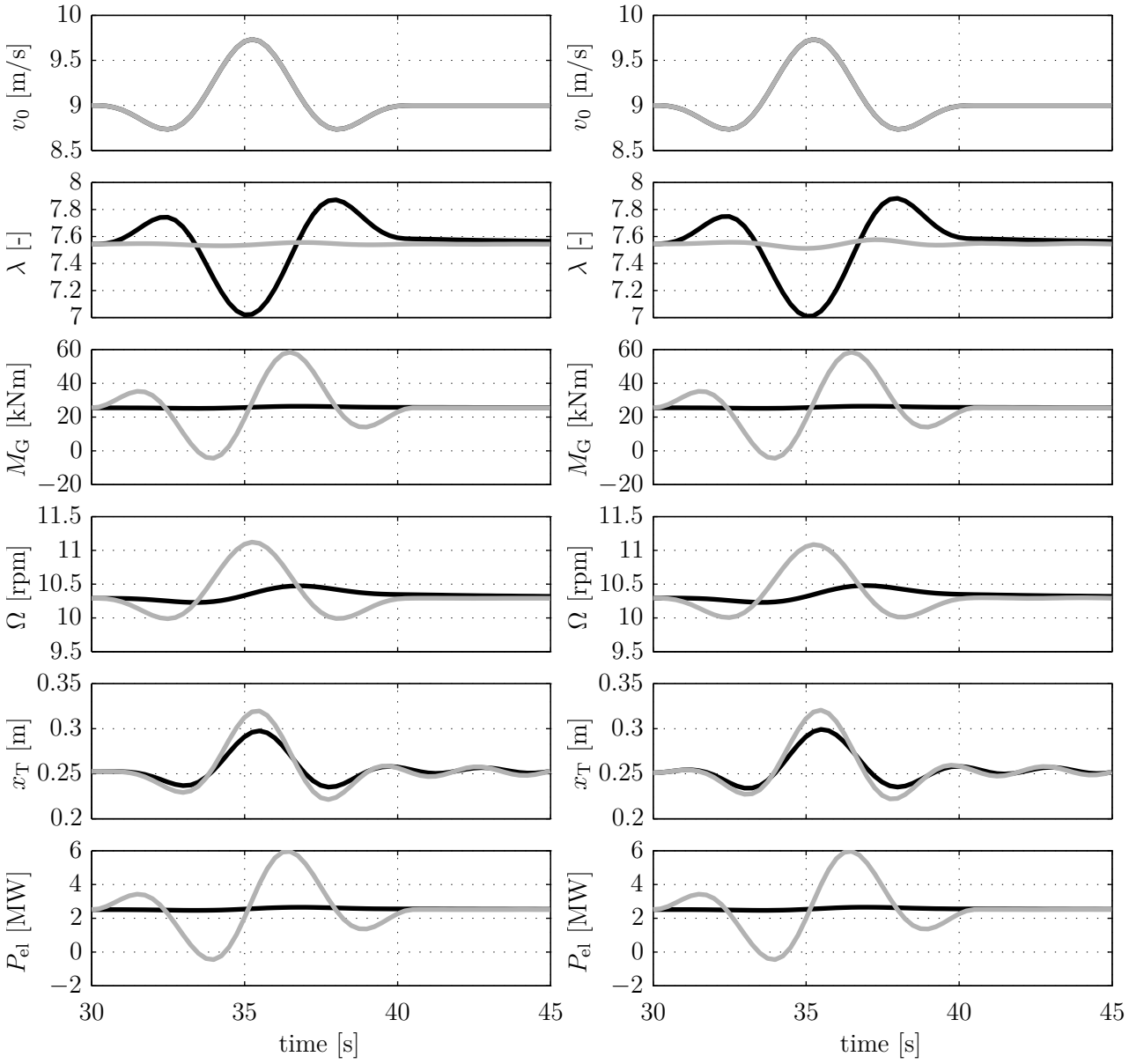

Figure 7.5: Reaction to a small gust at 9 m/s in the case of perfect wind preview using the 5 MW reference wind turbine. Simulated with reduced SLOW model (left) and full FAST model (right): Baseline torque controller only (ISC, black) and with additional feedforward (DSC, gray).

7.4 Simulations Using Simulated Lidar Measurements

The previous simulation study with perfect wind preview has shown that it is in principle possible to track the optimal tip speed ratio with the DSC based on a perfect wind preview. Although the DSC is designed based on a nonlinear model with only one dynamic state (rotor motion), it is able to maintain the tip speed ratio of the full nonlinear simulation model close to its optimal value, which indicates that the DSC is sufficiently robust against model uncertainties.

In a second simulation study, the robustness against measurement uncertainties of the wind preview is investigated by using simulated lidar measurements. As discussed in Section 7.1.1, an adaptive filter is necessary to fit the lidar estimate of the rotor effective wind speed to the real rotor effective wind speed. The filter depends on the mean wind speed and cancels out all uncorrelated frequencies and thus avoids unnecessary and harmful control action.

For this investigation, a turbulent wind field with mean wind speed of 9 m/s and a turbulence intensity of 8 % is used. The low turbulence level is chosen such that the rotor effective wind speed will always be within region 2 (from 7.9 to 10.2 m/s) during the 3630 s simulation. More details can be found in Table C.5. The simulations are done first with the feedback controller only (ISC, see Figure 7.2, the CPC is inactive due to the low wind speeds) and then with the additional direct speed controller, the adaptive filter, and the lidar simulator (ISC, DSC, AF, and L). The lidar simulator from Section 3.5, the optimized trajectory from Section 5.6, and the dynamic wind field reconstruction from Section 4.3 are used. As before, wind evolution is neglected for simplicity. The DSC is activated 30 s after the start and deactivated 30 s before the end of the simulation, so that the differences in energy production are not due to differences in the stored kinetic energy of the rotor.

Figure 7.6 illustrates the last 300 s of the simulation. In the upper part of the figure the rotor effective wind speed v_0 extracted from the wind field using (3.20) and its lidar estimate $v_{0\mathrm{L}}$ are displayed. At 30 s before the end, the feedforward gain g_{FF} is set to zero and thus both simulations coincide to end with the same kinetic energy in the rotor. The figure confirms the improved tracking of λ_{opt}, as seen before in the gust simulation with the reduced turbine model. However, the figure also displays a much higher generator torque and power variation.

In Figure 7.7 the lower PSD of the tip speed ratio λ when applying direct speed control can be observed most notably for frequencies below $f_{\mathrm{cutoff}} = \hat{k}\bar{u}/(2\pi) = 0.100\,\mathrm{Hz}$. However, the spectrum of the generator torque M_{G} is significantly increased over a broad frequency band due to the multiplication with $\dot{v}_0$ in (7.4). In addition, the rotor speed and the tower base fore-aft bending moment are increased for low frequencies.

A positive result is that as intended, the standard deviation STD(λ) is significantly reduced (see Table 7.2) due to the DSC. However, there is only a marginal increase of 0.0097 % in the

Table 7.2: Comparison of the results for the 1 h simulation at 9 m/s using the indirect speed controller (ISC) and using the direct speed controller (DSC).

	DEL(M_{yT}) [MNm]	DEL(M_{LSS}) [MNm]	DEL(M_{oop1}) [MNm]	STD(Ω) [rpm]	STD(λ) [-]	STD(P_{el}) [MW]	EP [MWh]
ISC	22.9	0.89	4.88	0.463	0.106	0.336	2.474955
DSC	23.8	1.63	4.91	0.489	0.039	0.393	2.475195
$\frac{\text{DSC}}{\text{ISC}}$ [%]	104.1	182.4	100.8	105.5	36.6	117.2	100.00970

energy production EP and a large increase in structural loads. The DELs for the tower base fore-aft bending moment M_{yT}, the low-speed shaft torque M_{LSS}, and the out-of-plane blade root bending moment M_{oop1} are calculated based on a rainflow counting with a Wöhler exponent of 4 (tower, shaft) or 10 (blades), a lifetime of 20 years, and a reference number of 2×10^6 cycles. The loads rise by approximately 5 %, 80 %, and 1 %. An additional negative effect is the increase of almost 20 % in power variation expressed by the standard deviation.
Furthermore, the results are compared with the theoretical potential from Section 7.2. Based on the reduction in STD(λ) from 0.106 to 0.039, the relative power extraction can be increased from 99.98806 % to 99.99839 %, see Figure 7.8. Thus, only an increase of 0.01033 % can be expected, which is quite close to the 0.0097 % obtained in the aero-elastic simulations.
The results from this simulation study are summarized as follows:

- The direct speed controller is able to significantly reduce the deviations from the optimal tip speed ratio also for simulations with simulated lidar measurements and the full aero-elastic model.
- The increase in energy production is marginal. The value accords to theoretical considerations. Since the baseline torque controller regulates the tip speed ratio already very close to the optimal value, even with the improved tracking of the tip speed ratio no large additional energy can be expected. This is due to the relatively flat power coefficient curve $c_P(\lambda)$ near λ_{opt} and the low variation of the tip speed ratio λ under normal conditions.
- As an important drawback of this technology, the structural loads primarily on the rotor shaft and the power variation are tremendously increased.

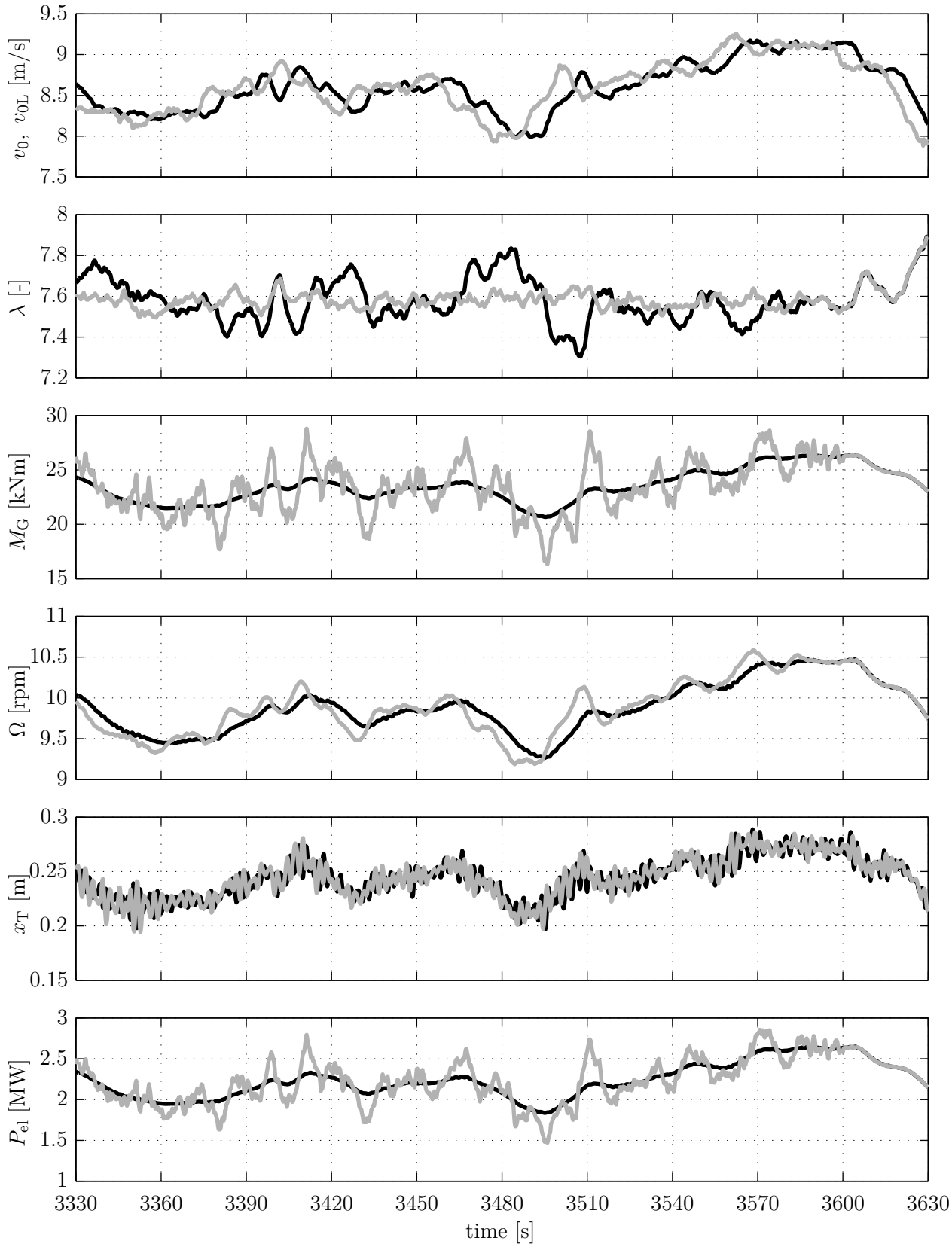

Figure 7.6: Reaction to a turbulent wind field with mean wind speed of 9 m/s using the FAST model of the 5 MW reference wind turbine (last 5 min). Top: rotor effective wind speed (black) and its lidar estimate (gray). Rest: Indirect speed controller (black) and direct speed controller (gray) using simulated lidar measurements.

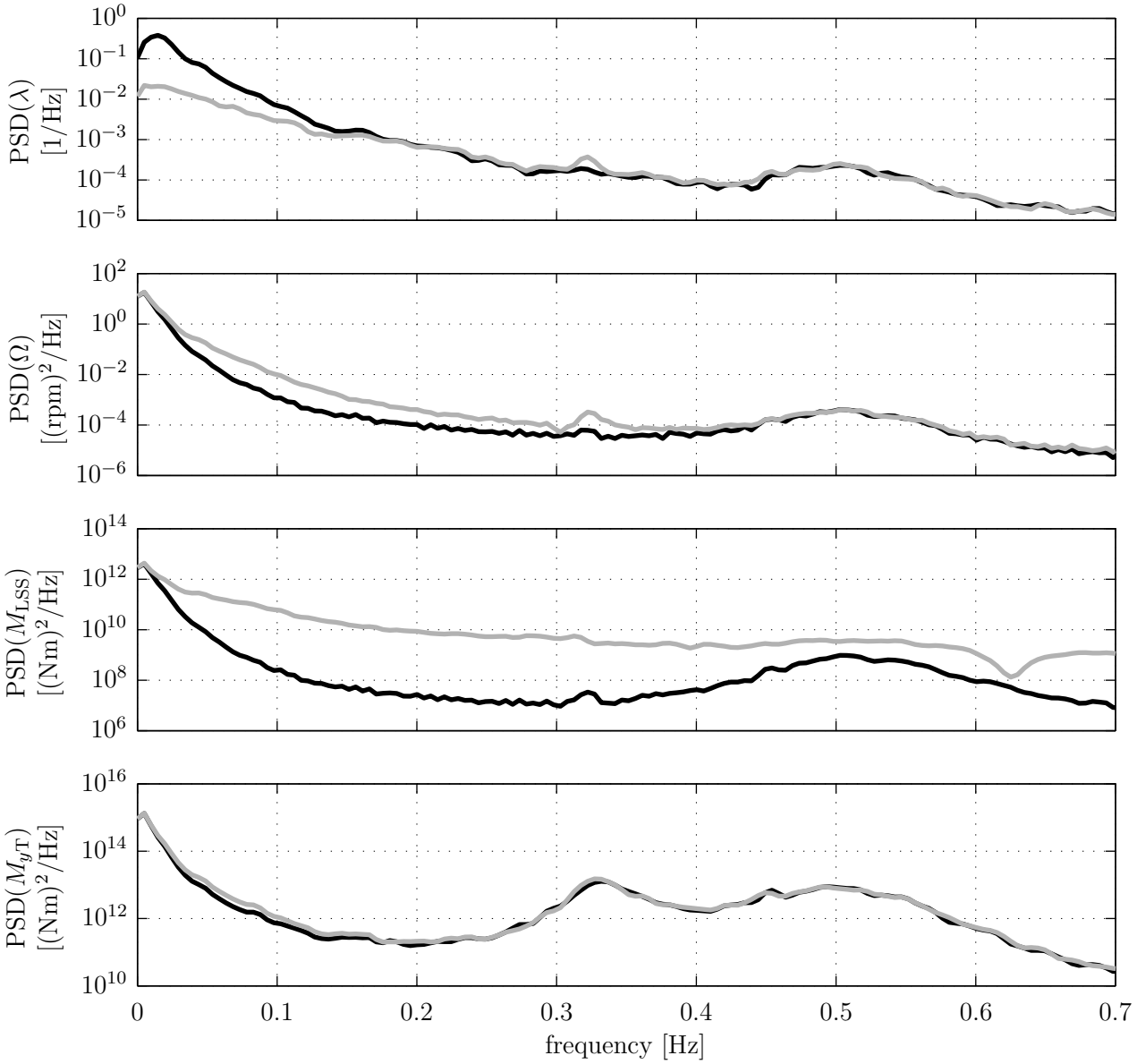

Figure 7.7: PSDs for the 1 h simulation at 9 m/s: Indirect speed controller (black) and direct speed controller (gray).

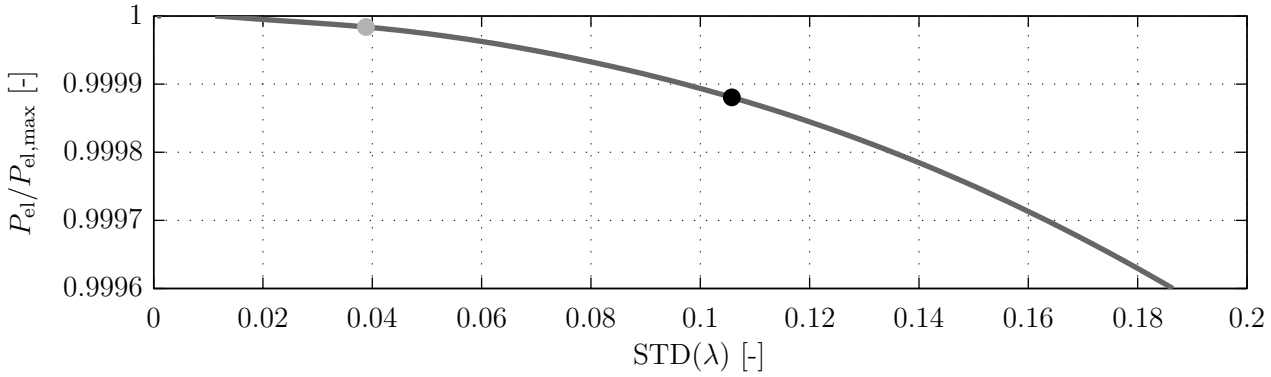

Figure 7.8: Relative power extraction for the 5 MW reference wind turbine. Dots: results from simulations with turbulent wind field with mean wind speed of 9 m/s: DSC (gray) and ISC (black).

In a next step, a lifetime of the 5 MW reference wind turbine is simulated similar to Section 6.3. With the turbulent wind fields of turbulence class "A" from Table C.4, the 5 MW reference wind turbine is simulated using the FAST model and both controllers. If simulated with the DSC, the lidar simulator with the optimal scan and the adaptive filter described above are used. The results such as DELs and STDs are weighted using a Weibull distribution with the scale parameter $C_{\mathrm{WB}} = 12\,\mathrm{m/s}$ and the shape parameter $k_{\mathrm{WB}} = 2$ (see Section 2.1.3 and 2.2.2).
The direct speed control algorithm is only applied if a wind within region 2 is detected by the simulated lidar using the feedforward gain g_{FF} from Figure 7.2. This is the case in the simulations with mean wind speed up to 16 m/s. In the other simulations, the wind speed is over 10.4 m/s over the full 3630 s. Also, the effect of the DSC is minor in the simulations with mean wind speed of 4 m/s and 6 m/s as can be seen in Figure 7.9, where the lifetime weighted results are plotted over the mean wind speed $\bar{u}$. Additionally, the difference between the energy production EP over the lifetime using the indirect and the direct speed controller is shown. As already indicated by the simulation with the reduced turbulence intensity above, the increase in energy is only marginal in the simulations where the wind turbine operates mainly in region 2. At higher wind speeds (14 m/s and 16 m/s), the effect is even negative because the maximum torque is reached and the DSC cannot perform as designed and energy is lost in the transition to full load operations. A negative impact is the significantly increased loads on the low-speed shaft torque M_{LSS} for the simulations from 6 m/s to 16 m/s. Furthermore, the tower base fore-aft moment $M_{y\mathrm{T}}$ and the blade root out-of-plane bending moment M_{oop1} of blade 1 are increased slightly.
Table 7.3 displays the overall performance. Similar to the investigation above, the energy increase of 34.3 MWh or 0.006 % over the lifetime is very small. This increase is bought dearly by increasing loads affecting the whole drive train including rotor shaft, gear box, generator, and bearings, represented by the low-speed shaft torque M_{LSS}, where the DEL increases by 36.2 %. The DELs on tower base and blade root and the STD on the pitch rate are only increased by less than 1 %. Additionally, the STD on rotor speed and electrical power rise by approximately 5 % and 12 %.
In summary, the results confirm that the concept of lidar-assisted direct speed control is considered achievable for large wind turbines but not attractive. Unfortunately, this holds also for smaller wind turbines as described in the next section.

Table 7.3: Comparison of the lifetime-weighted results for the DLC1.2 simulations using the indirect speed controller (ISC) and using the direct speed controller (DSC).

	DEL(M_{yT}) [MNm]	DEL(M_{LSS}) [MNm]	DEL(M_{oop1}) [MNm]	STD(Ω) [rpm]	STD($\dot{\theta}$) [deg/s]	STD(P_{el}) [MW]	EP [GWh]
ISC	85.3	2.85	13.12	0.579	0.447	0.5134	547.2914
DSC	85.9	3.89	13.19	0.608	0.450	0.5779	547.3257
$\frac{\text{DSC}}{\text{ISC}}$[%]	100.7	136.2	100.5	105.0	100.6	112.6	100.006

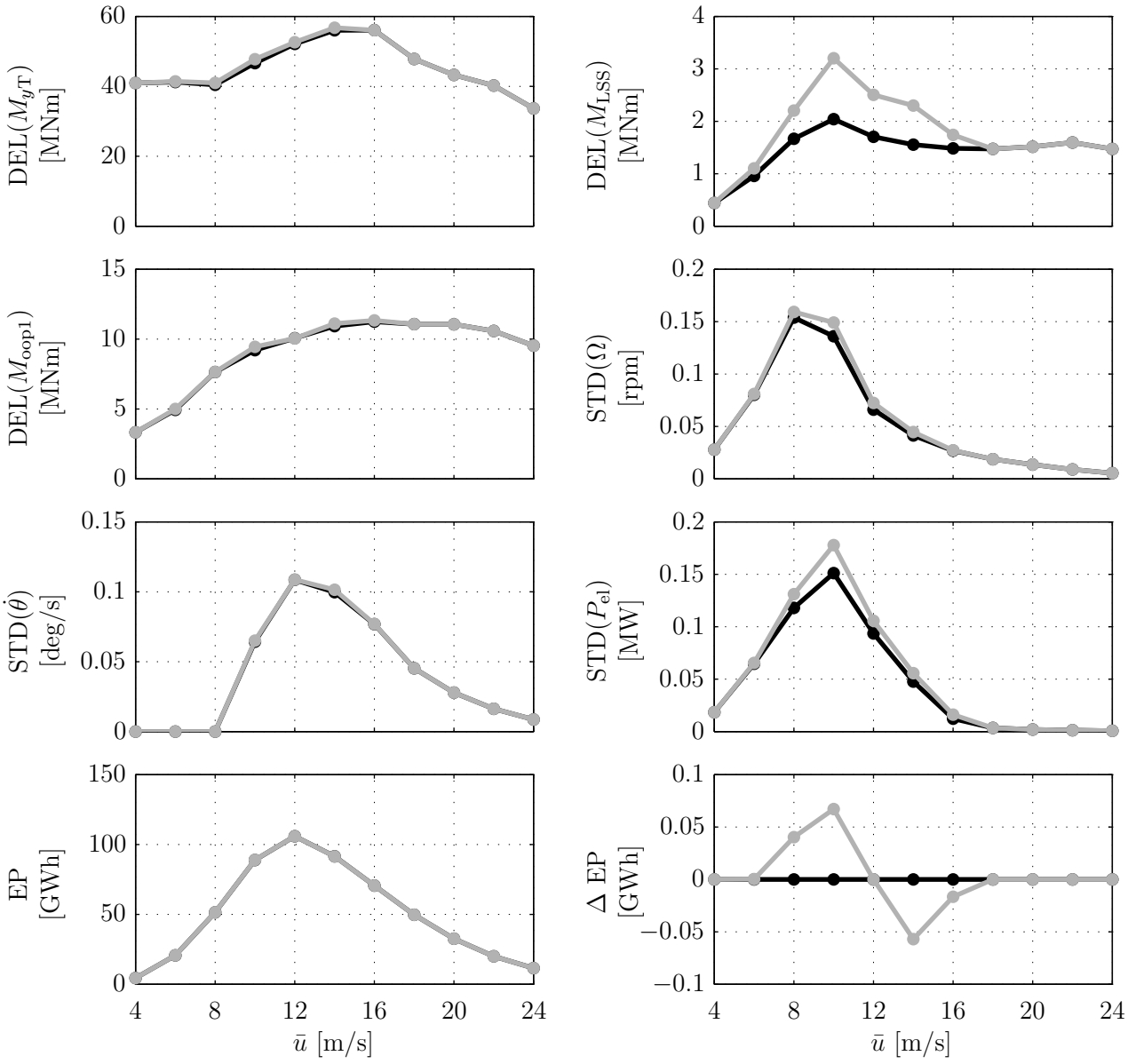

Figure 7.9: Lifetime-weighted results for the DLC1.2 simulations plotted over the mean wind speed: Indirect speed controller (black) and direct speed controller (gray).

Figure 7.10: The CART2 with the SWE scanning lidar system and the CART3 with a commercial lidar system at the NWTC during the field testing (May 2012).

7.5 Simulations Using Real Turbine and Lidar Data

Previous sections have indicated that for large turbines the marginal benefit of the direct speed controller in terms of increased power does not compensate for the increase of the shaft loads. However, the technique has not yet been adequately tested to make this determination conclusively. Further, it seems to be possible on a first glance that applying DSC to smaller turbines could be worthwhile because of the higher rotor speed fluctuations and the small rotor inertia. Additionally, the operation of optimal tip speed ratio of the CART3 spans over a relatively larger range of wind speeds (8 m/s) compared to that of the 5 MW reference wind turbine (2 m/s).

This section extends the previous work on direct speed controllers and provides a realistic examination into the benefits and detriments of using the DSC technique. A DSC is developed for the 600 kW CART3 experimental turbine at the NWTC and is evaluated theoretically and in simulation. Because this turbine already had a lidar system mounted for the field testing of collective pitch control [88], a field testing of the DSC was planned at the end of the wind season, when the CART3 was operating mostly at below rated power due to lower wind speeds. In a first step, data was collected from the turbine and lidar during operation and used to perform a hybrid simulation and evaluate the trade-offs involved with the inclusion of DSC. This technique allowed a realistic simulation to be performed, which provided good agreement with theoretical

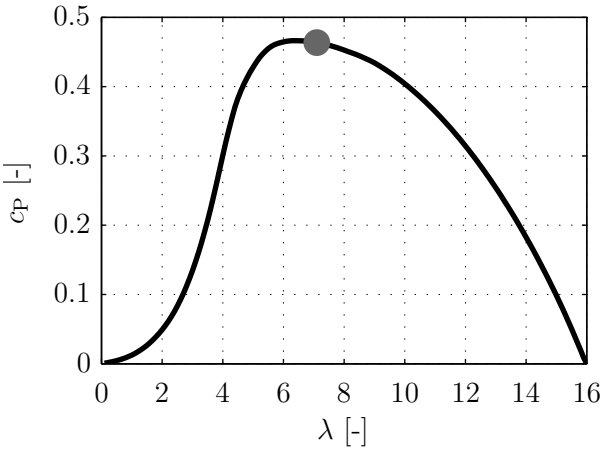

(a) Power coefficient c_P as a function of tip speed ratio λ for the CART3. Dot: $c_{P,max}$ at chosen λ_{opt} for region 2.

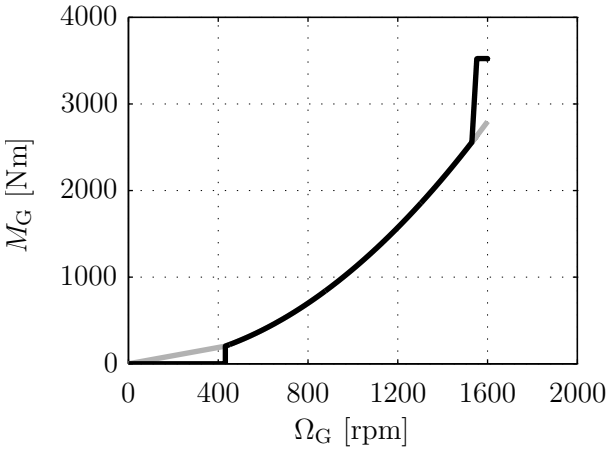

(b) Optimal relation of rotor speed and generator torque (gray), state feedback (black), and region 2 (overlapping region of the two lines).

Figure 7.11: Indirect speed control of the CART3.

predictions. The detailed simulation study with the mid-scale turbine yielded similar results compared to the 5 MW reference wind turbine: only marginal gain in energy production can be achieved with an additional increase of loads on the rotor shaft. Further, using the two-bladed CART2 as an alternative was no promising option, because the gain in energy production was expected to be marginal as well, since the shape of the power coefficient curve is similar to the CART3. Eventually, it was decided that the hybrid simulations sufficiently proved the point that the proposed concept is achievable but not attractive.
This section is based on [77] and is organized as follows. In Section 7.5.1, the lidar data processing and the controllers used are outlined. The correlation of the lidar and the turbine is described in Section 7.5.2. Section 7.5.3 presents the results of a simulation study based on the data. More details of the test environment can be found in Appendix A.2.

7.5.1 Controller Design

This subsection gives a short overview of the reconstruction of the rotor effective wind speed from the lidar data and the baseline and lidar-assisted torque controllers.

Indirect Speed Controller for the CART3

The main purpose of variable speed control for wind turbines below rated wind speed is to maximize the electrical power extraction by tracking the optimal tip speed ratio by adjusting the generator torque M_G. The optimal tip speed ratio can be found at the peak $c_{P,max}$ of the power coefficient curve, which depends below rated wind speed only on λ (see Figure 7.11a for the CART3). Typically, the generator torque is set such that λ is maintained optimally

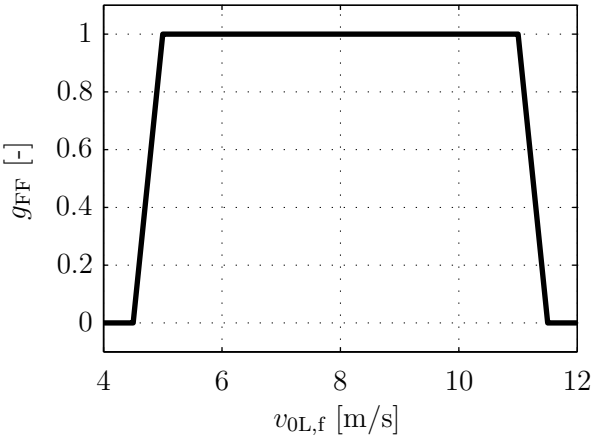

Figure 7.12: Feedforward gain for the CART3 to enable the feedforward update only in region 2 and to have a smooth transition.

in the static case. Nonlinear state feedback controllers are commonly used in wind energy to control λ indirectly by using measurements of the generator speed Ω_{G}. See Section 3.4.1 for more details. Figure 7.11b shows the piecewise defined ISC state feedback law $M_{\mathrm{G,ISC}}$ based on (3.39) for the CART3 with linear ramps for the transitions from startup ("region 1") and to full load ("region 3").

Lidar Data Processing and Direct Speed Controller for the CART3

The basic idea of the proposed DSC is to keep the ISC feedback law and to find a feedforward update to compensate for changes in the wind speed and therefore can easily be integrated into the existing control strategy. The DSC is designed for the CART3 according to Section 7.1 and is implemented into the same Dynamic Link Library (DLL) for the field testing of the collective pitch feedforward control.

It is only necessary to track the optimal tip speed ratio in "region 2". Therefore, the control update to the feedback controller ISC is multiplied with a feedforward gain g_{FF} depending on the rotor effective wind speed. For the CART3, region 2 is active approximately from 3.3 m/s to 11.5 m/s for $\rho = 1.0\,\mathrm{kg/m^3}$, the typical air density at NWTC. As illustrated in Figure 7.12, the feedforward gain g_{FF} is chosen to be 0 for values below 4.5 m/s (usually the CART3 is not operated below this point) and above 11.5 m/s and to be 1 for values between 5 m/s and 11 m/s with a linear ramp in between for smooth transitions.

The pulsed Optical Control System (OCS) from BlueScout Technologies used in this campaign measures the wind field along the line of sight of three independent fixed beams at three range gates upwind of the CART3. See Appendix A.2 for more details. Horizontal wind speed and direction as well as vertical wind speed and angle are derived from these measurements and then transferred to the control system for each range gate. Only the first range gate at 50 m is

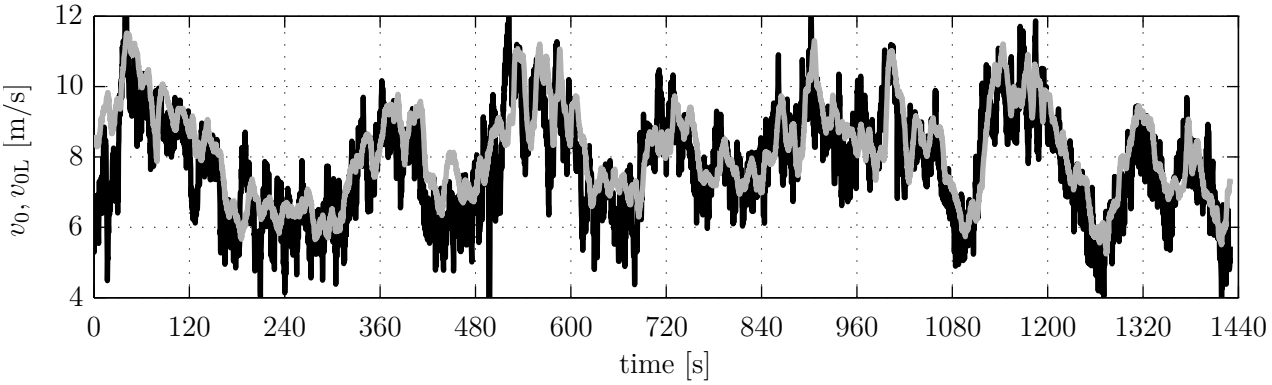

Figure 7.13: Comparison of the rotor effective wind speed estimated from the lidar system (black) and from turbine data (gray).

used in this investigation. In the control system, the longitudinal wind component is calculated from the horizontal wind speed and direction, which is then used as the lidar estimate of the rotor effective wind speed v_{0L}. Since v_{0L} contains uncorrelated frequencies, it cannot be used directly for feedforward control. As described earlier, an adaptive filter needs to be designed. This is done in the next subsection based on a correlation study.

7.5.2 Correlation Study

In this correlation study, the maximum coherent wavenumber $\hat{k}$ and the prediction time τ are determine for the filter design. Although no prediction time is needed in the controller design in Section 7.5.1, τ is used to compensate errors in the expected preview time or delays in the measurement process. Therefore, the estimated rotor effective wind speed v_{0L} from the lidar system is compared to the rotor effective wind speed v_0 from turbine data.

Estimator for the Rotor Effective Wind Speed

The rotor effective wind speed v_0 is obtained from simultaneously measured turbine sensor data by an estimator as proposed in Section 3.2.5. With the reduced system (3.26) and measured data of the rotor speed Ω, the pitch angle θ, and the low-speed shaft torque M_{LSS}, the aerodynamic torque M_a can be calculated and reorganized in a cubic equation in λ as in (3.28). The equation is solved a priori for a set of M_a, Ω, and θ, and a three-dimensional look-up table $v_0(M_a, \Omega, \theta)$ is generated, which can then be used online to yield a time series of v_0 by a three-dimensional interpolation. The turbine raw data is filtered by notch filters at turbine resonance and disturbance frequencies (such as 3P) before being used. The rotor effective wind speed v_0 is necessary for the filter design, but will also be used for simulations with real data.

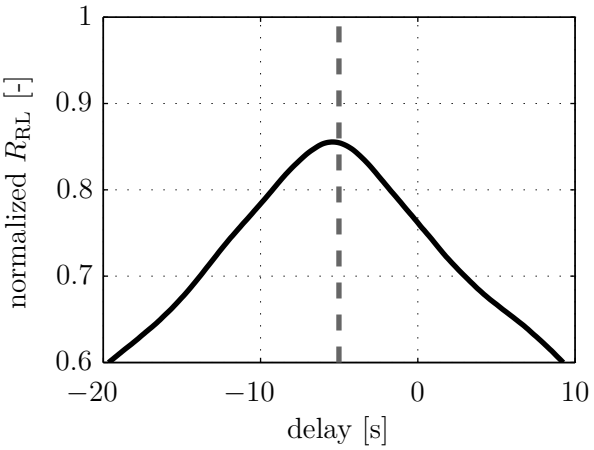

(a) Cross correlation between the turbine and the lidar (solid). The predicted preview based on Taylor's Hypothesis (dashed).

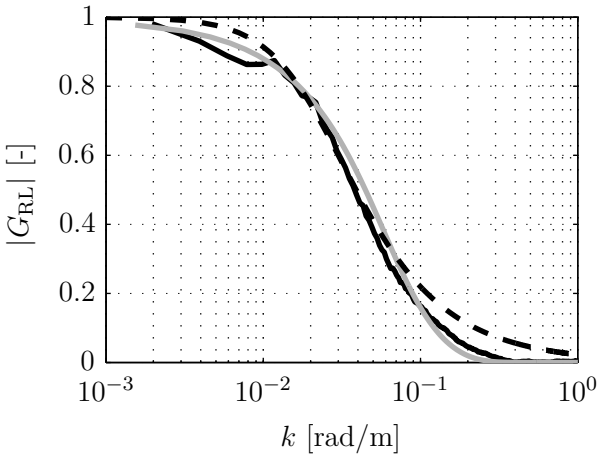

(b) Transfer function between the turbine and the lidar (black) and from the analytic correlation model (gray). The used filter (dashed).

Figure 7.14: Results from the correlation study between the CART3 and the OCS.

Design of the Adaptive Filter

For the filter design and the simulations, a 24-minute data set (21:44 - 22:08) from 03/29/2012 is analyzed with a mean wind speed of 8.37 m/s and a turbulence intensity of 16.7 % as measured by the met mast, fitting to lower turbulence characteristics (Class "C") according to current standards [50]. Figure 7.13 shows the rotor effective wind speed estimated from the lidar data and turbine data, showing the preview of the lidar measurement. This is more obvious in the cross correlation plot in Figure 7.14a: with $\tau = 0.6\,\mathrm{s}$, the time shift is close to the time shift according to Taylor's Frozen Turbulence Hypothesis.
Figure 7.14b depicts the measured transfer function between the v_0 and $v_{0\mathrm{L}}$ as well as the chosen filter. Additionally, the transfer function is calculated using the analytic model from Chapter 5. The measured and modeled transfer function agree very well and thus larger measurement errors can be filtered out. The maximum coherent wavenumber, as a compromise, is identified as $\hat{k} = 0.0225\,\mathrm{rad/m}$.

Expected Improvement

The tip speed ratio can be calculated with the signals of the rotor effective wind speed v_0 and the rotor speed Ω. Figure 7.15a confirms that a Gaussian distribution of the tip speed ratio λ is a reasonable assumption. For the data set, the measured mean value is $\bar{\lambda} = 7.26$ and the standard deviation $\mathrm{STD}(\lambda) = 0.589$. With these values and (7.7), the expectable increase in power can be calculated. Neglecting the deviation from $\lambda_{\mathrm{opt}} = 7.1$, the applied ISC is already at 99.6 % of the optimal value, according to the theory of Section 7.2.

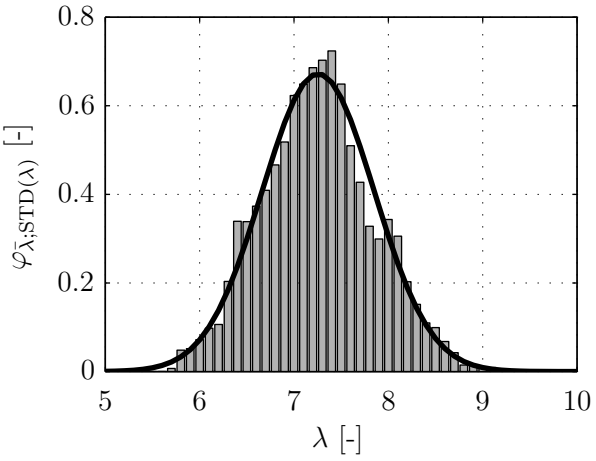

(a) Histogram of the measured tip speed ratio (gray) and assumed Gaussian distribution (black).

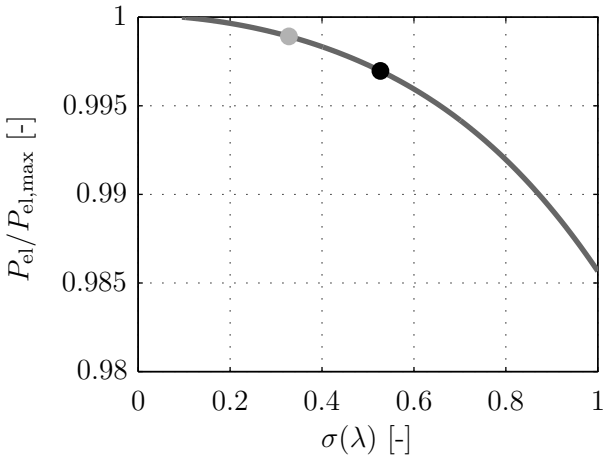

(b) Relative power extraction for the CART3. Dots: results from hybrid simulations with DSC (gray) and ISC (black).

Figure 7.15: Comparison of the theoretical potential of the DSC with real/simulated data.

7.5.3 Results of Hybrid Simulations

The raw lidar data and the estimated v_0 are used for simulations to test the DSC. The simulations are done with an aero-elastic model of the CART3 implemented in FAST, disturbed by a hub height wind field of v_0. FAST can be simulated in the MATLAB/Simulink environment, using the same controller that is exported to a DLL for field testing.

The hybrid simulation technique described in Section 3.5.2 is used for simulations to test the DSC under realistic conditions. In this case, the benefits over conventional simulations with lidar simulation and wind evolution models are that effects such as measurement errors and delays, real wind evolution, and site specific problems can be included into the simulations. If used along with the ISC controller, the simulated turbine's reaction will be close to the measured turbine data due to the fact that the used estimation of the rotor effective wind speed v_0 is an inverse process to the simulation. If used along with the DSC controller, it can be estimated in a realistic way, which effect the DSC would have produced in this specific situation. Furthermore, the DSC can be tuned to the real data.

For better evaluation, the DSC is activated 30 s after the start and deactivated 30 s before the end of the simulation. Thus, the differences in energy production is not due to differences in the stored kinetic energy.

Forty-nine simulations with different $\hat{k}$ and τ have been run. Figure 7.16 shows the changes in the standard deviation of λ and damage equivalent loads on the low-speed shaft, calculated based on a rainflow counting with Wöhler exponents of 4, which is typical for steel. The optimal values for $\hat{k} = 0.025\,\mathrm{rad/m}$ and $\tau = 1\,\mathrm{s}$ from a brute force optimization (minimizing $\mathrm{STD}(\lambda)$) are close to the values from Section 7.5.2. This confirms that it is important to filter the data

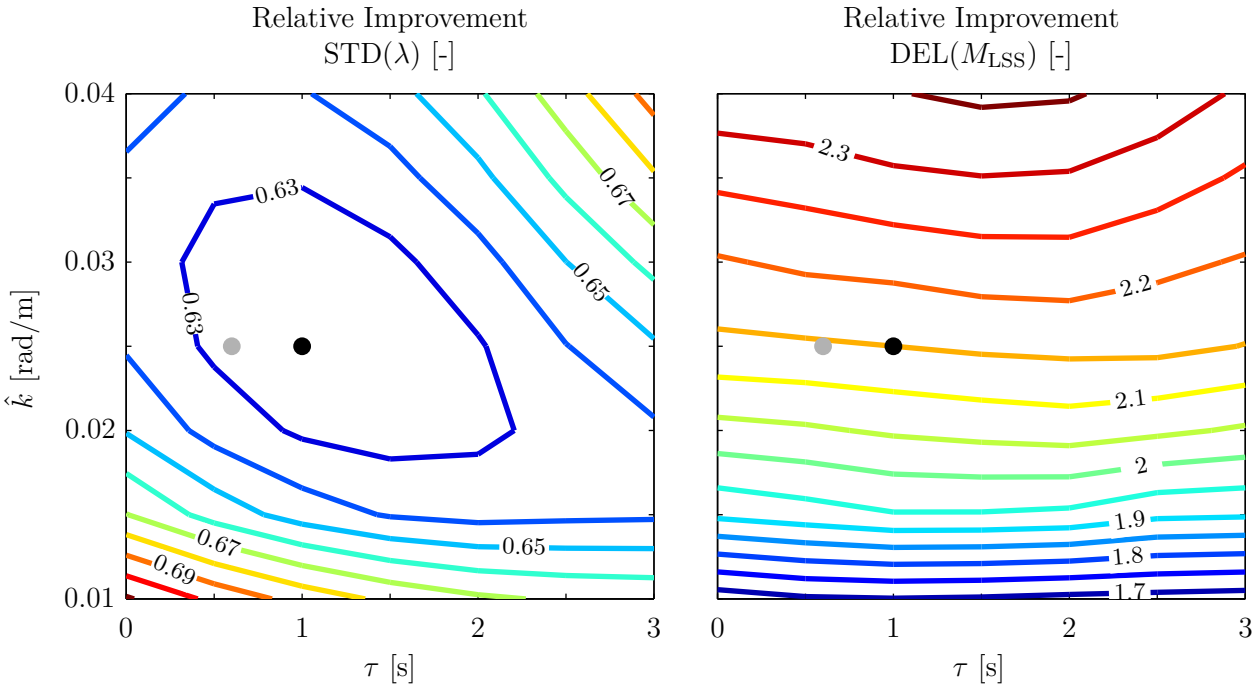

Figure 7.16: Relative changes of the DSC in the standard deviation of λ and low-speed shaft loads compared to the ISC. Dots: optimal case (black) and identified case (gray).

according to the specific correlation. It is not possible to lower $\hat{k}$ more than approximately $\hat{k} = 0.01\,\mathrm{rad/m}$ to reduce the low-speed shaft loads because the resulting time delay of the filter will cause the feedforward signal to be too late.

In Figure 7.17 and 7.18, the results of the optimal case can be seen in the time and frequency domain. The fluctuation in λ can be reduced by the DSC at the expense of higher fluctuation in the generator torque M_G. Here, STD(λ) can be reduced from 0.527 to 0.328, resulting in a power production increase of 0.3 %, which is close to the theoretical value of 0.2 % from Figure 7.15b. Changes may be due to slight changes in the mean value of λ.

However, the loads on the shaft are approximately doubled. This demonstrates that only marginal benefit can be gained by tracking the optimal tip speed ratio, which does not justify the usage due to the higher loads on the shaft.

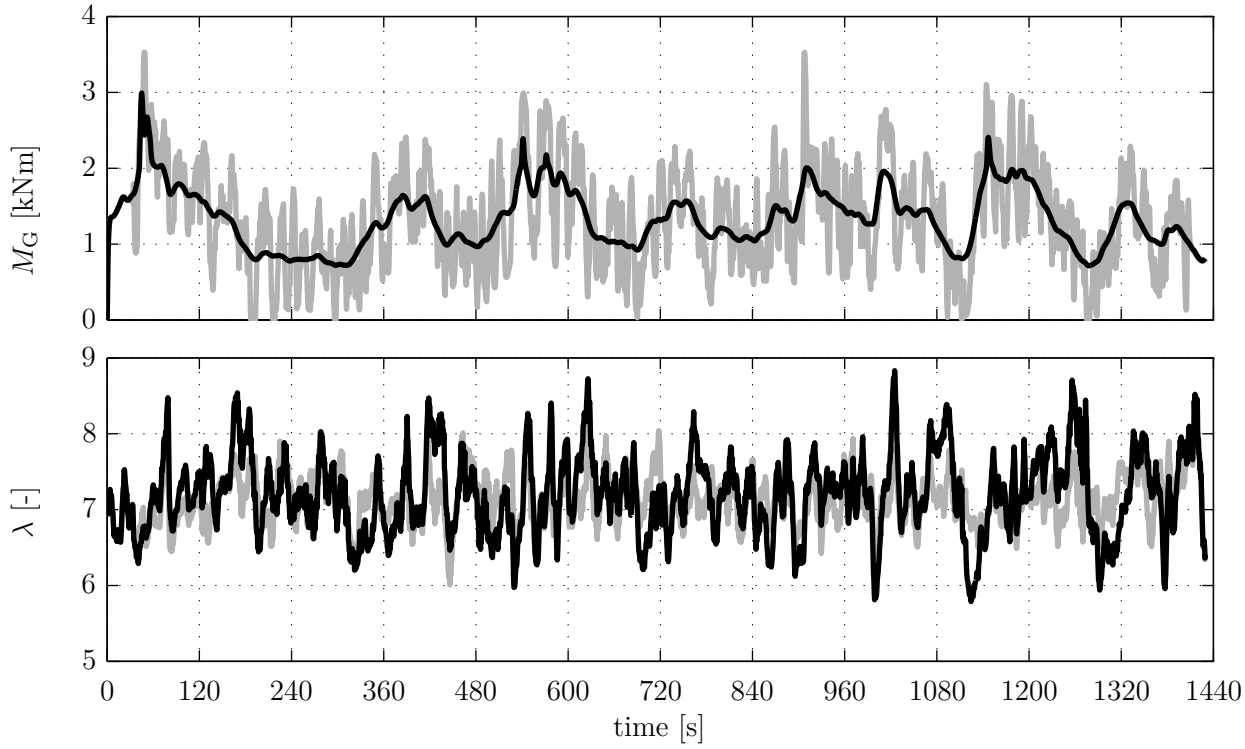

Figure 7.17: Simulated reaction of the CART3 to the wind of Figure 7.13: ISC (black) and DSC (gray).

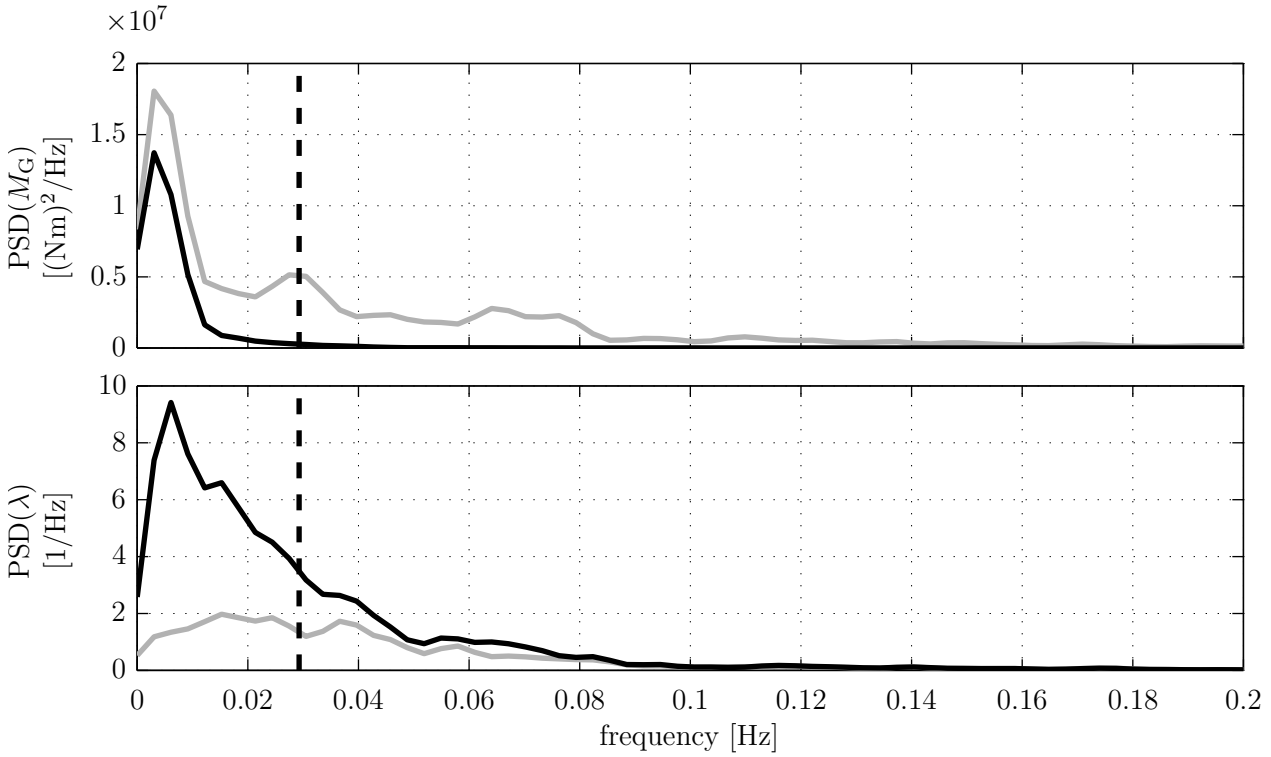

Figure 7.18: PSDs of the generator torque and tip speed ratio from Figure 7.17, ISC (black) and DSC (gray). Average cut-off frequency of the adaptive filter (dashed).

7.6 Summary and Possible Extensions for Direct Speed Control

In this chapter, a lidar-assisted feedforward update on a baseline torque controller has been presented to track the optimal tip speed ratio. Since lidar measurements make a direct measurement of the tip speed ratio possible, the controller is considered a Direct Speed Controller.

The controller is first designed assuming perfect wind preview using a reduced nonlinear wind turbine model. Under these assumptions, the controller is able to almost perfectly track the optimal tip speed ratio for the full aero-elastic model. However, only marginal increase in energy production can be achieved even using perfect wind preview. An estimation of the theoretical potential assuming Gaussian distribution of the tip speed ratio shows that a large reduction in the standard deviation of the tip speed ratio is necessary to have meaningful increase in energy production.

In a next step, the 5 MW reference turbine is simulated using a full aero-elastic model, a turbulent wind field, and a realistic lidar simulator. The rotor effective wind speed is then reconstructed from the lidar data and filtered by an adaptive filter to provide a signal, which is as close as possible to the real rotor effective wind speed, to the direct speed controller. In these simulations, the standard deviation of the tip speed ratio was shown to be reduced significantly by the direct speed controller compared to the baseline controller. However, the energy increase is still marginal, since the baseline controller already achieves a relatively low standard deviation of the tip speed ratio and the turbine operates already very close to the aerodynamic optimum. The low benefit in energy production can be confirmed by the theoretical considerations. Additionally, the damage equivalent loads on the shaft torsion are increased by 80 % due to the large inertia, which makes this approach even less attractive for large wind turbines. A lifetime analysis with higher turbulence intensity showed that there can be even negative effects to the energy production because of the generator torque limits. Over the lifetime of 20 years, there is only an increase of 0.006 % in energy production at the expense of almost 40 % increase of damage equivalent loads on the rotor shaft.

In a next step, simulations based on real data have been presented which show similar findings under real conditions with smaller turbines. With sensor data from a research turbine and the simultaneously gathered data from a commercial lidar system installed on the nacelle, the direct speed controller is optimized to account for the correlation of the lidar system and the turbine. The simulations emphasize that it is important to filter the data according to the correlation between the lidar data and the turbine data. The theoretical considerations about the limits of the direct speed controller can be validated. Although a reduction of 37.8 % in the standard deviation of the tip speed ratio can be achieved, the resulting energy gain is only 0.3 %. The loads on the shaft are approximately doubled. It was decided that the hybrid simulations sufficiently demonstrate that the proposed concept is achievable but also not attractive for

smaller turbines.
The results of this chapter indicate that future research with lidar-assisted control of wind turbines should focus on pitch and yaw control. However, assisting the torque control might still be useful for the following applications:

1. Lidar systems might be a good instrument to adjust the gain k_{ISC} of conventional torque controllers, if the aerodynamics of the blades are degraded by factors such as dirt or icing. By measuring the rotor effective wind speed independent from turbine parameters, long term drifts from the optimal tip speed ratio and can be detected. Additionally, the power coefficient can be displayed as a function of the tip speed ratio and the k_{ISC} can be adjusted with (3.39).

2. Feedforward control might be beneficial for baseline torque controller, which use a PI controller in the transition region from partial to full load for the generator torque instead of a ramp like the baseline controller in this work. The feedforward controller then could use the static generator torque curve similar to the collective pitch feedforward control and may introduce less loads on the shaft, since the rotor speed only needs to be held constant in this region and does not need to follow the wind changes as in region 2.

3. In combination with collective pitch control, a lidar-assisted generator torque control is very promising. Advanced feedforward control (see next chapter) or the NMPC approach [25, 29] show improvements over the collective pitch feedforward control especially in the transition region from partial to full load.

8

Flatness-Based Feedforward Control

The reduction of structural loads by advanced control is an important lever to lower the cost of wind energy. The feedforward collective pitch control presented in Chapter 6 is able to reduce structural loads for high wind speeds and can be easily combined with traditional feedback controllers for real life applications [95, 88]. However, computationally more complex controllers can mitigate loads even better by solving an optimal control problem and adjusting blade pitch and generator torque also around rated wind speed, where most of the turbine's damage is accumulated [25, 29, 30]. This chapter evaluates a flatness-based feedforward approach, which is considered by [99] to be a promising alternative to solving optimal control problems for industrial applications. The Tower EQUILibirum Accommodation (TEQUILA) introduced in [100] makes use of the flatness property of a reduced nonlinear wind turbine model. The approach allows the calculation of the control action based on trajectories of the rotor speed and tower motion using wind measurements. The trajectories are planned online, considering actuator constraints, to regulate the rotor speed and minimize tower movements. Providing a feedforward signal for both control inputs – collective pitch and generator torque – allows load reduction especially in the transition region between partial and full power operation. The control inputs are calculated with low computational effort and can be combined with conventional feedback control. This facilitates the application on commercial wind turbines. Simulations using a realistic lidar simulator and a full aero-elastic model show considerable reduction of tower and shaft loads. This chapter is organized as follows: In Section 8.1 the flatness-based feedforward controller is derived and evaluated in Sections 8.2 and 8.3 by simulations using perfect wind preview and simulated lidar measurements. Section 8.4 summarizes the chapter and points out possibilities for future work.

8.1 Controller Design

In this section, the flatness-based feedforward controller is derived. In a first step, perfect wind preview is assumed. In a next step, the controller is extended to deal with realistic wind preview such as provided by lidar systems.

8.1.1 Flatness-based Feedforward Controller for Perfect Wind Preview

For the considered 5 MW turbine and baseline controller, the highest static aerodynamic thrust and thus the largest tower deflection is at the rated wind speed $v_{\mathrm{rated}} = 11.3\,\mathrm{m/s}$, where the CPC starts to pitch the blades, see Figure 8.1. This results in high dynamic loading in the transition region, where the wind changes from below to above rated wind speed. The feedforward (FF) controller described in Chapter 6 uses the derivative of the static pitch curve and the wind speed measurement $v_{0\mathrm{L}}$ when the turbulence hits the turbine. It compensates the effect of wind speed changes to the rotor speed in (3.3a), neglecting the effects of the ISC. The benefit for the industrial application is that only a simple update to common baseline controllers is necessary. At high wind speeds, holding the aerodynamic torque M_{a} constant results in smaller changes in the aerodynamic thrust F_{a} and thus leads to tower load reduction (see Figure 6.5). But the FF control is only able to react if the PI controller is not saturated. Furthermore, close to v_{rated}, holding M_{a} constant results in high fluctuations of F_{a} due to the nonlinearities in c_{P} and c_{T}. Limiting the feedforward pitch rate close to v_{rated} is a heuristic solution. Designing a feedforward controller to hold F_{a} constant would cause contradicting control goals in the feedback and feedforward controllers.

A more direct solution is the NMPC, where a time series of the wind speed preview and a nonlinear model including the tower motion can be used to calculate repetitively an optimal trajectory for both the collective pitch command θ_{c} and the generator torque M_{G} while also taking the actuator and state constraints into account [29]. But solving the optimal control problem is computationally intensive and there is no guarantee to find the global minimum in the allotted time slot. Furthermore, the tower states x_{T} and $\dot{x}_{\mathrm{T}}$ have to be estimated, because only the acceleration signal $\ddot{x}_{\mathrm{T}}$ is available on standard wind turbines. The work in [30] concentrates on the transition region and proposes the combination of offline calculation based on dynamic programming and an online Trajectory Tracking Controller (TTC). Using a model of the rotor motion, higher load reduction compared to the FF without the need of state estimation and the computational effort of the NMPC can be achieved. Both NMPC and TTC may be the best solution in the future, but they have the drawback that they replace the baseline feedback controller. Thus, they are less attractive to turbine manufacturers. Because of safety concerns, the industrial state-of-the-art extends the baseline controller by various additional control loops such as tower feedback damping and individual pitch control [101].

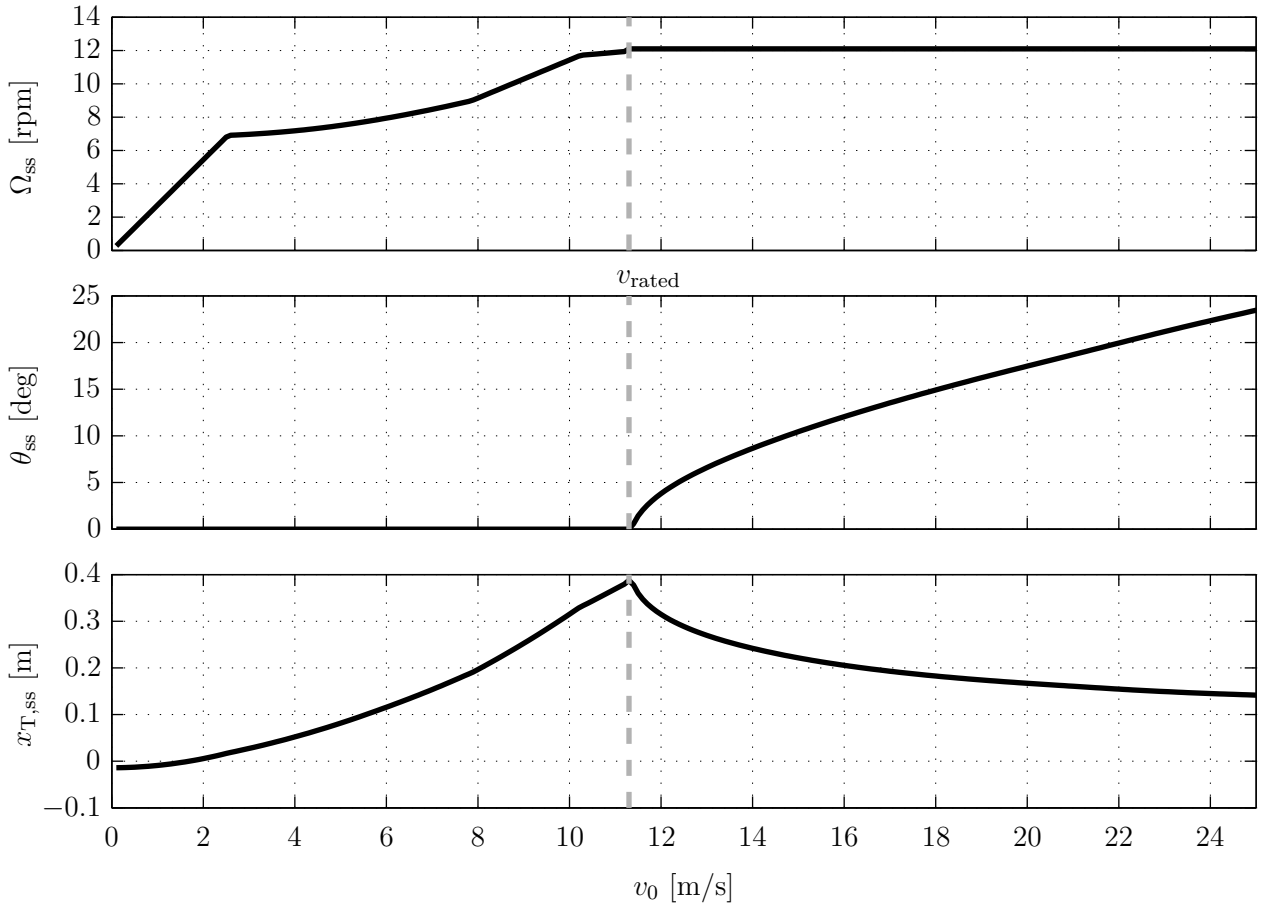

Figure 8.1: Steady-state values of the 5 MW reference wind turbine.

The proposed TEQUILA combines the advantages of the feedforward controller (update on existing feedback), the NMPC (considering tower deflection and wind preview over a time horizon, multivariable, considering constraints) and TTC (tracking of trajectories without extensive computational effort). It consists of a flatness-based feedforward controller and a trajectory planning algorithm and can be combined with a conventional feedback controller.

The Flat Wind Turbine

Flatness is a system property introduced by [102] that extends the concept of controllability from linear to nonlinear systems. A system is flat if a – not necessarily physical – so-called flat output exists such that all system states and inputs can be explicitly expressed in terms of the flat output and a finite number of its derivatives. This property can be used to plan an input trajectory on a nonlinear system based on the flat output.

The wind turbine model (3.3)-(3.11) with the states Ω, x_{T}, and θ and the control inputs M_{G} and θ_{c} is a flat system with the flat outputs x_{T} and Ω. Thus, all states and the system inputs can be expressed by the desired trajectories $x_{\mathrm{T,d}}$ and Ω_{d}, and their derivatives, which will be subsequently explained in detail. The disturbance v_0 can be considered as a time-varying

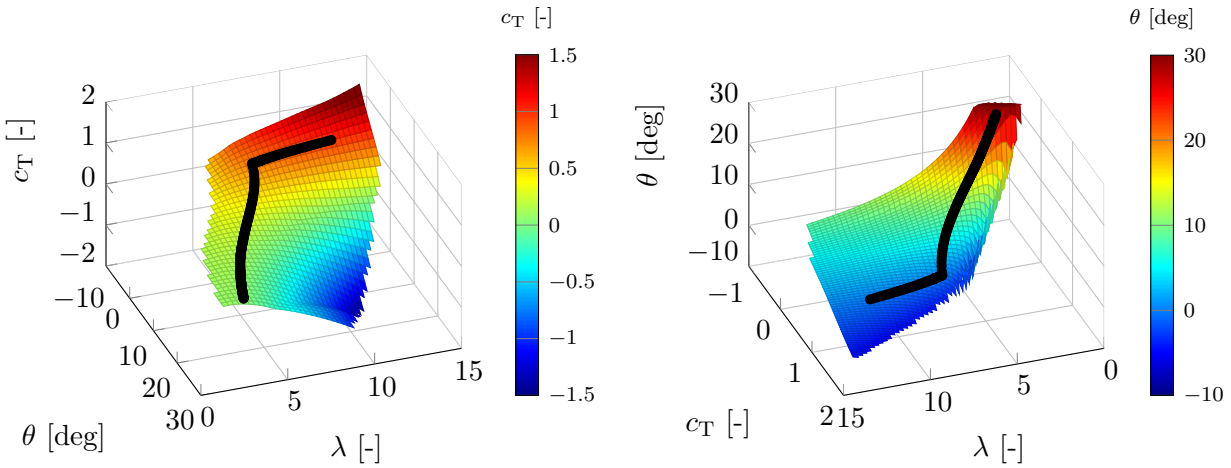

Figure 8.2: Considered area of the thrust coefficient (left) and its inverse regarding the pitch angle (right). Black lines are the steady values. Discretization of figures is reduced for better illustration.

parameter.

Using (3.10) and (3.11), the desired tip speed ratio λ_d and the desired relative wind speed are

$$\lambda_\mathrm{d} = \frac{\Omega_\mathrm{d} R}{v_\mathrm{rel,d}}, \tag{8.1a}$$

$$v_\mathrm{rel,d} = (v_0 - \dot{x}_\mathrm{T,d}). \tag{8.1b}$$

Based on (3.3b) and (3.9b) the desired thrust coefficient is

$$c_\mathrm{T,d} = \frac{2F_\mathrm{a,d}}{\rho\pi R^2 v_\mathrm{rel,d}^2}, \tag{8.2a}$$

$$\text{with } F_\mathrm{a,d} = m_\mathrm{eT}\ddot{x}_\mathrm{T,d} + c_\mathrm{eT}\dot{x}_\mathrm{T,d} + k_\mathrm{eT}(x_\mathrm{T,d} - x_\mathrm{0T}). \tag{8.2b}$$

The inverse $\theta(\lambda, c_\mathrm{T})$ of the three-dimensional look-up table $c_\mathrm{T}(\lambda, \theta)$ has been calculated, see Figure 8.2. Since a bijective relationship is necessary for the inversion (only one value of θ for each set of λ and c_T), only a sub-set of the look-up table for c_T is used. The bounds have been chosen such that the variation from the steady states under normal operation for wind speeds from 4 m/s to 30 m/s is covered.

With the inverse $\theta(\lambda, c_\mathrm{T})$, one obtains the desired pitch angle

$$\theta_\mathrm{d} = \theta(\lambda_\mathrm{d}, c_\mathrm{T,d}). \tag{8.3}$$

Due to the time delay T_B in (3.1), the future desired pitch angle is needed to calculate the desired demanded pitch angle $\theta_\mathrm{c,d}$, which is the first system input:

$$\theta_\mathrm{c,d}(t) = \theta_\mathrm{d}(t + T_\mathrm{B}). \tag{8.4}$$

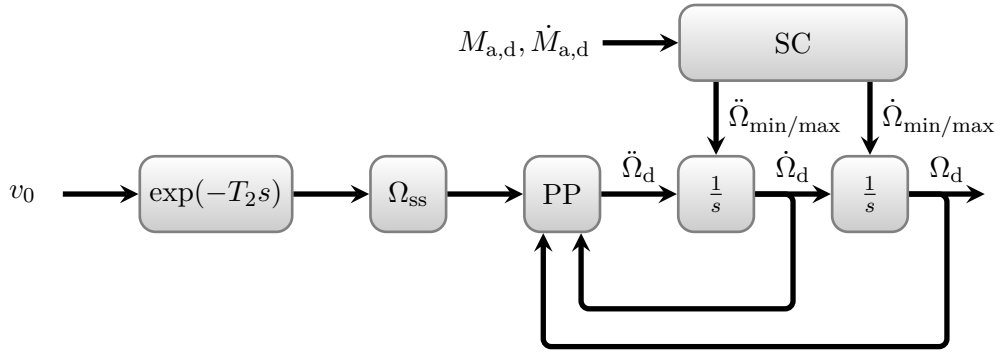

Figure 8.3: Online trajectory planning for the rotor motion.

Finally, the desired generator torque $M_{\mathrm{G,d}}$ – the second system input – can be obtained using (3.3a) and (3.9a):

$$M_{\mathrm{a,d}} = \frac{1}{2}\rho\pi R^3 \frac{c_{\mathrm{P}}(\lambda_{\mathrm{d}}, \theta_{\mathrm{d}})}{\lambda_{\mathrm{d}}} v_{\mathrm{rel,d}}^2, \tag{8.5a}$$

$$M_{\mathrm{G,d}} = i_{\mathrm{GB}} \left(M_{\mathrm{a,d}} - J\dot{\Omega}_{\mathrm{d}} \right). \tag{8.5b}$$

This confirms that the wind turbine model is flat with respect to the outputs Ω and x_{T}. There are unique trajectories for $M_{\mathrm{G,d}}$ and θ_{d} based on the desired trajectory for the tower and rotor states and the given wind speed v_0. Continuously differentiable trajectories for $x_{\mathrm{T,d}}, \dot{x}_{\mathrm{T,d}}, \ddot{x}_{\mathrm{T,d}}, \Omega_{\mathrm{d}}, \dot{\Omega}_{\mathrm{d}}$ are designed in the next section to provide smooth control.

Trajectory Planning

Flatness-based control is often used for trajectory planning to transfer a system from one equilibrium point to another. For wind turbine control, an online trajectory planning of the flat output is necessary to account for the changes in wind conditions. In this work, the trajectory planning is based on a second-order system for the rotor motion and a third-order system for the tower motion following [103].

For the trajectory of the rotor motion (see Figure 8.3), the rotor effective wind speed $v_{0\mathrm{L}}$ is first delayed by the buffer time T_2 and then transferred to a rotor speed set point with the static function Ω_{ss} (see Figure 8.1). The rotor motion is then shaped by the Pole Placement (PP). By choosing the two poles p_{21} and p_{22}, the second derivative of the rotor speed is

$$\ddot{\Omega}_{\mathrm{d}} = (p_{21}p_{22})\Omega_{\mathrm{ss}} + (p_{21} + p_{22})\dot{\Omega}_{\mathrm{d}} - (p_{21}p_{22})\Omega_{\mathrm{d}}. \tag{8.6}$$

In the block System Constraint (SC), the limits $\ddot{\Omega}_{\mathrm{min/max}}$ and $\dot{\Omega}_{\mathrm{min/max}}$ are calculated online based on $M_{\mathrm{a,d}}$ and its derivative from (8.5a) such that constraints for the generator torque

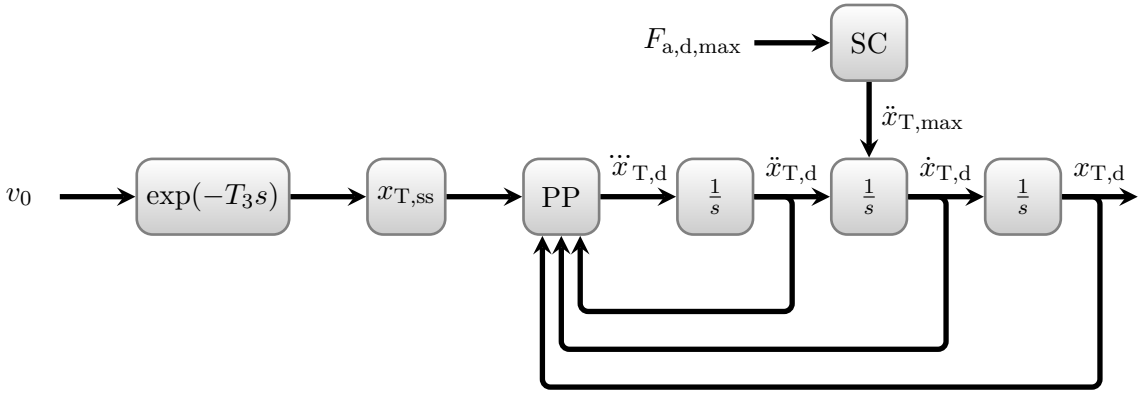

Figure 8.4: Online trajectory planning for the tower motion.

$M_{\mathrm{G,max/min}}$ and its rate $\dot{M}_{\mathrm{G,max/min}}$ are not violated:

$$\dot{\Omega}_{\mathrm{min/max}} = \frac{M_{\mathrm{a,d}}}{J} - \frac{M_{\mathrm{G,max/min}}}{i_{\mathrm{GB}} J}, \tag{8.7a}$$

$$\ddot{\Omega}_{\mathrm{min/max}} = \frac{\dot{M}_{\mathrm{a,d}}}{J} - \frac{\dot{M}_{\mathrm{G,max/min}}}{i_{\mathrm{GB}} J}. \tag{8.7b}$$

The desired rotor motion trajectories $\dot{\Omega}_{\mathrm{d}}$ and Ω_{d} are then obtained by applying the constraints and successive integration following [104]. The rotor dynamics are designed for low frequency tracking of the desired speed. The buffer time T_2 is set such that the rotor speed changes with the arrival of the wind field at the rotor.
The desired tower trajectories are planned in a similar way by choosing a buffer time T_3 and the poles p_{31}, p_{32}, and p_{33}, see Figure 8.4. With the poles and the steady tower position $x_{\mathrm{T,ss}}$, the third derivative of the tower top displacement is

$$\dddot{x}_{\mathrm{T,d}} = -(p_{31}p_{32}p_{33})x_{\mathrm{T,ss}} + (p_{31}+p_{32}+p_{33})\ddot{x}_{\mathrm{T,d}} - (p_{31}p_{32}+p_{31}p_{33}+p_{32}p_{33})\dot{x}_{\mathrm{T,d}} + (p_{31}p_{32}p_{33})x_{\mathrm{T,d}}. \tag{8.8}$$

The maximum allowed thrust $F_{\mathrm{a,d,max}}$ to stay above the minimum pitch angle θ_{min} is calculated and used to limit the tower acceleration:

$$F_{\mathrm{a,d,max}} = \frac{1}{2}\rho\pi R^2 c_{\mathrm{T}}(\lambda_{\mathrm{d}}, \theta_{\mathrm{min}}) v_{\mathrm{rel,d}}^2, \tag{8.9a}$$

$$\ddot{x}_{\mathrm{T,max}} = \frac{F_{\mathrm{a,d,max}} - c_{\mathrm{eT}}\ \dot{x}_{\mathrm{T,d}} - k_{\mathrm{eT}}\ (x_{\mathrm{T,d}} - x_{0\mathrm{T}})}{m_{\mathrm{eT}}}. \tag{8.9b}$$

The maximum pitch angle and pitch rate could be considered similarly. This was omitted here, because the exceedance of these constraints have been determined to be very unlikely.

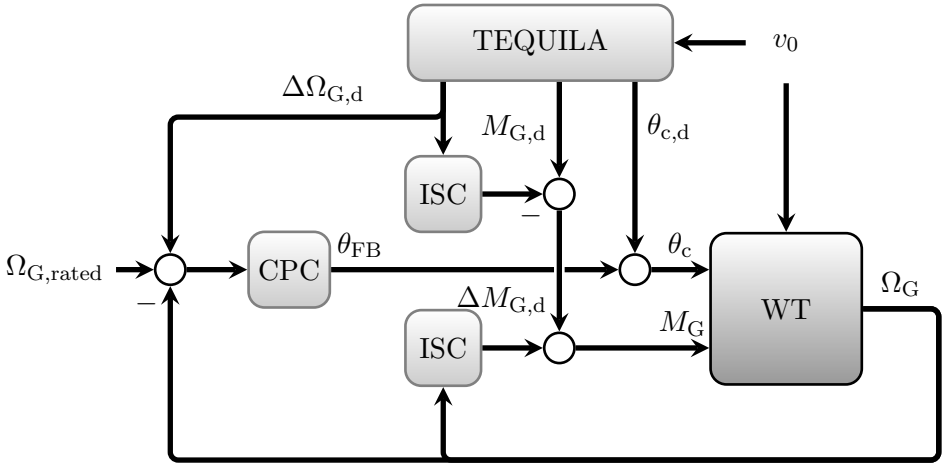

Figure 8.5: Closed loop of the combined feedforward-feedback controller.

Combined Feedforward-Feedback Controller

There are two main issues when combining the TEQUILA controller with the feedback controller as illustrated in Figure 8.5. First, all controllers need to have the same control objective. The common CPC has a constant reference value $\Omega_{\mathrm{G,rated}}$, while the desired generator speed

$$\Omega_{\mathrm{G,d}} = \frac{\Omega_{\mathrm{d}}}{i_{\mathrm{GB}}} \tag{8.10}$$

falls below this value for wind speeds below v_{rated}. This issue is solved by adding the deviation from the rated generator speed to the reference signal:

$$\Delta\Omega_{\mathrm{G,d}} = \Omega_{\mathrm{G,d}} - \Omega_{\mathrm{G,rated}}. \tag{8.11}$$

The desired generator speed could be used as in [100] as well. However, using $\Delta\Omega_{\mathrm{G,d}}$ gives the possibility to set this signal simply to zero if no wind speed preview is available.
The second issue is that the desired generator torque $M_{\mathrm{G,d}}$ cannot be simply applied to the nonlinear state feedback of the ISC. Thus, the desired generator speed $\Omega_{\mathrm{G,d}}$, the desired pitch angle θ_{d}, and an additional ISC are used to calculate a desired generator torque update $\Delta M_{\mathrm{G,d}}$. Furthermore, the generator torque in the transition from $M_{\mathrm{G,2.5}}$ in region 2.5 and $M_{\mathrm{G,3}}$ in region 3 of both ISCs is linearly interpolated using the switching signal σ_{R3} as proposed in [94] to avoid large differences if both ISCs are not switching simultaneously:

$$M_{\mathrm{G}} = \sigma_{\mathrm{R3}} M_{\mathrm{G,3}} + (1 - \sigma_{\mathrm{R3}}) M_{\mathrm{G,2.5}} \text{ with } \sigma_{\mathrm{R3}} = \begin{cases} 0, & \theta \leq \theta_{\mathrm{fine}} \\ 1, & \theta > \theta_{\mathrm{fine}} \end{cases} \tag{8.12}$$

Here, θ_{fine} is the minimum blade pitch angle for ensuring region 3 torque. Additionally, σ_{R3} is filtered by a first-order low pass filter with a time constant of 5 s.

8.1.2 Flatness-based Feedforward for Realistic Wind Preview

In the previous subsection, perfect knowledge of the rotor effective wind speed v_0 is required for TEQUILA. The lidar technology however is only able to provide an estimate $v_{0\mathrm{L}}$ as pointed out in Chapter 4.
Similar to the adjustment of the collective pitch feedforward controller in Section 6.1 and the direct speed controller in Section 7.1, the adaptive filter proposed in Section 5.5 is used to fit the lidar estimate $v_{0\mathrm{L}}$ to the rotor effective wind speed v_0.
This is done at two locations:

1. The lidar estimate $v_{0\mathrm{L}}$ is used unfiltered for the trajectory planning (instead of v_0 in Figure 8.3 and 8.4). However, the changing correlation with changing mean wind speed $\bar{u}$ is taken into account by choosing the first pole in both PPs as a function of the maximum coherent wavenumber $\hat{k}$ as

$$p_{21} = p_{31} = \frac{\hat{k}}{\bar{u}}. \tag{8.13}$$

   The two other poles of the tower trajectory planning are parameterized by the damping ratio D_3 and the frequency ω_3:

$$p_{32} = -D_3\omega_3 + \omega_3\sqrt{(D_3^2 - 1)},$$
$$p_{33} = -D_3\omega_3 - \omega_3\sqrt{(D_3^2 - 1)}.$$

   Thus, the flatness-based feedforward controller has the following 5 design parameters:

   - time delay T_2 for second-order system (rotor motion)
   - pole p_{22} for second-order system (rotor motion)
   - time delay T_3 for third-order system (tower motion)
   - damping ratio D_3 for third-order system (tower motion)
   - frequency ω_3 for third-order system (tower motion)

2. The lidar estimate $v_{0\mathrm{L}}$ is filtered by the adaptive filter and shifted in time such that the signal is available with time $\tau = T_{\mathrm{B}}$ before it reaches the rotor as described in Section 4.3. This signal is then used, on the one hand, to calculate the desired pitch angle θ_{d} and the desired generator torque $M_{\mathrm{G,d}}$ using (8.1) to (8.5b). On the other hand, it is used for the calculation of the constraints in (8.7) and (8.9).

8.2 Simulations Using Perfect Wind Preview

In this section, the flatness-based controller is compared to the feedback controller and the feedforward controller from Chapter 6 assuming perfect wind measurement. For this purpose, the reduced SLOW model (see Section 3.1.2) and the full aero-elastic FAST model (see Section 3.1.1) are disturbed by an EOG at $v_{\text{rated}} = 11.3\,\text{m/s}$ according to [50].
In the first simulation with the SLOW model, neither the feedback controller alone nor with the additional feedforward controller are able to avoid over-speeding of the rotor, see Figure 8.6 (left). The feedforward is able to hold the rotor speed very close to the rated value for 13 m/s (see Figure 6.4), but in this case the wind speed is partly below v_{rated} and thus the collective pitch feedforward controller is unable to react, since the static pitch curve θ_{ss} is zero. An oscillation of the tower cannot be avoided with the feedforward of the collective pitch alone. The flatness-based controller, which applies an update to the collective pitch and the generator torque, is not only maintaining the rotor speed below the rated value, but also is reducing significantly the movement of the tower. Since the static curve of the tower top displacement and the rotor speed vary with changing wind speed (Ω_{ss} is only constant for $v_0 > v_{\text{rated}}$), no constant values can be expected. The rotor and tower motion follow exactly the desired values even if the constraint of the minimum pitch angle is reached, because in this case, the simulation model and the internal controller model are identical. Only minor deviations occur because of numerical differences in the interpolation for the thrust coefficient and its inverse.
In the second simulation with the full aero-elastic FAST model shown in Figure 8.6 (right), the results are very similar. Table 8.1 lists the maximum values for the deviation from Ω_{rated} and the maximum tower base fore-aft bending moment $M_{y\text{T}}$. Both combined lidar-assisted controllers have lower values compared to the FB alone, but the TEQUILA performs significantly better than the FF. As the desired rotor speed is used for the reference value, the controller is able to raise the pitch angle without the need to compensate a negative speed error.
Finally, these results can be summarized by:

- Although perfect wind preview is unrealistic, the simulations show that TEQUILA using the internal SLOW model is robust with respect to model uncertainties when controlling the FAST model. Only small deviations from the desired trajectories are observed.
- For simulations with perfect wind preview and the reduced nonlinear model, the flatness-based controller is able to track exactly trajectories for the rotor and tower motion and thus holding the tower in its wind-speed-dependent equilibrium. For simulations with the full aero-elastic model, small deviations from the desired trajectories occur.
- For a EOG at rated wind speed, not only can rotor over speed be avoided, but the tower oscillation is also significantly reduced.

Table 8.1: Maximum values of the reaction to an EOG at $v_{\text{rated}} = 11.3\,\text{m/s}$ in the case of perfect wind preview using the 5 MW reference wind turbine (see Figure 8.6).

	SLOW		FAST	
	$\Delta\Omega$ [rpm]	$M_{y\text{T}}$ [MNm]	$\Delta\Omega$ [rpm]	$M_{y\text{T}}$ [MNm]
FB	1.59	112.6	1.71	115.6
FB+FF	0.58	94.7	0.59	92.1
FB+TEQUILA	0.24	65.5	0.38	66.8
$\frac{\text{FB+TEQUILA}}{\text{FB}}$ [%]	14.9	58.1	22.0	57.8

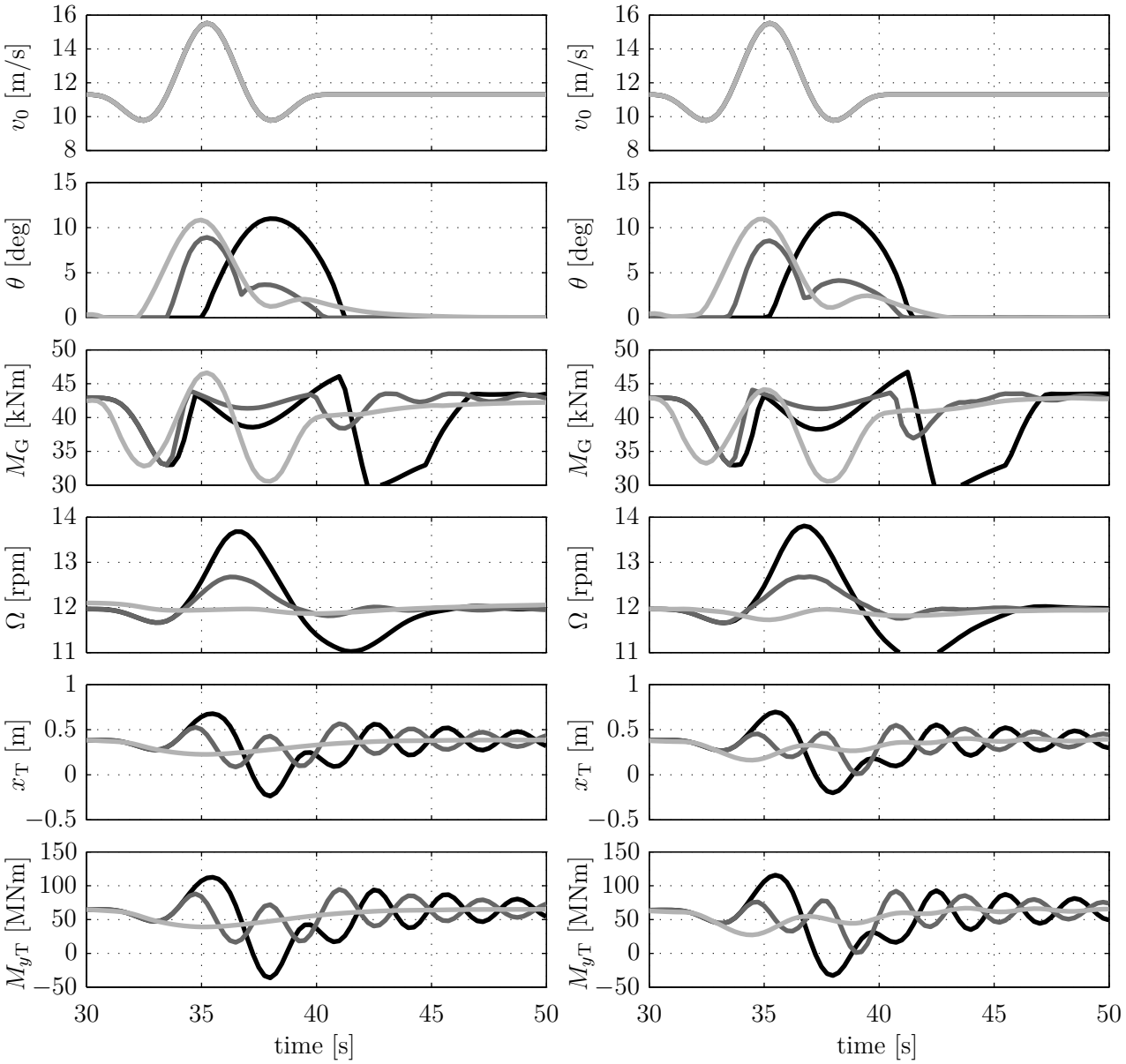

Figure 8.6: Reaction to an EOG at $v_{\text{rated}} = 11.3\,\text{m/s}$ in the case of perfect wind preview using the 5 MW reference wind turbine. Simulated with reduced SLOW model (left) and full FAST model (right): Feedback controller only (black), with additional feedforward (dark gray) and additional flatness-based feedforward (light gray).

8.3 Simulations Using Simulated Lidar Measurements

The previous simulation study with perfect wind preview showed that the flatness-based feedforward controller is able to shape the motion of the rotor speed and tower motion even in the nonlinear transition from partial to full load operations with an update of the collective pitch and generator torque to the baseline feedback controller. The wind turbine follows exactly the trajectories, if the reduced nonlinear model is used for simulations and is sufficiently robust against model uncertainties, if the simulation is performed with the full aero-elastic model.
In a second comparison, the flatness-based controller is evaluated regarding its behavior in turbulent wind conditions to investigate the robustness against measurement uncertainties. For this purpose, a wind field with mean wind speed of $\bar{u} = 12\,\mathrm{m/s}$ and a turbulence intensity of 14.6 % (IEC Class "C") is generated. The low turbulence level is chosen to focus on the transition between partial and full load operations. Details can be found in Table C.6. The simulation with the FF and the TEQUILA is performed with the lidar simulator from Section 3.5, the optimized trajectory from Section 5.6 and the dynamic wind field reconstruction from Section 4.3.
Figure 8.7 depicts that TEQUILA is able to reduce the oscillation of the tower compared to the FB only case – especially when the wind speed is crossing v_{rated}. Damage equivalent loads of the tower base fore-aft bending moment $M_{y\mathrm{T}}$, the low-speed shaft torque M_{LSS}, and the blade root out-of-plane bending moment M_{oop1} can be alleviated by approximately 30 %, 10 %, and 10 %, respectively. This is achieved with a reduced standard deviation of the pitch rate (about 40 %) and without increasing the power variation, see Table 8.2. Additionally the mean of the electrical power P_{el} is improved by more than 0.5 %. Only the standard deviation of the rotor speed is increased by 5 %. Compared to the collective pitch feedforward controller (FB+FF case), improvements can be achieved mainly in tower loads and pitch activity. However, the benefits in this work are less significant compared to the one reported in [100], since on the FB and the FF have been modified, but the FB is not re-tuned. Also the PSDs in Figure 8.8 show similar behavior for both lidar-assisted controller with slightly larger improvements over the FB case for the flatness-based controller. Oscillations at the damped tower eigenfrequency (0.322 Hz) and the blade passing frequency (0.605 Hz) are not affected.
However, finding a good set of the five tuning parameters of the flatness-based controller listed above has been difficult, since no intuitive way could be found for the adjustment of the control actions. With the proposed trajectory planning, the trajectories of the control inputs cannot be influenced directly as for example in the cost functional of an NMPC [29].
Finally, the flatness-based feedforward controller is able to outperform the collective pitch feedforward controller also in simulations using simulated lidar measurements, but showed less robustness against the measurement uncertainties and is more difficult to tune.

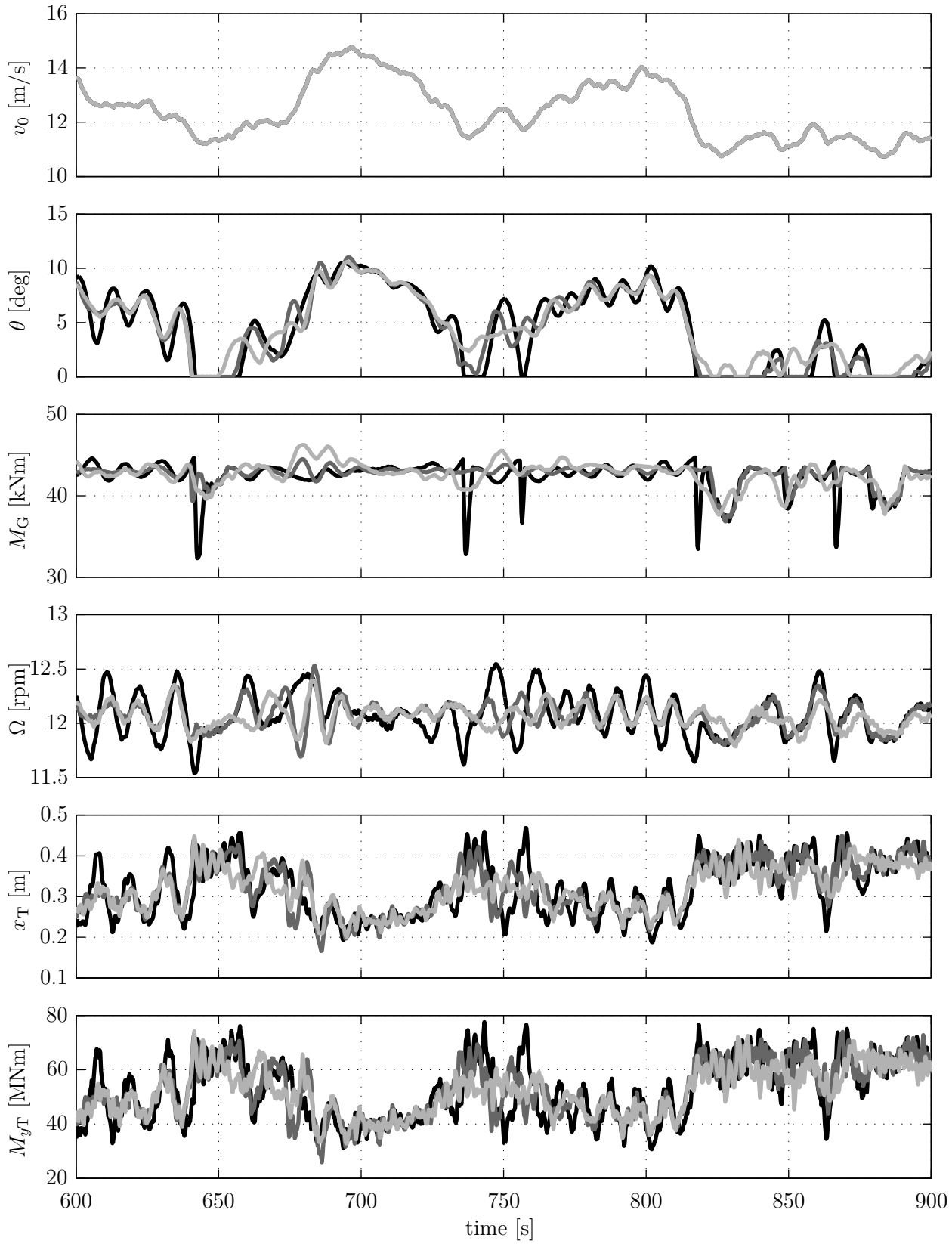

Figure 8.7: Reaction to a turbulent wind field with mean wind speed of 12 m/s using the FAST model of the 5 MW reference wind turbine (illustrative 5 min excerpt). Top: rotor effective wind speed (black) and its lidar estimate (gray). Rest: Feedback controller only (black) and with additional feedforward (dark gray) with additional flatness-based feedforward (light gray).

Table 8.2: Comparison of the results for the 1 h simulation at 12 m/s using the feedback controller alone (FB), using feedback and feedforward controller (FB+FF), and using feedback and flatness-based feedforward controller (FB+TEQUILA).

	DEL(M_{yT}) [MNm]	DEL(M_{LSS}) [MNm]	DEL(M_{oop1}) [MNm]	STD(Ω) [rpm]	STD($\dot{\theta}$) [deg/s]	STD(P_{el}) [MW]	EP [MWh]
FB	74.3	2.33	10.46	0.324	0.730	0.5316	4.7128
FB+FF	57.1	2.07	9.57	0.279	0.508	0.5231	4.7373
FB+TEQUILA	52.3	2.07	9.20	0.343	0.452	0.5304	4.7394
$\frac{\text{FB+TEQUILA}}{\text{FB}}$ [%]	70.4	88.8	87.9	105.9	61.9	99.8	100.564

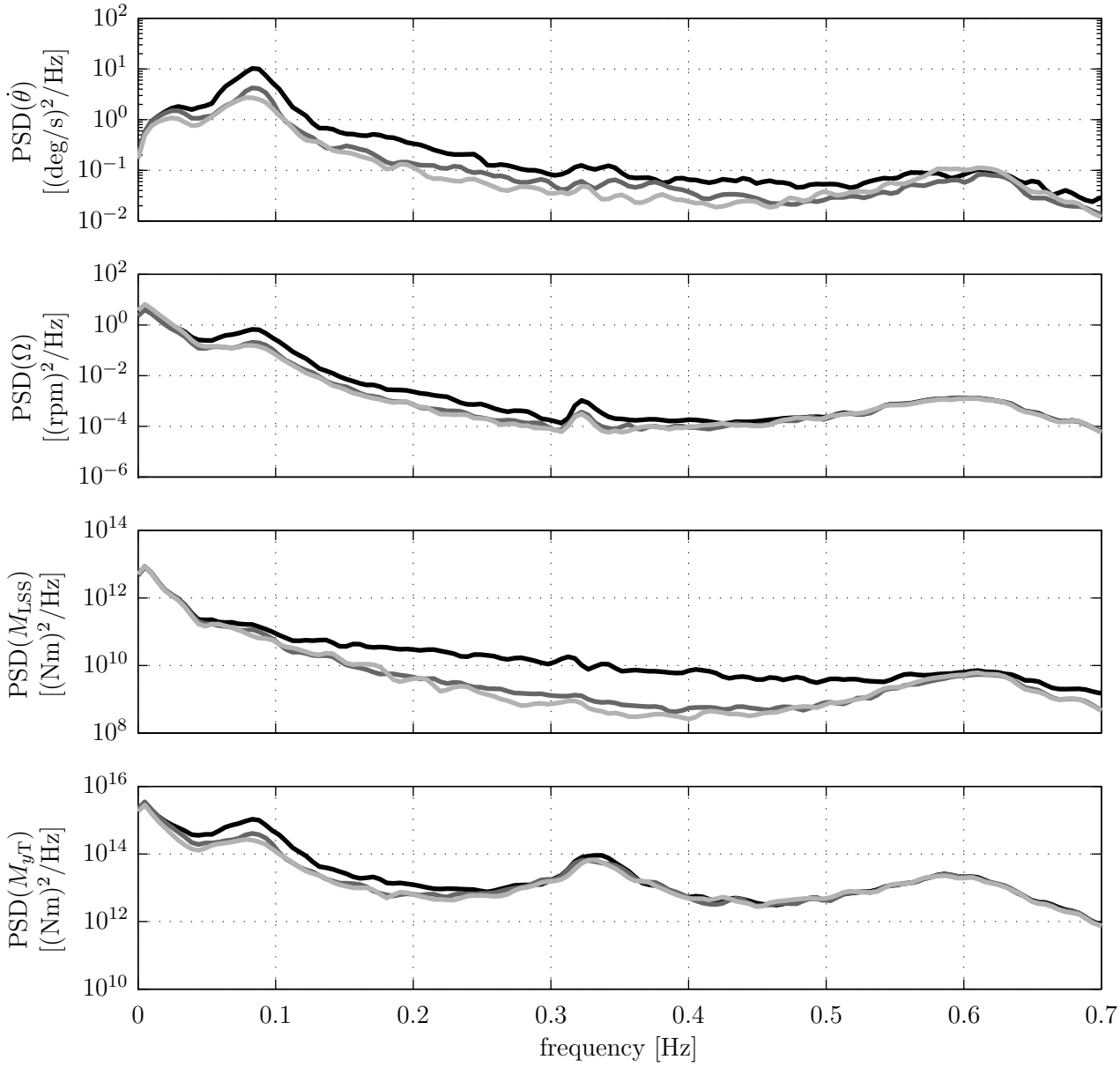

Figure 8.8: PSDs for the 1 h simulation at 12 m/s of FB (black), FB+FF (dark gray), and FB+TEQUILA (light gray).

8.4 Summary and Possible Extensions for Flatness-Based Control

This chapter presents a flatness-based approach to improve wind turbine control based on the preview wind information provided by lidar technology. It can be shown that the reduced nonlinear wind turbine model features the system property of differential flatness. Based on the wind speed of a simulated lidar device and considering the system constraints, trajectories of rotor speed and tower movement are continuously designed during operation and due to the flatness translated into trajectories for the pitch angle and generator torque control inputs. The trajectories are planned to hold the tower on its equilibrium manifold during the transition between partial and full load operations. The flatness-based feedforward controller is combined with a conventional feedback controller. If perfect wind preview is assumed, the flatness-based controller outperforms also the collective pitch feedforward controller of Chapter 6 because of the possibility to provide an update for the collective pitch angle and the generator torque simultaneously. The flatness-based controller is also able to hold the full aero-elastic model on the designed trajectories and thus exhibits sufficient robustness against model uncertainties. Simulations with turbulent wind and a lidar simulator still show good performance in the presence of additional measurement uncertainties. Close to rated wind speed, significant load reduction on tower and shaft compared to the feedback controller alone can be achieved. Additionally, a small improvement in energy production can be obtained.
However, the tuning of the parameters is not intuitive and only the dynamics of the rotor and tower motion can be directly shaped, but not the motion of the generator torque and collective pitch angle. If the flatness-based controller is not properly tuned, extreme torque and pitch action are necessary to track the desired trajectories for the tower and rotor motion. Additionally, the baseline torque controller needs to be slightly modified to minimize rapid switching between partial and full load operations.
Future research might address the following issues:

- Because of the usage of a dynamic internal model, the effects of the measurement uncertainties to the flatness-based control are more severe compared to the collective pitch feedforward control. Based on the results in [100], it can be expected that a re-tuned, less aggressive feedback controller would have further positive effects similar to the relaxing of the feedback controller proposed for collective pitch feedforward control. Further investigations are necessary to quantify this effect and to provide a method to tune the controller based on the quality of the lidar measurements.

- Appropriate methods to enable and disable the flatness-based feedforward controller and to switch to the baseline feedforward controller for high wind speeds should be developed. One possibility might be to simply multiply the feedforward signals of the flatness-based

controller with a gain g_{FF} and the collective pitch feedforward controller with $1 - g_{\mathrm{FF}}$. The gain g_{FF} can then be changed linearly from 1 to 0 for high wind speeds.

- If the promising results can be further confirmed by a more detailed simulation study, a field testing should be pursued.
- The critical issue of the proposed controller is the trajectory planning. A better algorithm might be developed that also includes techniques to avoid extreme control actions.
- The flat wind turbine model can be used for other advanced control concepts such as full state linearization.

9

Conclusions and Recommendations

In this final chapter, the main conclusions of the research presented in this thesis are summarized in Section 9.1 and recommendations for future research are given in Section 9.2. The main contributions are recapitulated in Section 9.3.

9.1 Conclusions

In this thesis, two main interacting research objectives have been addressed: the development of lidar data processing methods to provide usable signals for lidar-assisted control, as well as the design and evaluation of lidar-assisted control concepts. In this section, the conclusions on each of the two objectives are presented.

9.1.1 Development of Lidar Data Processing Methods

Lidar systems are able to measure line-of-sight wind speeds in front of wind turbines. This technology paves the way for new control concepts, helping to compensate the effect of changes in the inflowing wind field to the rotor and support structure. However, the raw lidar data needs to be transformed into usable wind preview signals. For this purpose, wind field reconstruction methods have been developed in Chapter 4 as well as an analytical model for the correlation between the wind speed measured by the lidar and the one experienced by the rotor in Chapter 5.

The developed wind field reconstruction methods are based on a system-theoretical view on lidar measurements in a wind field. Conventional techniques for site assessment use a wind model of

homogeneous flow, which causes problems in situations where the wind flow differs significantly from the assumed one. In this thesis, appropriate models for ground based, floating, and nacelle based applications have been derived and used in model-based wind field reconstruction methods. In simulations and also with real data, the reconstruction methods are able to improve the average wind speed measurements compared to the conventional techniques. For control purposes, the wind field needs to be reconstructed much faster and temporal information needs to be included. Therefore, the model-based wind field reconstruction has been extended to include simple dynamic wind models, which assume that the wind field propagates with the mean wind speed according to Taylor's Frozen Turbulence Hypothesis. With this assumption, an estimate for wind characteristics such as the rotor effective wind speed can be provided. The most important consideration of Chapter 4 is that lidar systems measure line-of-sight wind speeds and all other information needs to be estimated. The quality of the results depends on the accuracy of the lidar and the wind model as well as on the used estimation technique.
The analytic correlation model helps to evaluate the quality of the reconstruction, to improve it, and to adjust the estimated signals for use in lidar-assisted control. With the model, the correlation of the rotor effective wind speed between a lidar system and a wind turbine can be calculated in terms of spectral quantities such as coherence and transfer functions. The model considers different rotor diameters, the spatial averaging of the individual lidar system, different scanning patterns and wind evolution, which – in combination – are responsible for the level of correlation. Very good agreement with data from a field testing campaign has shown that the model is sufficiently accurate to be usable for the following applications: First, the correlation of real or simulated lidar measurements can be compared to its expected value to identify errors in the measurement procedure or data processing. Second, the correlation model can be used to optimize the configuration or scan pattern of lidar systems, such that it provides a wind speed signal which exhibits a high correlation to the wind speed affecting the turbine and a signal which can be transferred to the control system with the preview required by the individual control approach. Third, based on the correlation model, an adaptive filter can be designed which filters out all uncorrelated frequencies for a given experimental setup. This wind field reconstruction and adaptive filter design have been combined with various lidar-assisted controllers.

9.1.2 Design and Evaluation of Lidar-Assisted Control Concepts

The controllers in this thesis have all been designed in light of their applicability on real wind turbine control systems with inputs from real lidar systems.

All controllers have been first designed independently of the measurement quality provided by a lidar system, thus assuming perfect wind preview. This approach provides the possibility to distinguish between the robustness against model uncertainties and robustness against uncertainties in the provided wind preview.

Further, a reduced nonlinear model has been used for the design of all controllers. Linear controllers might provide a good control performance at a single operation point, but the dynamics and control goals of a wind turbine over the full range of wind speeds violate the linearity assumption. Additionally, simple but sufficiently accurate nonlinear models not only enable the possibilities to apply advanced nonlinear controllers, but also contribute to the fundamental understanding of the wind turbine's behavior.

The work focuses on three lidar-assisted control concepts. All three are designed to accommodate changes in the rotor effective wind speed and thus are combined with the adaptive filter and wind reconstruction methods described above.

The first concept is the collective pitch feedforward controller, which assists common collective pitch controllers to regulate the rotor speed in full load operations by providing an additive pitch angle command. In the case of perfect wind preview, the controller is able to almost perfectly cancel out the effect from the rotor effective wind to the rotor speed over the entire full load region and for the full aero-elastic model. This concept also indirectly reduces the impact on other states and thus decreases the structural loads of the turbine. A detailed load analysis using simulated lidar measurements and extrapolating the effects on the lifetime of a wind turbine showed promising reduction of tower, shaft, and blade loads as well as improved switching from full to partial load operations. Based on these results, field testing has been performed confirming that lidar systems are able to improve the control performance of wind turbines. Although only few data sets could be collected, the data demonstrates that it is essential to filter the data according to the correlation between the turbine and the lidar system to reduce rotor speed variation.

The second concept is the direct speed controller, which assists common generator torque controllers to track optimal inflow conditions in partial load operations. Simulations with the full aero-elastic model show that with the presented approach, the tip speed ratio can be held very close to its optimum. Although significant reduction in the deviation from the optimal tip speed ratio can be also achieved under very realistic conditions, the loads on the rotor shaft are heavily increased and the resulting energy gain is only marginal. The findings are consistent with theoretical considerations, which confirm that common torque controllers are already performing close to the aerodynamic optimum under normal inflow conditions. Finally,

the work points out that an increase of energy production in partial load operation is achievable but not attractive.
The third concept is the flatness-based feedforward controller which assists common collective pitch and generator torque controllers in the transition region between full and partial load operations. Since the reduced nonlinear wind turbine model features the system property of differential flatness, the generator torque and the collective pitch angle can be used to track trajectories of the rotor and tower motion. The trajectories are continuously designed during operation based on the wind preview. The trajectories are planned to hold the tower on its equilibrium manifold during the transition between partial and full load operations. If perfect wind preview is assumed, the flatness-based controller outperforms the collective pitch feedforward controller because of the possibility to provide an update for the collective pitch angle and the generator torque simultaneously. The flatness-based feedforward controller exhibits sufficient robustness against model uncertainties if it is used to control the full aeroelastic model, and shows good control performance in the presence of additional measurement uncertainties. However, the tuning of the parameters is not intuitive and the baseline torque controller needs to be slightly modified.
The collective pitch feedforward controller is considered the most promising approach because of its benefits to conventional wind turbine controllers that have been confirmed in field testing and its simplicity and robustness against model and measurement uncertainties.

9.2 Recommendations

In this section, recommendations for future research in the field of lidar-assisted control are presented. More details can be found at the end of the corresponding chapters.

9.2.1 Development of Lidar Data Processing Methods

Future work in the field of wind field reconstruction should focus on the improvement of wind flow models and advanced estimation techniques. During the field tests, the inflow angles have been assumed to be zero. For testing lidar-assisted individual pitch control on real wind turbines, the shears and the inflow angles need to be integrated into the estimation process. This could be done by integrating the measurements from several measurement distances into one single optimization problem by defining stages behind and in front of the turbine within the wind coordinate system. First simulation tests show promising results [84]. Another important improvement of the dynamic wind field reconstruction will be to include other, more realistic dynamic models such as differential equations as proposed in [5], which enable the application of estimation techniques such as Kalman filters commonly used for dynamic systems.
The analytic correlation model could be extended in future work for shear estimates. This will

allow the optimization of scan patterns and the design of corresponding filters to assist individual pitch control. Additionally, the model could be improved by integrating other turbulence and wind evolution models. The adaptive filter presented in this work currently changes with the mean wind speed once it has been designed with the correlation model. Further work should focus on an extension such that the filter is adjusted in the case of changing correlation caused by atmospheric changes or other external sources. Future investigation could also try to incorporate wind reconstruction and adaptive filtering in one single algorithm.

9.2.2 Design and Evaluation of Lidar-Assisted Control Concepts

All three lidar-assisted control concepts offer various possibilities of future research, listed below. Further investigations for the collective pitch feedforward controller are necessary to quantify the effect which a re-tuning of the feedback controller might provide. Additionally, future research might address the possible benefit of hybrid feedback-feedforward approaches which calculate the collective pitch feedforward-update based on measured turbine data as proposed in [21] and [22]. Finally, more field testing and economic studies are essential to increase the technology readiness level of the collective pitch feedforward approach.

This thesis showed that tracking the optimal inflow conditions during partial load operations based on lidar measurements is achievable but not attractive because of increased loads and marginal energy gain. However, it should be investigated if assisting the torque control is useful for PI controlled transition regions. Additionally, lidar systems might be a good instrument to adjust the feedback gain of conventional torque controllers.

Similar to the collective pitch feedforward controller, future investigations for the flatness-based feedforward controller should focus on the re-tuning of the feedback controller to better estimate the value of the approach. Appropriate methods to enable and disable the flatness-based feedforward controller and to switch to the collective pitch feedforward controller for high wind speeds should be developed. Further, better methods for the trajectory planning might be found and a field testing should be pursued.

In addition to these recommendations for the presented control approaches, future research should continue searching for other concepts for lidar-assisted control. Approaches incorporating the measurement uncertainties such as the one presented by [18] in combination with nonlinear methods should be pushed forward as well as optimal control strategies such as the NMPC.

9.3 Main Contributions

Within this thesis project, research has been carried out in the field of predictive control for onshore wind turbines. The thesis presents a technology to reduce the structural loads and to increase the energy yield of wind turbines, both making wind energy more competitive. The key challenges have not only been to develop appropriate control methods, but also to investigate lidar measurements and turbulence characteristics to provide a usable preview signal, which in combination made a proof-of-concept possible.
Thus, following three points are considered to be the main contributions of this thesis:

1. Development of predictive control concepts for wind turbines

   The thesis started with the development of a collective pitch feedforward controller to reduce loads of wind turbines based on preview wind speed information [92, 76, 83] Further concepts for cyclic pitch control [14, 15] for load reduction and for increasing the energy yield by improving the speed and yaw control [38, 77] were derived. A NMPC was introduced [29] and compared to the feedforward controller [24]. Additionally, the collective pitch feedforward controller was combined with a feedforward of the generator torque using a flatness-based approach [100]. The collective pitch feedforward controller was identified as the most promising and further investigation based on real measurements was carried out [89], showing the importance of the development of measurement techniques tailored for the use of lidar signals for control.

2. Development of lidar measurement and data processing techniques

   In parallel to the controller development, additional research was carried out to provide preview signals from a lidar system. This targeted the collaboration in the development of a scanning lidar system [105, 53], the development of lidar data processing techniques [38, 78], and the investigation of wind evolution [67]. Here, the main contribution is the derivation of an analytic model of the correlation between lidar systems and wind turbines, incorporating knowledge of turbulence models, signal processing, and lidar technology [85]. This model can be used to optimize lidar systems and to design an optimal filter for using a given lidar system for controlling a specific wind turbine.

3. Proof of concept of lidar-assisted control of wind turbines

   Based on the research results in control and lidar measurement techniques, lidar-assisted control could be tested on two different research turbines. Together with the NREL, the concept was proved in a worldwide first field testing campaign [88, 95]. Using the scanning lidar system developed by SWE and a commercial system, the collective pitch controller was able to reduce the rotor speed variation and the loads using the optimal filter designed for each campaign.

A

Experimental Setups

A.1 NREL CART2 Campaign

In this section the test site, turbine, and lidar system for the field testing are described.

A.1.1 Test Site

The field testing took place at NWTC in Boulder, Colorado, which is part of NREL. Due to its location directly in front of the Rocky Mountains Front Range, NWTC offers good conditions during the winter wind season to perform any kind of field test.

A.1.2 Test Turbine

Among several multi-megawatt turbines, the NWTC owns two mid-sized turbines (CART2 and CART3), which are dedicated to the testing of new and advanced control algorithms for wind turbines. These two turbines are two 600 kW Westinghouse WTG-600 turbines, which were originally deployed in a wind farm in Hawaii. The CART2 (Figure A.1a) is still equipped with the original two-bladed rotor, but was retrofitted with high-speed electromechanical pitch drives and a new fully controllable power electronics. It is heavily instrumented with strain gauges and accelerometers. It also has a dedicated meteorological tower installed 80 m in front of the turbine in the mean wind direction (292°). The turbine has a rotor diameter of $D = 42.7\,\mathrm{m}$ and a hub height of 36.9 m and runs at a rated rotor speed of 41.7 rpm. Since it is a two-bladed turbine, it has a teetered hub, which was free during the test runs. Furthermore,

a control system was developed and implemented in LabVIEW by NWTC engineers. This control system runs as a 400 Hz real-time system, which needs to be supervised by an engineer. Although it can handle all possible operating failures, an unattended run of this test turbine is not yet possible. However, it offers engineers an easy way of implementing their own controller code as a DLL, which is then loaded by the LabVIEW framework control system. For this work, the DLL was created as an export from MATLAB/Simulink code.

A.1.3 Lidar System

The scanning lidar system from the University of Stuttgart was installed on the CART2 in early 2012. It was placed on a frame which was mounted on the front top of the railing of the platform on top of the CART2's nacelle, as can be seen in Figure A.1b. To compensate for the 3.77° tilt of the CART2's nacelle, the lidar was mounted with a counter angle of about 3.7°, so that the system itself is horizontal aligned.

(a) The CART2.

(b) The SWE-lidar installed on the CART2.

(c) Two-DOF mirror seen from internal webcam.

(d) Andy Scholbrock, Paul Fleming, myself, and Florian Haizmann on the nacelle.

Figure A.1: The SWE scanning lidar system installed on the CART2 at the NWTC.

A.2 NREL CART3 Campaign

In this section, the test site, turbine, and lidar system for the field testing are described.

A.2.1 Test Site

Like the NREL CART2 Campaign described in Section A.1, the field testing took place at the National Wind Technology Center (NWTC) in Boulder, Colorado, which is part of NREL. Due to its location directly east of the Rocky Mountains Front Range, the NWTC offers good conditions during the wind season in winter to perform different kinds of field tests. Since the wind conditions are rather gusty and extreme, tests under extreme conditions can especially be performed there.

A.2.2 Test Turbine

Among several multi-megawatt turbines, the NWTC owns two mid-sized turbines (CART2 and CART3), which are dedicated to the testing of new and advanced control algorithms for wind turbines. These two turbines are two 600 kW Westinghouse WTG-600 turbines, which were originally deployed in a wind farm in Hawaii. The CART3 (Figure A.2a) was modified to have a three-bladed rotor and currently operates at 550 kW due to resonance issues [106]. The CART3 is instrumented with strain gauges, accelerometers, and a dedicated meteorological tower installed 80 m in front of the turbine's mean wind direction (292°). The turbine has a rotor diameter of $D = 40$ m, a hub height of 36.6 m, and runs at a rated rotor speed of 37 rpm. The control system offers an easy way of implementing new controller code as a DLL, which is then loaded by the 400 Hz real-time LabVIEW control system framework. For this work, the DLL was created and exported from MATLAB/Simulink code.

A.2.3 Lidar System

The lidar used in these tests to measure the wind in front of the turbine is a commercial, pulsed system from Blue Scout Technologies called OCS. The OCS simultaneously measures the Doppler shift of the light backscattered from aerosols at three range gates along the three fixed laser beams. It uses the line-of-sight wind speed to internally derive the horizontal and vertical wind speed and wind direction. For this campaign, all internal processing, such as filtering, has been reduced to the minimum to be able to use it for real-time feedforward and direct speed control. From these multiple inputs, a resulting rotor effective wind speed is determined by assuming that only the longitudinal wind component is responsible for power generation. Only the first range gate at 50 m is used in these tests, since the signal quality of the other two ranges was too low.

(a) The CART3.

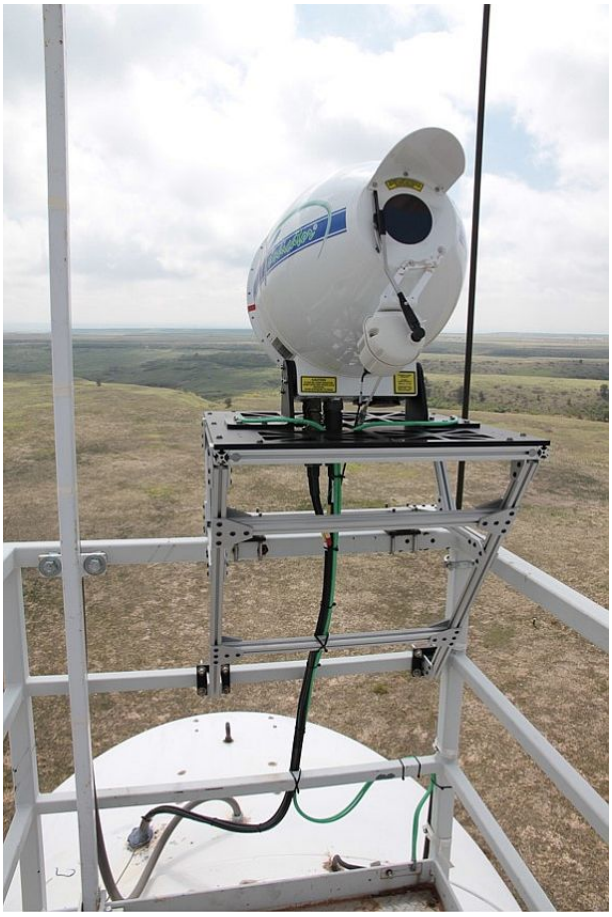

(b) The OCS (Photo by Lee Jay Fingersh).

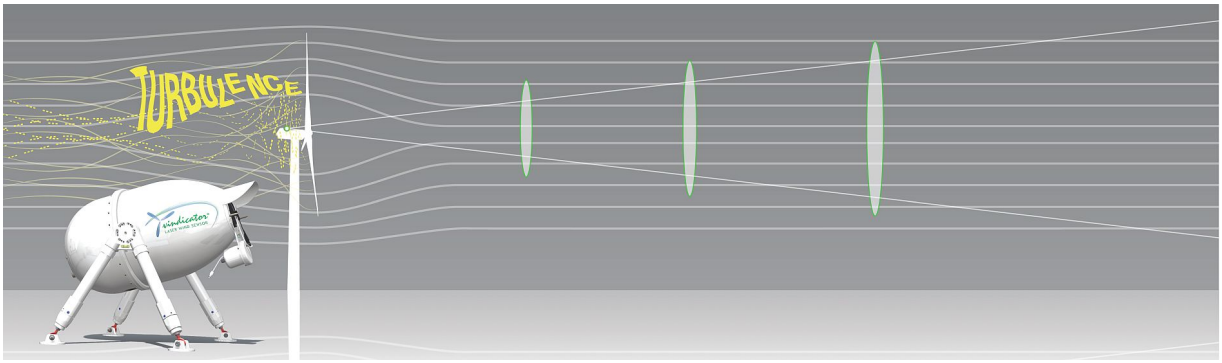

(c) Scope of the measurements of the OCS [107].

Figure A.2: The OCS installed on the CART3 at the NWTC.

B

SWE Scanning Lidar System

The SWE scanning lidar system has been developed for nacelle measurement campaigns in order to be able to redirect the laser beam of a standard Windcube lidar system [53]. The system consists of two parts: A Windcube V1 from Leosphere and a scanner unit developed at the University of Stuttgart. Since the original Windcube was designed for site assessment with its beam pointing upwards, a two-degree-of-freedom mirror for redirecting the beam in any position within the mirror's range was installed in a second casing, which allows pointing sideways, see Figure B.1a. The second housing can be connected to the original Windcube casing such that water tightness as well as structural stability could be assured. The mirror which deflects the beam in the original Windcube system is removed so that the laser beam goes through both casings and is redirected by the moving mirror. The accessible area is a

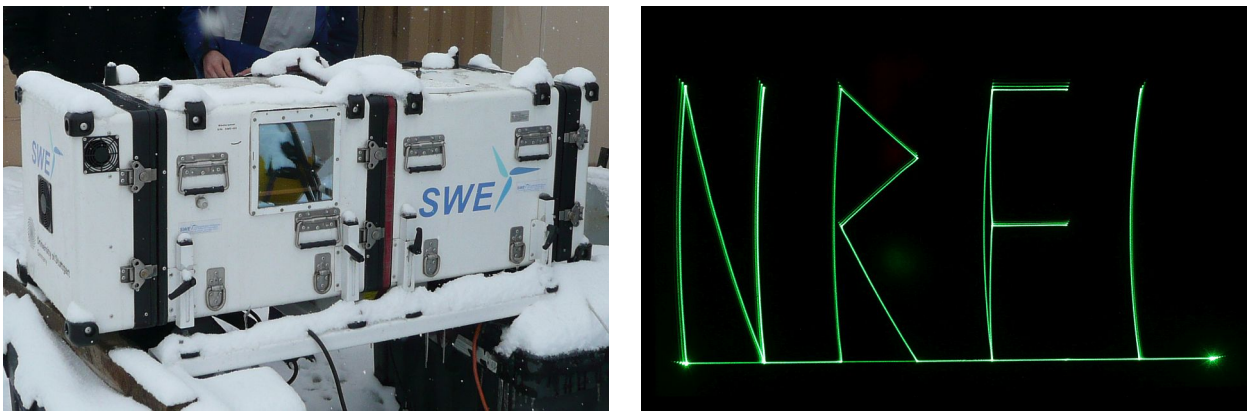

(a) Combined Windcube and Scanner. **(b)** Scan with visible laser.

Figure B.1: The SWE scanning lidar system.

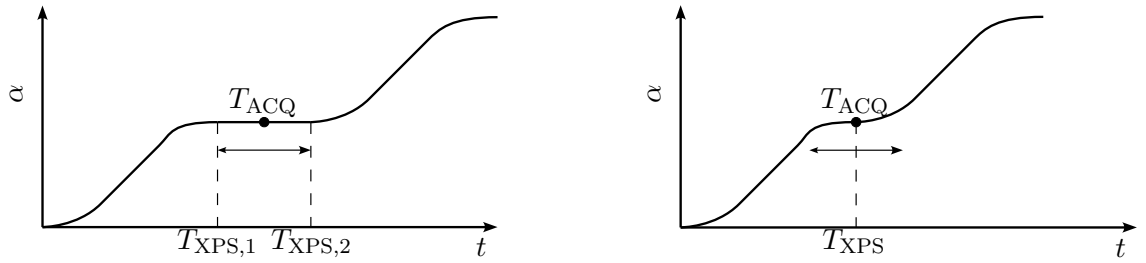

(a) "StartStop" scan mode. **(b)** "BangBang" scan mode.

Figure B.2: Scan modes of the SWE Scanning Lidar System.

$0.75D$ x $0.75D$ square in $1D$ distance. Figure A.1c shows a picture of the scanner's mirror and the side window through which the laser beam emits.

Modified software has been developed within the present thesis to synchronize the laser with the two motor stages. This software allows a free design of the scanning trajectories within the mechanical constraints. For instance, a possible scan trajectory consists of the "NREL" letters in Figure B.1b visualized with a common laser pointer aligned with the original laser source.

In the field testing campaign on the CART2 (see Appendix A.1) only two different scanning modes were used: In the "StartStop" mode (see Figure B.2a) the center of the acquisition time T_{ACQ} is centered between two stop times T_{XPS}. In the "BangBang" mode (see Figure B.2b) the center of the acquisition time T_{ACQ} coincides with one stop time T_{XPS} to be faster than the "StartStop" mode but to distribute the measurement over a small angle α. The raw lidar data are the line-of-sight wind speed v_{los}, the CNR, the two angular positions of the motors, the focus length along the beam for each focus distance and the times T_{ACQ} and T_{XPS}. The modified software allows up to 5 scan distances to be used.

C

Calculation Details

C.1 Used Wind Turbine Models

Table C.1: Specification of the used aeroelastic wind turbine model [63].

Rotor radius	R	63 m
Rotor diameter	D	126 m
Hub height	z_{H}	90 m
Hub inertia about low-speed shaft	J_{H}	115 926 kg/m^2
Blade inertia about low-speed shaft	J_{B}	11776.047 kg/m^2
Generator inertia about high-speed shaft	J_{G}	534.116 kg/m^2
Gear box ratio	i_{GB}	1/97
Mass tower	m_{T}	347 460 kg
Mass nacelle	m_{N}	240 000 kg
Mass hub	m_{H}	56780 kg
Mass blade	m_{B}	17740 kg
Natural frequency of first tower fore-aft bending	$f_{0,\mathrm{T}}$	0.324 Hz
Structural Damping ratio	$d_{\mathrm{s,T}}$	0.01
Static tower top displacement	$x_{0\mathrm{T}}$	−0.014 m
Generator efficiency	η_{el}	0.944
Undamped natural angular frequency of pitch actuator	ω_{PA}	2π rad/s
Damping factor of pitch actuator	ξ_{PA}	0.70
Distance from hub to first airfoil	r_{min}	9.7 m
Delay by pitch actuator and blades	T_{B}	0.5 s

C.2 Used Baseline Controller

Table C.2: Specification of the used baseline controller [63].

Rated power output	P_{rated}	5 MW
Rated generator torque	$M_{\text{G,rated}}$	43093.55 Nm
Rated rotor speed	Ω_{rated}	12.1 rpm
Rated wind speed	v_{rated}	11.3 m/s
Optimal tip speed ratio	λ_{opt}	7.55
Peak power coefficient	$c_{\text{P,max}}$	0.482
Pitch angle at which the rotor power has doubled	θ_{K}	6.3°
Minimum Blade Pitch for Ensuring Region 3 Torque	θ_{fine}	1°
Minimum collective pitch angle	θ_{min}	0°
Maximum collective pitch angle	θ_{max}	90°
Maximum absolute collective pitch rate	$\dot{\theta}_{\text{max}}$	8 °/s
Proportional gain of collective pitch controller	K_{P}	0.018 826 81 rad/(rad/s)
Integral gain of collective pitch controller	K_{I}	0.008 068 634 (rad/s)/(rad/s)

C.3 Used Turbulent Wind Fields

Table C.3: Parameters of TurbSim wind field for spectra estimation. All other parameters are set to the default values or unused.

Value	Identifier	Comment
1	`RandSeed(1)`	First random seed [-]
`RANLUX`	`RandSeed(2)`	Second random seed [-]
`True`	`ScaleIEC`	Scale hub-height IEC turbulence to target TI?
33	`NumGrid_Z/NumGrid_Y`	Number of vertical/horizontal grid-points [-]
0.25	`TimeStep`	Time step [s]
8192	`AnalysisTime/UsableTime`	Length of analysis/output time series [s]
90	`HubHt/RefHt`	Hub/reference height [m]
128	`GridHeight/GridWidth`	Grid height/width [m]
0	`VFlowAng/HFlowAng`	Vertical/Horizontal mean flow angle [deg]
`"IECKAI"`	`TurbModel`	Turbulence model
`"1-ED3"`	`IECstandard`	Number of IEC 61400-x standard
16.48	`IECturbc`	IEC turbulence characteristic
`"NTM"`	`IECWindType`	IEC turbulence type
20	`URef`	Mean wind speed at reference height [m/s]

Table C.4: Parameters of TurbSim wind fields for DLC 1.2 calculations. All other parameters are set to the default values or unused.

Value	Identifier	Comment
equal to `URef`	`RandSeed(1)`	First random seed [-]
`RANLUX`	`RandSeed(2)`	Second random seed [-]
`True`	`ScaleIEC`	Scale hub-height IEC turbulence to target TI?
33	`NumGrid_Z/NumGrid_Y`	Number of vertical/horizontal grid-points [-]
0.25	`TimeStep`	Time step [s]
3660	`AnalysisTime/UsableTime`	Length of analysis/output time series [s]
90	`HubHt/RefHt`	Hub/reference height [m]
128	`GridHeight/GridWidth`	Grid height/width [m]
0	`VFlowAng/HFlowAng`	Vertical/Horizontal mean flow angle [deg]
`"IECKAI"`	`TurbModel`	Turbulence model
`"1-ED3"`	`IECstandard`	Number of IEC 61400-x standard
`"A"`	`IECturbc`	IEC turbulence characteristic
`"NTM"`	`IECWindType`	IEC turbulence type
4,6,...,24	`URef`	Mean wind speed at reference height [m/s]

Table C.5: Parameters of TurbSim wind field for testing pure region 2 controllers. All other parameters are set to the default values or unused.

Value	Identifier	Comment
9	`RandSeed(1)`	First random seed [-]
`RANLUX`	`RandSeed(2)`	Second random seed [-]
`True`	`ScaleIEC`	Scale hub-height IEC turbulence to target TI?
33	`NumGrid_Z/NumGrid_Y`	Number of vertical/horizontal grid-points [-]
0.25	`TimeStep`	Time step [s]
8192	`AnalysisTime/UsableTime`	Length of analysis/output time series [s]
90	`HubHt/RefHt`	Hub/reference height [m]
128	`GridHeight/GridWidth`	Grid height/width [m]
0	`VFlowAng/HFlowAng`	Vertical/Horizontal mean flow angle [deg]
`"IECKAI"`	`TurbModel`	Turbulence model
`"1-ED3"`	`IECstandard`	Number of IEC 61400-x standard
8.00	`IECturbc`	IEC turbulence characteristic
`"NTM"`	`IECWindType`	IEC turbulence type
9	`URef`	Mean wind speed at reference height [m/s]

Table C.6: Parameters of TurbSim wind field for testing control performance in the transition from partial to full load operations. All other parameters are set to the default values or unused.

Value	Identifier	Comment
12	`RandSeed(1)`	First random seed [-]
`RANLUX`	`RandSeed(2)`	Second random seed [-]
`True`	`ScaleIEC`	Scale hub-height IEC turbulence to target TI?
33	`NumGrid_Z/NumGrid_Y`	Number of vertical/horizontal grid-points [-]
0.25	`TimeStep`	Time step [s]
8192	`AnalysisTime/UsableTime`	Length of analysis/output time series [s]
90	`HubHt/RefHt`	Hub/reference height [m]
128	`GridHeight/GridWidth`	Grid height/width [m]
0	`VFlowAng/HFlowAng`	Vertical/Horizontal mean flow angle [deg]
`"IECKAI"`	`TurbModel`	Turbulence model
`"1-ED3"`	`IECstandard`	Number of IEC 61400-x standard
14.6	`IECturbc`	IEC turbulence characteristic
`"NTM"`	`IECWindType`	IEC turbulence type
12	`URef`	Mean wind speed at reference height [m/s]

C.4 Closed-Form Solution of the Rotor Effective Wind Speed

The auto-spectrum of the rotor effective wind speed can be denoted in Cartesian coordinates (the subscript $\mathcal{I}$ is omitted for better readability):

$$S_{\mathrm{RR}} = \frac{S_{ii,u}}{(\pi R^2)^2} \underbrace{\int_{A_i(0,R)} \int_{A_j(0,R)} \exp(-\kappa r_{ij}) \, \mathrm{d}y_i \, \mathrm{d}z_i \, \mathrm{d}y_j \, \mathrm{d}z_j}_{D(R,\kappa)} \tag{C.1}$$

with

$$r_{ij} = \sqrt{(y_j - y_i)^2 + (z_j - z_i)^2}, \tag{C.2}$$

where $A_i(0, R)$ denotes a circular ring with inner radius 0 and outer radius R.
The main problem in solving the integral $D(R, \kappa)$ is the simultaneous dependency of r_{ij} on all variables of integration.
Therefore, the following technique is applied:

1. Differentiation of the integral with respect to a parameter to decrease the number of variables of integration, such that the remaining integral is solvable.
2. Solution of the differentiated integral.
3. Integration of the interim solution with respect to the chosen parameter.

The three steps are explained in the following.

1. Differentiation of the Integral

Here, the radius R is chosen for differentiation:

$$\frac{\mathrm{d}D(R,\kappa)}{\mathrm{d}R} = \lim_{\epsilon \to 0} \frac{1}{\epsilon} \left(D(R+\epsilon, \kappa) - D(R, \kappa) \right) \tag{C.3}$$

with

$$D(R+\epsilon, \kappa) = \int_{A_i(0,R+\epsilon)} \int_{A_j(0,R+\epsilon)} \exp(-\kappa r_{ij}) \, \mathrm{d}y_i \, \mathrm{d}z_i \, \mathrm{d}y_j \, \mathrm{d}z_j. \tag{C.4}$$

Due to the symmetry of the integral it can be split up into the following parts:

$$\int_{A_i(0,R+\epsilon)} \int_{A_j(0,R+\epsilon)} = \int_{A_i(0,R)} \int_{A_j(0,R)} + 2 \int_{A_i(0,R)} \int_{A_j(R,R+\epsilon)} + \int_{A_i(R,R+\epsilon)} \int_{A_j(R,R+\epsilon)} \tag{C.5}$$

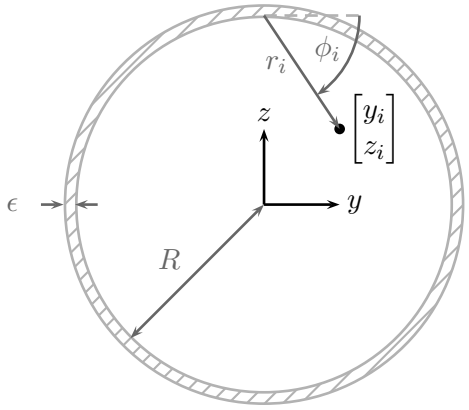

Figure C.1: Polar coordinates and change ϵ used for the differentiation.

Using polar coordinates in the last part yields

$$\begin{aligned}
&\lim_{\epsilon\to 0}\frac{1}{\epsilon}\int\limits_{A_i(R,R+\epsilon)}\int\limits_{A_j(R,R+\epsilon)}\exp(-\kappa r_{ij})\,\mathrm{d}y_i\,\mathrm{d}z_i\,\mathrm{d}y_j\,\mathrm{d}z_j\\
=&\lim_{\epsilon\to 0}\frac{R^2\epsilon^2}{\epsilon}\int_0^{2\pi}\int_0^{2\pi}\exp\left(-\kappa R\sqrt{2-2\cos(\phi_i-\phi_j)}\right)\,\mathrm{d}\phi_i\,\mathrm{d}\phi_j\\
=&0. \qquad \text{(C.6)}
\end{aligned}$$

The second part is independent of the location of y_j and z_j on the circular ring with an area of $2\pi R\epsilon$. By choosing $y_j = 0$ and $z_j = R$, the second part is

$$\begin{aligned}
&\lim_{\epsilon\to 0}\frac{2}{\epsilon}\int\limits_{A_i(0,R)}\int\limits_{A_j(R,R+\epsilon)}\exp(-\kappa r_{ij})\,\mathrm{d}y_i\,\mathrm{d}z_i\,\mathrm{d}y_j\,\mathrm{d}z_j\\
=&\lim_{\epsilon\to 0}\frac{4\pi R\epsilon}{\epsilon}\int\limits_{A_i(0,R)}\exp(-\kappa\sqrt{y_i^2+(R-z_i)^2})\,\mathrm{d}y_i\,\mathrm{d}z_i. \qquad \text{(C.7)}
\end{aligned}$$

By transforming into the polar coordinates with

$$\begin{aligned}
0 &\le \phi_i \le \pi\\
0 &\le r_i \le 2R\sin\phi\\
y_i &= r_i\cos\phi_i\\
z_i &= R - r_i\sin\phi_i \qquad \text{(C.8)}
\end{aligned}$$

one obtains

$$\begin{aligned}\frac{\mathrm{d}D(R,\kappa)}{\mathrm{d}R} &= 4\pi R \int_0^{\pi} \int_0^{2R\sin\phi_i} \exp(-\kappa r_i) r_i \,\mathrm{d}r_i \,\mathrm{d}\phi_i \\ &= \frac{4\pi R}{\kappa^2} \int_0^{\pi} \left[-\exp(-\kappa r_i)(\kappa r_i + 1)\right]_0^{2R\sin\phi_i} \,\mathrm{d}\phi_i \\ &= \frac{4\pi R}{\kappa^2} \int_0^{\pi} \left(-\exp(-\kappa 2R\sin\phi_i)(\kappa 2R\sin\phi_i + 1) + 1\right) \,\mathrm{d}\phi_i. \end{aligned} \tag{C.9}$$

2. Solution of the Differentiated Integral

This integral can now be solved in terms of special functions[1]:

$$\frac{\mathrm{d}D(R,\kappa)}{\mathrm{d}R} = \frac{4\pi^2 R}{\kappa^2}(L_0(2R\kappa) + 2R\kappa(I_1(2R\kappa) - L_{-1}(2R\kappa)) - I_0(2R\kappa) + 1) \tag{C.10}$$

where L are modified Struve functions[2] and I are modified Bessel functions of the first kind[3].

3. Integration of the Interim Solution

Finally, the closed-form solution for the auto-spectrum of the rotor effective wind speed is

$$\begin{aligned} S_{\mathrm{RR}} =& \frac{S_{ii,u}}{(\pi R^2)^2} \int_0^R \frac{\mathrm{d}D(R,\kappa)}{\mathrm{d}R} \mathrm{d}R \\ =& \frac{2S_{ii,u}}{(R\kappa)^3} \left(L_1(2R\kappa) - I_1(2R\kappa) - \frac{2}{\pi} + R\kappa(-2L_{-2}(2R\kappa) + 2I_2(2R\kappa) + 1) \right). \end{aligned} \tag{C.11}$$

However, this solution is not unique. Jakob Mann provided the following expression [85] using the regularized hypergeometric function[4] ${}_0\tilde{F}_1$ which gives identical values:

$$S_{\mathrm{RR}} = \frac{2S_{ii,u}}{(R\kappa)^3} \left(L_1(2R\kappa) + R\kappa \left(-3\,{}_0\tilde{F}_1(;2;(R\kappa)^2) - 2L_2(2R\kappa) - \frac{8}{3\pi} R\kappa + 2I_0(2R\kappa) + 1 \right) \right). \tag{C.12}$$

[1] Done with Wolfram Research, Inc., Mathematica, Version 9.0.1, Champaign, USA (2013). Thanks to Yves Klett for his help with the implementation.

[2] See `www.mathworld.wolfram.com/ModifiedStruveFunction.html`.

[3] See `www.mathworld.wolfram.com/ModifiedBesselFunctionoftheFirstKind.html`.

[4] See `www.mathworld.wolfram.com/RegularizedHypergeometricFunction.html`.

Bibliography

[1] M. Harris, M. Hand, and A. Wright, "Lidar for turbine control," NREL, Tech. Rep. TP-500-39154, 2006.

[2] K. A. Kragh, M. H. Hansen, and T. Mikkelsen, "Improving yaw alignment using spinner based LIDAR," in *Proceedings of the 49th AIAA Aerospace Sciences Meeting Including the New Horizons Forum and Aerospace Exposition*, Orlando, USA, 2011.

[3] T. Mikkelsen, N. Angelou, K. Hansen, M. Sjöholm, M. Harris, C. Slinger, P. Hadley, R. Scullion, G. Ellis, and G. Vives, "Lidar wind speed measurents from a rotating spinner," in *Proceedings of the European Wind Energy Conference*, Warsaw, Poland, 2010.

[4] S. Kapp and M. Kühn, "A five-parameter wind field estimation method based on spherical upwind lidar measurements," in *Proceedings of The Science of Making Torque from Wind*, Oldenburg, Germany, 2012.

[5] P. Towers and B. L. Jones, "Real-time wind field reconstruction from lidar measurements using a dynamic wind model and state estimation," *Wind Energy, published online*, 2014.

[6] A. T. Pedersen, M. Sjöholm, N. Angelou, T. Mikkelsen, B. F. Montes, J. E. Pedersen, C. Slinger, and M. Harris, "Full-scale field test of a blade-integrated dual-telescope wind lidar," in *European Wind Energy Association annual event*, Vienna, Austria, 2013.

[7] E. Simley, L. Y. Pao, N. Kelley, B. Jonkman, and R. Frehlich, "LIDAR wind speed measurements of evolving wind fields," in *Proceedings of the 50th AIAA Aerospace Sciences Meeting Including the New Horizons Forum and Aerospace Exposition*, Nashville, USA, 2012.

[8] E. Simley and L. Y. Pao, "Correlation between rotating LIDAR measurements and blade effective wind speed," in *Proceedings of the 51st AIAA Aerospace Sciences Meeting Including the New Horizons Forum and Aerospace Exposition*, Dallas, USA, 2013.

[9] E. Simley and L. Y. Pao, "Reducing lidar wind speed measurement error with optimal filtering," in *Proceedings of the American Control Conference*, Washington, USA, 2013.

[10] F. Dunne, L. Y. Pao, D. Schlipf, and A. K. Scholbrock, "Importance of lidar measurement timing accuracy for wind turbine control," in *Proceedings of the American Control Conference*, Portland, USA, 2014.

[11] F. Dunne, L. Y. Pao, A. D. Wright, B. Jonkman, and N. Kelley, "Combining standard feedback controllers with feedforward blade pitch control for load mitigation in wind turbines," in *Proceedings of the 48th AIAA Aerospace Sciences Meeting Including the New Horizons Forum and Aerospace Exposition*, Orlando, USA, 2010.

[12] F. Dunne, L. Y. Pao, A. D. Wright, B. Jonkman, N. Kelley, and E. Simley, "Adding feedforward blade pitch control for load mitigation in wind turbines: Non-causal series expansion, preview control, and optimized FIR filter methods," in *Proceedings of the 49th AIAA Aerospace Sciences Meeting Including the New Horizons Forum and Aerospace Exposition*, Orlando, USA, 2011.

[13] J. Laks, L. Y. Pao, A. D. Wright, N. Kelley, and B. Jonkman, "Blade pitch control with preview wind measurements," in *Proceedings of the 48th AIAA Aerospace Sciences Meeting Including the New Horizons Forum and Aerospace Exposition*, Orlando, USA, 2010.

[14] D. Schlipf, S. Schuler, P. Grau, F. Allgöwer, and M. Kühn, "Look-ahead cyclic pitch control using LiDAR," in *Proceedings of The Science of Making Torque from Wind*, Heraklion, Greece, 2010.

[15] F. Dunne, D. Schlipf, L. Y. Pao, A. D. Wright, B. Jonkman, N. Kelley, and E. Simley, "Comparison of two independent lidar-based pitch control designs," in *Proceedings of the 50th AIAA Aerospace Sciences Meeting Including the New Horizons Forum and Aerospace Exposition*, 2012.

[16] K. A. Kragh, M. H. Hansen, and L. C. Henriksen, "Sensor comparison study for load alleviating wind turbine pitch control," *Wind Energy*, vol. 17, no. 12, pp. 1891–1904, 2014.

[17] N. Wang, "Lidar-assisted feedforward and feedback control design for wind turbine tower load mitigation and power capture enhancement," Ph.D. dissertation, Colorado School of Mines, 2013.

[18] F. Dunne and L. Y. Pao, "Benefit of wind turbine preview control as a function of measurement coherence and preview time," in *Proceedings of the American Control Conference*, Washington, USA, 2013.

[19] M. Kristalny, D. Madjidian, and T. Knudsen, "On using wind speed preview to reduce wind turbine tower oscillations," *Control Systems Technology, IEEE Transactions on*, vol. 21, no. 4, pp. 1191–1198, 2013.

[20] E. Bossanyi, "Un-freezing the turbulence: improved wind field modelling for investigating lidar-assisted wind turbine control," in *Proceedings of the European Wind Energy Association annual event*, Copenhagen, Denmark, 2012.

[21] E. Bossanyi, A. Kumar, and O. Hugues-Salas, "Wind turbine control applications of turbine-mounted lidar," *Journal of Physics: Conference Series*, vol. 555, no. 1, p. 012011, 2014.

[22] I. Elorza, M. Iribas, and E. Miranda, "On the feasibility and limits of extreme load reduction for wind turbines via advanced sensing: A lidar case study," in *Proceedings of the American Control Conference*, Washington, USA, 2013.

[23] J. Laks, L. Y. Pao, E. Simley, A. Wright, N. Kelly, and B. Jonkman, "Model predictive control using preview measurements from LIDAR," in *Proceedings of the 49th AIAA Aerospace Sciences Meeting Including the New Horizons Forum and Aerospace Exposition*, Orlando, USA, 2011.

[24] D. Schlipf, L. Y. Pao, and P. W. Cheng, "Comparison of feedforward and model predictive control of wind turbines using LIDAR," in *Proceedings of the Conference on Decision and Control*, Maui, USA, 2012.

[25] A. Körber and R. King, "Nonlinear model predictive control for wind turbines," in *Proceedings of the European Wind Energy Association annual event*, Brussels, Belgium, 2011.

[26] M. Soltani, R. Wisniewski, P. Brath, and S. Boyd, "Load reduction of wind turbines using receding horizon control," in *Proceedings of the IEEE International Conference on Control Applications*, Denver, USA, 2011.

[27] L. Henriksen, M. Hansen, and N. Poulsen, "Wind turbine control with constraint handling: a model predictive control approach," *Control Theory Applications, IET*, vol. 6, no. 11, pp. 1722–1734, 2012.

[28] S. Gros, "An economic NMPC formulation for wind turbine control," in *Proceedings of the Conference on Decision and Control*, Florence, Italy, 2013.

[29] D. Schlipf, D. J. Schlipf, and M. Kühn, "Nonlinear model predictive control of wind turbines using LIDAR," *Wind Energy*, vol. 16, no. 7, pp. 1107–1129, 2013.

[30] J. Aho, L. Y. Pao, and J. Hauser, "Optimal trajectory tracking control for wind turbines during operating region transitions," in *Proceedings of the American Control Conference*, Washington, USA, 2013.

[31] M. Mirzaei, M. Soltani, N. Poulsen, and H. Niemann, "Model predictive control of wind turbines using uncertain lidar measurements," in *Proceedings of the American Control Conference*, Washington, USA, 2013.

[32] C. L. Bottasso, P. Pizzinelli, C. E. D. Riboldi, and L. Tasca, "Lidar-enabled model predictive control of wind turbines with real-time capabilities," *Renewable Energy*, vol. 71, pp. 442 – 452, 2014.

[33] A. A. Ozdemir, P. Seiler, and G. J. Balas, "Benefits of preview wind information for region 2 wind turbine control," in *Proceedings of the 51st AIAA Aerospace Sciences Meeting Including the New Horizons Forum and Aerospace Exposition*, Dallas, USA, 2013.

[34] K. S. T. Magar and M. J. Balas, "Modeling and direct adaptive control of utility-scale wind turbines for both onshore and offshore operation," in *Proceedings of the Systems Conference*, Ottawa, Canada, 2014.

[35] B. Boukhezzar and H. Siguerdidjane, "Nonlinear control of variable speed wind turbines

without wind speed measurement," in *Proceedings of the Conference on Decision and Control and European Control Conference*, Seville, Spain, 2005.

[36] N. Wang, K. Johnson, A. Wright, and C. Carcangiu, "Lidar-assisted wind turbine feedforward torque controller design below rated," in *Proceedings of the American Control Conference*, Portland, USA, 2014.

[37] E. Hau, *Wind Turbines: Fundamentals, Technologies, Application, Economics*. Springer, 2006.

[38] D. Schlipf, S. Kapp, J. Anger, O. Bischoff, M. Hofsäß, A. Rettenmeier, U. Smolka, and M. Kühn, "Prospects of optimization of energy production by LiDAR assisted control of wind turbines," in *Proceedings of the European Wind Energy Association annual event*, Brussels, Belgium, 2011.

[39] P. A. Fleming, A. K. Scholbrock, A. Jehu, S. Davoust, E. Osler, A. D. Wright, and A. Clifton, "Field-test results using a nacelle-mounted lidar for improving wind turbine power capture by reducing yaw misalignment," *Journal of Physics: Conference Series*, vol. 524, no. 1, p. 012002, 2014.

[40] A. Scholbrock, P. Fleming, A. Wright, C. Slinger, J. Medley, and M. Harris, "Field test results from lidar measured yaw control for improved yaw alignment with the NREL controls advanced research turbine," in *Proceedings of the 33rd Wind Energy Symposium AIAA SciTech Conference*, Kissimmee, USA, 2013.

[41] T. Burton, N. Jenkins, D. Sharpe, and E. Bossanyi, *Wind Energy Handbook*. New York, USA: John Wiley & Sons, 2011.

[42] Global Wind Energy Council (GWEC). (2014) Global wind report: annual market update 2013. Available from: www.gwec.net.

[43] D. Kaufer and P. W. Cheng, "Validation of an integrated simulation method with high resolution load measurements of the offshore wind turbine REpower 5M at Alpha Ventus," *Journal of Ocean and Wind Energy*, vol. 1, no. 1, pp. 30–40, 2014.

[44] J. Jonkman and M. L. Buhl, "FAST user's guide," NREL, Tech. Rep. EL-500-38230, 2005.

[45] G. Ingram. (2011, October) Wind turbine blade analysis using the blade element momentum method. Available from: www.dur.ac.uk/g.l.ingram.

[46] P. Moriarty and A. C. Hansen, "AeroDyn theory manual," NREL, Tech. Rep. TP–500-36881, 2005.

[47] E. Bossanyi, *GH Bladed Theory Manual*, Garrad Hassan and Partners Limited, September 2010, issue no. 20, 282/BR/009.

[48] G. Bir, "Blades and towers modal analysis code (bmodes): Verification of blade modal analysis capability," in *Proceedings of the 47th AIAA Aerospace Sciences Meeting Including the New Horizons Forum and Aerospace Exposition*, Orlando, USA, 2009.

[49] T. R. Kane and D. A. Levinson, *Dynamics: Theory and Applications*. New York: McGraw-Hill Inc., 1985.

[50] IEC 61400-1, *Wind turbines - Part 1: Design requirements*, International Electrotechnical Commission Std., Rev. third edition, 2005.

[51] W. Bierbooms, "Constrained stochastic simulation - generation of time series around some specific event in a normal process," *Extremes*, vol. 8, no. 3, pp. 207–224, 2005.

[52] EN 1993-1-9, *Eurocode 3: Design of steel structures - Part 1-9: Fatigue*, European Committee for Standardization Std., 2005.

[53] A. Rettenmeier, J. Anger, O. Bischoff, M. Hofsäß, D. Schlipf, and I. Würth, "Nacelle-based lidar systems," in *Remote Sensing for Wind Energy, DTU Wind Energy-E-Report-0029(EN)*, June 2013, ch. 8, pp. 157–170.

[54] I. Van der Hoven, "Power spectrum of horizontal wind speed in the frequency range from 0.0007 to 900 cycles per hour," *Journal of Meteorology*, vol. 14, pp. 160–164, 1957.

[55] R. A. Pielke and H. A. Panofsky, "Turbulence characteristics along several towers," *Boundary-Layer Meteorology*, vol. 1, pp. 115–130, 1970.

[56] L. Kristensen, "On longitudinal spectral coherence," *Boundary-Layer Meteorology*, vol. 16, pp. 145–153, 1979.

[57] B. J. Jonkman, "TurbSim user's guide," NREL, Tech. Rep. TP-500-46198, 2009.

[58] C. Weitkamp, *Lidar: Range-Resolved Optical Remote Sensing of the Atmosphere*, ser. Springer Series in Optical Sciences. Springer, 2005.

[59] A. Jelalian, *Laser Radar Systems*, ser. Artech House Radar Library. Artech House, Incorporated, 1992.

[60] J.-P. Cariou, "Pulsed lidars," in *Remote Sensing for Wind Energy, DTU Wind Energy-E-Report-0029(EN)*, June 2013, ch. 5, pp. 104–121.

[61] M. Pitter, C. Slinger, and M. Harris, "Introduction to continuous-wave doppler lidar," in *Remote Sensing for Wind Energy, DTU Wind Energy-E-Report-0029(EN)*, June 2013, ch. 4, pp. 72–103.

[62] E. Bossanyi and D. Witcher, "Controller for 5 MW reference turbine," Garrad Hassan and Partners Limited, UpWind Report 11593/BR/04, 2009.

[63] J. Jonkman, S. Butterfield, W. Musial, and G. Scott, "Definition of a 5-MW reference wind turbine for offshore system development," NREL, Tech. Rep. TP-500-38060, 2009.

[64] C. L. Bottasso, A. Croce, B. Savini, W. Sirchi, and L. Trainelli, "Aero-servo-elastic modelling and control of wind turbines using finite-element multibody procedures," *Multibody System Dynamics*, vol. 16, no. 3, pp. 291–308, 2006.

[65] R. Gasch, J. Twele, and P. Bade, *Windkraftanlagen: Grundlagen, Entwurf, Planung und Betrieb*. Wiesbaden, Germany: Teubner, 2005.

[66] G. I. Taylor, "The spectrum of turbulence," *Proceedings of the Royal Society of London. Series A - Mathematical and Physical Sciences*, vol. 164, no. 919, pp. 476–490, 1938.

[67] D. Schlipf, D. Trabucchi, O. Bischoff, M. Hofsäß, J. Mann, T. Mikkelsen, A. Rettenmeier, J. J. Trujillo, and M. Kühn, "Testing of frozen turbulence hypothesis for wind turbine applications with a scanning LIDAR system," in *Proceedings of the International Symposium for the Advancement of Boundary Layer Remote Sensing*, Paris, France, 2010.

[68] J. Laks, E. Simley, and L. Y. Pao, "A spectral model for evaluating the effect of wind evolution on wind turbine preview control," in *Proceedings of the American Control Conference*, Washington, USA, 2013.

[69] P. Fleming, P. Gebraad, J.-W. van Wingerden, S. Lee, M. Churchfield, A. Scholbrock, J. Michalakes, K. Johnson, and P. Moriarty, "The SOWFA super-controller: A high-fidelity tool for evaluating wind plant control approaches," NREL, Tech. Rep. CP-5000-57175, 2013.

[70] G. Leishman, *Principles of Helicopter Aerodynamics*, 2nd ed. Cambridge, UK: Cambridge University Press, Apr. 2006.

[71] E. van der Hooft and T. G. van Engelen, "Estimated wind speed feed forward control for wind turbine operation optimization," in *Proceedings of the European Wind Energy Conference*, London, November 2004.

[72] K. Z. Østergaard, P. Brath, and J. Stoustrup, "Estimation of effective wind speed," *Journal of Physics: Conference Series*, vol. 75, no. 1, p. 012082, 2007.

[73] K. Johnson, L. Pao, M. Balas, and L. Fingersh, "Control of variable-speed wind turbines," *IEEE Control Systems Magazine*, vol. 06, pp. 70–81, 2006.

[74] I. M. Horowitz, *Synthesis of feedback systems*. Academic New York, 1963.

[75] K. J. Åström and T. Hägglund, *PID Controllers: Theory, Design, and Tuning*. ISA-The Instrumentation, Systems, and Automation Society, 1995.

[76] D. Schlipf, J. J. Trujillo, V. Basterra, and M. Kühn, "Development of a wind turbine LIDAR simulator," in *Proceedings of the European Wind Energy Conference*, Marseille, France, 2009.

[77] D. Schlipf, P. Fleming, S. Kapp, A. Scholbrock, F. Haizmann, F. Belen, A. Wright, and P. W. Cheng, "Direct speed control using lidar and turbine data," in *Proceedings of the American Control Conference*, Washington, USA, 2013.

[78] D. Schlipf, A. Rettenmeier, F. Haizmann, M. Hofsäß, M. Courtney, and P. W. Cheng, "Model based wind vector field reconstruction from lidar data," in *Proceedings of the German Wind Energy Conference DEWEK*, Bremen, Germany, 2012.

[79] A. Rettenmeier, O. Bischoff, D. Schlipf, J. Anger, M. Hofsäß, P. W. Cheng, R. Wagner, M. Courtney, and J. Mann, "Turbulence and wind speed investigations using a nacelle-based lidar scanner and a met mast," in *European Wind Energy Association annual event*, Copenhagen, Denmark, 2012.

[80] F. Bingöl, "Complex terrain and lidars," in *Remote Sensing for Wind Energy, DTU Wind Energy-E-Report-0029(EN)*, June 2013, ch. 12, pp. 231–241.

[81] J. Gottschall, H. Lilov, G. Wolken-Möhlmann, and B. Lange, "Lidars on floating offshore platforms," in *European Wind Energy Association annual event*, Copenhagen, Denmark, 2012.

[82] D. Schlipf, O. Bischoff, M. Hofsäß, A. Rettenmeier, J. J. Trujillo, and M. Kühn, "Lidar and wind turbine control," in *Remote Sensing for Wind Energy, Risø-I-3184(EN)*, May 2010, ch. 8, pp. 137–146.

[83] D. Schlipf, T. Fischer, C. E. Carcangiu, M. Rossetti, and E. Bossanyi, "Load analysis of look-ahead collective pitch control using LiDAR," in *Proceedings of the German Wind Energy Conference DEWEK*, Bremen, Germany, 2010.

[84] S. Raach, D. Schlipf, F. Haizmann, and P. W. Cheng, "Three dimensional dynamic model based wind field reconstruction from lidar data," *Journal of Physics: Conference Series*, vol. 524, no. 1, p. 012005, 2014.

[85] D. Schlipf, J. Mann, and P. W. Cheng, "Model of the correlation between lidar systems and wind turbines for lidar assisted control," *Journal of Atmospheric and Oceanic Technology*, vol. 30, no. 10, pp. 2233–2240, 2013.

[86] J. S. Bendat and A. G. Piersol, *Random data; analysis and measurement procedures*. New York, USA: John Wiley & Sons, 1971.

[87] G. C. Carter, C. Knapp, and A. H. Nuttall, "Estimation of the magnitude-squared coherence function via overlapped fast fourier transform processing," *Audio and Electroacoustics, IEEE Transactions on*, vol. 21, no. 4, pp. 337–344, Aug 1973.

[88] A. Scholbrock, P. Fleming, L. Fingersh, A. Wright, D. Schlipf, F. Haizmann, and F. Belen, "Field testing LIDAR based feed-forward controls on the NREL controls advanced research turbine," in *Proceedings of the 51st AIAA Aerospace Sciences Meeting Including the New Horizons Forum and Aerospace Exposition*, Dallas, USA, 2013.

[89] D. Schlipf and P. W. Cheng, "Adaptive feed forward control for wind turbines," *at - Automatisierungstechnik*, vol. 61, no. 5, pp. 329–338, 2013.

[90] A. Oppenheim and R. Schafer, *Discrete-time Signal Processing*. Pearson, 2010.

[91] F. Haizmann, P. Fleming, D. Schlipf, A. K. Scholbrock, M. Hofsäß, A. D. Wright, and P. W. Cheng, "Implementation of an online correlation analysis for an adaptive lidar based feed-forward controller for wind turbines," in *European Wind Energy Association annual event*, Vienna, Austria, 2013.

[92] D. Schlipf and M. Kühn, "Prospects of a collective pitch control by means of predictive disturbance compensation assisted by wind speed measurements," in *Proceedings of the German Wind Energy Conference DEWEK*, Bremen, Germany, 2008.

[93] J. Lunze, *Regelungstechnik 1: Systemtheoretische Grundlagen, Analyse und Entwurf Einschleifiger Regelungen*, 7th ed. Springer-Verlag Berlin / Heidelberg, Germany, 2008.

[94] M. Hansen and L. C. Henriksen, "Basic DTU wind energy controller," DTU Wind Energy, E-Report 0028(E), 2013.

[95] D. Schlipf, P. Fleming, F. Haizmann, A. Scholbrock, M. Hofsäß, A. Wright, and P. W. Cheng, "Field testing of feedforward collective pitch control on the CART2 using a nacelle-based lidar scanner," *Journal of Physics: Conference Series*, vol. 555, no. 1, p. 012090, 2014.

[96] K. Johnson, L. J. Fingersh, and A. Wright, "Controls advanced research turbine: Lessons learned during advanced controls testing," NREL, Tech. Rep. NREL/TP-500-38130, 2005.

[97] A. D. Wright, P. Fleming, and J. W. van Wingerden, "Refinements and tests of an advanced controller to mitigate fatigue loads in the controls advanced research turbine," in *Proceedings of the 49th AIAA Aerospace Sciences Meeting Including the New Horizons Forum and Aerospace Exposition*, Orlando, USA, 2011.

[98] A. Stotsky, B. Egardt, and O. Carlson, "Control of wind turbines: A tutorial on proactive perspectives," in *Proceedings of the American Control Conference*, Washington, USA, 2013.

[99] T. Utz, V. Hagenmeyer, and B. Mahn, "Comparative evaluation of nonlinear model predictive and flatness-based two-degree-of-freedom control design in view of industrial application," *Journal of Process Control*, vol. 17, no. 2, pp. 129–141, 2007.

[100] D. Schlipf and P. W. Cheng, "Flatness-based feedforward control of wind turbines using lidar," in *Proceedings of the 19th World Congress of the International Federation of Automatic Control*, Cape Town, South Africa, 2014.

[101] E. Bossanyi, B. Savini, M. Iribas, M. Hau, B. Fischer, D. Schlipf, T. van Engelen, M. Rossetti, and C. E. Carcangiu, "Advanced controller research for multi-MW wind turbines in the UpWind project," *Wind Energy*, vol. 15, no. 1, pp. 119–145, 2012.

[102] M. Fliess, J. Lévine, P. Martin, and P. Rouchon, "Flatness and defect of non-linear systems: introductory theory and examples," *International Journal of Control*, vol. 61, no. 6, pp. 1327–1361, 1995.

[103] M. Zeitz, "Feedforward control design in the frequency domain: Offline or online," *at - Automatisierungstechnik*, vol. 60, no. 7, pp. 375–383, 2012.

[104] K. Graichen and M. Zeitz, "Inversion-based feedforward control design under input and output constraints," *at - Automatisierungstechnik*, vol. 54, no. 4, pp. 187–199, 2006.

[105] J. J. Trujillo, A. Rettenmeier, and D. Schlipf, "Arrangements for enhanced measurements of a large turbine near-wake using lidar from the nacelle," *IOP Conference Series: Earth and Environmental Science*, vol. 1, no. 012060, 2008.

[106] P. Fleming, A. Wright, L. Fingersh, and J.-W. van Wingerden, "Resonant vibrations resulting from the re-engineering of a constant-speed 2-bladed turbine to a variable-speed 3-bladed turbine," in *Proceedings of the 49th AIAA Aerospace Sciences Meeting Including the New Horizons Forum and Aerospace Exposition*, Orlando, USA, 2011.

[107] B. Fetzer, "Vindicator laser wind turbine control system," in *IIT Workshop on Wind Energy Research*, Chicago, USA, 2011.

Curriculum Vitae

David Schlipf was born on December 5th, 1980 in Baden-Baden, Germany.
In 2001 he started studies of Engineering Cybernetics with specialization in Energy Systems at the University of Stuttgart, Germany. In parallel to his studies he collaborated as a graduate assistant in the development of a fuel cell vehicle at the German Aerospace Center in Stuttgart. From June 2005 to May 2006 he wrote his mid-study thesis and took lectures in Chemical Engineering, Politics and Informatics at the Universidade Federal do Rio Grande do Sul, Porto Alegre, Brazil. Back in Stuttgart, he worked during a internship of eight months on an industrial research project on fuel cell systems at the Robert Bosch GmbH. He received his Diploma in September 2007. His Diploma thesis was entitled "Application of optimisation methods to the startup procedure of fossil fired steam power plants".
He continued with the University of Stuttgart and joined the Stuttgart Wind Energy (SWE) at the Institute of Aircraft Design as a Research and Teaching Assistant in January 2008. In parallel to his dissertation titled "Lidar-Assisted Control Concepts for Wind Turbines" he worked on several national and European research projects. He supervised several Diploma and M.Sc. students and carried out teaching activities in the wind energy master and bachelor program at the University of Stuttgart. He was also invited lecturer at the Ph.D. Summer School Remote Sensing in Wind Energy from 2009 to 2012 and 2015 at Risø DTU, Denmark. During his Ph.D. he had several research stays at the National Renewable Energy Laboratory (NREL) in Boulder, USA. Since January 2013, he leads the research group "Control, Optimization and Monitoring" at the SWE.
From October 2014 to September 2015, he was a research scholar at University of Colorado Boulder and NREL continuing field tests of lidar-assisted controllers and performing postdoctoral research in the field of floating wind turbine control.